

JOURNAL of SPECTROSCOPY

# Complex MOLECULAR SYSTEMS

GUEST EDITORS: YIZHUANG XU, ISAO NODA, AND EDYTA PRONIEWICZ





---

# **Complex Molecular Systems**

Journal of Spectroscopy

---

## **Complex Molecular Systems**

Guest Editors: Yizhuang Xu, Isao Noda, and Edyta Proniewicz



---

Copyright © 2014 Hindawi Publishing Corporation. All rights reserved.

This is a special issue published in "Journal of Spectroscopy." All articles are open access articles distributed under the Creative Commons Attribution License, which permits unrestricted use, distribution, and reproduction in any medium, provided the original work is properly cited.



## Editorial Board

João Abrantes, Portugal  
Khalique Ahmed, USA  
Faisal M. Alamgir, USA  
Gabriele Arnold, Germany  
Naoki Asakawa, Japan  
Veer P. S. Awana, India  
Luciano Bachmann, Brazil  
Adam G. Balogh, Germany  
Malgorzata Baranska, Poland  
Lahcen Bih, Morocco  
Dhananjay Bodas, India  
Lars H. Böttger, Germany  
Damien Boyer, France  
Stefano Caldarelli, France  
Jose S. Camara, Portugal  
Brian Cannon, USA  
Elizabeth A. Carter, Australia  
Jairo Castillo-Chara, USA  
R. Sreekanth Chakradhar, India  
Wee Chew, Singapore  
Jau-Wern Chiou, Taiwan  
Myong Y. Choi, Republic of Korea  
Daniel O. Cicero, Italy  
Malcolm R. Clench, UK  
Stephen Cooke, USA  
Mircea Cotlet, USA  
Vincenza Crupi, Italy  
Eugen Culea, Romania  
Eric Da Silva, Canada  
Lesley Davenport, USA  
Alessandro De Giacomo, Italy  
Marcella Dell'aglio, Italy  
Renata Diniz, Brazil  
Ana Dominguez-Vidal, Spain  
Xuezhong Du, China  
Christophe Dujardin, France  
Thomas R. Eykyn, UK  
Roberto Flammini, Italy

Nives Galić, Croatia  
Gianfranco Giubileo, Italy  
Andras Gorzsas, Sweden  
S. Hernandez-Rivera, Puerto Rico  
Shuchen Hsieh, Taiwan  
Xinyang Huang, China  
Hiromi Ikeura-Sekiguchi, Japan  
Fumiyuki Ito, Japan  
Rodolphe Jaffiol, France  
Christopher K. Jankowski, Canada  
ZhiLiang Jiang, China  
Dale Keefe, Canada  
Rizwan Hasan Khan, India  
Jeongkwon Kim, Republic of Korea  
Scott J. Kirkby, USA  
Piotr Koczon, Poland  
Nikolaos Kourkoumelis, Greece  
Christoph Krafft, Germany  
Nikša Krstulović, Croatia  
Violeta Lazic, Italy  
Young Jong Lee, USA  
Adam F. Lee, UK  
Nicolae Leopold, Romania  
Min Soo Lim, USA  
Paola Luches, Italy  
Burkhard Luy, Germany  
Mahmoud A. Mahmoud, USA  
Petre Makreski, Macedonia  
Dmitriy Malinovsky, UK  
Djordje Mandrino, Slovenia  
Mohamed S. Marzouk, Egypt  
Thomas G. Mayerhofer, Germany  
Yehia Mechref, USA  
Abdelkarim Mekki, Saudi Arabia  
Gellert Mezei, USA  
Shinichi Morita, Japan  
Kouichi Nakagawa, Japan  
Austin Nevin, Italy

Ozlem Oter, Turkey  
Masaki Oura, Japan  
Giancarlo Pace, Portugal  
Carlos Andres Palacio, Belgium  
Jisheng Pan, Singapore  
Jose M. Pedrosa, Spain  
Simona C. Pinzaru, Romania  
Piotr Przybylski, Poland  
Awadhesh Rai, India  
K. S. V. Krishna Rao, India  
Tomasz Ruman, Poland  
Davidson Sajan, India  
Alan C. Samuels, USA  
Stephane Schilt, Switzerland  
Feride Severcan, Turkey  
Zhifeng Shao, USA  
Masanori Shinohara, Japan  
Maciej Sitarz, Poland  
Rafal Sitko, Poland  
Yuh-chang Sun, Taiwan  
Massimo Tallarida, Germany  
Riadh Ternane, Tunisia  
Kong-Thon Tsen, USA  
Pedro D. Vaz, Portugal  
Stéphane Viel, France  
Annemarie Wagner, Sweden  
Chuji Wang, USA  
Hui-Fen Wu, Taiwan  
Chih-Che Wu, Taiwan  
Lu Yang, Canada  
Maria Yebra-Biurrun, Spain  
Guoqiang Yu, USA  
Junwei Zheng, China  
Guang Zhu, Hong Kong  
Kassym Zhumadilov, Japan  
Zoran Zujovic, New Zealand  
M. Gizdavic-Nikolaidis, New Zealand

## Contents

**Quasielastic Light Scattering and Structure of Nanodroplets Mixed with Polycaprolactone**, Soheil Sharifi  
Volume 2014, Article ID 409508, 6 pages

**Exploring the Isomer Dependent SERS Spectra of (diphenylphosphoryl)(pyridin-2, -3, and -4-yl)methanol Adsorbed on Gold Nanocolloids**, Ewa Pięta, Edyta Proniewicz, Bogdan Boduszek, Tomasz K. Olszewski, Younkoo Kim, and Leonard M. Proniewicz  
Volume 2014, Article ID 894749, 7 pages

**The Preparation and Performances of Self-Dispersed Nanomicron Emulsified Wax Solid Lubricant Ewax for Drilling Fluids**, Feng-shan Zhou, Ting-ting Wang, Zheng-qiang Xiong, Wen-yue Guo, Xi Xiang, Huan-na Wang, Xia-lei Zhu, Fang Liu, and Bao-lin Cui  
Volume 2014, Article ID 530284, 7 pages

**Terahertz Absorption Spectroscopy of Benzamide, Acrylamide, Caprolactam, Salicylamide, and Sulfanilamide in the Solid State**, Ye Jiang, Fengshan Zhou, Xiaodong Wen, Limin Yang, Guozhong Zhao, He Wang, Haiyan Wang, Yanjun Zhai, Jinguang Wu, Kexin Liu, and Jia'er Chen  
Volume 2014, Article ID 732802, 9 pages

**Interaction of Bradykinin and B<sub>2</sub> Bradykinin Receptor Antagonists with Colloidal Au Surface Explored by Surface-Enhanced Raman Scattering**, Dominika Skoluba, Dariusz Sobolewski, Adam Prah, and Edyta Proniewicz  
Volume 2014, Article ID 619373, 8 pages

**Analysis of an Alanine/Arginine Mixture by Using TLC/FTIR Technique**, Jun Liu, Feng-shan Zhou, Ran Guo, Ye Jiang, Xiaokun Fan, Anqi He, Yanjun Zhai, Shifu Weng, Zhanlan Yang, Yizhuang Xu, Isao Noda, and Jinguang Wu  
Volume 2014, Article ID 925705, 4 pages

**Structure Characterization of [N-Phenylamino(2-boronphenyl)-R-methyl]phosphonic Acid by Vibrational Spectroscopy and Density Functional Theory Calculations**, Natalia Piergies and Edyta Proniewicz  
Volume 2014, Article ID 247237, 8 pages

**Synthesis and Characterization of CdS/TiO<sub>2</sub>-Montmorillonite Nanocomposite with Enhanced Visible-Light Absorption**, Feng-shan Zhou, Dai-mei Chen, Bao-lin Cui, and Wei-heng Wang  
Volume 2014, Article ID 961230, 5 pages

**The Use of FTIR-ATR Spectrometry for Evaluation of Surgical Resection Margin in Colorectal Cancer: A Pilot Study of 56 Samples**, Hongwei Yao, Xueying Shi, and Yuanfu Zhang  
Volume 2014, Article ID 213890, 4 pages

**Assessment of the Inhibitory Effect of Rifampicin on Amyloid Formation of Hen Egg White Lysozyme: Thioflavin T Fluorescence Assay versus FTIR Difference Spectroscopy**, Gang Ma, Hong Zhang, Jianhua Guo, Xiaodan Zeng, Xiaoqian Hu, and Wenying Hao  
Volume 2014, Article ID 285806, 5 pages

**The In Situ Polymerization and Characterization of PA6/LiCl Composites**, Dandan Sun, Jiang Li, Qinghua Pan, Chaowei Hao, and Guoqiao Lai  
Volume 2013, Article ID 164275, 4 pages

**A Promising Material by Using Residue Waste from Bisphenol A Manufacturing to Prepare Fluid-Loss-Control Additive in Oil Well Drilling Fluid**, Zhi-Lei Zhang, Feng-Shan Zhou, Yi-He Zhang, Hong-Wei Huang, Ji-Wu Shang, Li Yu, Hong-Zhen Wang, and Wang-Shu Tong  
Volume 2013, Article ID 370325, 10 pages

**Analysis of a Benzamide/Cholesterol Mixture by Using TLC/FTIR Technique**, Xiaokun Fan, Ran Guo, Jia-jia Shi, Haijun Wu, Anqi He, Yongju Wei, Cuige Liu, Shifu Weng, Zhanlan Yang, Yizhuang Xu, Isao Noda, and Jinguang Wu  
Volume 2013, Article ID 976360, 5 pages

**Fluorescent Properties of Hymecromone and Fluorimetric Analysis of Hymecromone in Compound Dantong Capsule**, Huanhuan Zhi, Jingdan Wang, Shujing Wang, and Yongju Wei  
Volume 2013, Article ID 147128, 9 pages

**Preparation and Characterization of Lanthanum Carbonate Octahydrate for the Treatment of Hyperphosphatemia**, Anqi He, Fengshan Zhou, Fang Ye, Ying Zhang, Xiren He, Xin Zhang, Ran Guo, Xing Zhao, Yan Sun, Ming Huang, Qin Li, Zhanlan Yang, Yizhuang Xu, and Jinguang Wu  
Volume 2013, Article ID 593636, 6 pages

**Spectroscopic and Gas Chromatographic Studies of Pigments and Binders in Gdańsk Paintings of the 17th Century**, Justyna Olszewska-Świetlik, Bożena Szmelter-Fausek, Ewa Pięta, and Edyta Proniewicz  
Volume 2013, Article ID 187407, 8 pages

**Improved Extended Multiplicative Scatter Correction Algorithm Applied in Blood Glucose Noninvasive Measurement with FT-IR Spectroscopy**, Qingbo Li, Qishuo Gao, and Guangjun Zhang  
Volume 2013, Article ID 916351, 5 pages

**Effect of Nitric Acid on the Low Fluorescing Performance of Drilling Fluid Lubricant Based Animal and Vegetable Oils**, Feng-shan Zhou, Zheng-qiang Xiong, Bao-lin Cui, Feng-bao Liu, Guang-huan Li, Jin-ran Wei, and Hua Cui  
Volume 2013, Article ID 269280, 7 pages

## Research Article

# Quasielastic Light Scattering and Structure of Nanodroplets Mixed with Polycaprolactone

**Soheil Sharifi**

*Department of Physics, Faculty of Sciences, Ferdowsi University of Mashhad, Mashhad 91775-1436, Iran*

Correspondence should be addressed to Soheil Sharifi; [ssharifi@ferdowsi.um.ac.ir](mailto:ssharifi@ferdowsi.um.ac.ir)

Received 24 September 2013; Revised 10 May 2014; Accepted 12 May 2014; Published 23 June 2014

Academic Editor: Edyta Proniewicz

Copyright © 2014 Soheil Sharifi. This is an open access article distributed under the Creative Commons Attribution License, which permits unrestricted use, distribution, and reproduction in any medium, provided the original work is properly cited.

The interaction of polycaprolactone (PCL) with droplets of a microemulsion is studied with quasielastic light scattering and small angle X-ray scattering. At constant droplet size we vary the PCL concentration and there is clear evidence for an increasing attractive interaction of the droplets from structural investigations with small-angle X-ray scattering (SAXS). The collective diffusion coefficient ( $D_c$ ) of the droplets is monitored with quasielastic light scattering (QELS). We mainly focus on the variation of the dynamic behavior as a function of the PCL concentration and length scale (M.W. = 5000 and 10000) in microemulsion. With increasing PCL concentration and length scale the dynamics of the system slow down. A hard sphere model with depletion potential can fit well the SAXS experiment of microemulsion mixed with PCL. The results show with increase of PCL on microemulsion the size of droplets is constant at 83 Å but the size ratio of polymer to droplets is changing.

## 1. Introduction

Quasielastic light scattering is a very useful method to characterize the structure of microemulsion, polymers, and nanoparticles in solution [1–9].

If the scattering particles of solutions are moving, fluctuations in the scattered intensity with time are directly reflecting the so-called Brownian particle motion of the scattering particles (caused by thermal density fluctuations of the solvent). This is the case because of a change in the interference pattern with changing interparticle position, and correspondingly a change in the detected scattered intensity were measured at a given scattering angle [10–16].

The microemulsions are a mixture of water oil and surfactant that they can form in different shapes as water droplets to oil solutions or oil droplets to the water solutions phase. The microemulsions are optically transparent and they are good for optical experiments.

The  $C_{12}E_5$  microemulsion consists of nanometer-size oil (decane) nanodroplets in water matrix stabilized by the pentaethylene glycol monododecyl ether ( $C_{12}E_5$ ). The structure and phase behavior of such microemulsions are well investigated. The mixture of microemulsion with polymer is

an interesting topic on soft matter physics [17–20]. The interesting subject in this field is depletion effect [20] and network transition in the polymer/microemulsion mixture [21]. The depletion interaction was observed at 1925 and it is shown by adding soluble polymers to a colloidal mixture which led to the aggregation of the colloids. The first description of this phenomenon was given by Asakura and Oosawa at 1954. The depletion was observed in several polymer/microemulsion mixtures [20].

The PCL is a biopolymer that it is water-soluble and the solubility of PCL in water depends on the molecular weight and concentration of PCL [22]. The QELS is used to study the effect of PCL on motion of nanodroplets of  $C_{12}E_5$  microemulsion. We know that the  $C_{12}E_5$  microemulsion shows spherical oil surfactant to the water nanodroplet phase between 24°C and 30°C [23–25]. The increase of PCL on aqueous phase of  $C_{12}E_5$  microemulsion can change free volume of solutions and the interaction between the nanodroplets (oil surfactant).

In this work, we study the effect of concentration and length scale of polycaprolactone (PCL) on droplets of  $C_{12}E_5$ /water/decane by QELS and small angle X-ray scattering (SAXS).

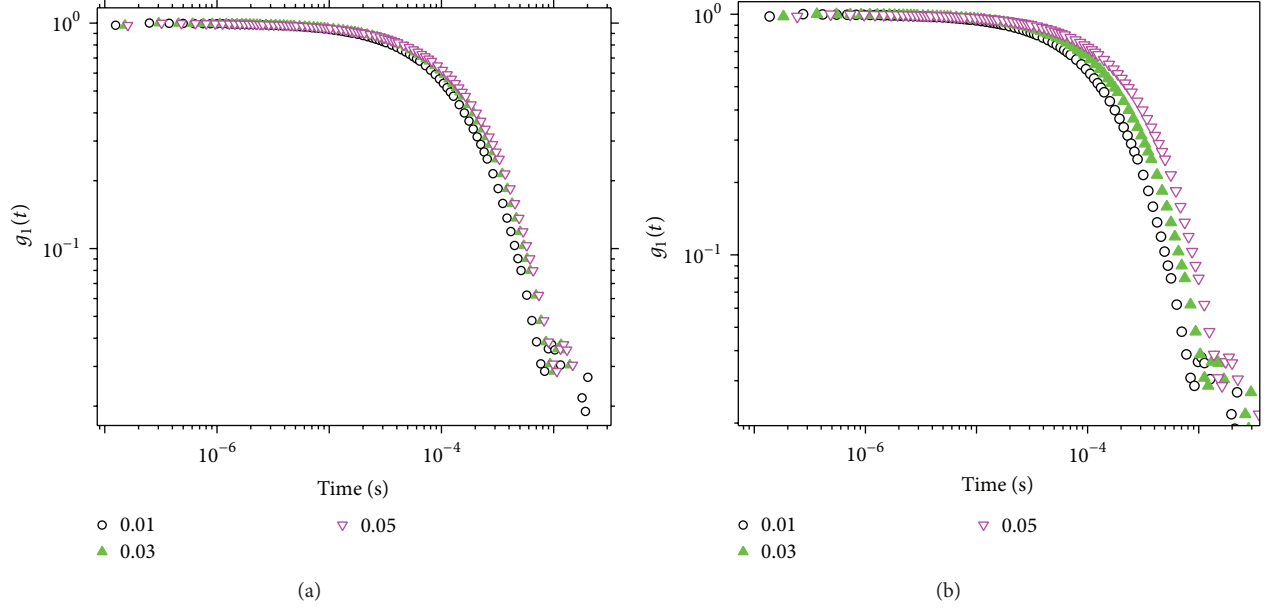


FIGURE 1: First-order field correlation function versus time for a mixture of  $C_{12}E_5$  microemulsion with PCL at droplet mass fraction (0.2) and  $m_{Dec}/m_{C_{12}E_5} = 1.08$  and different mass fractions of PCL (0.01, 0.03, and 0.05). (a) PCL with M.W. = 5000 and (b) PCL with M.W. = 10000.

## 2. Experiment

**2.1. Materials and Methods.** The pentaethylene glycol monododecyl ether ( $C_{12}E_5$ ) and n-decane were obtained from Sigma-Aldrich. Polycaprolactone (PCL) with molecular weight (M.W. = 5000 and 10000) was optioned from Polysciences company, Eppelheim, Germany. The microemulsion was prepared by weight, in terms of surfactant-oil mass ratio of 1.08 and the mass fraction of droplets ( $m_{f,drop} = (m_{Dec} + m_{C_{12}E_5})/(m_{Total})$ ), which varies by the respective mass of n-decane ( $m_{Dec}$ ),  $C_{12}E_5$  ( $m_{C_{12}E_5}$ ), and total sample mass ( $m_{Total}$ ). The samples of microemulsions with polymer were prepared by weight in terms of the mass fraction of triblock polymer ( $m_{f,poly} = m_{poly}/(m_{Total})$ ) that  $m_{poly}$  is the mass of polymer in the sample. The mixed samples were prepared at a constant surfactant-oil mass ratio of 1.08 with the different mass fractions of polycaprolactone (PCL) polymer. All samples were transparent at 25°C.

**2.2. Small Angle X-Ray Scattering.** Small angle X-ray scattering (SAXS) measurements were performed using the pinhole SAXS instrument at Nanolab company (KNL, Iran). A X'Pert Pro MPD small angle X-ray from PANalytical was employed to obtain SAXS patterns. The experiments were done at a fixed wavelength of  $\lambda = 1.54 \text{ \AA}$  and two different sample-detector distances.

**2.3. Quasielastic Light Scattering.** QELS measurements were performed using an ALV single-detector version compact goniometer system, from ALV-GmbH, Langen, Germany. The light source is a He-Ne laser, operating at a wavelength of 632 nm, with vertically polarized light. It has been seen that particles in dispersion are in a constant, random Brownian motion and that this causes the intensity of scattered light to

fluctuate as a function of time. The correlator used in a QELS instrument will construct the correlation function  $g(t)$  of the scattered intensity [1, 2]:

$$g(\tau) = \frac{\langle I(t) I(t + \tau) \rangle}{\langle I^2(t) \rangle}, \quad (1)$$

where  $\tau$  is decay times. For a large number of particles in Brownian motion, the correlation function is an exponential decaying function of the correlator time delay [1, 2]:

$$g(t) = A [1 + B \exp(-2\Gamma t)], \quad (2)$$

where  $A$  is the baseline of the correlation function and  $B$  is an intercept of the correlation function. Consider the following:

$$\Gamma = q^2 D, \quad (3)$$

where  $D$  is a translational diffusion coefficient and  $q = 4\pi n/\lambda \sin(\theta/2)$ , where  $n$ ,  $\lambda$ , and  $\theta$  are refractive index of dispersant, wavelength of the laser, and scattering angle.

## 3. Results and Discussions

Microemulsions were prepared by mixing  $C_{12}E_5$  with n-decane and water at a constant droplet mass fraction (0.2) and  $m_{Dec}/m_{C_{12}E_5} = 1.08$ . Figures 1 and 2 show the correlation function ( $g(\tau)$ ) as a function of decay time for  $C_{12}E_5$  microemulsion mixed with PCL (M.W. = 5000 and 10000). The correlation function of the scattered light intensity as a function of delay time showed a single exponential decay at all concentrations; see Figure 1.

From the inverse decay times, which vary linearly with the square of the momentum transfer, the collective diffusion

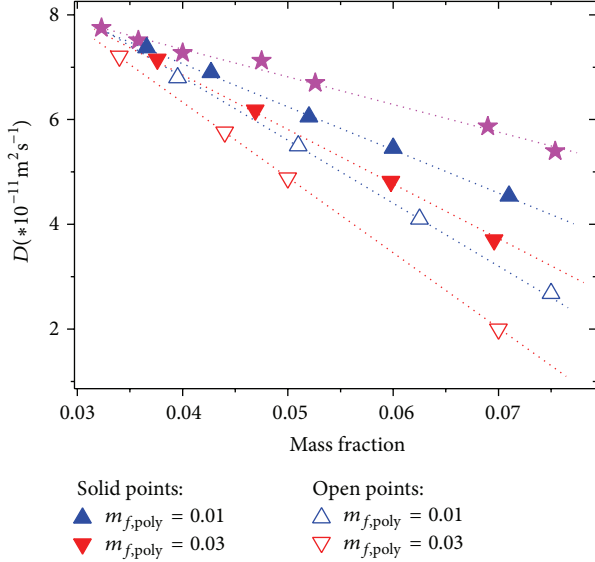


FIGURE 2: The collective diffusion of a mixture of  $C_{12}E_5$  microemulsion with PCL at constant droplet mass fraction (0.2) and  $m_{Dec}/m_{C_{12}E_5} = 1.08$ . The solid points are a mixture of  $C_{12}E_5$  with PCL with M.W. = 5000 and different polymer mass fractions and open points are a mixture of  $C_{12}E_5$  microemulsion with PCL with M.W. = 10000 and polymer mass fraction.

coefficient ( $D_c$ ) was extracted as a function of the droplet mass fraction from (2) and (3).

The negative slope of collective diffusion coefficient as a function of droplet mass fraction of pure  $C_{12}E_5$  microemulsion and polymer microemulsion shows attractive interaction between nanodroplets at microemulsion; see Figure 2. The decreasing slope of collective diffusion coefficient as a function of mass fraction shows the increasing attractive interaction between the droplets; see Figure 2.

In Figure 2, the mixture of microemulsion with two concentration polymer mass fractions ( $m_{f,poly} = 0.01$  up-triangle solid points and  $m_{f,poly} = 0.03$  down-triangle solid points) of PCL (M.W. = 5000) and the open up- and down-triangle points are microemulsion with PCL (M.W. = 10000). It is clear with the collective diffusion coefficient of droplets decreasing with the increase of molecular weight and concentrations of PCL inside the microemulsion.

A study with QELS shows that the mixture of  $C_{12}$ -polyethylene oxide- (PEO-)  $C_{12}$  with  $C_{12}E_5$  microemulsion induces a network between nanodroplets at  $C_{12}E_5$  microemulsion that it is found that the increase of  $C_{12}$ -PEO- $C_{12}$  can produce fast and slow motions (collective diffusion coefficient) in the microemulsion [21], and the origin of those motions comes from connected and nonconnected nanodroplets inside the  $C_{12}$ -PEO- $C_{12}/C_{12}E_5$  microemulsion. These two motions were observed from correlation function  $g(\tau)$  [21]. In our samples, the mixture of PCL with  $C_{12}E_5$  microemulsion shows a motion (collective diffusion coefficient), so we can propose that PCL cannot be able to produce a network between the nanodroplets.

The depletion effect was observed in the mixture of polyethylene glycol (PEG) with  $C_{12}E_5$  microemulsion

TABLE 1: The results of analyzing the SAXS experiments with hard sphere depletion model that is explained in the text; PDI is polydispersity of PCL/ $C_{12}E_5$  microemulsion.

M.W.	$m_{f,drop}$	$m_{f,poly}$	Size ratio	Core	Core + shell	PDI
5000	0.2	0.008	0.43	72	83	0.2
	0.2	0.012	0.38	72	83	0.2
	0.2	0.025	0.31	72	83	0.2
	0.2	0.05	0.27	72	83	0.2
	0.2	0.08	0.24	72	83	0.2
10000	0.2	0.007	0.51	72	83	0.2
	0.2	0.01	0.48	72	83	0.2
	0.2	0.02	0.46	72	83	0.2
	0.2	0.051	0.44	72	83	0.2
	0.2	0.08	0.41	72	83	0.2

[24, 25], and these results show the increase in PEG concentration lead to increasing depletion effect. The studied depletion effect with QELS shows that the depletion effect can show one single motion (collective diffusion coefficient) and with increase of PEG concentration the collective diffusion is decreasing [24, 25].

In order to characterize the structure of the pure as well as the PCL containing  $C_{12}E_5$  microemulsions we applied small angle X-ray scattering. The scattered intensity as a function of  $q$  for  $C_{12}E_5$ /water/n-decane mixed with PCL is showed in Figure 3.

The scattered intensity is recorded with a 2-dimensional detector at a distance of 150 cm from the sample leading to an accessible range of scattering vectors  $q = 0.002\text{\AA}^{-1} - 0.15\text{\AA}^{-1}$ .

In order to extract the structural information from the X-ray data, the following model will be employed. For analyzing the SAXS data's a hard sphere model with an attractive interaction is used. The results of analyzing are presented in Table 1.

The results of analyzing show the droplets size of microemulsion is constant at  $R_{SAXS} = 8.3\text{ nm}$  for different concentrations and molecular weights of PCL.

The size ratio (size ratio of nanodroplet over polymer) is changing from 0.43 to 0.24 with increase of polymer concentration with low molecular weight (M.W. = 5000) and it changes from 0.51 to 0.41 for high molecular weight of polymer (M.W. = 10000). For both cases with the increase of concentration the length scale is decreasing.

One possibility to obtain information about internal structure of the particles is the indirect Fourier transformation (IFT) technique, resulting in the pair density distribution function, PDDF. This calculation is performed completely model-free and requires only a rough estimate of the maximum dimension of the particle. This method is useful for dilute systems.

The influence of the interaction effects can be computed by simultaneous calculation of the form factor and the structure factor, leading to a PDDF limited to intraparticle contributions. This can be achieved by the generalized indirect Fourier transformation (GIFT) technique [26].

The GIFT with a model with a depletion potential is used to extract the structure factor (Figure 4). The  $S(q)$  as



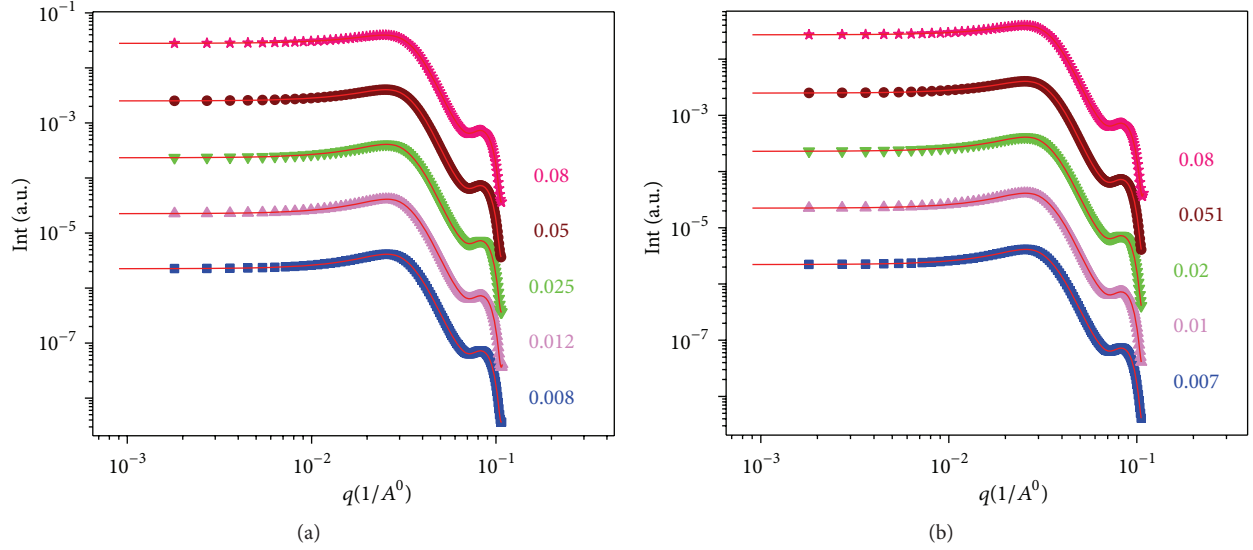


FIGURE 3: The SAXS experiment of a mixture of  $C_{12}E_5$ /water/n-decane PCL at a constant droplet mass fraction (0.2) and  $m_{Dec}/m_{C_{12}E_5} = 1.08$  with different concentrations of PCL. (a) PCL with M.W. = 5000 and (b) PCL with M.W. = 10000.

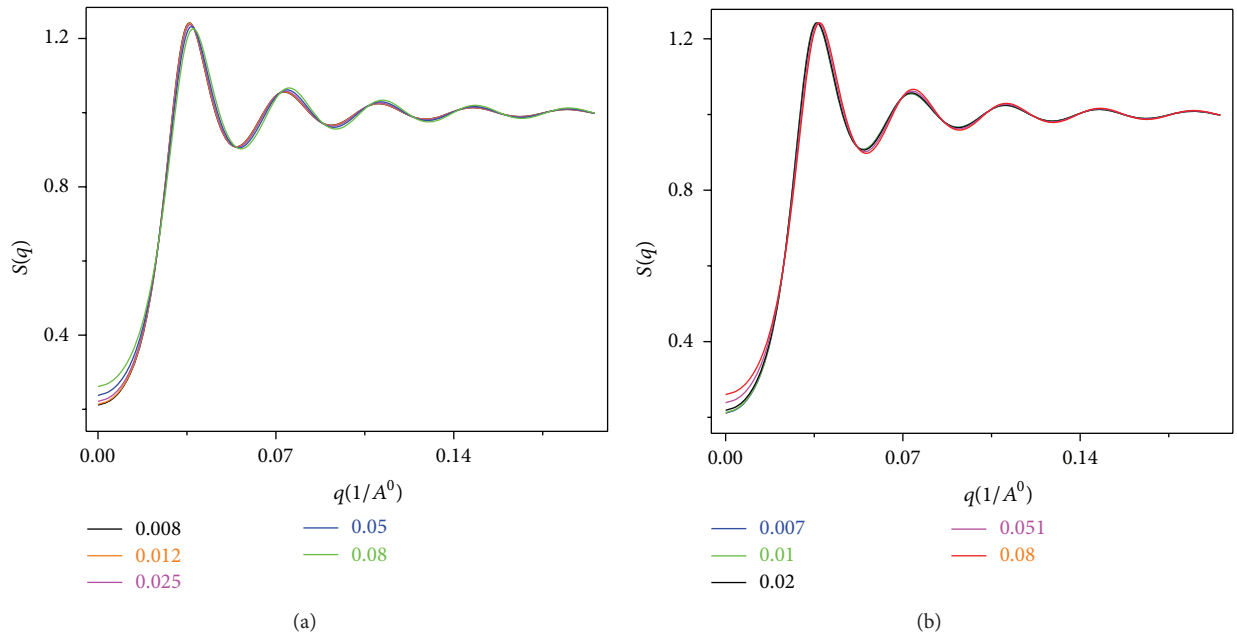


FIGURE 4: The structure factor of a mixture of  $C_{12}E_5$ /water/n-decane PCL at a constant droplet mass fraction (0.2) and  $m_{Dec}/m_{C_{12}E_5} = 1.08$  with different concentrations of PCL. (a) PCL with M.W. = 5000 and (b) PCL with M.W. = 10000.

a function of  $q$  for a mixture of  $C_{12}E_5$  microemulsion with different concentrations of PCL shows a peak at  $q = 0.036 \text{ \AA}^{-1}$  (Figure 4). This peak does not change with changing weight length and concentration of PCL but the value of the structure factor at low  $q$  ( $q = 0$ ) increases with increasing of PCL concentration (Figure 5). The different molecular weights of PCL (5000 and 10000) have similar effect on intensity of low  $q$  (Figure 5).

This behavior is similar to the mixture of PEG with  $C_{12}E_5$  microemulsion [24, 25]. In general, increasing of structure

factor at low  $q$  can explain type of interaction between droplets. The increasing of structure factor at low  $q$  shows increase of attractive interaction between droplets. So, in our case we can propose that increase of PCL concentration can increase attractive interaction between nanodroplets. A study on the mixture of end-capped polymer with microemulsion shows that the narrow peak at structure factor describes the increase of order in systems [21]; in the case of our system the first peak is constant at PCL/ $C_{12}E_5$  microemulsion which explains the order of droplets does not change with increase of PCL concentration.

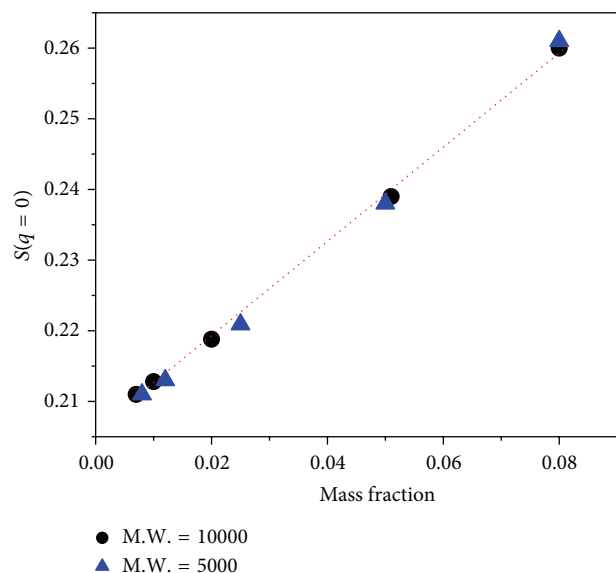


FIGURE 5: The structure factor of a mixture as a function of polymer mass fraction of  $C_{12}E_5$ /water/n-decane at  $q = 0$  at a constant droplet mass fraction (0.2) and  $m_{Dec}/m_{C_{12}E_5} = 1.08$ . The circle points are PCL with M.W. = 5000 and up-triangle is PCL with M.W. = 10000.

#### 4. Conclusions

SAXS and QELS have been used to study the mixture of different weight lengths and concentrations of PCL mixed with  $C_{12}E_5$ /water/n-decane microemulsion. The results show a depletion interaction due to the fact that the increase of amount of PCL can decrease the motion of nanodroplets inside microemulsion. The different molecular weights of PCL (5000 and 10000) have similar effect on attractive interaction. The SAXS data's could describe the depletion model quantitatively. The result of SAXS with data's shows the size of nanodroplets is constant but the size ratio is decreasing with increase of PCL in the microemulsion that it is due to aggregation of PCL in the solutions. The depletion effect can describe well the behavior of collective diffusion coefficient with increase of PCL concentrations.

#### Conflict of Interests

The author declares that there is no conflict of interests regarding the publication of this paper.

#### References

- [1] B. J. Berne and R. Pecora, *Dynamic Light Scattering: With Applications to Chemistry, Biology, and Physics*, John Wiley & Sons, 1976.
- [2] C. S. Johnson and D. A. Gabriel, *Lasers Light Scattering*, John Wiley & Sons, 1957.
- [3] B. Chu, *Laser Light Scattering: Basic Principles and Practice*, American Press, 1974.
- [4] J. Cieřła, A. Bieganowski, J. Narkiewicz-Michalek, and M. Szymula, "Use of a dynamic light scattering technique for SDS/water/pentanol studies," *Journal of Dispersion Science and Technology*, vol. 34, no. 4, pp. 566–574, 2013.
- [5] C. J. Doran, "Photon correlation spectroscopy and velocimetry," *Optica Acta: International Journal of Optics*, vol. 25, no. 3, pp. 271–272, 1978.
- [6] A. M. Bellocq, G. Fourche, P. Chabrat, L. Letamendia, J. Rouch, and C. Vaucamps, "Dynamic light scattering study of concentrated W/O microemulsions," *Optica Acta: International Journal of Optics*, vol. 27, no. 12, pp. 1629–1639, 1980.
- [7] J. P. Boon and S. Yip, "Correlated dynamics and light scattering in microemulsions," *Optica Acta: International Journal of Optics*, vol. 29, no. 9, pp. 1167–1169, 1982.
- [8] D. Caroline, "Measurement of suspended particles by quasi-elastic light scattering," *Optica Acta: International Journal of Optics*, vol. 31, no. 3, pp. 276–277, 1984.
- [9] M. Weinberg, "Light scattering: iandau-placzek ratio and total intensity," *Physics and Chemistry of Liquids*, vol. 4, no. 2-3, pp. 163–170, 1974.
- [10] P. R. Berman, "Light scattering," *Contemporary Physics*, vol. 49, no. 5, pp. 313–330, 2008.
- [11] A. Cao, "Light scattering. Recent applications," *Analytical Letters*, vol. 36, no. 15, pp. 3185–3225, 2003.
- [12] E. J. Derderian and T. B. MacRury, "Quasielastic light scattering on standard poly(styrene) lattices," *Journal of Dispersion Science and Technology*, vol. 2, no. 2-3, pp. 345–358, 1981.
- [13] N. B. Behzadi and S. Sharifi, "Light scattering and SAXS of spherical to cylindrical transition of AOT/ $H_2O$ /cyclohexane/PI," *Physics and Chemistry of Liquids*, vol. 52, no. 3, pp. 428–435, 2014.
- [14] N. Karimi, S. Sharifi, and M. Aliahma, "Photon correlation spectroscopy and SAXS study of mixture of NaCl with AOT Microemulsion at  $X = 6.7$ ," *Optics and Photonics Journal*, vol. 2, no. 1, pp. 54–58, 2012.
- [15] K. Nikjoo, M. Aliahmad, S. Sharifi, and M. Sargazi, "Photon correlation spectroscopy and SAXS study of cylindrical to spherical transition in the AOT microemulsion by changing solvent," *Soft Nanoscience Letters*, vol. 2, no. 2, pp. 17–21, 2012.
- [16] S. Sharifi, M. R. Mohammadi, M. Aliahmad, O. Marti, and M. Amirkhani, "The effect of TBAC on the collective diffusion coefficient and morphology of AOT microemulsion at  $X = 6.7$ ," *Physics and Chemistry of Liquids*, vol. 51, no. 4, pp. 469–479, 2013.
- [17] C.-A. Peng and F. Huang, "Formation of perfluorocarbon microemulsion by fluorinated polyethylene glycol," *Journal of Dispersion Science and Technology*, vol. 29, no. 1, pp. 46–51, 2008.
- [18] M. Bisceglia, D. H. Kurlat, J. P. Chéret, and B. Ginzberg, "Measurements of the Kerr effect in W/O microemulsions up to the proximity of a  $W_{II} \rightarrow W_{III}$  transition," *Physics and Chemistry of Liquids*, vol. 25, no. 2, pp. 127–134, 1993.
- [19] S. Sharifi, G. V. Jensen, J. S. Pedersen, O. Marti, and M. Amirkhani, "The mixture of poly(propylene-glycol)-block-poly(ethylene-glycol)-block-PPG with  $C_{12}E_5$  microemulsion," *Physics and Chemistry of Liquids*, vol. 52, no. 1, pp. 113–121, 2014.
- [20] S. Sharifi, O. Marti, S. S. Funari, and M. Amirkhani, "The effect of different polymer length on water droplets of reverse AOT microemulsion," *Physics and Chemistry of Liquids*, vol. 51, no. 5, pp. 586–594, 2013.
- [21] M. Amirkhani, S. Sharifi, and O. Marti, "The effect of simultaneous size reduction and transient network formation on the dynamics of microemulsions," *Journal of Physics D: Applied Physics*, vol. 45, no. 36, Article ID 365302, 2012.



- [22] C. Bordes, V. Fréville, E. Ruffin et al., "Determination of poly( $\epsilon$ -caprolactone) solubility parameters: application to solvent substitution in a microencapsulation process," *International Journal of Pharmaceutics*, vol. 383, pp. 236–243, 2010.
- [23] M. Nayeri, M. Zackrisson, and J. Bergenholtz, "Scattering functions of core-shell-structured hard spheres with Schulz-distributed radii," *Journal of Physical Chemistry B*, vol. 113, no. 24, pp. 8296–8302, 2009.
- [24] M. Zackrisson, R. Andersson, and J. Bergenholtz, "Depletion interactions in model microemulsions," *Langmuir*, vol. 20, no. 8, pp. 3080–3089, 2004.
- [25] S. Sharifi and M. Amirkhani, "Light scattering study of mixture of polyethylene glycol with  $C_{12}E_5$  microemulsion," *Soft Nanoscience Letters*, vol. 1, no. 3, pp. 76–80, 2011.
- [26] J. Brunner-Popela and O. Glatter, "Small-angle scattering of interacting particles. I. Basic principles of a global evaluation technique," *Journal of Applied Crystallography*, vol. 30, no. 4, pp. 431–442, 1997.

## Research Article

# Exploring the Isomer Dependent SERS Spectra of (diphenylphosphoryl)(pyridin-2-, -3, and -4-yl)methanol Adsorbed on Gold Nanocolloids

Ewa Pięta,<sup>1</sup> Edyta Proniewicz,<sup>2</sup> Bogdan Boduszek,<sup>3</sup> Tomasz K. Olszewski,<sup>3</sup> Younkyyo Kim,<sup>4</sup> and Leonard M. Proniewicz<sup>1</sup>

<sup>1</sup> Faculty of Chemistry, Jagiellonian University, ul. Ingardena 3, 30-060 Krakow, Poland

<sup>2</sup> Faculty of Foundry Engineering, AGH University of Science and Technology, ul. Reymonta 23, 30-059 Krakow, Poland

<sup>3</sup> Department of Organic Chemistry, Faculty of Chemistry, Wrocław University of Technology, Wybrzeże Wyspiańskiego 27, 50-370 Wrocław, Poland

<sup>4</sup> Department of Chemistry, Hankuk University of Foreign Studies, Yongin, Kyunggi-do 449-791, Republic of Korea

Correspondence should be addressed to Edyta Proniewicz; [proniewi@agh.edu.pl](mailto:proniewi@agh.edu.pl)

Received 2 September 2013; Accepted 2 March 2014; Published 29 May 2014

Academic Editor: Yizhuang Xu

Copyright © 2014 Ewa Pięta et al. This is an open access article distributed under the Creative Commons Attribution License, which permits unrestricted use, distribution, and reproduction in any medium, provided the original work is properly cited.

The surface-enhanced Raman scattering (SERS) spectra of three aminophosphonate derivatives of pyridine: (diphenylphosphoryl)(pyridin-2-yl)methanol ( $\alpha$ -Pyr), (diphenylphosphoryl)(pyridin-3-yl)methanol ( $\beta$ -Pyr), and (diphenylphosphoryl)(pyridin-4-yl)methanol ( $\gamma$ -Pyr) were measured after immobilization onto colloidal gold surface. Changes in the wavenumber, broadness, and enhancement between the corresponding Raman and SERS bands allowed to deduce orientation of the  $\alpha$ -,  $\beta$ -, and  $\gamma$ -isomers ( $\alpha$ -,  $\beta$ -, and  $\gamma$ -refer to the position of the substituent relative to the ring nitrogen atom) of aminophosphonate derivatives of pyridine on the gold surface. Briefly, it was demonstrated that the  $\alpha$ -Pyr and  $\beta$ -Pyr show the same mode of adsorption, whereas the adsorption process of the  $\gamma$ -Pyr isomer differs in this regard that pyridine assists in the interaction with the gold surface.

## 1. Introduction

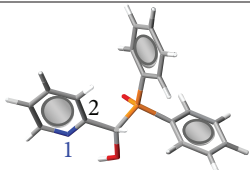
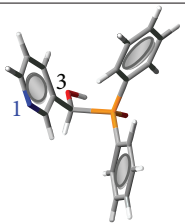
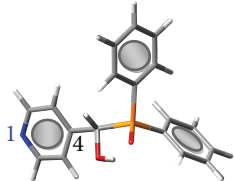
Aminophosphonic acids and their derivatives are very promising group of compounds due to their occurrence in organisms and numerous important biological activities [1]. Their biological capabilities are connected with the inter-action with metal ions [2]. In the last few years, there has been an increasing interest in the field of synthesis and investigation of pyridine aminophosphonic acids because of their potential and significant antitumor properties [2, 3]. The previous study on aminophosphonate derivatives of pyridine has proved the high reactivity of aminophosphonate ligands bearing *N*-heterocyclic donor atom [2, 4]. Consequently, it has been demonstrated that the nitrogen-containing heterocyclic compounds have a wide range of applications ranging from anticancer [5], antituberculosis [6], antiproliferation [7], to enzyme inhibitors or chelating agents for heavy metal ions [8]. Among the nitrogen-containing molecules, pyridine



derivatives play an essential role in many areas; that is, they are used as vitamins like nicotinic acid and nicotinic acid amide, vitamin B, herbicides, and insecticides [9].

In this study, we investigated three aminophosphonate derivatives of pyridine, including (diphenylphosphoryl)(pyridine-2-yl)methanol ( $\alpha$ -Pyr), (diphenylphosphoryl)(pyridin-3-yl)methanol ( $\beta$ -Pyr), and (diphenylphosphoryl)(pyridin-4-yl)methanol ( $\gamma$ -Pyr) (Table 1 shows molecular structures of these compounds) using surface-enhanced Raman scattering (SERS) technique. We focused on the spectral changes related to the different position of the substituent (1-(diphenylphosphoryl)metanol) with respect to the pyridine nitrogen atom, in  $\alpha$ -,  $\beta$ -, and  $\gamma$ -position, respectively.

Raman spectroscopy is a very useful method in the field of chemical analysis because it provides information about the vibrational structure and adsorption mode occurring at the solid/liquid interface [10]. However, the Raman process has extremely small cross section which limits its application

TABLE 1: Molecular structures of the investigated compounds.

Molecular structure	Abbreviation	Name
	$\alpha$ -Pyr	(diphenylphosphoryl)(pyridin-2-yl)methanol
	$\beta$ -Pyr	(diphenylphosphoryl)(pyridin-3-yl)methanol
	$\gamma$ -Pyr	(diphenylphosphoryl)(pyridin-4-yl)methanol

Color legend: : the carbon, : the oxygen, : the nitrogen, : the phosphorus, and : the hydrogen atoms.

[11]. This limitation can be overcome and strongly enhanced Raman spectra (by up to  $10^{14}$ - $10^{15}$ ) can be obtained when the molecule is adsorbed onto roughened or colloidal metal surface [12, 13]. The tremendous increase of the SERS signal can be achieved with relatively few metals: Ag, Au, Cu, and less frequently with Pt [14]. Generally, there are two major factors responsible for this enhancement. The first mechanism is due to the metal plasmon resonance excitation, which increases the local fields in close proximity to the roughened metal surface or metal nanoparticles. The second, less significant factors concern the chemical effects, in particular the metal-molecule charge-transfer transition and other changes due to the adsorption process [12]. Analysis of the SERS signal (enhancement, wavenumber, and broadness) due to the molecular fragment vibrations of the investigated compound is essential for description of the possible way in which the adsorbate can interact with the surrounding medium [15–20]. Thus, SERS is a great tool for low-level detection and analysis, even for the single molecule detection. In a broader sense, this technique can be used for studying transport phenomenon across biological membranes or the kinetics of charge-transfer processes at an electrochemically roughened substrate [14].

## 2. Materials and Methods

**2.1. (Diphenylphosphoryl)(pyridin-2, -3, and -4-yl)methanol Synthesis.** (Diphenylphosphoryl)(pyridin-2-yl)methanol, (diphenylphosphoryl)(pyridin-3-yl)methanol, and (diphenylphosphoryl)(pyridin-4-yl)methanol were synthesized according to a previously described procedure [21, 22]. The purity and chemical structures of the samples were proved by

$^1\text{H}$ ,  $^{31}\text{P}$ , and  $^{13}\text{C}$  NMR spectra and electrospray mass spectrometry analysis.

**2.2. FT-Raman Measurements.** The FT-Raman spectra were recorded using a Nicolet spectrometer (model NXR 9650) coupled with a liquid-nitrogen-cooled germanium detector. All spectra were acquired with a resolution of  $4\text{ cm}^{-1}$  and 1000 scans were usually collected. The spectrometer was equipped with a continuum-wave Nd:YAG laser emitting light at 1064 nm with total output power of up to 200 mW.

**2.3. SERS Measurements.** Colloidal gold nanoparticles (20 nm, concentration: 0.02 mg/mL in aqueous buffer, contains sodium citrate as stabilizer) were purchased from Sigma-Aldrich Co. (Poznan, Poland). Aqueous sample solutions were prepared by dissolving each compound in deionized water. The concentration of the sample before mixing with the colloid was adjusted to  $10^{-4}\text{ M}$ . Briefly, 20  $\mu\text{L}$  of the aqueous sample solution was added to 40  $\mu\text{L}$  of the gold colloid and stirred vigorously.

The SERS spectra of the investigated compounds were collected three times with InVia Renishaw spectrometer equipped with an air-cooled charge-coupled device (CCD) detector. The spectral resolution was set at  $4\text{ cm}^{-1}$ . The continuous-wave diode laser (HP NIR) with the 785 nm excitation line was used as an excitation source. The laser power at the sample was set at 10 mW.

All of the SERS spectra were recorded within one hour of adding the sample to the Au colloid. The obtained spectra were almost identical, except for small differences (up to 5%) in some band intensities. No spectral changes that could be

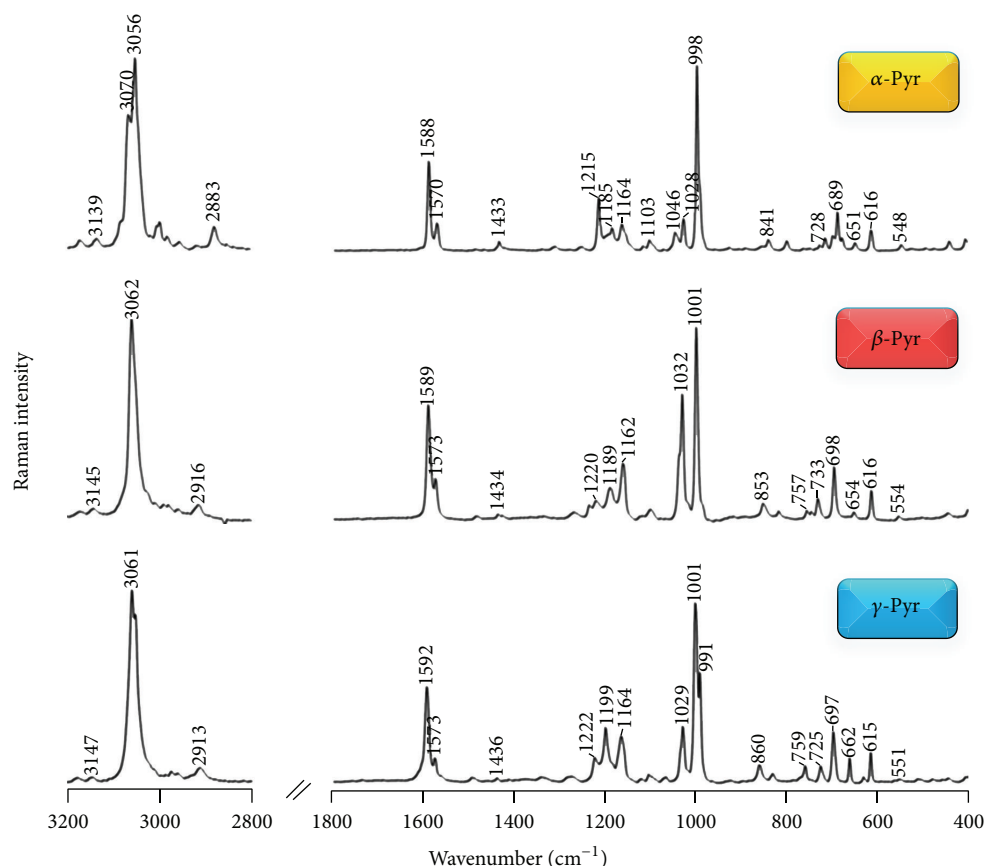


FIGURE 1: The FT-RS spectra of  $\alpha$ -Pyr,  $\beta$ -Pyr, and  $\gamma$ -Pyr in the spectral ranges of 3200–2800 and 1800–400  $\text{cm}^{-1}$ .

associated with sample decomposition were observed during these measurements.

### 3. Results and Discussion

Figure 1 shows the FT-Raman spectra of the three aminophosphonate derivatives of pyridine:  $\alpha$ -Pyr,  $\beta$ -Pyr, and  $\gamma$ -Pyr, in the solid state in the spectral ranges between 3200–2800 and 1800–400  $\text{cm}^{-1}$ . Figure 2 presents the SERS spectra of these compounds in an aqueous gold sol. Table 2 summarized wavenumbers, full band widths at half maximum (FWHM), and proposed band assignments of the SERS bands together with those observed in the corresponding Raman spectra. The proposed band allocation to the normal mode motions is based on the density functional theory calculations performed for these molecules [23] and the Raman spectra of compounds that contain similar molecular fragments [10, 24–32].

Comparison of the SERS (Figure 2) spectrum of each of the investigated pyridine  $\alpha$ -hydroxymethyl biphenyl phosphine oxides with the proper Raman spectrum (Figure 1) reveals similarity in the corresponding bands width and wavenumbers (see Table 2). However, few differences are noticeable in the enhancement of certain bands. These differences concern mainly the 1570 [ $\nu_{8b}$ ], 1215 [ $\nu_{9a}(\text{Pyr})$ ], 1046 [ $\nu_{12}(\text{Pyr})$ ], and 992  $\text{cm}^{-1}$  [ $\nu_1(\text{Pyr})$ ] Raman and

the 550 [ $\gamma(\text{CO}) + \rho_{as}(\text{Phe})$ ] and 530  $\text{cm}^{-1}$  [ $\gamma(\text{CO}) + \rho(\text{CP}=\text{O}) + \rho_{as}(\text{Phe}) + \delta_{oop}(\text{CC}(\text{P})\text{C})$ ] SERS bands (see Table 2 for detailed band wavenumbers). The former Raman spectral features are weak or absent in the SERS spectra. In addition, increase in the relative intensity of the 998 [ $\nu_{12}(\text{Phe})$ ] and 1102  $\text{cm}^{-1}$  [ $\nu(\text{CO}) + \nu(\text{PC}_{\text{phe}})$ ] SERS signals and decrease in the 1588  $\text{cm}^{-1}$  [ $\nu_{8a}$ ] SERS band relative enhancement are evident for all the investigated molecules in comparison with those in the Raman spectra.

Group theory provides the most elegant framework to use of the aforementioned bands' relative intensity changes to predict the geometries of aromatic molecules adsorbed onto SERS-active substrates [33]. Under assumptions that the vibrations involving atoms close to the metal surface are enhanced due to their interactions with the metal surface, the “surface selection rules” for a perpendicular ring orientation designate the in-plane vibrations to be enhanced to a greater extent than the out-of-plane vibrations. The opposite should be the case for the horizontal adsorption geometry. In addition, according to the propensity rules of the electromagnetic mechanism of SERS, the strongest SERS bands of the perpendicular phenyl ring with respect to the metal surface are due to the  $\nu_{12}$  mode [34]. Gao and Weaver reported that  $\nu_{12}$  of alkylbenzenes shifts down by 10–15  $\text{cm}^{-1}$  upon adsorption at the surface. In contrast, the observed downshift by 4–5  $\text{cm}^{-1}$  for this mode of halogenobenzenes

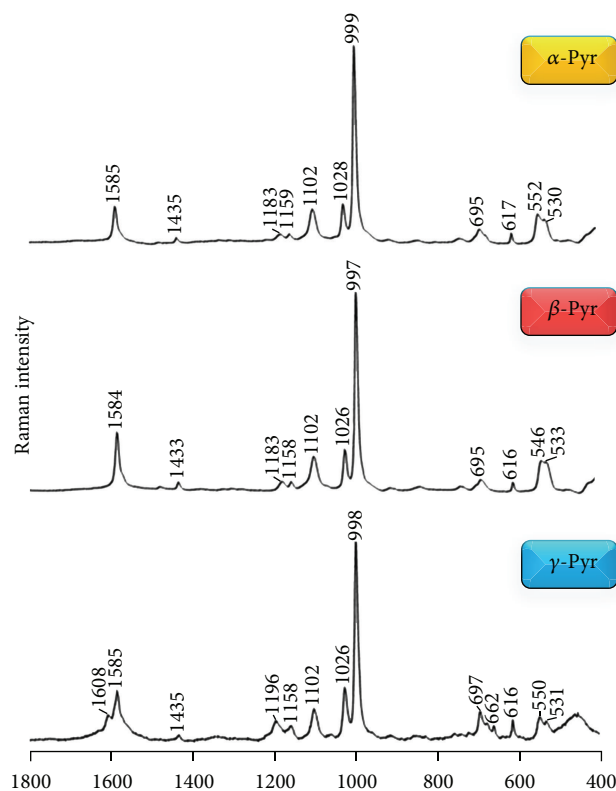


FIGURE 2: The SERS spectra of  $\alpha$ -Pyr,  $\beta$ -Pyr, and  $\gamma$ -Pyr adsorbed onto colloidal gold surface.

was interpreted as evidence of no direct interaction between the  $\pi$ -electron systems and the metal surface. Also, significant band broadening for the aromatic ring modes was reported in the case of  $\pi$  adsorption caused by an interaction between the ring and the metal surface [35].

The foregoing “surface selection rules” and spectral changes as well as the c.a. 1590 [ $\nu_{8a}$ ], c.a. 1435 [ $\nu_{19b}$ ], c.a. 1198 [ $\nu_{9a}$  and/or  $\nu_{sym}(C_\beta C_\gamma H_2 C_\delta)$ ], c.a. 1026 [ $\nu_{18a}$ ], c.a. 998 [ $\nu_{12}$ ], c.a. 695 [ $\nu_{6a}$ ], and c.a. 616  $cm^{-1}$  [ $\nu_{6b}(Phe)$ ] SERS signals imply an essentially perpendicular orientation of the phenyl rings of  $\alpha$ -Pyr,  $\beta$ -Pyr, and  $\gamma$ -Pyr on the colloidal gold nanoparticles, whereas the pyridine ring of these molecules is not involved in the adsorption process. However, considering the molecular structure of pyridine  $\alpha$ -hydroxymethyl biphenyl phosphine oxides, it seems unlikely that both the phenyl rings adopt the same vertical geometry with respect to the gold surface (one the 998  $cm^{-1}$  band, FWHM = 9  $cm^{-1}$ ). Thus, we postulate that only one of the equivalent phenyl rings is involved in the interaction with Au. On the other hand, the moderate strengthening of the 1102, 550, and 530  $cm^{-1}$  spectral features between the Raman and SERS spectra results from bonding interaction between Au and the  $-OCP(=O)-$  molecular fragment. Therefore, the O–C and P=O bonds should adopt a tilted orientation with respect to the gold surface. Such an arrangement favors interaction of the oxygen atom's lone pair with the metal surface.

The modes at 1608 [ $\nu_{8a}(Pyr)$ ] and 662  $cm^{-1}$  [ $\rho_{as}(Pyr) + \delta(C_{pyr}CO) + \delta(C_{pyr}CP)$ ] distinguish the SERS spectrum

of  $\gamma$ -Pyr from those of  $\alpha$ -Pyr and  $\beta$ -Pyr. The appearance of these two bands in the  $\gamma$ -Pyr SERS spectrum and the slight strengthening of the 1196 and 1158  $cm^{-1}$  spectral features (see Table 2 for bands assignment) suggest that in the case of 4-isomer of  $\alpha$ -hydroxymethyl biphenyl phosphine oxide pyridine assists in the adsorption process of this molecule.

## 4. Conclusions

In this work, we discussed the mode of adsorption for three isomers (2-, 3-, and 4-) of pyridine  $\alpha$ -hydroxymethyl biphenyl phosphine oxide immobilized onto a colloidal gold surface. We demonstrated that the investigated molecules interact with the gold substrate surface through the phenyl ring that is oriented vertically in respect to the surface. For  $\gamma$ -Pyr, we suggested also that the pyridine ring located in the vicinity of the gold surface is able to assist in the adsorption process. Although the interaction of  $\alpha$ -Pyr,  $\beta$ -Pyr, and  $\gamma$ -Pyr with the gold surface was suggested by the phenyl ring, the hydroxyl ( $-OH$ ) and phosphonate oxygen ( $=O$ ) fragments assisted in this process.

## Conflict of Interests

The authors declare that there is no conflict of interests regarding the publication of the paper.

TABLE 2: Wavenumbers, full band widths at half maximum, and proposed band assignments for FT-RS and SERS spectra of  $\alpha$ -Pyr,  $\beta$ -Pyr, and  $\gamma$ -Pyr adsorbed onto colloidal gold surface.

Mode	FT-RS		SERS Au colloid	
	$\nu$ [cm <sup>-1</sup> ]	FWHM [cm <sup>-1</sup> ]	$\nu$ [cm <sup>-1</sup> ]	FWHM [cm <sup>-1</sup> ]
$\alpha$ -Pyr				
$\nu(\text{CO}) + \rho(\text{CP=O}) + \rho_{\text{as}}(\text{Phe}) + \delta_{\text{oop}}(\text{CC(P)C})$	528	6	530	17
$\nu(\text{CO}) + \rho_{\text{as}}(\text{Phe})$	548	7	552	14
$\nu_{6a}(\text{Pyr})$ and/or $\nu_{6b}(\text{Phe})$	616	7	617	6
$\rho_{\text{as}}(\text{Pyr}) + \delta(\text{C}_{\text{pyr}}\text{CO}) + \delta(\text{C}_{\text{pyr}}\text{CP})$	651	7	—	—
$\nu_{11}(\rho_{\text{as}}(\text{Pyr}))$ and/or $\nu_{6a}(\text{Phe}; \delta_{\text{oop}}(\text{CC(H)C}))$	689	6	695	17
$\nu_{10b}(\rho_t(\text{Pyr}))$ and/or $\rho_{\text{as}}(\text{Phe}) + \nu(\text{PC}_{\text{phe}})$	728	3	—	—
$\nu_{10a}(\text{Phe}; \nu(\text{CH}))$	841	9	—	—
$\nu_1(\text{Pyr}; \delta_{\text{oop}}(\text{CC(H)C}) + \nu(\text{CN}) + \delta_{\text{trig}}(\text{Pyr}))$	992	7	—	—
$\nu_{12}(\text{Phe})$	998	5	999	9
$\nu_{18a}(\text{Phe})$	1028	7	1028	9
$\nu_{12}(\text{Pyr})$	1046	11	—	—
$\rho_r(\text{CC(H)C})_{\text{pyr}} + \nu(\text{CC})_{\text{pyr}} + \nu(\text{CO}) + \nu(\text{PC}_{\text{phe}})$	1103	9	1102	11
$\nu(\text{P=O})$ and/or $\delta(\text{CH})$	1164	6	1159	7
$\nu_{9a}(\text{Phe}; \delta(\text{CH}))$ and/or $\nu_{\text{sym}}(\text{C}_{\beta}\text{C}_{\gamma}\text{H}_2\text{C}_{\delta})$	1185	6	1183	18
$\nu_{9a}(\text{Pyr})$ and/or $\nu_{7a}(\text{Phe}; \text{phenyl-C stretch})$	1215	7	—	—
$\nu_{19b}(\text{Pyr/Phe})$	1433	8	1435	8
$\nu_{8b}(\text{Pyr/Phe})$	1570	10	—	—
$\nu_{8a}(\text{Pyr/Phe})$	1588	10	1585	9
$\beta$ -Pyr				
$\nu(\text{CO}) + \rho(\text{CP=O}) + \rho_{\text{as}}(\text{Phe}) + \delta_{\text{oop}}(\text{CC(P)C})$	534	10	533	17
$\nu(\text{CO}) + \rho_{\text{as}}(\text{Phe})$	554	7	546	14
$\nu_{6a}(\text{Pyr})$ and/or $\nu_{6b}(\text{Phe})$	616	6	616	6
$\rho_{\text{as}}(\text{Pyr}) + \delta(\text{C}_{\text{pyr}}\text{CO}) + \delta(\text{C}_{\text{pyr}}\text{CP})$	654	7	—	—
$\nu_{11}(\rho_{\text{as}}(\text{Pyr}))$ and/or $\nu_{6a}(\text{Phe}; \delta_{\text{oop}}(\text{CC(H)C}))$	698	8	695	11
$\nu_{10b}(\rho_t(\text{Pyr}))$ and/or $\rho_{\text{as}}(\text{Phe}) + \nu(\text{PC}_{\text{phe}})$	733	6	—	—
$\nu_{\text{as}}(\text{Pyr}) + \delta_{\text{oop}}(\text{CC(H)C})_{\text{phe}} + \delta_{\text{oop}}(\text{CC}_{\text{phe}}(\text{P)C})$	757	7	—	—
$\nu_{10a}(\text{Phe}; \nu(\text{CH}))$	853	12	—	—
$\nu_{12}(\text{Phe})$	1001	6	997	9
$\nu_{18a}(\text{Phe})$	1032	8	1026	9
$\nu_{12}(\text{Pyr})$	1041	7	—	—
$\rho_r(\text{CC(H)C})_{\text{pyr}} + \nu(\text{CC})_{\text{pyr}} + \nu(\text{CO}) + \nu(\text{PC}_{\text{phe}})$	1103	9	1102	10
$\nu(\text{P=O})$ and/or $\delta(\text{C-H})$	1162	14	1157	9
$\nu_{9a}(\text{Phe}; \delta(\text{CH}))$ and/or $\nu_{\text{sym}}(\text{C}_{\beta}\text{C}_{\gamma}\text{H}_2\text{C}_{\delta})$	1189	19	1183	17
$\nu_{9a}(\text{Pyr})$ and/or $\nu_{7a}(\text{Phe}; \text{phenyl-C stretch})$	1220	20	—	—
$\nu_{19b}(\text{Pyr/Phe})$	1434	8	1433	8
$\nu_{8b}(\text{Pyr/Phe})$	1573	8	—	—
$\nu_{8a}(\text{Pyr/Phe})$	1589	8	1584	14
$\gamma$ -Pyr				
$\nu(\text{CO}) + \rho(\text{CP=O}) + \rho_{\text{as}}(\text{Phe}) + \delta_{\text{oop}}(\text{CC(P)C})$	528	4	531	14
$\nu(\text{CO}) + \rho_{\text{as}}(\text{Phe})$	551	9	550	14
$\nu_{6a}(\text{Pyr})$ and/or $\nu_{6b}(\text{Phe})$	615	5	616	5
$\rho_{\text{as}}(\text{Pyr}) + \delta(\text{C}_{\text{pyr}}\text{CO}) + \delta(\text{C}_{\text{pyr}}\text{CP})$	662	5	662	5
$\nu_{11}(\rho_{\text{as}}(\text{Pyr}))$ and/or $\nu_{6a}(\text{Phe}; \delta_{\text{oop}}(\text{CC(H)C}))$	697	9	697	8
$\nu_{10b}(\rho_t(\text{Pyr}))$ and/or $\rho_{\text{as}}(\text{Phe}) + \nu(\text{PC}_{\text{phe}})$	725	9	—	—
$\nu_{\text{as}}(\text{Pyr}) + \delta_{\text{oop}}(\text{CC(H)C})_{\text{phe}} + \delta_{\text{oop}}(\text{CC}_{\text{phe}}(\text{P)C})$	759	5	—	—
$\nu_{10a}(\text{Phe}; \nu(\text{CH}))$	860	11	—	—



TABLE 2: Continued.

Mode	FT-RS		SERS Au colloid	
	$\nu$ [cm <sup>-1</sup> ]	FWHM [cm <sup>-1</sup> ]	$\nu$ [cm <sup>-1</sup> ]	FWHM [cm <sup>-1</sup> ]
$\nu_1$ (Pyr; $\delta_{oop}$ (CC(H)C) + $\nu$ (CN) + $\delta_{trig}$ (Pyr))	991	6	—	—
$\nu_{12}$ (Phe)	1001	6	998	9
$\nu_{18a}$ (Phe)	1029	9	1026	10
$\rho_t$ (CC(H)C) <sub>pyr</sub> + $\nu$ (CC) <sub>pyr</sub> + $\nu$ (CO) + $\nu$ (PC <sub>phe</sub> )	1103	8	1102	11
$\nu$ (P=O) and/or $\delta$ (C–H)	1164	15	1158	16
$\nu_{9a}$ (Phe; $\delta$ (CH)) and/or $\nu_{sym}$ (C <sub><math>\beta</math></sub> C <sub><math>\gamma</math></sub> H <sub>2</sub> C <sub><math>\delta</math></sub> )	1199	12	1196	—
$\nu_{9a}$ (Pyr) and/or $\nu_{7a}$ (Phe; phenyl-C stretch)	1222	13	—	—
$\nu_{19b}$ (Pyr/Phe)	1436	5	1435	9
$\nu_{8b}$ (Pyr/Phe)	1573	8	1585	10
$\nu_{8a}$ (Pyr/Phe)	1592	11	1608	15

## Acknowledgments

This work was supported by the National Research Center (Grant no. N N204 544339 to E.P.). Younkoo Kim gratefully acknowledges HUFs for financial support. Bogdan Boduszek and Tomasz K. Olszewski acknowledge financial support from a statutory activity subsidy from the Polish Ministry of Science and Higher Education for the Faculty of Chemistry, Wrocław University of Technology.

## References

- [1] B. Lejczak and P. Kafarski, "Biological activity of aminophosphonic acids and their short peptides," in *Phosphorous Heterocycles I*, vol. 20 of *Topics in Heterocyclic Chemistry*, pp. 31–63, 2009.
- [2] B. Zurowska, K. Ślepokura, U. Kalinowska-Lis, and B. Boduszek, "Synthesis, spectroscopy and magnetic properties of transition-metal complexes with diethyl [(n-butylamino-N)(pyridin-2-yl)methylphosphonate (2-pmape): structure of [Co(2-pmape)<sub>2</sub>](ClO<sub>4</sub>)<sub>2</sub> complex," *Inorganica Chimica Acta*, vol. 384, pp. 143–148, 2012.
- [3] E. D. Naydenova, P. T. Todorov, and K. D. Troev, "Recent synthesis of aminophosphonic acids as potential biological importance," *Amino Acids*, vol. 38, no. 1, pp. 23–30, 2010.
- [4] B. Zurowska and B. Boduszek, "Synthesis, spectroscopy and magnetic properties of transition-metal complexes with aminophosphonate derivatives of pyridine," *Materials Science-Poland*, vol. 29, no. 2, pp. 105–111, 2011.
- [5] G. Gakhar, T. Ohira, A. Shi, D. H. Hua, and T. A. Nguyen, "Antitumor effect of substituted quinolines in breast cancer cells," *Drug Development Research*, vol. 69, no. 8, pp. 526–534, 2008.
- [6] S. N. Pandeya, A. S. Raja, and G. Nath, "Synthesis and antimicrobial evaluation of some 4- or 6-chloroisatin derivatives," *Indian Journal of Chemistry B: Organic and Medicinal Chemistry*, vol. 45, no. 2, pp. 494–499, 2006.
- [7] M. Sedic, M. Poznic, P. Gehrig et al., "Differential antiproliferative mechanisms of novel derivative of benzimidazo[1,2- $\alpha$ ]quinoline in colon cancer cells depending on their p53 status," *Molecular Cancer Therapeutics*, vol. 7, no. 7, pp. 2121–2132, 2008.
- [8] T. K. Olszewski and B. Boduszek, "Application of bis(trimethylsilyl) phosphonite in the efficient preparation of new heterocyclic  $\alpha$ -aminomethyl-H-phosphinic acids," *Synthesis*, no. 3, Article ID T18810SS, pp. 437–442, 2011.
- [9] Y. S. Higasio and T. Shoji, "Heterocyclic compounds such as pyrroles, pyridines, pyrrolidines, piperdines, indoles, imidazol and pyrazins," *Applied Catalysis A: General*, vol. 221, no. 1-2, pp. 197–207, 2001.
- [10] S. F. Simpson and J. M. Harris, "Raman spectroscopy of the liquid-solid interface: monolayer and bilayer adsorption of pyridine on silica," *Journal of Physical Chemistry*, vol. 94, no. 11, pp. 4649–4654, 1990.
- [11] K. Kneipp, H. Kneipp, I. Itzkan, R. R. Dasari, and M. S. Feld, "Surface-enhanced Raman scattering and biophysics," *Journal of Physics Condensed Matter*, vol. 14, no. 18, pp. R597–R624, 2002.
- [12] C. M. Aikens and G. C. Schatz, "TDDFT studies of absorption and SERS spectra of pyridine interacting with Au<sub>20</sub>," *Journal of Physical Chemistry A*, vol. 110, no. 49, pp. 13317–13324, 2006.
- [13] R. L. Birke, V. Znamenskiy, and J. R. Lombardi, "A charge-transfer surface enhanced Raman scattering model from time-dependent density functional theory calculations on a Ag<sub>10</sub> - pyridine complex," *Journal of Chemical Physics*, vol. 132, no. 21, Article ID 214707, 2010.
- [14] A. R. Tao, S. Habas, and P. Yang, "Shape control of colloidal metal nanocrystals," *Small*, vol. 4, no. 3, pp. 310–325, 2008.
- [15] E. Proniewicz, E. Pieta, A. Kudelski et al., "Vibrational and theoretical studies of the structure and adsorption mode of m - nitrophenyl a-guanidinomethylphosphonic acid analogues on silver surfaces," *Journal of Physical Chemistry A*, vol. 117, pp. 4963–4972, 2013.
- [16] N. Piergies, E. Proniewicz, Y. Ozaki, Y. Kim, and L. M. Proniewicz, "Influence of substituent type and position on the adsorption mechanism of phenylboronic acids: infrared, Raman, and surface-enhanced Raman spectroscopy studies," *Journal of Physical Chemistry A*, vol. 117, no. 27, pp. 5693–5705, 2013.
- [17] E. Proniewicz, Y. Ozaki, Y. Kim, and L. M. Proniewicz, "Adsorption mode of neurotensin family peptides onto a colloidal silver surface: SERS studies," *Journal of Raman Spectroscopy*, vol. 44, no. 3, pp. 355–361, 2013.
- [18] E. Proniewicz, N. Piergies, Y. Ozaki, Y. Kim, and L. M. Proniewicz, "Investigation of adsorption mode of a novel group of N-benzylamino(boronphenyl)methylphosphonic acids using SERS," *Spectrochimica Acta A: Molecular and Biomolecular Spectroscopy*, vol. 103, pp. 167–172, 2013.

- [19] N. Piergies, E. Proniewicz, A. Kudelski et al., "Fourier transform infrared and Raman and surface-enhanced Raman spectroscopy studies of a novel group of boron analogues of aminophosphonic acids," *Journal of Physical Chemistry A*, vol. 116, no. 40, pp. 10004–10014, 2012.
- [20] E. Podstawka-Proniewicz, A. Kudelski, Y. Kim, and L. M. Proniewicz, "Adsorption of neurotensin-family peptides on SERS-active Ag substrates," *Journal of Raman Spectroscopy*, vol. 43, no. 9, pp. 1196–1203, 2012.
- [21] B. Boduszek, T. Olszewski, W. Goldeman, and M. Konieczna, "Aminophosphinic acids in a pyridine series: cleavage of pyridine-2- and pyridine-4-methyl(amino)phosphinic acids in acidic solutions," *Phosphorus, Sulfur and Silicon and the Related Elements*, vol. 181, no. 4, pp. 787–795, 2006.
- [22] W. Goldeman, T. K. Olszewski, B. Boduszek, and W. Sawka-Dobrowolska, "Aminophosphine oxides in a pyridine series. Studies on the cleavage of pyridine-2- and pyridine-4-yl-(N-benzylamino)-methyldiphenylphosphine oxides in acidic solutions," *Tetrahedron*, vol. 62, no. 18, pp. 4506–4518, 2006.
- [23] E. Proniewicz, E. Pięta, K. Zborowski et al., "Surface-enhanced Raman scattering and the adsorption behavior of (diphenylphosphoryl)(pyridin-2-, -3, and -4-yl)methanol onto different silver surfaces," *Journal of Physical Chemistry A*. Accepted.
- [24] E. Podstawka, T. K. Olszewski, B. Boduszek, and L. M. Proniewicz, "Adsorbed states of phosphonate derivatives of N-heterocyclic aromatic compounds, imidazole, thiazole, and pyridine on colloidal silver: comparison with a silver electrode," *Journal of Physical Chemistry B*, vol. 113, no. 35, pp. 12013–12018, 2009.
- [25] E. Podstawka, A. Kudelski, T. K. Olszewski, and B. Boduszek, "Surface-enhanced Raman scattering studies on the interaction of phosphonate derivatives of imidazole, thiazole, and pyridine with a silver electrode in aqueous solution," *Journal of Physical Chemistry B*, vol. 113, no. 29, pp. 10035–10042, 2009.
- [26] T. D. Klots, "Raman vapor spectrum and vibrational assignment for pyridine," *Spectrochimica Acta A: Molecular and Biomolecular Spectroscopy*, vol. 54, no. 10, pp. 1481–1498, 1998.
- [27] Z. Zhang, T. Imae, H. Sato, A. Watanabe, and Y. Ozaki, "Surface-enhanced Raman scattering and surface-enhanced infrared absorption spectroscopic studies of a metalloporphyrin monolayer film formed on pyridine self-assembled monolayer-modified gold," *Langmuir*, vol. 17, no. 15, pp. 4564–4568, 2001.
- [28] M. Muniz-Miranda, G. Cardini, and V. Schettino, "Surface-enhanced Raman spectra of pyridine and pyrazolide on silver colloids: chemical and electromagnetic effects," *Theoretical Chemistry Accounts*, vol. 111, no. 2–6, pp. 264–269, 2004.
- [29] L. Corrsin, B. J. Fax, and R. C. Lord, "The vibrational spectra of pyridine and pyridine-d<sub>5</sub>," *The Journal of Chemical Physics*, vol. 21, no. 7, pp. 1170–1176, 1953.
- [30] C. H. Kline Jr. and J. Turkevich, "The vibrational spectrum of pyridine and the thermodynamic properties of pyridine vapors," *The Journal of Chemical Physics*, vol. 12, no. 7, pp. 300–309, 1944.
- [31] G. S. Kürkçüoğlu, T. Arslan, and C. Öğretir, "Theoretical studies of the molecular structure and vibrational spectra of some dimethyl substituted pyridine derivatives," *Journal of Molecular Modeling*, vol. 15, no. 1, pp. 79–90, 2009.
- [32] F. Partal, M. Fernández-Gómez, J. J. L. López-González, A. Navarro, and G. J. Kearley, "Vibrational analysis of the inelastic neutron scattering spectrum of pyridine," *Chemical Physics*, vol. 261, no. 1-2, pp. 239–247, 2000.
- [33] J. L. Castro, M. R. López Ramírez, I. López Tocón, and J. C. Otero, "Vibrational study of the metal-adsorbate interaction of phenylacetic acid and  $\alpha$ -phenylglycine on silver surfaces," *Journal of Colloid and Interface Science*, vol. 263, no. 2, pp. 357–363, 2003.
- [34] M. Moskovits, "Surface selection rules," *The Journal of Chemical Physics*, vol. 77, no. 9, pp. 4408–4416, 1982.
- [35] P. Gao and M. J. Weaver, "Surface-enhanced Raman spectroscopy as a probe of adsorbate-surface bonding: benzene and monosubstituted benzenes adsorbed at gold electrodes," *Journal of Physical Chemistry*, vol. 89, no. 23, pp. 5040–5046, 1985.



## Research Article

# The Preparation and Performances of Self-Dispersed Nanomicron Emulsified Wax Solid Lubricant Ewax for Drilling Fluids

Feng-shan Zhou,<sup>1</sup> Ting-ting Wang,<sup>1</sup> Zheng-qiang Xiong,<sup>2</sup> Wen-yue Guo,<sup>1</sup>  
Xi Xiang,<sup>1</sup> Huan-na Wang,<sup>1</sup> Xia-lei Zhu,<sup>1</sup> Fang Liu,<sup>1</sup> and Bao-lin Cui<sup>1</sup>

<sup>1</sup> School of Materials Science and Technology, China University of Geosciences, Beijing 100083, China

<sup>2</sup> Beijing Institute of Exploration Engineering, Beijing 100083, China

Correspondence should be addressed to Feng-shan Zhou; zhoufs@cugb.edu.cn

Received 5 October 2013; Accepted 14 December 2013; Published 17 April 2014

Academic Editor: Yizhuang Xu

Copyright © 2014 Feng-shan Zhou et al. This is an open access article distributed under the Creative Commons Attribution License, which permits unrestricted use, distribution, and reproduction in any medium, provided the original work is properly cited.

An oil-in-water nanomicron wax emulsion with oil phase content 45 wt% was prepared by using the emulsifying method of surfactant-in-oil. The optimum prepared condition is 85°C, 20 min, and 5 wt% complex emulsifiers. Then the abovementioned nanomicron emulsifying wax was immersed into a special water-soluble polymer in a certain percentage by the semidry technology. At last, a solidified self-dispersed nanomicron emulsified wax named as Ewax, a kind of solid lubricant for water based drilling fluid, was obtained after dried in the special soluble polymer containing emulsifying wax in low temperature. It is shown that the adhesion coefficient reduced rate ( $\Delta K_f$ ) is 73.5% and the extreme pressure (E-P) friction coefficient reduced rate ( $\Delta f$ ) is 77.6% when the produced Ewax sample was added to fresh water based drilling fluid at dosage 1.0 wt%. In comparison with other normal similar liquid products, Ewax not only has better performances of lubrication, filtration loss control property, heat resistance, and tolerance to salt and is environmentally friendly, but also can solve the problems of freezing in the winter and poor storage stability of liquid wax emulsion in oilfield applications.

## 1. Introduction

Drilling fluid lubricants can be generally divided into liquid lubricants and solid lubricants according to their existential status, the former typically containing liquid mineral oil, vegetable oil, and surfactant while the latter including solid graphite, plastic ball, glass bead, and so on. However, the liquid lubricants such as mineral oil and vegetable oil always freeze at low temperature, and meanwhile the amount of these toxic lubricants like mineral oil, asphalt, and graphite for industrial utilization is reducing gradually year by year due to environmental protection requirement [1]. Hence, it is significant and urgent to develop a kind of solid lubricant with less toxicity and good feasibility at low temperature for drilling mud.

It is acknowledged that wax is a kind of oil organics with strong cohesive force and neither water soluble nor saponification. Thus, wax emulsion applied in multiple phase

disperse systems shows good stability and dispersibility even without heating to melted or organic solvent for dissolved. Wax emulsion expressed good lubricity in drilling fluid by forming a well-distributed film on the drilling string and borehole wall. In addition, wax emulsion also has other superiorities such as low fluorescence, nontoxicity, and noncorrosiveness. All of the above-distinguished properties endow wax emulsion as an important special wax product.

The nanomicron wax emulsion with stable particles was introduced into drilling fluid by Wang et al. [2–4] from Shandong University; since then, wax emulsion has become focus in many applied researches. So far, it has been well recognized that nanomicron wax emulsion possesses good lubricity performance and inhibitive ability. In spite of these distinguished properties, it shows many defects in storage stability, antifreeze property, filtration property, and cost performance which prevent wax emulsion from promoting conveniently.

In order to solve the above problems, this work investigated the preparation technology of self-dispersed nanomicro emulsified wax solid lubricant based on wax and its derived by-products. Meanwhile, its drilling performances such as lubricity performance, rheological behavior, filtration loss control in high temperature and high pressure (HTHP), tolerance to salt, and inhibitive ability for shale formations were also evaluated in depth in this work.

## 2. Experimental Details

**2.1. Materials and Instruments.** The all industrial grade samples such as wax, ceratum, white oil, and sodium hydroxide are purchased from Beijing Chemical Reagent Co., Ltd., China. The multicomponent emulsifier TE, inorganic-organic compound stabilizer TS, and a special water soluble polymer cellulose graft starch (PPS) are self-made.

Model NF-1 adhesion coefficient tester for drilling fluid, Model GGS42-2 high-temperature high-pressure filter press apparatus, and Model ZNN-D6S six-speed rotational viscometer are made in Haitongda Special Instruments Co., Ltd, China. The digital extreme pressure (EP) lubricity tester for drilling fluids was made in OFITE, USA. Model F-4600 fluorescence spectrophotometer was made in Hitachi, Japan. Mastersizer 2000 laser particle analyzer was made by Malvern Instruments Ltd, England. JSM-6460LV high resolution scanning electron microscope was made in JEOL, Japan.

### 2.2. Performance Evaluation Methods

**2.2.1. Lubricity Evaluation.** The adhesion coefficient reduced rate ( $\Delta K_f$ ) and the extreme pressure (E-P) friction coefficient reduced rate ( $\Delta f$ ) were applied to evaluate the lubricity performances and specific evaluation can refer to the technical standard from China National Petroleum Corporation (CNPC) of liquid lubricants for water based drilling fluid (Q/SY 1088-2007).

**2.2.2. Rheological Behavior Evaluation.** Apparent viscosity (AV), plastic viscosity (PV), yield point (YP), and API (American Petroleum Institute) filter loss ( $FL_{API}$ ) were applied to evaluate the rheological behavior and specific evaluation method can refer to China national standards "petroleum and natural gas industries-field testing of drilling fluids-part 1: water-based fluids (GB-T 16783.1-2006)".

**2.2.3. Filtration Property Evaluation.** The evaluation method of filtration property can refer to the technical profession standard of filtrate reducer tolerant to salt and high temperature for drilling fluid (Q/SH 0047-2007).

**2.2.4. Fluorescence Performance Evaluation.** According to the measuring method of the fluorescence emitted by the drilling fluid additive reported by Patel et al. [5], three-dimensional fluorescence spectrum was used to quantitatively measure the

maximum fluorescence intensity  $F_{max}$ , the optimum excitation wavelength EX, and the corresponding emission wavelength EM. The detailed measuring method was described as follows: the test samples and hexane were mixed at mass ratio 1:400 first followed by the fluorescence characteristic measurement performed on fluorescence spectrophotometer. The main test parameters were listed as follows: the slit width of the excitation wavelength is 2.5 nm; the slit width of the emission wavelength is 2.5 nm; PMT voltage is 700 V; scanning speed is 1200 nm/min.

**2.2.5. Microscope Structure.** The measuring method and scattering condition were set on laser particle analyzer Mastersizer 2000 according to the ISO 13320 standard operation procedure and Mie Theory.

### 2.3. Preparation

**2.3.1. Preparation of Wax Emulsion.** Wax and its derived by-products were selected as the raw materials and they were heated together with white oil to get melted in a three-round flask. Then NaOH solution was added into the above mixture for preemulsification, as plenty of experiments and researches [6–8] indicated that the emulsification effect of compound emulsifier compounded by two or more surfactants took distinguished advantages over that of the single emulsifier. Span-80 and Tween-80 were certainly selected as the principal emulsifier while surfactant A and B were taken as the coemulsifiers in this work to obtain compound emulsifier TE which was added into the system after the preemulsification reaction. The emulsion stabilizer TS and other modifiers were selectively added into the system repeatedly to adjust the water phase. With the emulsifying method of surfactant-in-oil, the stable nanomicro wax emulsion was prepared under the optimized condition: emulsifying time was 20 minutes and emulsifying temperature was 85°C which slowly cooled to room temperature in the process of stirring.

**2.3.2. Preparation of the Solid Wax Lubricant.** The nanomicro wax emulsion made from Section 2.3.1 and a kind of special water soluble polymer material PPS were mixed together to react sufficiently at certain temperature for a period of time in kneader via the semidry technology [9, 10]. The self-dispersed nanomicro emulsified wax solid lubricant Ewax was finally obtained after the sample was dried at low temperature and broken to pieces. The complete preparation technological process was illustrated in Figure 1.

## 3. Impact of Ewax on the Performance of Drilling Fluid

**3.1. Lubricity Performance.** Figure 2 shows the effect of Ewax additive dosage on the adhesion coefficient reduced rate ( $\Delta K_f$ ) and the extreme pressure (E-P) friction coefficient reduced rate ( $\Delta f$ ) of sodium bentonite based mud for experimental utilization with 5.2 wt%. As indicated in Figure 2, when the additive dosage of Ewax was 0.5 wt%, 1.0 wt%, 1.5 wt%, and 2.0 wt%; the lubricity performance of the based

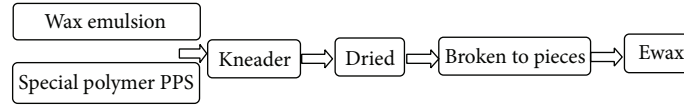


FIGURE 1: The preparing process for solid lubricant Ewax.

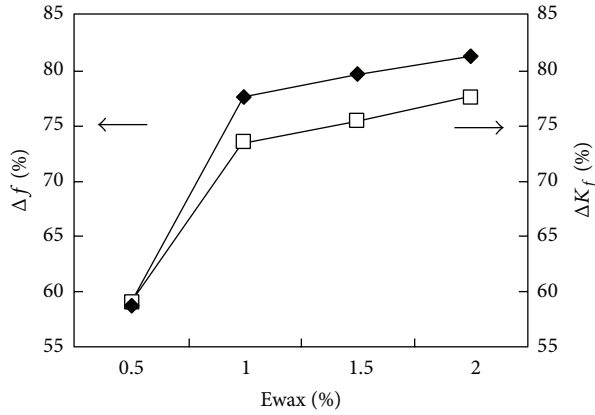


FIGURE 2: Effect of Ewax additive dosage on lubrication.

mud was generally enhanced continuously as suggested by the positive slope of the curve, which was much steep between the first two points but rather steady for the last three points. Nevertheless, if the impact of the produced sample additive dosage on drilling fluid system and the cost of treatment agents were both taken into account for the final evaluation, it was reasonable to conclude that the Ewax additive dosage at 1.0 wt% was appropriate. Therefore, 1.0 wt% was determined as the unified dosage for the evaluation of drilling fluid performances before and after adding Ewax.

The drilling additive could be seriously affected by temperature and salinity in the process of oilfield drilling. The lubricity performance of both the fresh water based mud and 4.0 wt% brine base mud was investigated in depth with the Ewax additive dosage at 1.0 wt%. Besides, the comparable evaluation was also made between the lubricity performance of the system at room temperature (RT) and that of the same system aged at high temperature ( $120^\circ\text{C} \times 16\text{ h}$ ) just as shown in Table 1.

As it can be clearly seen in Table 1 that  $\Delta K_f$  and  $\Delta f$  of fresh water based mud with 1.0 wt% Ewax aged for 16 h at  $120^\circ\text{C}$  slightly decreased compared to that of the same system at room temperature. However, the situation was rather different in the 4.0 wt% brine based mud in which  $\Delta K_f$  of the system aged for 16 h at  $120^\circ\text{C}$  ascended while its  $\Delta f$  almost kept the same value. This suggested that Ewax possessed good lubricity performance in both fresh water and 4.0 wt% brine based mud. Besides, it also exhibited superior resistance ability to high temperature and salt.

Table 2 showed the comparison results of the performances of Ewax and other lubricants. Apparently, Ewax possessed better overall lubricity performance over other commercial lubricant products in China including DZ (from Dezhou, Shandong), DY (from Dongyin, Shandong),

TABLE 1: Lubricity evaluation of Ewax in different based mud and at different temperature.

Ewax additive dosage/wt%	Based mud	Condition	$\Delta K_f/\%$	$\Delta f/\%$
1.0	Fresh water <sup>a</sup>	R.T.	73.5	77.6
		$120^\circ\text{C} \times 16\text{ h}$	63.8	68.0
1.0	4.0 wt% brine <sup>b</sup>	R.T.	76.5	64.1
		$120^\circ\text{C} \times 16\text{ h}$	78.5	63.1

Remarks: <sup>a</sup>fresh water based mud is 5.2% bentonite based mud; <sup>b</sup>brine based mud is 5.2% bentonite based mud adding 4.0% NaCl.

Slube (from Bingzhou, Shandong), and GD-2 (from Renqiu, Hebei).

**3.2. Rheological Behavior.** The rheological behavior of drilling fluid could reflect its flow and deformation properties which were measured by shear stress and shear rate [11]. It is well recognized that the rheological behavior of drilling fluid is directly related to many factors such as its washdown capability to shaft bottom, solids carrying and suspending capability, the delivery ability of water power, and wall stabilization. The changing result of rheological behavior of drilling fluid based mud before and after the addition of Ewax was shown in Table 3.

As indicated in Table 3, AV, PV, and  $\text{Gel}_{10''/10'}$  of the system showed little change before and after the addition of Ewax, suggesting that Ewax had almost no influences on the rheological behavior of drilling fluid. Meanwhile, YP of the system increased slightly and 30 min  $\text{FL}_{\text{API}}$  decreased a little after the addition of Ewax indicating that Ewax showed certain filtration loss control effect which was beneficial to ensure the wellbore stability.

**3.3. HTHP Filtration Loss.** Filtrate loss reducer is a kind of important drilling fluid additive to ensure the stable performance of drilling fluid. It was reported that the stable wellbore as well as regular and consistent borehole gauge could be achieved via reducing the invasion of drilling fluid into stratum and preventing the hydrating and swelling of shale formations [12]. Both the HPHT  $120^\circ\text{C} \times 3.5\text{ MPa}$  filter loss performance in fresh water based mud and 4.0 wt% brine based mud were tested and compared to those of other two products DZ and DY as recorded in Table 4. The brine based mud was obtained based on the fresh water based mud by adding 4.0 wt% NaCl into it under vigorous stirring for 20 min followed by the addition of 1.0 wt% Ewax under continuously stirring for another 5 min. It was clear in Table 4 that Ewax exhibited fluid loss property in both fresh water and brine based mud, with the latter being more apparent.

TABLE 2: Comparison of different lubricants.

Sample	Principal component	Particle size	Product modality	$\Delta K_f/\%$	$\Delta f/\%$
Ewax	wax (ceratum)	nanomicon	solid	73.5	77.6
DZ	wax	nanoscope	emulsion	65.3	72.5
DY	wax	nanoscope	emulsion	71.5	73.3
Slube	Inflating crystalline graphite	nanomicon	solid	57.0	64.0
GD-2	Crystalline graphite	nanomicon	solid	26.3	65.0

TABLE 3: Impact of Ewax on drilling fluid rheology.

Mud type	Ewax additive dosage/wt%	AV/mPa·s	PV/mPa·s	YP/Pa	$G_{10''/10'}/(\text{Pa/Pa})$	$FL_{API}/(\text{mL/30 min})$
Fresh water based mud <sup>a</sup>	0	13.5	7.0	6.5	6.5/12.0	14.0
	1.0	15.5	8.0	7.5	6.0/11.5	12.2
Drilling fluid <sup>bc</sup>	0	13.5	11.0	2.5	1.0/1.0	10.0
	1.0	13.5	10.0	3.5	1.0/1.0	9.6

Remarks: <sup>a</sup>fresh water based mud is 6.0 wt% sodium-bentonite based mud.

<sup>b</sup>Drilling fluid is 4.0 wt% sodium-bentonite based mud + 0.2 wt% HV-CMC + 0.3 wt% NPAN + 0.2 wt% SiM + 0.1 wt% KPAM.

<sup>c</sup>HV-CMC is technical-grade high-viscosity carboxymethylcellulose as viscosifier; NPAN is hydrolysed ammonium polyacrylonitrile as filter loss control agent; SiM is silicone grafted starch film former as inhibitor; KPAM is potassium copolymer of acrylamide and acrylic acid as flocculant.

TABLE 4: Comparison of HTHP filtration loss control ability.

Sample	Fresh water based mud <sup>a</sup>		Brine based mud <sup>b</sup>		Brine based mud Aged at high temperature <sup>c</sup>	
	A <sup>d</sup>	B <sup>e</sup>	A	B	A	B
Based mud	29.0	—	78.0	—	98.0	—
Ewax	19.0	34.5	38.0	51.3	49.0	50.0
DZ	25.0	13.8	75.0	3.9	—	—
DY	24.5	15.5	74.5	4.5	—	—

Remarks: <sup>a</sup>fresh water based mud is 6.0% bentonite based mud.

<sup>b</sup>Brine based mud is 6.0% bentonite based mud added 4.0% NaCl.

<sup>c</sup>Brine based mud aged at high temperature is 6.0% bentonite based mud added 4.0% NaCl aged at 120°C for 16 h.

<sup>d</sup>A is filter loss in mL/30 min.

<sup>e</sup>B is reducing rate of water loss in percent.

The reducing rate of water loss of brine based mud even approached 51.3%, 10 times higher than the same kind of products.

In order to investigate the filtration control performance of Ewax at high temperature and salinity, HPHT<sub>120°C × 3.5 MPa</sub> filter loss performance testing was taken on brine base mud containing 6.0 wt% bentonite base mud and 4.0 wt% NaCl and its mixture with Ewax together aged at 120°C for 16 h as shown in Table 4. The reducing rate of filter loss as high as 50.0% indicated that Ewax shows superior resistance ability to high temperature and salt in filtration control ability, which took distinguished advantage over other similar products.

**3.4. Inhibitive Ability.** The inhibitive ability of drilling additives is mainly shown in two aspects: preventing the hydrating and swelling of shale formations and its scattering. In this work, the inhibitive ability of Ewax was simulated by measuring the reducing rate of yield of clay. First, Ewax and Na-bentonite were added together into distilled water and the rheological parameters were measured after a 12-hour hydration process. Meanwhile, comparable result with

bentonite based mud without any Ewax was made as recorded in Table 5. Clearly, AV and PV of the based mud containing Ewax both decreased together with the decrease of the yield of clay suggesting that Ewax could inhibit clay from hydrating and swelling.

**3.5. Microscope Structure.** Figure 3 is SEM images of the produced wax emulsion, and Figure 4 is the laser particle size distribution of wax emulsion (a) and Ewax (b), respectively. Apparently, the size of wax emulsion particles was generally distributed between 200 nm and 10  $\mu\text{m}$  as shown in Figure 3 while that of Ewax was generally distributed between 0.3  $\mu\text{m}$  and 120  $\mu\text{m}$  as shown in Figure 3. These two particle distribution spectra further confirmed that the nanomicon emulsified wax solid lubricant was obtained which could disperse well in base mud and drilling fluid and plug the pore like what nanomicon wax did to protect the stability of the formations.

Figure 5 showed the scanning electron photographs of the particles morphology of special water-soluble polymer material (a) and Ewax (b). Obviously, the emulsified wax



TABLE 5: Inhibitive ability of Ewax.

Based mud	AV/(mPa·s)	$\Delta$ AV/%	PV/(mPa·s)	$\Delta$ PV/%
6.0 wt% bentonite $\rightarrow$ a 12 h hydration process	13.5	—	7.0	—
1.0 wt% Ewax + 6.0 wt% bentonite $\rightarrow$ a 12 h hydration process	11.5	14.8	6.0	14.3

TABLE 6: Fluorescence performance of Ewax.

Sample	$F_{\max}$	EX/nm	EM/nm
Ewax	176.4	256.0	436.2

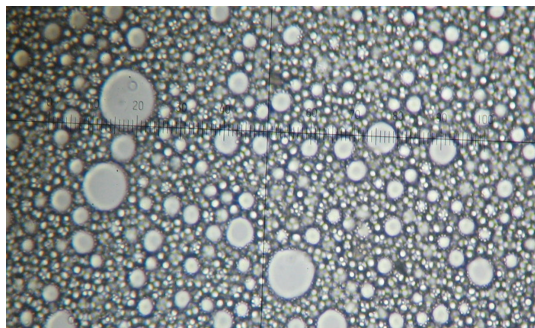


FIGURE 3: SEM images of the produced wax emulsion.

covered the surface of the special polymer material in the form of wax spheres as shown in Figure 5(b) and made the polymer's surface much smoother, which was critical for the appearance of good lubricity performance. Besides, the particle size of Ewax was also shown to be about 20  $\mu\text{m}$ , consistent with the result in Figure 3.

**3.6. Fluorescence Performance.** Three-dimensional fluorescence spectrum was employed to quantitatively measure the maximum fluorescence intensity  $F_{\max}$ , the optimum excitation wavelength EX, and the corresponding emission wavelength EM. It was reported in the patent by Patel et al. [5] that the additive would emit strong fluorescence when its  $F_{\max}$  was beyond 800. As shown in Figure 6 and Table 6, the maximum fluorescence intensity  $F_{\max}$  of Ewax was only 176.4, suggesting that its fluorescence level was relatively low. Meanwhile, the characteristic peak of Ewax was at 256.0/436.2 and did not overlap with that of the crude oil and natural gas shown in Table 7 [13], indicating that Ewax would not influence the geological logging process to explore oil and gas.

**3.7. Antiadhesion Performance.** Adhesion phenomenon might appear in the long-time storage and transportation process of solid wax powder. The following method was applied to evaluate the antiadhesion performance in this work: firstly, certain amount of sample (more than 200 g) was put into a sealed bag which should consequently be squeezed heavily to let the air out. After the sample was pressured to be flattened, it should be transferred into a constant temperature oven followed by a 24-hour pressure process at 50 kPa at 50°C–60°C on the surface of the sample. Finally,

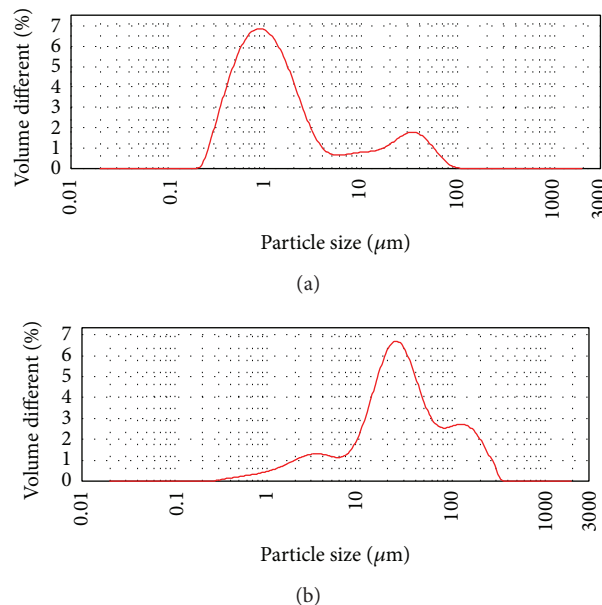


FIGURE 4: Laser particle size distribution of wax emulsion (a) and Ewax (b).

the sample should be taken out to examine its adhesion state and dispersion property. The results already indicated that pressure did not have any effect on the lubricity performance and dispersion property of Ewax, which showed good antiadhesion performance.

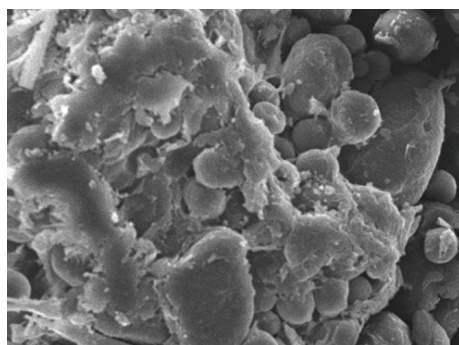
**3.8. Environmentally Friendly Behavior.** As the absorption carrier in this experiment was a kind of special water-soluble polymer PPS with good biodegradability and the main lubricity component was wax, all these materials would not do any harm to the environment. Besides, wax spheres with low fluorescence intensity could plug the pore and flow back easily, which would not disrupt the geological logging process. This great advantage made it possess light application prospect in mainland drilling especially for marine drilling. From the above discussion, it was clear to conclude that Ewax was a kind of environmentally friendly drilling fluid solid lubricant product.

## 4. Conclusions

- (1) The optimized technology with wax or ceratum as basic raw materials was finally established in which emulsifying temperature is 85°C, emulsifying time is 20 min, complex emulsifiers is 5 wt%, and oil phase content is 45 wt%. The uniform and stable

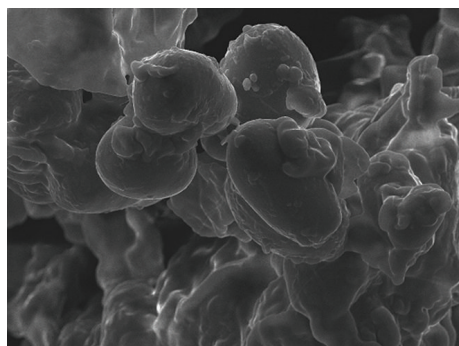
TABLE 7: Three-dimensional fluorescence spectra features of different crude oil and natural gas.

Characteristic peak EX/EM	268/322	284/336	256/360	228/342
Oil and gas properties	Gas and condensate gas	Condensate oil and light oil	Medium oil and heavy oil	Common peak



60 μm

(a)



60 μm

(b)

FIGURE 5: SEM images of special water-soluble polymer (a) and Ewax (b).

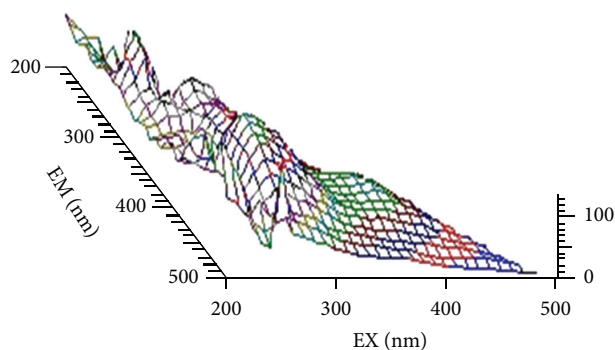


FIGURE 6: 3D fluorescence spectra of Ewax.

nanomicon wax emulsion was prepared under the optimized process.

- (2) A solid self-dispersed nanomicon emulsified wax named as Ewax was prepared by the semidryer technology in which the nanomicon emulsifying wax was immersed into a special water-soluble polymer followed by drying continuously at low temperature.

- (3) The adhesion coefficient reduced rate ( $\Delta K_f$ ) and the extreme pressure (E-P) friction coefficient reduced rate ( $\Delta f$ ) of the base mud could approach over 70% when the amount of Ewax in drilling fluid reached 1.0 wt%, indicating its good lubricity performance. Meanwhile, Ewax also exhibited nice HTHP filtration qualities and multiple functions, which made Ewax superior to other similar products.
- (4) The preparation of Ewax in this work thoroughly solved the problems of freezing in winter and poor storage stability of traditional emulsified wax liquid lubricants.

## Disclaimer

The authors confirm that the paper is the authors' own work, is original and unpublished, and is not being considered for publication elsewhere, and all authors agree that it should be submitted to *Journal of Spectroscopy*.

## Conflict of Interests

The authors declare that there is no conflict of interests regarding the publication of this paper.

## References

- [1] X.-H. Yang, "Advances in preparation and uses of drilling fluid additives in China in recent 5 years," *Oilfield Chemistry*, vol. 26, no. 2, pp. 210–217, 2009.
- [2] B. F. Wang, Y. D. Zhang, and D. J. Sun, "Preparation and application of wax emulsion," *Shandong Chemical Industry*, vol. 33, no. 2, pp. 14–17, 2004.
- [3] T. Wu and D. J. Sun, "Preparation of wax emulsion and application in dispersion system," *Journal of Shandong University*, vol. 41, no. 4, pp. 141–144, 2006.
- [4] Q. Lan, C.-M. Su, W.-R. Liu, F. Yang, B.-Y. Guo, and D.-J. Sun, "Emulsions and emulsifying technique and their application in drilling and completion fluid technology," *Drilling Fluid and Completion Fluid*, vol. 23, no. 2, pp. 61–69, 2006.
- [5] A. D. Patel, E. Stamatakis, S. Young et al., "High performance water based drilling fluid," US 2008/0009422 A1, 2008-1-10.
- [6] Y. X. Liu, C. S. Zhao, and L. Han, "Factors affecting the emulsification of paraffin," *Paper Chemicals*, vol. 16, no. 4, pp. 30–32, 2004.
- [7] Z. M. He, Y. Xue, G. L. Zeng et al., "Application of wax emulsion lubricants in drilling operations in Jiangsu oilfield," *Petroleum Drilling Techniques*, vol. 38, no. 3, pp. 63–66, 2010.
- [8] Y. Tian, J.-C. Zhang, F.-J. Zuo et al., "The laboratory preparation and evaluation of a emulsified wax," *Drilling Fluid and Completion Fluid*, vol. 25, no. 4, pp. 29–33, 2008.

- [9] G. F. Fanta, H. M. Muijs, K. Eskins, F. C. Felker, and S. M. Erhan, "Starch-containing lubricant systems for oil field applications," US 6461999 B1, 2002.
- [10] X. Wang, P. Yu, and S. Liu, "The synthesis of a solid emulsion lubricant," *Drilling Fluid and Completion Fluid*, vol. 27, no. 2, pp. 16–88, 2010.
- [11] D.-C. Qian, K.-C. Wang, H. Yang et al., "Development and application of cationic surfactant emulsified wax for use in aqueous drilling fluid," *Oilfield Chemistry*, vol. 26, no. 3, pp. 238–241, 2009.
- [12] J. Chen, X. Wang, Y. Gao, and J. Zhang, "Application of nano-wax emulsion drilling fluid technology in horizontal wells," *Drilling Fluid and Completion Fluid*, vol. 27, no. 4, pp. 87–89, 2010.
- [13] J. Song and B. Tang, "Study on the characteristic and significance of three dimensional fluorescence spectra of petroleum samples," *Spectroscopy and Spectral Analysis*, vol. 20, no. 1, pp. 115–118, 2000.

## Research Article

# Terahertz Absorption Spectroscopy of Benzamide, Acrylamide, Caprolactam, Salicylamide, and Sulfanilamide in the Solid State

Ye Jiang,<sup>1</sup> Fengshan Zhou,<sup>2</sup> Xiaodong Wen,<sup>3</sup> Limin Yang,<sup>3</sup> Guozhong Zhao,<sup>4</sup> He Wang,<sup>4</sup> Haiyan Wang,<sup>4</sup> Yanjun Zhai,<sup>1</sup> Jinguang Wu,<sup>5</sup> Kexin Liu,<sup>3</sup> and Jia'er Chen<sup>3</sup>

<sup>1</sup> College of Pharmacy, Liaoning University of Traditional Chinese Medicine, Dalian 116600, China

<sup>2</sup> School of Materials Science and Technology, China University of Geosciences, Beijing 100083, China

<sup>3</sup> State Key Laboratory of Nuclear Physics and Technology, Institute of Heavy Ion Physics, School of Physics, Peking University, Beijing 100871, China

<sup>4</sup> Department of Physics, Capital Normal University, Beijing 100037, China

<sup>5</sup> The State Key Laboratory of Rare Earth Materials Chemistry and Applications, College of Chemistry and Molecular Engineering, Peking University, Beijing 100871, China

Correspondence should be addressed to Fengshan Zhou; zhousf@cugb.edu.cn and Yanjun Zhai; lnzyzyj@sohu.com

Received 6 September 2013; Accepted 14 December 2013; Published 16 February 2014

Academic Editor: Yizhuang Xu

Copyright © 2014 Ye Jiang et al. This is an open access article distributed under the Creative Commons Attribution License, which permits unrestricted use, distribution, and reproduction in any medium, provided the original work is properly cited.

Terahertz (THz) absorption spectra of the similarly structured molecules with amide groups including benzamide, acrylamide, caprolactam, salicylamide, and sulfanilamide in the solid phase at room temperature and 78 K for salicylamide are reported and compared to infrared vibrational spectral calculations using density functional theory. The results of THz absorption spectra show that the molecules have characteristic bands in the region of 0.2–2.6 THz ( $\sim 7\text{--}87\text{ cm}^{-1}$ ). THz technique can be used to distinguish different molecules with amide groups. In the THz region benzamide has three bands at 0.83, 1.63, and 1.73 THz; the bands are located at 1.44 and 2.00 THz for acrylamide; the bands at 1.24, 1.66 and 2.12 THz are observed for caprolactam. The absorption bands are located at 1.44, 1.63, and 2.39 THz at room temperature, and at 1.22, 1.46, 1.66, and 2.41 THz at low temperature for salicylamide. The bands at 1.63, 1.78, 2.00, and 2.20 THz appear for sulfanilamide. These bands in the THz region may be related to torsion, rocking, wagging, and other modes of different groups in the molecules.

## 1. Introduction

Spectroscopy is a powerful technique for measuring, analyzing, and identifying various molecules. Frequencies in the far-infrared (FIR,  $650\text{--}50\text{ cm}^{-1}$ ) and terahertz (THz) ( $0.1\text{--}10\text{ THz}$ , or  $3.3\text{--}333.6\text{ cm}^{-1}$ ) ranges correspond to motions of the entire molecular structure, involving relatively large masses and relatively shallow potentials [1, 2]. THz spectroscopy is being used for a number of important analytical applications in such areas as threat detection [3–5] and pharmaceutical characterization [6–8]. Its utility stems from solid-state compounds and molecules containing low-energy vibrations that, taken as a whole in this region, serve as spectral “fingerprints” usable for their detection and characterization. THz spectroscopy of condensed-phase biological

samples are investigated ranging from the simple crystalline forms of amino acids, carbohydrates, and polypeptides to the more complex aqueous forms of small proteins, DNA, and RNA [9–14]. THz hydration studies uncovered that the dynamical hydration shell of saccharides consists of several hundred water molecules and up to thousand water molecules for proteins [15–17]. THz spectroscopy is regarded as the renaissance of far-infrared spectroscopy [18].

Amide groups contribute significantly to the protein structure. A variety of techniques such as IR, NMR, Raman, ultrasonic absorption, and UV/Vis spectroscopies have been used to characterize both the intermolecular and intramolecular bonding in amide compounds [19–22]. Salicylamide is a nonsteroidal anti-inflammatory agent with analgesic and antipyretic properties. Its therapeutic action and potential



toxicity are still the subject of research, which makes it necessary to control its presence in biological fluids [23]. For acrylamide, it is found that its administration to laboratory animals caused tumor formation in various organs, the exact mechanism involved still being unclear [24, 25]. Sulfanilamides are successfully employed as effective chemotherapeutic agents for the prevention and cure of bacterial infections in human biological systems. Determination of molecules with amide groups is essential in many analyses of biological and clinical applications.

Here we have investigated the low-frequency vibrational motions of salicylamide, benzamide, acrylamide, caprolactam, and sulfanilamide in the solid state by concentrating on the spectral region between 7 and 650  $\text{cm}^{-1}$  where crystal lattice vibrations, hydrogen bond bending modes and collective modes, and so forth may occur [26]. The experimental results indicate that FIR and THz time-domain technique can be effective tools to detect different molecules with amide groups and the bands in the region may be related to torsion, rocking, wagging, and other modes of different groups of the molecules.

## 2. Experimental

**2.1. Materials.** Salicylamide, benzamide, acrylamide, caprolactam, and sulfanilamide were obtained from commercial sources and used without further purification.

**2.2. Physical Measurements.** The THz absorption spectra were recorded on the THz time-domain device of Capital Normal University of China, based on photoconductive switches for generation and electrooptical crystal detection of the far-infrared light. The experimental apparatus for terahertz transmission measurements has been discussed in detail elsewhere [27]. The preparation of the samples was by pressing mixed pellets with polyethylene powder (pure sample for benzamide); the diameter of the samples is 13 mm and the thickness of the samples is about 0.8 mm. The detection of THz absorption spectra was carried out at  $\text{N}_2$  atmosphere to avoid the influence of water vapor. The resolution of the spectra is 40 GHz. The THz frequency-domain spectra were obtained from the corresponding THz time-domain spectra via Fast Fourier Transform. Through comparison of THz frequency-domain spectra of the samples and corresponding references, the THz absorption spectra of the samples were obtained. Effective spectrum range is 0.2–2.6 THz, respectively.

The FIR spectra of benzamide, acrylamide, caprolactam, and salicylamide were measured using common used Nujol mull method, because mineral oil has no absorption in the far-IR region and the method can protect sample in solid state against wet and avoid distortion of bands or happening of ion exchange. Samples were suspended in the Nujol mull and then were daubed on a thin polyethylene window and another thin polyethylene window as background for comparison. Far infrared spectra in the range of 650–50  $\text{cm}^{-1}$  were taken on a Nicolet Magna-IR 750-II Spectrometer at room temperature and at 8  $\text{cm}^{-1}$  resolution, 128 scans. The optical bench was

purged with dried air. The FIR spectrum of sulfanilamide was measured on a Bruker VERTEX 80v FTIR spectrometer at 4  $\text{cm}^{-1}$  resolution and 32 scans. The preparation of the sample was by pressing mixed pellets with polyethylene powder.

All theoretical calculations were performed with the Gaussian 03 software package [28]. Density functional theory (DFT) calculations were used to determine the equilibrium structures and harmonic vibrational frequencies of the molecules. The B3LYP [29] hybrid density functional was used with the 6-311++G (3df, 2pd), Gaussian-type basis set [30]. Full geometry optimizations were conducted in each case and harmonic frequency analyses performed on these optimized structures.

## 3. Results and Discussion

The molecular structures of benzamide, acrylamide, caprolactam, salicylamide, and sulfanilamide are shown in Figure 1. The THz and FIR spectra of benzamide, acrylamide, caprolactam, salicylamide, and sulfanilamide are shown in Figures 2 and 3, respectively. The corresponding band positions in the FIR and THz absorption spectra of the samples and possible assignments are listed in Table 1.

**3.1. The THz Absorption Spectra of the Molecules.** All of the structures of benzamide, acrylamide, caprolactam, salicylamide and sulfanilamide have amide groups. The difference of benzamide, and salicylamide is that there is one more OH group in the structure of salicylamide, and both of the two molecules have benzene ring (ph). The THz absorption spectra of benzamide, acrylamide, caprolactam, salicylamide and sulfanilamide in Figure 2 show that in the THz region benzamide has three bands: 0.83, 1.63, and 1.73 THz (38, 54, 58  $\text{cm}^{-1}$ ); acrylamide has two bands located at 1.44 and 2.00 THz (48 and 67  $\text{cm}^{-1}$ ); caprolactam has three bands at 1.24, 1.66 and 2.12 THz (41, 55 and 71  $\text{cm}^{-1}$ ). The absorption bands of salicylamide are located at 1.44, 1.63, and 2.39 THz (48, 54, 80  $\text{cm}^{-1}$ ) at room temperature, and its bands have shifted to 1.46, 1.66, and 2.41 THz (49, 55 and 80  $\text{cm}^{-1}$ ), and 1.22 THz (41  $\text{cm}^{-1}$ ) band becomes clear at low temperature. For sulfanilamide, the bands are located at 1.63, 1.78, 2.00 and 2.20 THz (54, 59, 67, and 73  $\text{cm}^{-1}$ ). For these molecules, some of the peak positions are similar, for example, 1.63 THz for benzamide, salicylamide, and sulfanilamide, 1.66 THz for caprolactam; 1.22 and 1.24 THz for salicylamide and caprolactam; 2.00 THz for benzamide and sulfanilamide; 1.44 and 1.46 THz for caprolactam and salicylamide, respectively. However, most of the bands are different in peak positions and relative intensities, which show that THz method is sensitive to different molecular structures.

To clarify the bands in the THz region, second derivatives have been performed using Omnic 5.0 software for the THz spectra of the samples, and the results show that main bands and some relatively minor bands are observed in the second derivatives results (shown in Figure 4). The main bands are observed for each sample, which has a good agreement with the corresponding THz absorption spectrum. For benzamide, only three main bands are observed, it is the same as

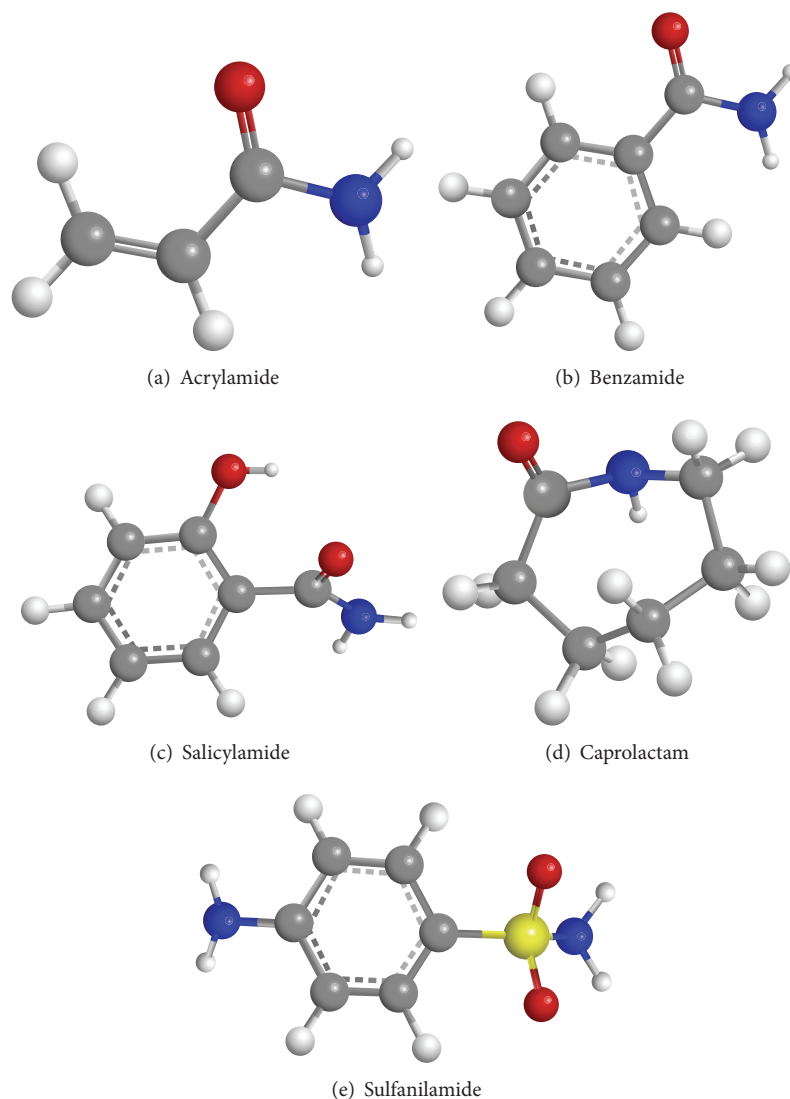


FIGURE 1: The molecular structures of acrylamide, benzamide, salicylamide, caprolactam, and sulfanilamide. (a) Acrylamide; (b) benzamide; (c) salicylamide; (d) caprolactam; (e) sulfanilamide.

the THz spectrum. For sulfanilamide, in the second derivatives results, 54, 60, 66, 72, 74, 81  $\text{cm}^{-1}$  are observed (54, 59, 67, and 73  $\text{cm}^{-1}$  in the absorption spectrum), so 73  $\text{cm}^{-1}$  band is formed by 72 and 74  $\text{cm}^{-1}$  bands; for caprolactam, 71  $\text{cm}^{-1}$  band is formed by 66, 69, and 71  $\text{cm}^{-1}$  child-bands; for acrylamide, weak band at 48  $\text{cm}^{-1}$  is emphasized in the second derivatives results, 67  $\text{cm}^{-1}$  band mainly has several child-bands: 64, 67, 70, 74, and 82  $\text{cm}^{-1}$ ; for salicylamide, 40, 48, 54, 64, 69, 79  $\text{cm}^{-1}$  bands are observed compared to 48, 54, and 80  $\text{cm}^{-1}$  in the absorption spectrum. 40  $\text{cm}^{-1}$  band is observed at low temperature. It seems that there is a band at 64  $\text{cm}^{-1}$  for salicylamide. The results show that second derivatives methods help observing the THz bands.

### 3.2. The FIR Spectra of the Five Molecules with Amide Group.

The FIR spectra of benzamide, acrylamide, caprolactam,

salicylamide and sulfanilamide, after automatic baseline correction shown in Figure 3 indicate that the five molecules have different band positions and relative band intensities.

For salicylamide, it has many bands in the region: 608, 564, 526, 515, 456, 421, 385, 296, 160, 146, 108, and 93  $\text{cm}^{-1}$ . For benzamide, its bands are as follows: 635, 529, 412, 382, 251, 177, 151, 110, 89, and 54  $\text{cm}^{-1}$ ; for acrylamide, it has several bands in the region: 619, 508, 314, 185, 122, and 67  $\text{cm}^{-1}$ ; for caprolactam, it has relatively more bands in the region: 581, 503, 488, 398, 337, 323, 258, 195, 129, 87, 69, and 56  $\text{cm}^{-1}$ . Sulfanilamide has the bands located at 641, 626, 563, 541, 497, 450, 414, 365, 302, 224, 132, 88, 72, and 58  $\text{cm}^{-1}$  in its FIR spectrum. The FIR and THz results are consistent for the samples in the 100–50  $\text{cm}^{-1}$  region as shown in Table 1.

For benzamide and salicylamide, there is one OH difference. Their FIR spectra have various peak positions and relative intensities; only several peak positions are close,

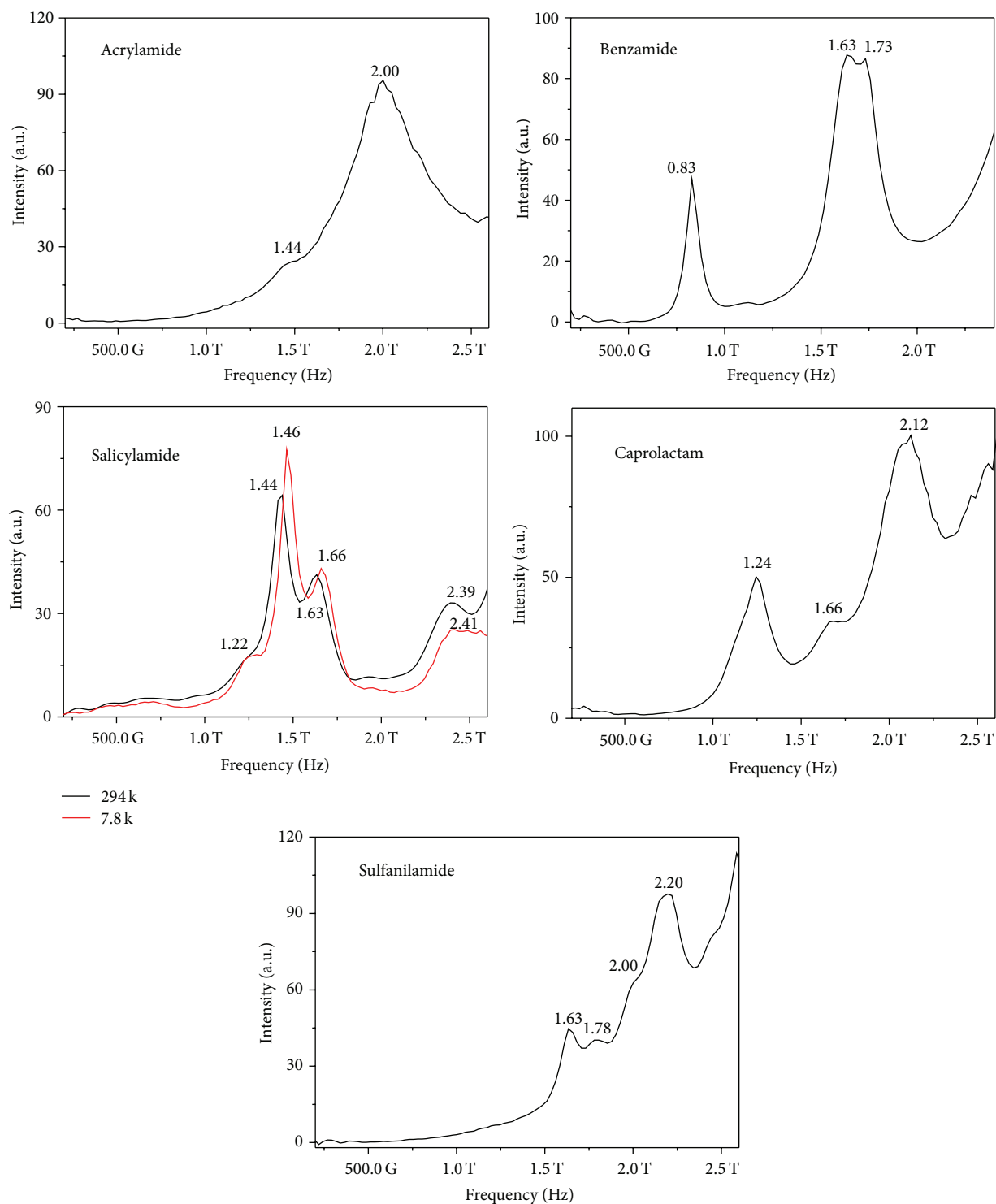


FIGURE 2: THz absorption spectra of acrylamide, benzamide, salicylamide, caprolactam, and sulfanilamide.

such as 529(benzamide)/526(salicylamide); 382/385; 151/146; 110/108; 89/93  $\text{cm}^{-1}$ . Other bands are located at different positions. For acrylamide and caprolactam, the bands at 508/503, 314/323, 185/195, 122/129, and 67/69  $\text{cm}^{-1}$  are similar in some extent. Caprolactam has relatively more bands in the FIR region. Sulfanilamide has two strong bands located at 563

and 541  $\text{cm}^{-1}$ , and the band at 365  $\text{cm}^{-1}$  is relatively strong, and other bands are weak. The five molecules have different characteristic bands in the FIR region.

*3.3. DFT Calculation and Analyses for the FIR and THz Spectra of the Molecules.* The assignment of the spectra in the FIR and

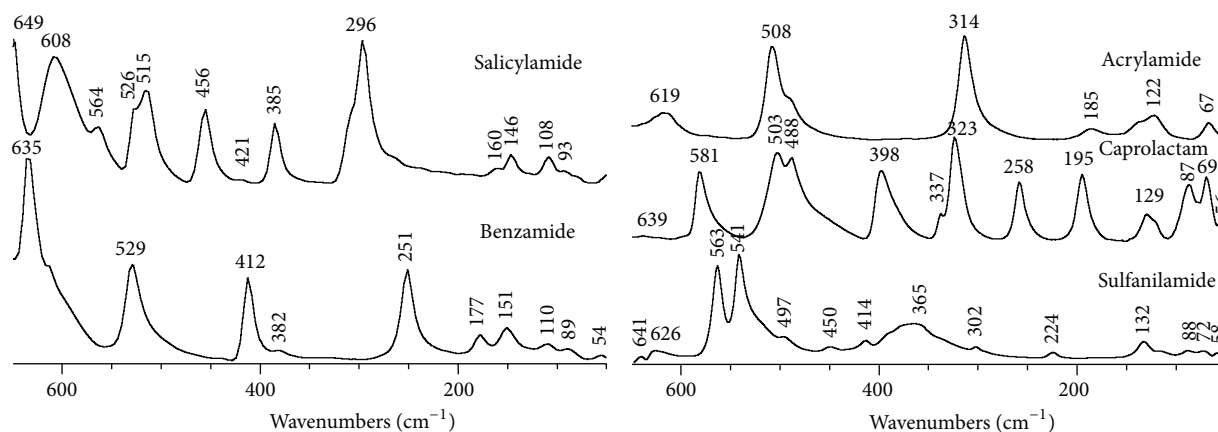


FIGURE 3: FIR spectra of acrylamide, benzamide, salicylamide, caprolactam, and sulfanilamide in the 650–50  $\text{cm}^{-1}$  region.

THz region is difficult. Fortunately, there are some calculation results for benzamide, salicylamide, and sulfanilamide [31–36]. Using similar method shown in the references, based on the calculated results of RB3LYP/6-311++G (3df, 2pd), and with the aid of visualization software of Gaussian View 4.1, the observed vibrational modes in the far-infrared and THz region can be assigned as shown in Table 1. The assignment is dependent on the result of calculation from molecular structure and patterns of vibrational modes. Some calculation results for the bands below 100  $\text{cm}^{-1}$  are shown in Figure 5. The calculated band positions are similar to experimental results in some extent as the calculations in [31–36], but the relative intensities of the bands compared to experimental results are not good as the calculation results for four vitamin molecules [37].

According to the DFT calculation results (shown in Table 1), the bands in the FIR and THz region mainly consist of movement of whole molecular skeleton. The absorption bands in the THz region are related to torsion, rocking, wagging, twisting, and other modes of different groups in the molecules. For example, in the calculation results, the main absorption bands of sulfanilamide below 100  $\text{cm}^{-1}$  are centered at 15 and 85  $\text{cm}^{-1}$ . The 15  $\text{cm}^{-1}$  band corresponds to out-of-plane wagging of ph ring and twisting of  $\text{NH}_2$  (the one in  $\text{S(=O)-NH}_2$ ); 85  $\text{cm}^{-1}$  band is related to out-of-plane wagging of ph ring and wagging of two  $\text{NH}_2$ ; 113  $\text{cm}^{-1}$  band is related to rocking of  $\text{NH}_2$ ; 167  $\text{cm}^{-1}$  band is related to deformation of  $\text{S(=O)-NH}_2$  and in-plane wagging of ph. For benzamide, 554  $\text{cm}^{-1}$  band is assigned to twisting of  $\text{NH}_2$  and wagging of ph; 503  $\text{cm}^{-1}$  band is assigned to in-plane wagging of ph and amide; 415  $\text{cm}^{-1}$  band is assigned to out-of-plane folding of ph ring; 375  $\text{cm}^{-1}$  band is assigned to in-plane rocking of amide, wagging of ph, and stretching of CC. 341  $\text{cm}^{-1}$  band is assigned to wagging of  $\text{NH}_2$ ; 217  $\text{cm}^{-1}$  band is assigned to in-plane rocking of the ring, and rocking of  $\text{C=O-NH}_2$ ; 152  $\text{cm}^{-1}$  band is assigned to out-of-plane vibration of ph ring and rocking of  $\text{NH}_2$ ; 57  $\text{cm}^{-1}$  band

is assigned to out-of-plane vibration of  $\text{ph-CONH}_2$  and wagging of  $\text{NH}_2$ .

For salicylamide, 30  $\text{cm}^{-1}$  band is assigned to twisting of  $\text{ph-CONH}_2$ ; 141  $\text{cm}^{-1}$  band is assigned to out-of-plane vibration of whole molecule; 184  $\text{cm}^{-1}$  band is assigned to wagging of  $\text{NH}_2$ ; 247  $\text{cm}^{-1}$  band is assigned to out-of-plane wagging of whole molecule, especially ph ring; 275  $\text{cm}^{-1}$  band is assigned to rocking of  $\text{NH}_2$ , rocking of ph; 383  $\text{cm}^{-1}$  band is assigned to in-plane vibration of ph and torsion of ( $\text{C=O-NH}_2$  and  $\text{COH}$ ); 419  $\text{cm}^{-1}$  band is assigned to out-of-plane folding of ph and stretching of  $\text{NH}$ ; 439  $\text{cm}^{-1}$  band is assigned to in-plane wagging of ph; twisting of ( $\text{C=O-NH}_2$  and  $\text{COH}$ ); 509  $\text{cm}^{-1}$  band is assigned to rocking of  $\text{NH}_2$ , rocking of ( $\text{C=O}$  and  $\text{OH}$ ), in-plane wagging of ph, and so forth. For acrylamide, 114  $\text{cm}^{-1}$  band is assigned to wagging of  $\text{NH}_2$  and wagging of  $\text{CH=CH}_2$ ; 190  $\text{cm}^{-1}$  band is assigned to wagging of  $\text{NH}_2$ ; 277  $\text{cm}^{-1}$  band is assigned to rocking of ( $\text{CH=CH}_2$ ) and rocking of ( $\text{C=O-NH}_2$ ); 468  $\text{cm}^{-1}$  band is assigned to rocking of  $\text{NH}_2$  and wagging of ( $\text{CH=CH}_2$ ); 470  $\text{cm}^{-1}$  band is assigned to twisting of ( $\text{CH=CH}_2$ ) and twisting of  $\text{NH}_2$ ; 613  $\text{cm}^{-1}$  band is assigned to twisting of  $\text{NH}_2$  and twisting of  $\text{CH}_2$ , and so forth. For caprolactam, 107  $\text{cm}^{-1}$  band is assigned to wagging of  $\text{CH}_2$ , stretching of  $\text{C=O}$ , and out-of-plane vibration of the ring; 158  $\text{cm}^{-1}$  band is assigned to rocking of  $\text{CH}_2$  and in-plane vibration of the ring; 258  $\text{cm}^{-1}$  band is assigned to rocking of  $\text{CH}_2$ , wagging of  $\text{CH}_2$ , stretching of  $\text{NH}$ , stretching of  $\text{C=O}$ , and so forth; 301  $\text{cm}^{-1}$  band is assigned to stretching of  $\text{NH}$  and in-plane vibration of the ring; 323  $\text{cm}^{-1}$  band is assigned to rocking of  $\text{CH}_2$ ; 402  $\text{cm}^{-1}$  band is assigned to in-plane vibration of the ring, and so forth. In most of the cases whole molecule is involved in the vibration modes. The calculation results are similar in some extent to the results in [31–37]. The calculations in Table 1 are only preliminary results, because only single molecule and in gas phase have been considered here, so it is reasonable that the calculation and experimental results have some differences.

TABLE 1: Calculated and experimental vibrational frequencies for salicylamide, benzamide, acrylamide, caprolactam, and sulfanilamide ( $\text{cm}^{-1}$ )<sup>a</sup>.

Compounds	Experiment		Calculation	Vibrational assignments
	FIR	THz-TDS	6-311++G(3df, 2pd)	
Salicylamide	526		538	$\tau_{\text{ph}}$
	515		509	$\rho\text{NH}_2$ , $\rho(\text{C}=\text{O}$ and $\text{OH})$ , in-plane wagging of ph
	456		439	In-plane wagging of ph, $t(\text{C}=\text{O}-\text{NH}_2$ and $\text{COH})$
			419	Out-of-plane folding of ph, $\nu\text{NH}$
	385		383	$\beta_{\text{ph}}$ , $\tau(\text{C}=\text{O}-\text{NH}_2$ and $\text{COH})$
	296		275	$\rho\text{NH}_2$ , $\rho(\text{ph})$
			247	Out-of-plane wagging of whole molecule, especially ph ring
	161		184	$\omega\text{NH}_2$
	146			
	108		141	$\gamma(\text{whole molecule})$
	94			
		80		
		54 (55*)		
		48 (49*)		
		41*	30	$t(\text{ph}-\text{C}=\text{O}-\text{NH}_2)$
Benzamide			503	In-plane wagging of ph and amide
			415	Out-of-plane folding of ph ring
	412		414	Out-of-plane folding of ph ring, $\rho\text{NH}_2$
	383		375	In-plane rocking of amide group, $\omega_{\text{ph}}$ , $\nu_{\text{CC}}$
			341	$\omega\text{NH}_2$
	251		217	In-plane rocking of ph ring, $\rho(\text{C}=\text{O}-\text{NH}_2)$
	178			
	151		152	$\gamma_{\text{ph}}$ ; $\rho\text{NH}_2$
	110			
	90			
		58		
Acrylamide	54	54	57	$\gamma(\text{ph}-\text{CONH}_2)$ , $\omega\text{NH}_2$
		38		
	508		470	$t(\text{CH}=\text{CH}_2)$ , $t\text{NH}_2$
			468	$\rho\text{NH}_2$ , $\omega(\text{CH}=\text{CH}_2)$
	314		277	$\rho(\text{CH}=\text{CH}_2)$ , $\rho(\text{C}=\text{O}-\text{NH}_2)$
	185		190	$\omega\text{NH}_2$
	122		114	$\omega\text{NH}_2$ , $\omega(\text{CH}=\text{CH}_2)$
Caprolactam	67	67		
		48		
	503		508	$\nu\text{NH}$ ; $\rho\text{CH}_2$
	488		437	$\nu\text{C}=\text{O}$ ; $\nu\text{NH}$ ; $\omega\text{CH}_2$ ;
	398		402	$\beta_{\text{ring}}$
	337		323	$\rho\text{CH}_2$
	323		301	$\nu\text{NH}$ ; $\beta_{\text{ring}}$
	258		258	$\rho\text{CH}_2$ ; $\omega\text{CH}_2$ ; $\nu\text{NH}$ ; $\nu\text{C}=\text{O}$ ;
	195		158	$\rho\text{CH}_2$ , $\beta_{\text{ring}}$
	129		107	$\omega\text{CH}_2$ ; $\nu\text{C}=\text{O}$ ; $\gamma_{\text{ring}}$
	87			
	69	71		
	56	55		
		41		

TABLE I: Continued.

Compounds	Experiment		Calculation	Vibrational assignments
	FIR	THz-TDS	6-311++G(3df, 2pd)	
Sulfanilamide		73	85	Out-of-plane wagging of ph, $\omega\text{NH}_2$
		67		
		59		
		54	15	Out-of-plane wagging of ph, $\text{tNH}_2$

<sup>a</sup>  $\beta$ : in-plane vibration;  $\tau$ : torsion;  $\gamma$ : out-of-plane vibration;  $\nu$ : stretching;  $\omega$ : wagging;  $\rho$ : rocking;  $\text{t}$ : twisting, ph: benzene ring.

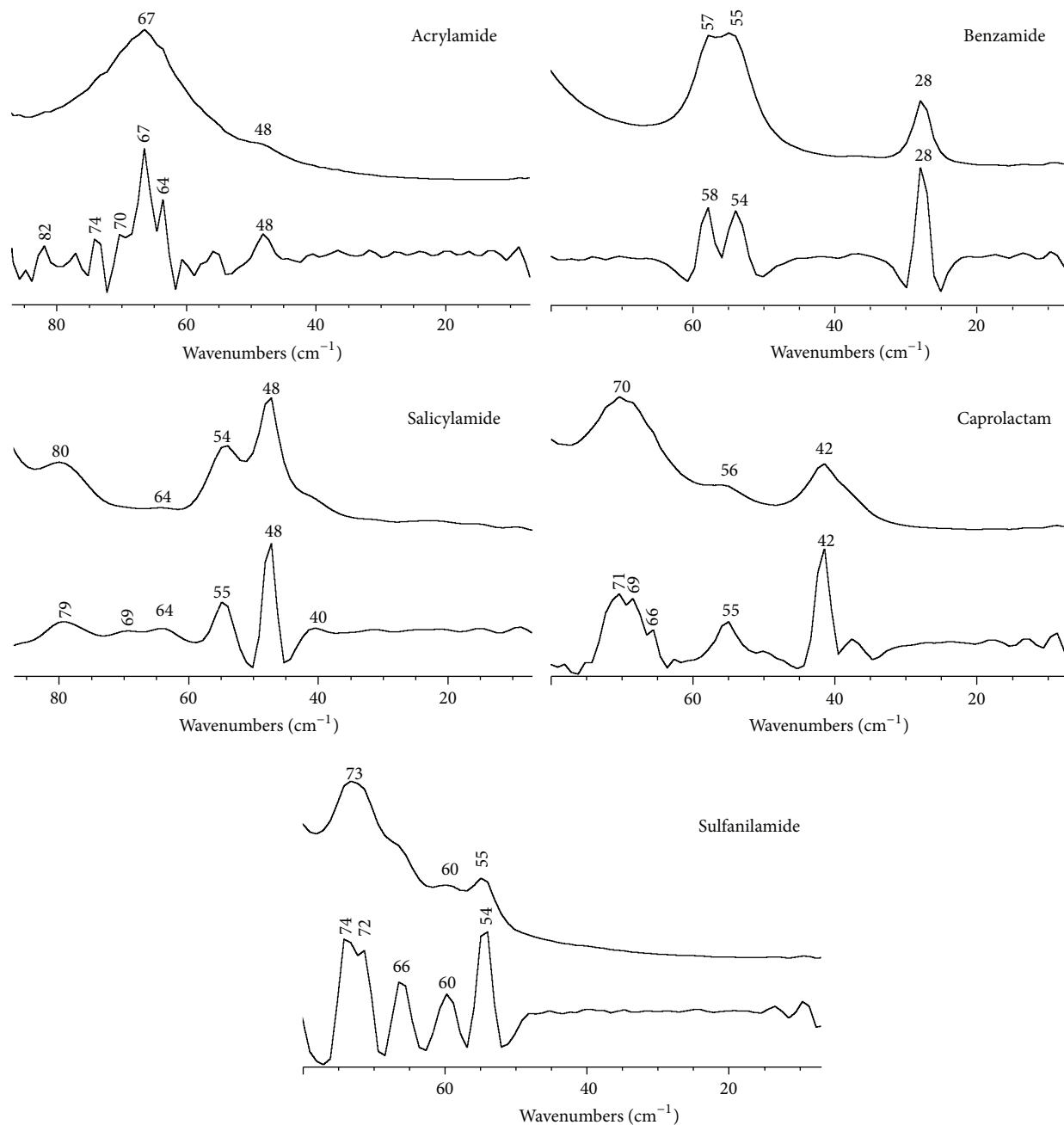


FIGURE 4: The second derivatives results for the THz spectra of the samples using Omnic 5.0 software.



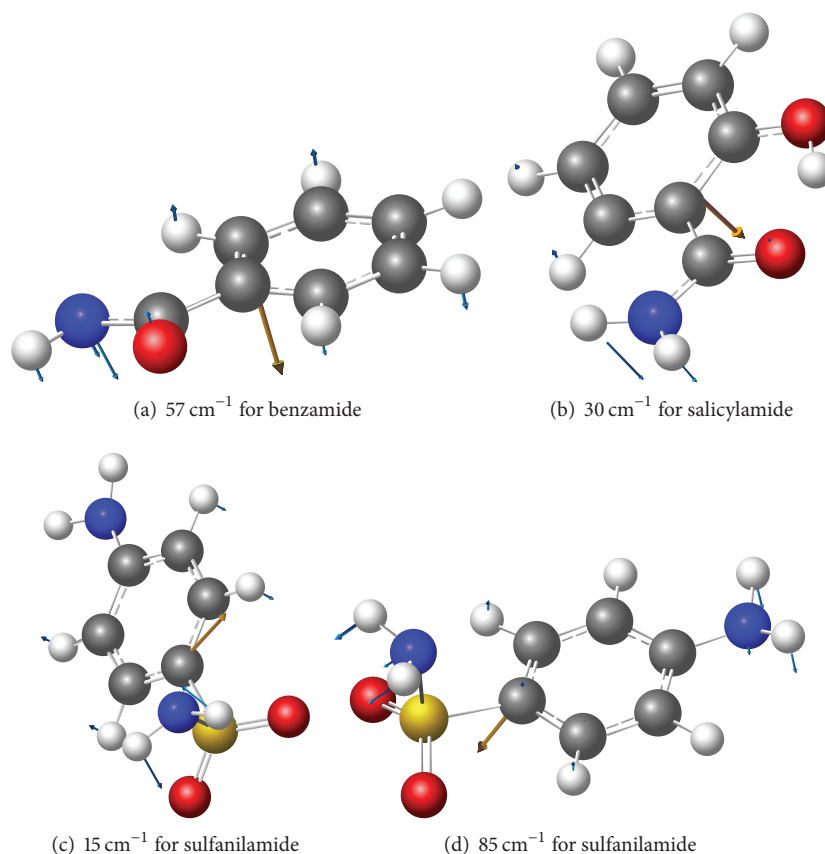


FIGURE 5: Low-frequency vibrational modes of the molecules below  $100\text{ cm}^{-1}$ . (a)  $57\text{ cm}^{-1}$  for benzamide; (b)  $30\text{ cm}^{-1}$  for salicylamide; (c)  $15\text{ cm}^{-1}$  for sulfanilamide; (d)  $85\text{ cm}^{-1}$  for sulfanilamide.

#### 4. Conclusions

The FIR and THz characteristic bands of five molecules with amide groups are observed using FIR and terahertz time-domain spectroscopy. The five molecules exhibit several bands in the THz region, which may be related to torsion, rocking, wagging, and other modes of different groups in the molecules according to calculation and the assignments in the references. THz spectra are effective method to distinguish different molecules with amide groups. In addition, it is also the basis for investigation on hydration of amide group, and so forth.

#### Conflict of Interests

The authors declare that there is no conflict of interests regarding the publication of this paper.

#### Acknowledgments

The authors gratefully acknowledge the financial support by National Natural Science Foundation of China for the Grants (21001009 and 50973003), the State Key Project for Fundamental Research of MOST (2011CB808304), National High-tech R&D Program of China (863 Program) of MOST

(2010AA03A406), and the Scientific Research Project of Beijing Municipal Commission of Education and Beijing Natural Science Foundation (Grant no. KZ201310028032). Limin Yang is one of the corresponding authors.

#### References

- [1] S. G. Liu, "Recent development of terahertz science and technology," *China Basic Science*, vol. 1, pp. 7–12, 2006.
- [2] M. C. Beard, G. M. Turner, and C. A. Schmuttenmaer, "Terahertz spectroscopy," *Journal of Physical Chemistry B*, vol. 106, no. 29, pp. 7146–7159, 2002.
- [3] M. C. Kemp, P. F. Taday, B. E. Cole, J. A. Cluff, A. J. Fitzgerald, and W. R. Tribe, "Security applications of terahertz technology," in *Terahertz for Military and Security Applications*, Proceedings of SPIE, pp. 44–52, April 2003.
- [4] M. R. Leahy-Hoppa, M. J. Fitch, and R. Oslander, "Terahertz spectroscopy techniques for explosives detection," *Analytical and Bioanalytical Chemistry*, vol. 395, no. 2, pp. 247–257, 2009.
- [5] A. G. Davies, A. D. Burnett, W. Fan, E. H. Linfield, and J. E. Cunningham, "Terahertz spectroscopy of explosives and drugs," *Materials Today*, vol. 11, no. 3, pp. 18–26, 2008.
- [6] P. M. Hakey, M. R. Hudson, D. G. Allis, W. Ouellette, and T. M. Korter, "Examination of phencyclidine hydrochloride via cryogenic terahertz spectroscopy, solid-state density functional

- theory, and X-ray diffraction,” *Journal of Physical Chemistry A*, vol. 113, no. 46, pp. 13013–13022, 2009.
- [7] C. J. Strachan, T. Rades, D. A. Newnham, K. C. Gordon, M. Pepper, and P. F. Taday, “Using terahertz pulsed spectroscopy to study crystallinity of pharmaceutical materials,” *Chemical Physics Letters*, vol. 390, no. 1–3, pp. 20–24, 2004.
- [8] P. F. Taday, I. V. Bradley, D. D. Arnone, and M. Pepper, “Using Terahertz pulse spectroscopy to study the crystalline structure of a drug: a case study of the polymorphs of ranitidine hydrochloride,” *Journal of Pharmaceutical Sciences*, vol. 92, no. 4, pp. 831–838, 2003.
- [9] L. J. Xie, Y. Yao, and Y. B. Ying, “The application of terahertz spectroscopy to protein detection: a review,” *Applied Spectroscopy Reviews*, vol. 49, no. 6, pp. 448–461, 2014.
- [10] B. Born, H. Weingärtner, E. Bründermann, and M. Havenith, “Solvation dynamics of model peptides probed by terahertz spectroscopy. observation of the onset of collective network motions,” *Journal of the American Chemical Society*, vol. 131, no. 10, pp. 3752–3755, 2009.
- [11] M. V. Tsurkan, N. S. Balbekin, E. A. Sobakinskaya, A. N. Panin, and V. L. Vaks, “Terahertz spectroscopy of DNA,” *Optics and Spectroscopy*, vol. 114, pp. 894–898, 2013.
- [12] T. M. Korter, R. Balu, M. B. Campbell, M. C. Beard, S. K. Gregurick, and E. J. Heilweil, “Terahertz spectroscopy of solid serine and cysteine,” *Chemical Physics Letters*, vol. 418, no. 1–3, pp. 65–70, 2006.
- [13] L. Yang, G. Zhao, W. Li et al., “Low-frequency vibrational modes of dl-homocysteic acid and related compounds,” *Spectrochimica Acta Part A*, vol. 73, no. 5, pp. 884–891, 2009.
- [14] L. Yang, H. Sun, S. Weng et al., “Terahertz absorption spectra of some saccharides and their metal complexes,” *Spectrochimica Acta Part A*, vol. 69, no. 1, pp. 160–166, 2008.
- [15] D. F. Plusquellic, K. Siegrist, E. J. Heilweil, and O. Esenturk, “Applications of terahertz spectroscopy in biosystems,” *ChemPhysChem*, vol. 8, no. 17, pp. 2412–2431, 2007.
- [16] B. Born, S. J. Kim, S. Ebbinghaus, M. Gruebele, and M. Havenith, “The terahertz dance of water with the proteins: the effect of protein flexibility on the dynamical hydration shell of ubiquitin,” *Faraday Discussions*, vol. 141, pp. 161–173, 2008.
- [17] B. Born and M. Havenith, “Terahertz dance of proteins and sugars with water,” *Journal of Infrared, Millimeter, and Terahertz Waves*, vol. 30, no. 12, pp. 1245–1254, 2009.
- [18] H. H. Mantsch and D. Naumann, “Terahertz spectroscopy: the renaissance of far infrared spectroscopy,” *Journal of Molecular Structure*, vol. 964, no. 1–3, pp. 1–4, 2010.
- [19] N. C. Comelli, N. E. Massa, E. A. Castro, and A. H. Jubert, “Spectroscopy properties of the amide group in valpromide and some derivatives with antiepileptic activity,” *Journal of Raman Spectroscopy*, vol. 40, no. 12, pp. 1797–1809, 2009.
- [20] K. M. Gough, L. Tzadu, M. Z. Kastyak, A. C. Kuzyk, and R. L. Julian, “Theoretical and experimental considerations for interpretation of amide I bands in tissue,” *Vibrational Spectroscopy*, vol. 53, no. 1, pp. 71–76, 2010.
- [21] H. Maekawa and N.-H. Ge, “Comparative study of electrostatic models for the amide-I and -II modes: linear and two-dimensional infrared spectra,” *Journal of Physical Chemistry B*, vol. 114, no. 3, pp. 1434–1446, 2010.
- [22] A. S. Kutsenko, R. A. Motiyenko, L. Margules, and J. C. Guillemin, “The extended spectroscopic database for deuterated species of formamide up to 1 THz,” *Astronomy and Astrophysics*, vol. 549, article A128, 4 pages, 2013.
- [23] C.-S. Su and Y.-P. Chen, “Recrystallization of salicylamide using a batch supercritical antisolvent process,” *Chemical Engineering and Technology*, vol. 28, no. 10, pp. 1177–1181, 2005.
- [24] V. O. Sheftel, *Indirect Food Additives and Polymers: Migration and Toxicology*, Lewis, London, UK, 2000.
- [25] A. S. R. Duarte, A. M. Amorim Da Costa, and A. M. Amado, “On the conformation of neat acrylamide dimers—a study by ab initio calculations and vibrational spectroscopy,” *Journal of Molecular Structure: THEOCHEM*, vol. 723, no. 1–3, pp. 63–68, 2005.
- [26] R. J. Falconer and A. G. Markelz, “Terahertz spectroscopic analysis of peptides and proteins,” *Journal of Infrared, Millimeter, and Terahertz Waves*, vol. 33, no. 10, pp. 973–988, 2012.
- [27] Y. Hu, X.-H. Wang, L.-T. Guo, C.-L. Zhang, H.-B. Liu, and X.-C. Zhang, “Absorption and dispersion of vegetable oil and animal fat in THz range,” *Acta Physica Sinica*, vol. 54, no. 9, pp. 4124–4128, 2005.
- [28] M. J. Frisch, G. W. Trucks, H. B. Schlegel, C. Gonzalez, and J. A. Pople, *Gaussian 03, Revision C.02*, Gaussian, Inc., Wallingford, Conn, USA, 2004.
- [29] P. J. Stephens, F. J. Devlin, C. F. Chabalowski, and M. J. Frisch, “Ab initio calculation of vibrational absorption and circular dichroism spectra using density functional force fields,” *Journal of Physical Chemistry*, vol. 98, no. 45, pp. 11623–11627, 1994.
- [30] R. Krishnan, J. S. Binkley, R. Seeger, and J. A. Pople, “Self-consistent molecular orbital methods. XX. A basis set for correlated wave functions,” *The Journal of Chemical Physics*, vol. 72, no. 1, pp. 650–654, 1980.
- [31] J. Palomar, J. L. G. De Paz, and J. Catalán, “Vibrational study of intramolecular hydrogen bonding in o-hydroxybenzoyl compounds,” *Chemical Physics*, vol. 246, no. 1–3, pp. 167–208, 1999.
- [32] N. Sundaraganesan, N. Puvvarasan, and S. Mohan, “Vibrational spectra, assignments and normal coordinate calculation of acrylamide,” *Talanta*, vol. 54, no. 2, pp. 233–241, 2001.
- [33] H. T. Varghese, C. Y. Panicker, and D. Philip, “Vibrational spectroscopic studies and ab initio calculations of sulfanilamide,” *Spectrochimica Acta Part A*, vol. 65, no. 1, pp. 155–158, 2006.
- [34] C. Topacli and A. Topacli, “Semi-empirical infrared spectra simulations of metal complexes of sulfanilamide,” *Journal of Molecular Structure*, vol. 654, no. 1–3, pp. 153–159, 2003.
- [35] C. Topacli and A. Topacli, “Ab initio calculations and vibrational structure of sulfanilamide,” *Journal of Molecular Structure*, vol. 644, no. 1–3, pp. 145–150, 2003.
- [36] G. Ogruc Ildiz and S. Akyuz, “Conformational analysis and vibrational study of sulfanilamide,” *Vibrational Spectroscopy*, vol. 58, pp. 12–18, 2012.
- [37] G. Z. Zhao, B. Yu, and C. L. Zhang, “Terahertz spectroscopic investigation of four kinds of vitamins,” *Journal of Applied Physics*, vol. 106, Article ID 104702, 5 pages, 2009.



## Research Article

# Interaction of Bradykinin and B<sub>2</sub> Bradykinin Receptor Antagonists with Colloidal Au Surface Explored by Surface-Enhanced Raman Scattering

Dominika Skořuba,<sup>1</sup> Dariusz Sobolewski,<sup>2</sup> Adam Prahl,<sup>2</sup> and Edyta Proniewicz<sup>3</sup>

<sup>1</sup> Faculty of Chemistry, Jagiellonian University, Ulica Ingardena 3, 30-060 Krakow, Poland

<sup>2</sup> Department of Chemistry, University of Gdansk, Sobieskiego 18, 80-592 Gdansk, Poland

<sup>3</sup> Faculty of Foundry Engineering, AGH University of Science and Technology, ul. Reymonta 23, 30-059 Krakow, Poland

Correspondence should be addressed to Edyta Proniewicz; [proniewi@agh.edu.pl](mailto:proniewi@agh.edu.pl)

Received 2 September 2013; Accepted 12 October 2013; Published 4 February 2014

Academic Editor: Yizhuang Xu

Copyright © 2014 Dominika Skořuba et al. This is an open access article distributed under the Creative Commons Attribution License, which permits unrestricted use, distribution, and reproduction in any medium, provided the original work is properly cited.

Bradykinin (BK), an endogenous peptide hormone, which is involved in a number of physiological and pathophysiological processes, and the potent B<sub>2</sub> bradykinin receptor antagonists, [D-Arg<sup>0</sup>,Hyp<sup>3</sup>,Thi<sup>5,8</sup>,L-Pip<sup>7</sup>]BK, Aaa[D-Arg<sup>0</sup>,Hyp<sup>3</sup>,Thi<sup>5,8</sup>,L-Pip<sup>7</sup>]BK, [D-Arg<sup>0</sup>,Hyp<sup>3</sup>,Thi<sup>5</sup>,D-Phe<sup>7</sup>,L-Pip<sup>8</sup>]BK, and Aaa[D-Arg<sup>0</sup>,Hyp<sup>3</sup>,Thi<sup>5</sup>,D-Phe<sup>7</sup>,L-Pip<sup>8</sup>]BK, were deposited onto colloidal Au particles of 20 nm size. Interaction of these molecules with colloidal Au surface was explored by surface-enhanced Raman scattering (SERS). Briefly, it was shown that BK adsorbs on the Au surface mainly through the Phe<sup>5</sup>/Phe<sup>8</sup> residues. In case of the BK specifically modified analogues mainly the Pip and Thi rings are involved in the interaction process; however, Pip and Thi adopt slightly different orientation with respect to Au for each of the analogues. In addition, the lack of the Aaa vibrations, together with the enhancement of the Thi, Pip, or Phe modes, emphasizes the importance of the C-terminus in the interaction with the Au surface.

## 1. Introduction

Bradykinin (BK; Arg<sup>1</sup>-Pro<sup>2</sup>-Pro<sup>3</sup>-Gly<sup>4</sup>-Phe<sup>5</sup>-Ser<sup>6</sup>-Pro<sup>7</sup>-Phe<sup>8</sup>-Arg<sup>9</sup>) is an important endogenous oligopeptide counted from the family of kinins [1]. Biological activities of BK are associated with a number of physiological and pathophysiological processes, including regulation of vascular permeability, formation of edema, stimulation of nerve endings, and inflammation process [2, 3]. It is also a potent cancers growth factor, especially prostate and lung carcinoma [4, 5]. Biological effects of BK are mediated by activation of the G protein coupled seven transmembrane receptors (GPCRs), named B<sub>1</sub> and B<sub>2</sub> [6]. GPCRs are the largest group of the membrane receptors [7]. The B<sub>1</sub> receptors are poorly detectable under physiological conditions, whereas the B<sub>2</sub> receptors are continuously produced. The B<sub>2</sub> receptors mediate most of the biological effects and demonstrate a high affinity for BK [8].

The biological significance of BK motivated researchers to explore behavior of this peptide at different solid/liquid interfaces. For example, studies using nuclear magnetic resonance (NMR) [9, 10], circular dichroism (CD) [11], and molecular dynamics [12] have explored mode of BK binding to different membranes and pointed out the formation of the BK C-terminal (Ser<sup>6</sup>-Arg<sup>9</sup>)  $\beta$ -turn structure in the membrane-bound state of BK that is crucial for this binding to the B<sub>2</sub> receptor [12, 13]. Studies on BK adsorbed onto the electrochemically roughened Ag, Au, and Cu electrode surfaces in an aqueous solution at physiological pH at different applied electrode potential have shown that BK interacts mainly through the two Phe (L-phenylalanine), Arg (L-arginine), and Pro (L-proline) residues, but in different arrangements, with each of the metal surfaces [14]. These results are similar to those from the biological activity studies [15]. Also, experiments for isotopically labeled BK deposited onto the Ag electrode have demonstrated that the reorientation

of the BK phenyl rings cannot keep up with the electrode potential changes at the electrode potential range from  $-0.8$  to  $-0.4$  V [16]. Another examination of four of the  $B_2$  BK receptor antagonists immobilized onto Ag SERS-active: ROC (prepared in the reduction-oxidation cycles) and colloidal substrates have demonstrated that the adsorption mode of BK varied in time on the ROC substrate and the ROC surface is more selective than the colloidal one [17, 18].

In this work, using surface-enhanced Raman spectroscopy (SERS) we characterized adsorption mode of BK and its four synthetic  $B_2$  BK receptor antagonists: [D-Arg<sup>0</sup>,Hyp<sup>3</sup>,Thi<sup>5,8</sup>,L-Pip<sup>7</sup>]BK, Aaa[D-Arg<sup>0</sup>,Hyp<sup>3</sup>,Thi<sup>5,8</sup>,L-Pip<sup>7</sup>]BK, [D-Arg<sup>0</sup>,Hyp<sup>3</sup>,Thi<sup>5</sup>,D-Phe<sup>7</sup>,L-Pip<sup>8</sup>]BK, and Aaa[D-Arg<sup>0</sup>,Hyp<sup>3</sup>,Thi<sup>5</sup>,D-Phe<sup>7</sup>,L-Pip<sup>8</sup>]BK (where Aaa denotes 1-adamantaneacetic acid, Hyp—L-hydroxyproline, Thi—L-thienylalanine, and Pip—L-pipecolic acid) onto colloidal Au spheres with the diameters of approximately 20 nm. The SERS technique was earlier used in our laboratory to correlate the structural components of the many different peptides, including bombesin, vasopressin, neurotensin, and their modified analogs with their capability to interact with the proper metabotropic receptor [19–22]. Also, our aim is correlation of information resulting from the spectroscopic and biological activity investigations.

Since 1979, it is known that the composition of the metallic nanostructures has influence on the intensity of the SERS signal. Ag enhances the Raman signal more (10–100-fold) than Au because of the plasmon resonance [23]. In addition, Ag can be excited in the light range from the UV to the IR, whereas Au is limited to the red or IR due to damping by the interband transitions [24]. Despite these limitations, essential structural studies for living organisms are commonly performed for Au. It is due to significantly higher biocompatibility and better control of the size and shape of Au in comparison to the Ag nanostructures [25].

## 2. Materials and Methods

**2.1. Peptide Synthesis.** BK, [D-Arg<sup>0</sup>,Hyp<sup>3</sup>,Thi<sup>5,8</sup>,L-Pip<sup>7</sup>]BK, Aaa[D-Arg<sup>0</sup>,Hyp<sup>3</sup>,Thi<sup>5,8</sup>,L-Pip<sup>7</sup>]BK, [D-Arg<sup>0</sup>,Hyp<sup>3</sup>,Thi<sup>5</sup>,D-Phe<sup>7</sup>,L-Pip<sup>8</sup>]BK, and Aaa[D-Arg<sup>0</sup>,Hyp<sup>3</sup>,Thi<sup>5</sup>,D-Phe<sup>7</sup>,L-Pip<sup>8</sup>]BK were obtained by the solid-phase method using the Fmoc-strategy starting from Fmoc-Arg(Pbf)-Wang resin (GL Biochem Shanghai Ltd., 1% DVB, 100–200 mesh, 0.47 mmol/g) [26]. Fmoc was removed by 20% piperidine in DMF. A 3-fold excess of the respective Fmoc-amino acids was activated *in situ* using HATU (1 eq)/HOAt (1 eq) in a mixture of DMF/NMP (1:1 v/v) containing 1% Triton, and the coupling reactions were base-catalyzed with NMM (2 eq). The amino acid side-chain-protecting groups were Bu<sup>t</sup> for Hyp and Ser and Pbf for Arg and D-Arg. All of the Fmoc-protected amino acids were commercially available (NovaBiochem, Bad Soden, Germany). Aaa (1-adamantaneacetic acid) was coupled in the final coupling step (for acylated peptides) using the same procedure as that for Fmoc-amino acids. Cleavage of the peptides from the resin with side-chain deprotection was performed by treatment with TFA:H<sub>2</sub>O:TIS (95:2.5:2.5 v/v/v) for

4 h. The total volume of the TFA filtrate was reduced to approximately 1 mL by evaporation *in vacuo*. The peptides were precipitated with cold diethyl ether and filtered through a Schott funnel. All of the peptides were purified by semipreparative high-performance liquid chromatography (HPLC). HPLC was executed on a Waters (analytical and semipreparative) chromatograph equipped with a UV detector ( $\lambda = 226$  nm). The purity of the peptides was determined on a Discovery HS C<sub>18</sub> column (5  $\mu$ m, 100  $\text{\AA}$ ; 250  $\times$  4.6 mm). The solvent systems were (A) 0.1% aqueous trifluoroacetic acid (TFA) and (B) 80% acetonitrile in aqueous 0.1% TFA (v/v). A linear gradient from 1 to 80% of (B) over 30 min was applied for peptides at a flow rate of 1 mL/min. Semipreparative HPLC was performed using a Kromasil C<sub>8</sub> column (5  $\mu$ m, 100  $\text{\AA}$ ; 16  $\times$  250 mm) in a linear gradient from 10 to 40% of (B) for 90 min at a flow rate of 8 mL/min. The mass spectra of the peptides were recorded on a Bruker BIFLEX III MALDI TOF mass spectrometer (ionization: 337 nm nitrogen laser).

**2.2. SERS Measurement in Au Colloid Solution.** The Au colloid was purchased from Sigma Aldrich (stabilized suspension in citrate buffer, diameter 20 nm). Aqueous solution of the peptides was prepared by dissolution of the peptides in deionized water. The concentration of the peptide solutions was adjusted to  $10^{-4}$  M before them being mixed with the Au colloid. 10  $\mu$ L of peptide sample was mixed with 20  $\mu$ L of Au nanoparticles. The SERS spectra of the peptides were obtained using Renishaw spectrometer (model inVia) operating in confocal mode combined with a Peltier cooled CCD detector and a Leica microscope (50x long-distance objective). Excitation wavelength at 785 nm was used from HP NIR diode laser. The laser power at the laser output was set at approximately 20 mW. Generally, the SERS spectra were measured at four spots on the surfaces of the colloidal Au nanoparticles and were obtained during 2 h of sample addition to the Au solution. The spectra from the series were nearly identical, except for small differences in some band intensities. During measurements no spectral changes due to the sample decomposition or desorption processes were observed.

**2.3. Spectral Analysis.** The spectral analysis was performed using the GRAMS/AI 8.0 (Thermo Electron Corp.).

## 3. Results and Discussion

Figure 1 presents the SERS spectra of Figure 1(a) BK and its four potent  $B_2$  BK receptor antagonists: Figure 1(b) [D-Arg<sup>0</sup>,Hyp<sup>3</sup>,Thi<sup>5,8</sup>,L-Pip<sup>7</sup>]BK, Figure 1(c) Aaa[D-Arg<sup>0</sup>,Hyp<sup>3</sup>,Thi<sup>5,8</sup>,L-Pip<sup>7</sup>]BK, Figure 1(d) [D-Arg<sup>0</sup>,Hyp<sup>3</sup>,Thi<sup>5</sup>,D-Phe<sup>7</sup>,L-Pip<sup>8</sup>]BK, and Figure 1(e) Aaa[D-Arg<sup>0</sup>,Hyp<sup>3</sup>,Thi<sup>5</sup>,D-Phe<sup>7</sup>,L-Pip<sup>8</sup>]BK (see Table 1 for molecular structures) in the Au aqueous solution excited with 785 nm line. The spectral positions of the enhanced bands in these spectra, given in wavenumbers, are summarized in Table 2 together with the proposed vibrational assignments. This assignment leans on the earlier studies of amino acids lyophilized and deposited

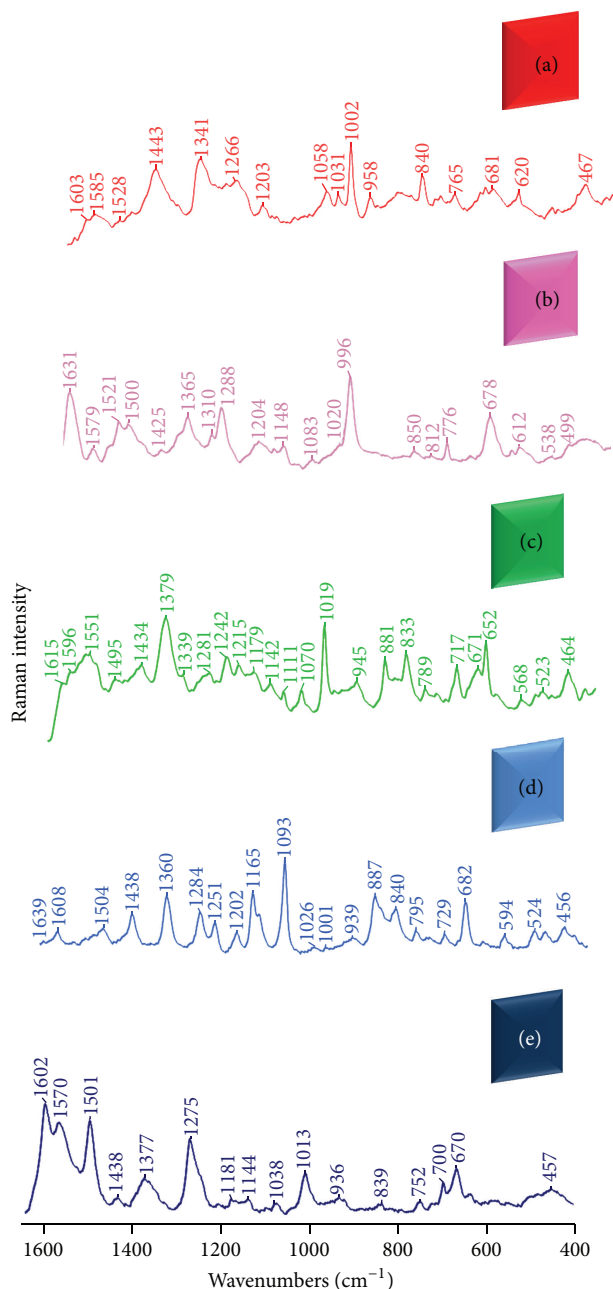


FIGURE 1: The SERS spectra of (a) BK and its analogues: (b) [D-Arg<sup>0</sup>,Hyp<sup>3</sup>,Thi<sup>5,8</sup>,L-Pip<sup>7</sup>] BK, (c) Aaa[D-Arg<sup>0</sup>,Hyp<sup>3</sup>,Thi<sup>5,8</sup>,L-Pip<sup>7</sup>]BK, (d) [D-Arg<sup>0</sup>,Hyp<sup>3</sup>,Thi<sup>5</sup>,D-Phe<sup>7</sup>,L-Pip<sup>8</sup>]BK, and (e) Aaa[D-Arg<sup>0</sup>,Hyp<sup>3</sup>,Thi<sup>5</sup>,D-Phe<sup>7</sup>,L-Pip<sup>8</sup>]BK adsorbed onto a colloidal Au particles surface in an aqueous solution.

onto the colloidal Au surface [27, 28], BK, and its modified analogs [16–18], piperidine (Pip) [29, 30] and thiophene (Thi) [31–33]. Based on the analysis of the changes in the bands enhancement, bands width, and shift in bands wavenumber between corresponding Raman [14, 16–18] and SERS spectra conclusions about the adsorption process of BK and its four analogs deposited onto the colloidal Au surface were drawn as described below.

The SERS spectrum of BK (Figure 1(a)) is dominated by 1603 [ $\nu_{8a}$ ], 1585 [ $\nu_{8b}$ ], 1443 [ $\nu_{19b}$ ], 1203 [ $\nu_{7a}$ ], 1031 [ $\nu_{18a}$ ],

1002 [ $\nu_{12}$ ], and 620 cm<sup>-1</sup> [ $\nu_{6b}$ ] bands due to the Phe residues (Phe<sup>5</sup>/Phe<sup>8</sup>) vibrations. According to the so-called surface selection rules, the phenyl ring orientation with respect to the colloidal Au substrate could be predicted based on the relative intensity of the aforementioned bands [34, 35]. For a perpendicular orientation of an aromatic ring onto metal surface these rules postulate that the in-plane modes should be mainly enhanced in the SERS spectra. On the other hand, for a horizontal orientation of the aromatic ring on the metal surface the out-of-plane vibrations should be stronger than

TABLE 1: Amino acid sequence of bradykinin (BK) and its specifically mutated analogues investigated in this work.

Analogue	0'	0	Amino acid sequence								
			1 <sup>a</sup>	2 <sup>a</sup>	3	4 <sup>a</sup>	5	6 <sup>a</sup>	7	8	9 <sup>a</sup>
BK			Arg	Pro	Pro	Gly	Phe	Ser	Pro	Phe	Arg
[D-Arg <sup>0</sup> ,Hyp <sup>3</sup> ,Thi <sup>5,8</sup> ,L-Pip <sup>7</sup> ]BK		D-Arg	Arg	Pro	Hyp	Gly	Thi	Ser	L-Pip	Thi	Arg
Aaa[D-Arg <sup>0</sup> ,Hyp <sup>3</sup> ,Thi <sup>5,8</sup> ,L-Pip <sup>7</sup> ]BK		Aaa D-Arg	Arg	Pro	Hyp	Gly	Thi	Ser	L-Pip	Thi	Arg
[D-Arg <sup>0</sup> ,Hyp <sup>3</sup> ,Thi <sup>5</sup> ,D-Phe <sup>7</sup> ,L-Pip <sup>8</sup> ]BK		D-Arg	Arg	Pro	Hyp	Gly	Thi	Ser	D-Phe	L-Pip	Arg
Aaa[D-Arg <sup>0</sup> ,Hyp <sup>3</sup> ,Thi <sup>5</sup> ,D-Phe <sup>7</sup> ,L-Pip <sup>8</sup> ]BK		Aaa D-Arg	Arg	Pro	Hyp	Gly	Thi	Ser	D-Phe	L-Pip	Arg



Aaa: 1-adamantaneacetic acid



Hyp: L-hydroxyproline

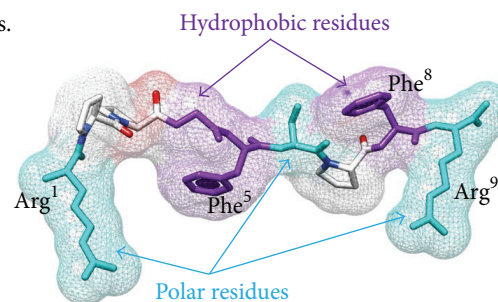


Thi: L-thienylalanine



Pip: L-pipecolic acid

<sup>a</sup>Common amino acid in the sequence of all investigated analogues.



the in-plane vibrations. Thus, based on the propensity rules and phenomenon that the in-plane  $1002\text{ cm}^{-1}$  band is the strongest band in the BK SERS spectrum and is less intense than that in the BK Raman spectrum it can be suggested that the BK phenyl rings adopt the tilted orientation with respect to the Au nanoparticles surface [14, 16]. The neglected shift in wavenumber and  $4\text{ cm}^{-1}$  band broadening of the  $1002\text{ cm}^{-1}$  SERS signal in comparison with those in the corresponding Raman spectrum together with the symmetric shape of this band indicate that the BK phenyls rings do not interact directly with Au. Thus, should be located in slight distance from Au.

Apart from the phenyl rings, the Arg and Pro residues are also involved in the interaction of BK with the colloidal Au surface. The Arg and Pro oscillations at  $1443\text{ cm}^{-1}$  [ $\delta(\text{NH})$ ],  $1341\text{ cm}^{-1}$  [ $\rho_{\text{sb}}(\text{CH}_3)$ ],  $1058\text{ cm}^{-1}$  [ $\nu(\text{CC}) + \nu(\text{NC})$ ], and  $840\text{ cm}^{-1}$  [ $\delta(\text{NH})$ ]  $\text{cm}^{-1}$  and at  $1528$ ,  $1443$ , and  $765\text{ cm}^{-1}$  (see Table 2 for the bands assignment), respectively, determine this interaction.

In the SERS spectrum of [D-Arg<sup>0</sup>,Hyp<sup>3</sup>,Thi<sup>5,8</sup>,L-Pip<sup>7</sup>]BK (Figure 1(b)) the weak  $1579$ ,  $1310$ ,  $1148$ ,  $1020$ ,  $850$ ,  $776$ ,  $612$ , and  $499\text{ cm}^{-1}$  and the strong  $1288$  and  $996\text{ cm}^{-1}$  spectral features (see Table 2 for bands assignment) point out the interaction between Pip<sup>7</sup> and the colloidal Au surface. The broadness and pronounced intensity of the last two SERS bands additionally suggest the participation of the free electron-pair on the Pip<sup>7</sup> nitrogen atom in this interaction. This is possible when the Pip<sup>7</sup> ring adopts the tilted orientation. Also, Thi and Arg contribute to the SERS spectrum of [D-Arg<sup>0</sup>,Hyp<sup>3</sup>,Thi<sup>5,8</sup>,L-Pip<sup>7</sup>]BK onto the Au surface. This conclusion is based on the

appearance of the  $1521$ ,  $1500[\delta(\text{CH}) + \nu(\text{C}=\text{C})]$ , in-plane],  $1365$  [ $\delta(\text{CH}) + \nu(\text{C}=\text{C})$ , in-plane],  $1083$  [ $\rho_{\text{r}}(\text{CH})$ , in-plane],  $850$  [ $\delta(\text{ring}) + \nu(\text{CC})_{\text{ring}}$ , in-plane], and  $678\text{ cm}^{-1}$  [ $\nu(\text{CH})$ , out-of-plane] bands due to Thi [31, 32]. The similar medium relative enhancement of the in-plane and out-of-plane Thi modes implies the tilted orientation of the Thi ring with respect to the Au nanoparticles surface. On the other hand, the interaction of the guanidine group with colloidal Au surface is manifested by the  $1631$ ,  $1425$ , and  $1365\text{ cm}^{-1}$  SERS signals.

Addition of Aaa at the N-terminal end of [D-Arg<sup>0</sup>,Hyp<sup>3</sup>,Thi<sup>5,8</sup>,L-Pip<sup>7</sup>]BK produces marked changes in the SERS spectral pattern as is evident in Figure 1(c) (the Aaa[D-Arg<sup>0</sup>,Hyp<sup>3</sup>,Thi<sup>5,8</sup>,L-Pip<sup>7</sup>]BK analog). In the spectrum of Aaa[D-Arg<sup>0</sup>,Hyp<sup>3</sup>,Thi<sup>5,8</sup>,L-Pip<sup>7</sup>]BK in the Au solution, the  $1596$ ,  $1551$ ,  $1379$ ,  $1281$ ,  $1242$ ,  $1179$ ,  $1142$ ,  $1019$ ,  $881$ ,  $833$ ,  $652$ , and  $464\text{ cm}^{-1}$  (see Table 2 for bands assignment) signals are due to Pip<sup>7</sup>. Among these, the  $1379$  and  $1019\text{ cm}^{-1}$  bands exhibit the predominant relative intensity (Figure 1(c)) what point out on the vertical orientation of Pip<sup>7</sup> on the Au surface. Although it seems that the Pip<sup>7</sup> nitrogen atom does not participate directly with this surface (weak  $1281\text{ cm}^{-1}$  band). Also, bands due to the Thi vibrations ( $1495$ ,  $1215$ ,  $1179$ ,  $1070$ ,  $881$ ,  $833$ ,  $671$ , and  $568\text{ cm}^{-1}$ ) are weakly enhanced in the Aaa[D-Arg<sup>0</sup>,Hyp<sup>3</sup>,Thi<sup>5,8</sup>,L-Pip<sup>7</sup>]BK SERS spectrum. This is why we suggest that Thi assists in the adsorption process onto the Au surface.

In the SERS spectrum of [D-Arg<sup>0</sup>,Hyp<sup>3</sup>,Thi<sup>5</sup>,D-Phe<sup>7</sup>,L-Pip<sup>8</sup>]BK (Figure 1(d)), the phenyl ring (D-Phe<sup>7</sup>) modes ( $1608$ ,  $1026$ , and  $1001\text{ cm}^{-1}$ ) are weakly enhanced. Unlike those, the

TABLE 2: Wavenumbers and proposed band assignments for SERS spectra of A: BK, B: [D-Arg<sup>0</sup>,Hyp<sup>3</sup>,Thi<sup>5,8</sup>,L-Pip<sup>7</sup>]BK, C: Aaa[D-Arg<sup>0</sup>,Hyp<sup>3</sup>,Thi<sup>5,8</sup>,L-Pip<sup>7</sup>]BK, D: [D-Arg<sup>0</sup>,Hyp<sup>3</sup>,Thi<sup>5</sup>,D-Phe<sup>7</sup>,L-Pip<sup>8</sup>]BK, and E: Aaa[D-Arg<sup>0</sup>,Hyp<sup>3</sup>,Thi<sup>5</sup>,D-Phe<sup>7</sup>,L-Pip<sup>8</sup>]BK adsorbed onto colloidal gold surface.

	Wavenumber/cm <sup>-1</sup>				
	A	B	C	D	E
$\rho_s(\text{NH}_2)$ , Arg[ $\nu_s(\text{C}=\text{N})$ ], and/or Amide I	—	1631	1615	1639	—
Phe[ $\nu_{8a}$ ] and/or Arg[ $\delta(\text{NH}_2^+) + \nu_s(\text{C}=\text{N})$ ]	1603	—	—	1608	1602
Phe[ $\nu_{8b}$ ] and/or Pip and/or Arg[ $\delta(\text{NH})$ ]	1585	1579	1596	—	1570
Pip	—	—	1551	—	—
Imide II' and/or Thi[ $\nu(\text{CC})$ ]	1528	1521	—	—	—
Thi[ $\nu(\text{C}-\text{C})$ ]	—	1500	1495	1504	1501
Phe[ $\nu_{19b}$ ], Arg[ $\delta(\text{NH})$ ], and/or tertiary amide IIp marker	1443	1425	1434	1438	1438
Thi[ $\delta(\text{CH}) + \nu(\text{C}=\text{C})$ ], Pip combination, and/or $\nu(\text{COO}^-)$	—	1365	1379	1360	1377
Arg[ $\rho_{sb}(\text{CH}_3)$ ]	1341	—	1339	—	—
Pip[ $\rho_w(\text{CH}_2)$ ]	—	1310	—	—	—
Pip[ $\nu(\text{CN}) + \rho_b(\text{CCH}) + \rho_{t/t}(\text{CH}_2)$ ] and/or Amide III	—	1288	1281	1284	1275
Phe[ $\nu_4$ ]	1266	—	—	—	—
Pip[ $\rho_t(\text{CH}_2)$ ] and/or Amide III	—	—	1242	1251	—
Phe[ $\nu_{7a}$ ]	1203	—	—	—	—
Thi[ $\nu(\text{CH})$ ]	—	1204	1215	1202	1212
Arg[ $\nu(\text{CN})$ ] and/or Thi[ $\rho_t(\text{CH})$ ]	—	1170	1179	1165	1181
Arg[ $\nu(\text{CCC})$ ] and/or Pip[ $\rho_t(\text{CH}_2)$ ]	—	1148	1142	1151	1144
Aaa[ $\nu(\text{CC})$ ]	—	—	1111	—	1102
Thi[in-plane $\rho_t(\text{CH})$ ] and/or Arg [ $\nu(\text{CN})$ ]	—	—	—	1093	—
Arg[ $\nu(\text{CN})$ ] and/or Thi[ $\rho_t(\text{CH})$ ]	—	1083	1070	—	1083
Arg[ $\nu(\text{CC}) + \nu(\text{NC})$ ]	1058	—	—	—	1045
Phe[ $\nu_{18a}$ ]	1031	—	—	1026	—
Pip[skeletal stretching]	—	1020 996	1019	—	1013
Phe[ $\nu_{12}$ ]	1002	—	—	1000	—
$\nu(\text{CC}) + \rho_t(\text{CH}_2)$	958	—	945	957	—
	—	—	—	939	936
Arg[ $\rho_b(\text{NH}_2)$ ], Pip[ $\rho_t(\text{CH})$ ], and/or Thi[ $\rho_w(\text{CH}_2) + \gamma(\text{ring})$ ]	—	—	—	—	925
Thi[ $\delta(\text{ring}) + \nu(\text{CS})$ ] and/or Pip skeletal stretching	—	—	881	887	—
Arg[ $\delta(\text{NH})$ ], Thi[ $\delta(\text{ring}) + \nu(\text{CC})$ ], and/or Pip $\nu(\text{CC})$	840	850	—	840	—
Pip ring breathing, Arg[ $\rho_w(\text{NH}_2)$ ], and/or Thi[ $\nu(\text{CC}) + \delta(\text{ring})$ ]	—	812	833	—	839
Pip[ring breathing]	—	776	763	763	752
Pro[ $\rho_t(\text{CH}_2)_{\text{ring}}$ ]	765	—	—	—	—
Pip	—	723	—	729	725
Pip	—	—	717	—	700
Thi[ $\rho_w(\text{CH})$ ] and/or Arg [ $\delta(\text{COO}^-)$ ]	681	678	671	682	670
$\rho_b(\text{COO})$ and/or Amide	—	—	652	—	—
Phe[ $\nu_{6b}$ ]	620	—	—	—	—
Pip	—	612	—	594	—
Thi[ $\gamma(\text{ring}) + \rho_w(\text{CH}_2)$ ]	—	—	568	—	—
$\rho_b(\text{CO})$ and/or $\rho_t(\text{CH}_2)$	—	538	—	534	—
Pip	—	499	—	—	—
Skeletal	467	—	464	—	457
Thi[ $\gamma(\text{ring})$ ]	—	—	426	—	—

$\nu$ : stretching,  $\delta$ : deformation,  $\gamma$ : torsion,  $\rho_t$ : twisting,  $\rho_b$ : bending  $\rho_r$ : rocking,  $\rho_w$ : wagging, and  $\rho_s$ : scissoring vibrations; Phe: phenylalanine, Arg: arginine, Thi: L-thienylalanine, Aaa: 1-adamantaneacetic acid, and Pip: L-pipecolic acid.



bands mainly connected with the  $\text{Thi}^5$  ring dominate this spectrum (at 1504, 1360, 1165, 1093, 887, 840, and  $682\text{ cm}^{-1}$ ). These results are in contrast to those obtained for the abovementioned analog adsorbed on the colloidal Ag surface [18] and suggest that the  $\text{D-Phe}^7$  ring is removed from the Au surface (no shift in the Phe bands wavenumber and width), whereas the  $\text{Thi}^5$  adopts the vertical arrangement on this surface. The appearance bands at 1284, 1251, 1151, 887, 840, 763, 729, and  $594\text{ cm}^{-1}$  indicate that also  $\text{Pip}^8$  contributed to the SERS spectrum on Au surface. Of these bands, 1284 and  $1151\text{ cm}^{-1}$  SERS signals (mainly enhanced) are due to the in-plane  $\text{Pip}^8$  ring vibrations. For this reason we imply that  $\text{Pip}^8$  assists in adsorption process and is oriented vertically on this substrate through the lone electron pair of the nitrogen atom. The  $\text{Arg}\cdots\text{Au}$  interactions cannot be excluded for this peptide because of the 1639, 1608, 1438, 1165, 939, and  $840\text{ cm}^{-1}$  spectral features. Based on these observations mainly the guanidine group appear to be in proximity to the Au surface (Table 2).

In the case of  $\text{Aaa}[\text{D-Arg}^0, \text{Hyp}^3, \text{Thi}^5, \text{D-Phe}^7, \text{L-Pip}^8]\text{BK}$  SERS spectrum (Figure 1(e)), both the  $\text{Pip}^8$  and  $\text{Thi}^5$  rings modes are enhanced.  $\text{Pip}^8$  gives rise to the 1570, 1275, 1181, 1144, 1013, 839, and  $752\text{ cm}^{-1}$  spectral features, whereas the 1501 (the most intense, in-plane mode), 1377, 1144, and  $670\text{ cm}^{-1}$  SERS signals are related to the  $\text{Thi}^5$  vibrations. Analysis of the  $\text{Pip}^8$  bands' relative intensity, bands width, and bands wavenumber changes suggested that, similarly as in the case of  $[\text{D-Arg}^0, \text{Hyp}^3, \text{Thi}^{5,8}, \text{L-Pip}^7]\text{BK}$ ,  $\text{Pip}^8$  in  $\text{Aaa}[\text{D-Arg}^0, \text{Hyp}^3, \text{Thi}^5, \text{D-Phe}^7, \text{L-Pip}^8]\text{BK}$  being tilted with respect to the colloidal Au surface interacts with this surface through the nitrogen-free electrons pair. However, it seems that the strength of this interaction is higher for  $\text{Aaa}[\text{D-Arg}^0, \text{Hyp}^3, \text{Thi}^5, \text{D-Phe}^7, \text{L-Pip}^8]\text{BK}$  than for  $[\text{D-Arg}^0, \text{Hyp}^3, \text{Thi}^{5,8}, \text{L-Pip}^7]\text{BK}$ . Much of the same analysis for the  $\text{Thi}^5$  bands implies that the  $\text{Thi}^5$  ring assists in the adsorption process adopting the near-edge-on orientation onto the colloidal Au surface. What is interesting in case of the  $\text{Aaa}[\text{D-Arg}^0, \text{Hyp}^3, \text{Thi}^5, \text{D-Phe}^7, \text{L-Pip}^8]\text{BK}$  SERS spectrum (Figure 1(e)) is that we observed apart from bands at 1438, 1083, 936, 839, and  $670\text{ cm}^{-1}$  very significantly enhanced overlapped, broad bands at 1602  $[(\delta(\text{NH}_2^+) + \nu_s(\text{C}=\text{N}))]$  and 1570  $[\delta(\text{NH})]$ . Based on these observations we suggest that we above all observed interaction between  $\text{Arg}$ 's  $-\text{NH}_2$ -group from the guanidine group and Au surface.

#### 4. Conclusions

In this study, we reported the mode of adsorption of BK and its potent  $\text{B}_2$  receptor antagonists:  $[\text{D-Arg}^0, \text{Hyp}^3, \text{Thi}^{5,8}, \text{L-Pip}^7]\text{BK}$ ,  $\text{Aaa}[\text{D-Arg}^0, \text{Hyp}^3, \text{Thi}^{5,8}, \text{L-Pip}^7]\text{BK}$ ,  $[\text{D-Arg}^0, \text{Hyp}^3, \text{Thi}^5, \text{D-Phe}^7, \text{L-Pip}^8]\text{BK}$ , and  $\text{Aaa}[\text{D-Arg}^0, \text{Hyp}^3, \text{Thi}^5, \text{D-Phe}^7, \text{L-Pip}^8]\text{BK}$  adsorbed on the colloidal Au surface. We showed the following.

- (i) The  $\text{Phe}^5/\text{Phe}^8$  residues (in tilted orientation of the rings) are mainly involved in the BK interaction with the colloidal Au surface, whereas  $\text{D-Phe}^7$

in  $[\text{D-Arg}^0, \text{Hyp}^3, \text{Thi}^5, \text{D-Phe}^7, \text{L-Pip}^8]\text{BK}$  and  $\text{Aaa}[\text{D-Arg}^0, \text{Hyp}^3, \text{Thi}^5, \text{D-Phe}^7, \text{L-Pip}^8]\text{BK}$  is moved out of this surface; thus it is located on the opposite side of the polypeptide backbone.

- (ii) Pip and Thi adsorb on the colloidal Au surface for all the investigated BK analogues. The Thi and Pip residues in  $[\text{D-Arg}^0, \text{Hyp}^3, \text{Thi}^{5,8}, \text{L-Pip}^7]\text{BK}$  adsorb in the tilted orientation on the Au surface (Pip through the piperidine nitrogen atom). Elongation of the peptide backbone by the addition of Aaa at the N-termini (the  $\text{Aaa}[\text{D-Arg}^0, \text{Hyp}^3, \text{Thi}^{5,8}, \text{L-Pip}^7]\text{BK}$  analog) produces rearrangement of the Pip ring (it rises and there is no longer interaction between the piperidine nitrogen atom and Au) with respect to the Au surface and weakening of the  $\text{Thi}\cdots\text{Au}$  interaction. On the other hand, the substitution of  $\text{Pip}^7$  by  $\text{D-Phe}^7$  and  $\text{Thi}^8$  by  $\text{Pip}^8$  (the  $[\text{D-Arg}^0, \text{Hyp}^3, \text{Thi}^5, \text{D-Phe}^7, \text{L-Pip}^8]\text{BK}$  analog) triggers rise of  $\text{Thi}^5$  and  $\text{Pip}^8$  interacts mainly through the piperidine nitrogen atom and adopts vertical orientation with respect to the Au surface. Subsequent modification (the  $\text{Aaa}[\text{D-Arg}^0, \text{Hyp}^3, \text{Thi}^5, \text{D-Phe}^7, \text{L-Pip}^8]\text{BK}$  analog) moves the  $\text{Thi}^5$  away from the Au surface and forces tilting of the  $\text{Pip}^8$  ring on this surface.
- (iii) The Arg residue of BK and its three analogues:  $[\text{D-Arg}^0, \text{Hyp}^3, \text{Thi}^{5,8}, \text{L-Pip}^7]\text{BK}$ ,  $[\text{D-Arg}^0, \text{Hyp}^3, \text{Thi}^5, \text{D-Phe}^7, \text{L-Pip}^8]\text{BK}$ , and  $\text{Aaa}[\text{D-Arg}^0, \text{Hyp}^3, \text{Thi}^5, \text{D-Phe}^7, \text{L-Pip}^8]\text{BK}$  evidently participate in the adsorption process on the colloidal Au surface; the lack of Aaa SERS bands and the enhancement of the modes due to the residues from the C-terminal peptide end (at 5, 7, and 8 positions in the amino acid sequence) designate Arg at 9 position to be that one which interacts with the Au surface.

#### Conflict of Interests

The authors declare that there is no conflict of interests regarding the publication of the paper.

#### Acknowledgment

This work was supported by the National Research Center of the Ministry of Science and Higher Education (Grant no. N N204 544339 to Edyta Proniewicz and Grant no. 2012/05/N/ST4/00175 to Dominika Skořuba). Dominika Skořuba acknowledges the Marian Smoluchowski Krakow Scientific Consortium: "Matter-Energy-Future" (KNOW) for financial support, scholarship.

#### References

- [1] J. M. Stewart, "Bradykinin antagonists: development and applications," *Biopolymers*, vol. 37, no. 2, pp. 143–155, 1995.
- [2] D. Regoli, S. Nsa Allogho, A. Rizzi, and F. J. Gobeil, "Bradykinin receptors and their antagonists," *European Journal of Pharmacology*, vol. 348, no. 1, pp. 1–10, 1998.



- [3] M. Maurer, M. Bader, M. Bas et al., "New topics in bradykinin research," *Allergy*, vol. 66, no. 11, pp. 1397–1406, 2011.
- [4] J. M. Stewart, "Bradykinin antagonists as anti-cancer agents," *Current Pharmaceutical Design*, vol. 9, no. 25, pp. 2036–2042, 2003.
- [5] P. A. Bunn Jr., D. Chan, D. G. Dienhart, R. Tolley, M. Tagawa, and P. B. Jewett, "Neuropeptide signal transduction in lung cancer: clinical implications of bradykinin sensitivity and overall heterogeneity," *Cancer Research*, vol. 52, no. 1, pp. 24–31, 1992.
- [6] J. Enquist, C. Skróder, J. L. Whistler, and L. M. F. Leeb-Lundberg, "Kinins promote B<sub>2</sub> receptor endocytosis and delay constitutive B<sub>1</sub> receptor endocytosis," *Molecular Pharmacology*, vol. 71, no. 2, pp. 494–507, 2007.
- [7] F. Horn, E. Bettler, L. Oliveira, F. Campagne, F. E. Cohen, and G. Vriend, "GPCRDB information system for G protein-coupled receptors," *Nucleic Acids Research*, vol. 31, no. 1, pp. 294–297, 2003.
- [8] X. Zhang, J. L. Lowry, V. Brovkovich, and R. A. Skidgel, "Characterization of dual agonists for kinin B<sub>1</sub> and B<sub>2</sub> receptors and their biased activation of B2 receptors," *Cellular Signalling*, vol. 24, pp. 1619–1631, 2012.
- [9] C. Bonechi, S. Ristori, G. Martini, S. Martini, and C. Rossi, "Study of bradykinin conformation in the presence of model membrane by nuclear magnetic resonance and molecular modelling," *Biochimica et Biophysica Acta*, vol. 1788, no. 3, pp. 708–716, 2009.
- [10] J. K. Young and R. P. Hicks, "NMR and molecular modeling investigations of the neuropeptide bradykinin in three different solvent systems: DMSO, 9 : 1 dioxane/water, and in the presence of 7.4 mM lyso phosphatidylcholine micelles," *Biopolymers*, vol. 34, no. 5, pp. 611–623, 1994.
- [11] D. J. Kyle, S. Chakravarty, J. A. Sinsko, and T. M. Stormann, "A proposed model of bradykinin bound to the rat B<sub>2</sub> receptor and its utility for drug design," *Journal of Medicinal Chemistry*, vol. 37, no. 9, pp. 1347–1354, 1994.
- [12] M. Manna and C. Mukhopadhyay, "Molecular dynamics simulations of the interactions of kinin peptides with an anionic POPG bilayer," *Langmuir*, vol. 27, no. 7, pp. 3713–3722, 2011.
- [13] S. C. Lee, A. F. Russell, and W. D. Laidig, "Three-dimensional structure of bradykinin in SDS micelles. Study using nuclear magnetic resonance, distance geometry, and restrained molecular mechanics and dynamics," *International Journal of Peptide and Protein Research*, vol. 35, no. 5, pp. 367–377, 1990.
- [14] E. Proniewicz, D. Skoluba, I. Ignatjev et al., "Influence of applied potential on bradykinin adsorption onto Ag, Au, and Cu electrodes," *Journal of Raman Spectroscopy*, vol. 44, pp. 655–664, 2013.
- [15] M. Śleszyńska, T. H. Wierzb, K. Malinowski et al., "Novel bradykinin analogues modified in the N-terminal part of the molecule with a variety of acyl substituents," *International Journal of Peptide Research and Therapeutics*, vol. 18, pp. 117–124, 2012.
- [16] E. Proniewicz, I. Ignatjev, G. Niaura, D. Sobolewski, A. Prah, and L. M. Proniewicz, "Role of Phe-D5 isotopically labeled analogues of bradykinin on elucidation of its adsorption mode on Ag, Au, and Cu electrodes. Surface-enhanced Raman spectroscopy studies," *Journal of Raman Spectroscopy*.
- [17] E. Proniewicz, D. Skoluba, A. Kudelski et al., "B2 bradykinin receptor antagonists: adsorption mechanism on electrochemically roughened Ag substrate," *Journal of Raman Spectroscopy*, vol. 44, pp. 205–211, 2013.
- [18] D. Sobolewski, E. Proniewicz, D. Skoluba et al., "Characterization of adsorption mode of new B2 bradykinin receptor antagonists onto colloidal Ag substrate," *Journal of Raman Spectroscopy*, vol. 44, pp. 212–218, 2013.
- [19] E. Podstawka, Y. Ozaki, and L. M. Proniewicz, "Structures and bonding on a colloidal silver surface of the various length carboxyl terminal fragments of bombesin," *Langmuir*, vol. 24, no. 19, pp. 10807–10816, 2008.
- [20] E. Podstawka-Proniewicz, I. Ignatjev, G. Niaura, and L. M. Proniewicz, "Phe-MetNH<sub>2</sub> terminal bombesin subfamily peptides: potential induced changes in adsorption on Ag, Au, and Cu electrodes monitored by SERS," *Journal of Physical Chemistry C*, vol. 116, no. 6, pp. 4189–4200, 2012.
- [21] E. Podstawka-Proniewicz, D. Sobolewski, A. Prah, Y. Kim, and L. M. Proniewicz, "Structure and conformation of Arg8 vasopressin modified analogs," *Journal of Raman Spectroscopy*, vol. 43, no. 1, pp. 51–60, 2012.
- [22] E. Podstawka-Proniewicz, A. Kudelski, Y. Kim, and L. M. Proniewicz, "Structure of monolayers formed from neurotensin and its single-site mutants: vibrational spectroscopic studies," *Journal of Physical Chemistry B*, vol. 115, no. 20, pp. 6709–6721, 2011.
- [23] J. Zhao, A. O. Pinchuk, J. M. McMahon et al., "Methods for describing the electromagnetic properties of silver and gold nanoparticles," *Accounts of Chemical Research*, vol. 41, no. 12, pp. 1710–1720, 2008.
- [24] J. Kneipp, H. Kneipp, M. McLaughlin, D. Brown, and K. Kneipp, "In vivo molecular probing of cellular compartments with gold nanoparticles and nanoaggregates," *Nano Letters*, vol. 6, no. 10, pp. 2225–2231, 2006.
- [25] C. J. Murphy, A. M. Gole, J. W. Stone et al., "Gold nanoparticles in biology: beyond toxicity to cellular imaging," *Accounts of Chemical Research*, vol. 41, no. 12, pp. 1721–1730, 2008.
- [26] S.-S. Wang, "p-Alkoxybenzyl alcohol resin and p-alkoxybenzyloxycarbonylhydrazide resin for solid phase synthesis of protected peptide fragments," *Journal of the American Chemical Society*, vol. 95, no. 4, pp. 1328–1333, 1973.
- [27] E. Podstawka, Y. Ozaki, and L. M. Proniewicz, "Part III: surface-enhanced Raman scattering of amino acids and their homodipeptide monolayers deposited onto colloidal gold surface," *Applied Spectroscopy*, vol. 59, no. 12, pp. 1516–1526, 2005.
- [28] A. E. Aliaga, C. Garrido, P. Leyton et al., "SERS and theoretical studies of arginine," *Spectrochimica Acta Part A*, vol. 76, no. 5, pp. 458–463, 2010.
- [29] C. Parlak, "Theoretical and experimental vibrational spectroscopic study of 4-(1-pyrrolidinyl)piperidine," *Journal of Molecular Structure*, vol. 966, no. 1–3, pp. 1–7, 2010.
- [30] Y. Hao and Y. Fang, "Piperidine adsorption on two different silver electrodes: a combined surface enhanced Raman spectroscopy and density functional theory study," *Journal of Nanoparticle Research*, vol. 9, no. 5, pp. 817–824, 2007.
- [31] D. K. Singh, S. K. Srivastava, A. K. Ojha, and B. P. Asthana, "Vibrational study of thiophene and its solvation in two polar solvents, DMSO and methanol by Raman spectroscopy combined with ab initio and DFT calculations," *Journal of Molecular Structure*, vol. 892, no. 1–3, pp. 384–391, 2008.
- [32] J. Yang, J. Li, and Y. Mo, "The vibrational structures of furan, pyrrole, and thiophene cations studied by zero kinetic energy photoelectron spectroscopy," *Journal of Chemical Physics*, vol. 125, no. 17, Article ID 174313, 2006.
- [33] T. Matsuura and Y. Shimoyama, "Growth kinetics of self-assembled monolayers of thiophene and terthiophene on

Au(111): an infrared spectroscopic study,” *European Physical Journal E*, vol. 7, no. 3, pp. 233–240, 2002.

- [34] M. Moskovits, “Surface selection rules,” *The Journal of Chemical Physics*, vol. 77, no. 9, pp. 4408–4416, 1982.
- [35] P. Gao and M. J. Weaver, “Surface-enhanced Raman spectroscopy as a probe of adsorbate-surface bonding: benzene and monosubstituted benzenes adsorbed at gold electrodes,” *Journal of Physical Chemistry*, vol. 89, no. 23, pp. 5040–5046, 1985.

## Research Article

# Analysis of an Alanine/Arginine Mixture by Using TLC/FTIR Technique

**Jun Liu,<sup>1,2</sup> Feng-shan Zhou,<sup>3</sup> Ran Guo,<sup>2</sup> Ye Jiang,<sup>2,4</sup> Xiaokun Fan,<sup>2,5</sup> Anqi He,<sup>2</sup> Yanjun Zhai,<sup>4</sup> Shifu Weng,<sup>2</sup> Zhanlan Yang,<sup>2</sup> Yizhuang Xu,<sup>2</sup> Isao Noda,<sup>6</sup> and Jinguang Wu<sup>2</sup>**

<sup>1</sup> Department of Biochemistry, Wenshan University, Wenshan 663000, China

<sup>2</sup> College of Chemistry and Molecular Engineering, Peking University, Beijing 100871, China

<sup>3</sup> School of Materials Science and Technology, China University of Geosciences, Beijing 100083, China

<sup>4</sup> College of Pharmacy, Liaoning University of Traditional Chinese Medicine, Shenyang 11660, China

<sup>5</sup> College of Chemistry and Material Science, Hebei Normal University, Shijiazhuang 050024, China

<sup>6</sup> Department of Materials Science and Engineering, University of Delaware, Newark, DE 19716, USA

Correspondence should be addressed to Fengshan Zhou; [zhoufs@cugb.edu.cn](mailto:zhoufs@cugb.edu.cn) and Yizhuang Xu; [xyz@pku.edu.cn](mailto:xyz@pku.edu.cn)

Received 6 September 2013; Accepted 14 November 2013; Published 28 January 2014

Academic Editor: Edyta Proniewicz

Copyright © 2014 Jun Liu et al. This is an open access article distributed under the Creative Commons Attribution License, which permits unrestricted use, distribution, and reproduction in any medium, provided the original work is properly cited.

We applied TLC/FTIR coupled with mapping technique to analyze an alanine/arginine mixture. Narrow band TLC plates prepared by using AgI as a stationary phase were used to separate alanine and arginine. The distribution of alanine and arginine spots was manifested by a 3D chromatogram. Alanine and arginine can be successfully separated by the narrow band TLC plate. In addition, the FTIR spectra of the separated alanine and arginine spots on the narrow band TLC plate are roughly the same as the corresponding reference IR spectra.

## 1. Introduction

Thin-layer chromatography (TLC) is a widely used separation method and has been extensively applied in the analysis of various mixed samples [1, 2]. In conventional TLC experiments, separated samples are identified by color, UV-Vis absorbance, or fluorescence signals. Thus, it becomes difficult for TLC in the analysis of samples that lack UV-Vis absorbance and fluorescence signals. Since visualization reagent may not be suitable for all substances with a broad range of molecular structures, the utility of visualization reagents for unknown TLC spot identification is somewhat limited. Moreover, UV-Vis and fluorescent signal provide rather limited information concerning molecular structure of separated spots. Thus, alternative spectroscopic method is needed to be applied after TLC separation. FTIR spectrum is a universal tool that can identify various organic substances without any requirement on UV-VIS absorbance or fluorescence signals. Additionally, FTIR spectrum provides a large amount of information relevant to functional groups of separated substances [3, 4]. Moreover, it might be possible

to directly recognize unknown separated spots on TLC plate based on their FTIR spectra. In addition, the advancement in mapping/imaging techniques of FTIR microscope enables us to obtain FTIR spectra of every microregion on a TLC plate automatically. Thus, it has become possible to perform TLC/FTIR analysis in a quick and convenient manner.

Since the 1960s, some TLC/IR technique appeared in the literature [5, 6]. In such an experiment, suitable solvents were used to transfer each separated analyte out of the TLC plate. IR spectrum of the obtained sample was recorded after removing the solvent by vaporization. The procedure is tedious and time-consuming, and the analysis is under a risk of sample loss and contamination. Later, Percival and Griffiths, Zuber et al., Lloyd et al., and White developed a more practical *in situ* TLC/IR technique [7–12]. This approach is quick, convenient, and free of the risk of sample loss since FTIR spectrum is directly obtained from the separated sample spot on a TLC plate. However, traditional TLC stationary phases, such as silica and alumina, exhibit a strong background absorption that can bring about significant interference to sample identification. Danielson et

al. proposed to use zirconium oxide that has no absorbance in mid-IR region as a new stationary phase for TLC/FTIR analysis [13, 14]. However, the problem of interference from stationary phase is not adequately addressed, since water adsorbed on zirconium oxide still brings about severe interference in the measurement of FTIR spectra. Consequently, there have been only few papers [15, 16] relevant to TLC/FTIR published around the world during the past decade.

We proposed to use IR-transparent, insoluble inorganic salt particles as novel stationary phases for TLC/FTIR analysis to solve the above problem. Since the stationary phase is transparent for infrared light, the interference caused by IR absorption from stationary phase is naturally removed. The inorganic salt should be insoluble so that the possibility of stationary phase being destroyed by mobile phase can be avoided. Controlling the size of the inorganic salt particles is helpful to improve the performance of TLC/FTIR analysis due to the following reasons. (1) Decreasing the size of stationary phase particles alleviates the effect of light scattering so that the quality of the corresponding FTIR spectra can be improved. (2) As the size of the particles of stationary phase decreases, the efficiency of TLC separation is enhanced. (3) Decreasing the size of the inorganic salt particle results in the increasing of the specific area of the stationary phase. Thus, more analytes are allowed to be adsorbed on the surface of the stationary phase. This advantage is helpful to alleviate the overloading problem and improve the sensitivity of detection of separated sample by using FTIR measurement.

Based on the above consideration, a systematic work on the TLC/FTIR analysis has been conducted in our laboratory in recent years [17–19]. Our experiments showed that barium fluoride and silver iodide particles may be used as new stationary phases for TLC/FTIR analysis. Experimental result demonstrated that  $\text{BaF}_2$  particles tend to retain significant amount of adsorbed water, while it is much easier to remove adsorbed water completely for silver iodide particles. Thus, we focus on the TLC/FTIR studies by using AgI particles as stationary phase.

In parallel, we have made considerable effort to develop new approach to prepare TLC plates. In the traditional way of the preparation of TLC plate, polymeric adhesive is utilized to bind stationary phase particles together. This is not suitable for TLC/FTIR analysis, since polymeric adhesive has strong absorbance in IR region and brings about significant interference in the FTIR detection. Recently, we propose a new technique to prepare narrow band TLC plates [20]. Experimental results demonstrate that the performance of TLC/FTIR is significantly improved by using the narrow band TLC plates.

To validate whether TLC/FTIR technique is applicable to real chemical system, we used narrow band TLC plate to separate alanine and arginine. Subsequently, FTIR microscope with mapping techniques was used to reveal the distribution of colorless alanine and arginine band on the narrow band TLC plate.

## 2. Experimental

All reagents are of AR grade. Alanine, arginine, n-butanol, formic acid, acetic acid, and silver nitrate were obtained from

Beijing Chemical Factory. Potassium iodide was a product of Sinopharm Chemical Reagent Co., Ltd.

Silver iodide was synthesized by a reaction between silver nitrate and potassium iodide. The experimental detail of the preparation of silver iodide particles can be found in our previous work [18]. The diameters of the silver iodide particles are around 100 nm.

## 3. Apparatus

A Thermo-Fischer Nicolet iN10 MX FTIR spectrometer equipped with an IR microscope was used in the experiments.

## 4. Procedures

**4.1. Preparation of Mixed Sample Solutions.** 0.150 g alanine was dissolved in 10.0 mL formic acid to prepare a 1.5 wt% alanine solution. Similarly, 1.5 wt% arginine solution was prepared by dissolving 0.150 g arginine in 10.0 mL formic acid.

A mixed solution sample was prepared by mixing equal volumes of 1.5 wt% alanine solution and 1.5 wt% arginine solution together.

**4.2. Narrow Band TLC Analysis.** We prepared narrow band TLC plate to conduct the experiment. The preparation process of the narrow band TLC plates is described in detail in our previous work [20].

The sample solution was manually spotted at one end of narrow band TLC plate by using a glass capillary (0.3 mm in diameter). After evaporation of solvent, the narrow band TLC plate was developed by using butanol/acetic acid/water mixture as a mobile phase (the volume ratio among butanol, acetic acid, and water is 8 : 1 : 1). The typical development time was about 20–30 minutes.

**4.3. In Situ TLC-FTIR Detection.** Considering that the boiling temperature of butanol is quite high, the following pretreatment is performed: narrow band TLC plate after separation was first heated at 80°C for 4 hours. Then the temperature was elevated to 120°C and kept at that temperature for 4 hours. At last, the TLC plate was heated at 140°C for 4 hours. The above procedure is necessary to remove the residual mobile phase completely. Then TLC plates were examined directly by using the FTIR microscope. To reveal the distribution of alanine and arginine spots on the narrow band TLC plate, FTIR mapping technique under linear scan mode was utilized. That is to say, FTIR spectrum of every tiny region on TLC plate ( $100\ \mu\text{m} \times 100\ \mu\text{m}$ ) is obtained sequentially along the direction of the diffusion of mobile phase. All the spectra were recorded under reflection mode at a resolution of  $16\ \text{cm}^{-1}$ . To improve the signal-to-noise ratio, reflect spectrum from gold mirror was used as background spectrum.

3D chromatogram that is utilized to reveal the distribution of alanine and arginine spots was generated via a program written in our lab by using the software of MATLAB.



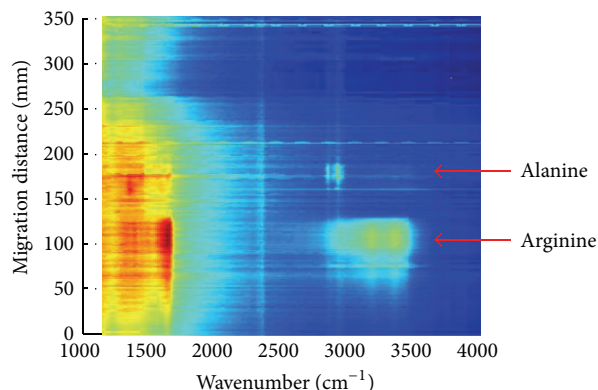


FIGURE 1: 3D chromatograph to characterize the distribution of arginine and alanine spots on a narrow band TLC plate.

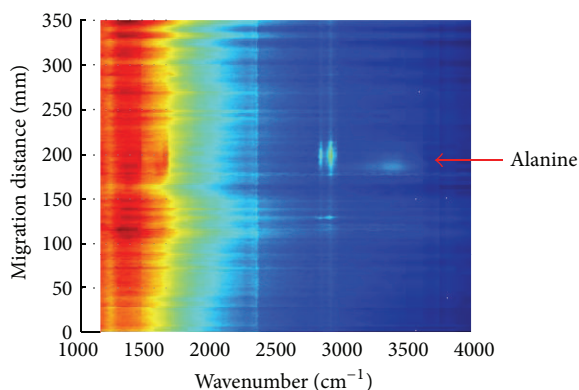


FIGURE 2: 3D chromatograph to locate the alanine spot on the narrow band TLC plate.

## 5. Results and Discussion

Since both alanine and arginine are colorless substances, no separated sample spot can be observed on the narrow band TLC plate. To reveal the distribution of alanine and arginine spots on the narrow band TLC plate, FTIR microscope with mapping technique is utilized. In the experiment, FT-IR spectrum of each tiny region on the narrow band TLC plate is sequentially recorded. The obtained FT-IR spectra are organized along the direction of the diffusion of mobile phase so that a 3D chromatogram (the first dimension is wavenumber from FTIR spectrum, the second dimension is migration distance, and the third dimension is absorbance) is constructed. The 3D chromatogram is manifested via a contour map mode. As shown in Figure 1, two separated spots can be clearly visualized in the 3D chromatogram. To confirm that the above two spots are alanine and arginine, respectively, we used two solution samples that contain 1.5 wt% alanine only and 1.5 wt% arginine only for TLC/FTIR analysis. The experimental procedure is similar to those described previously. The resultant 3D chromatograms are shown in Figures 2 and 3. Then we compare the FTIR spectra from the separated band shown in Figure 1 with the bands illustrated in Figures 2 and 3. Typical FTIR spectra of the two spots, which

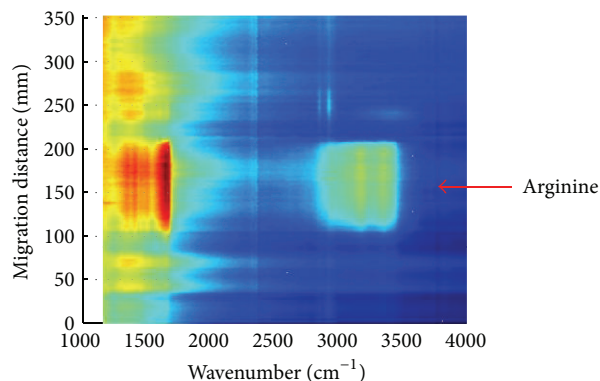


FIGURE 3: 3D chromatograph to locate the arginine spot on a narrow band TLC plate.

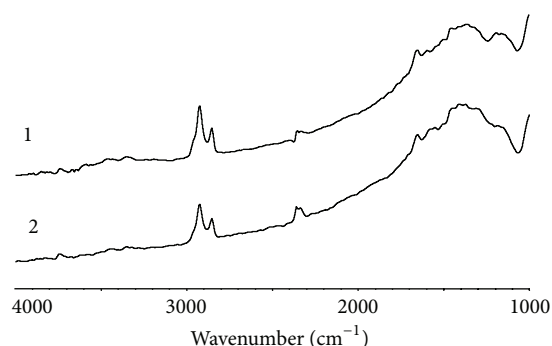


FIGURE 4: FTIR spectrum of alanine spot (trace 1) on a narrow band TLC plate. For comparison, a reference FTIR spectrum of pure alanine (trace 2) is also included.

are obtained by slicing the 3D chromatogram on the center of the sample spots, are shown as trace 1 in Figures 4 and 5. FTIR spectra from the slices on the alanine and arginine spots shown in Figures 2 and 3 are used as reference spectra and displayed as trace 2 in Figures 4 and 5. FTIR spectra of upper and lower spot are almost the same as the reference spectra of alanine and arginine, respectively. These results confirm that the separated spots shown in Figure 1 are indeed alanine and arginine. It should be pointed out that alanine and arginine can accept proton or release proton as the pH changes. The variation of ionization states brings about drastic change in the corresponding FTIR spectra. On the other hand, alanine and arginine are often involved in complex hydrogen bond, which may bring about significant variation on the FTIR spectra. The above problems cause considerable difficulty on the spectral comparison between sample spectra and reference spectra. Thus, measuring the spectrum of separated spots and reference spectrum of corresponding standard material at the same experiment condition is very important to get reliable results.

## 6. Conclusion

In this work, we use narrow band TLC plates by using AgI as stationary phase to separate alanine and arginine. The

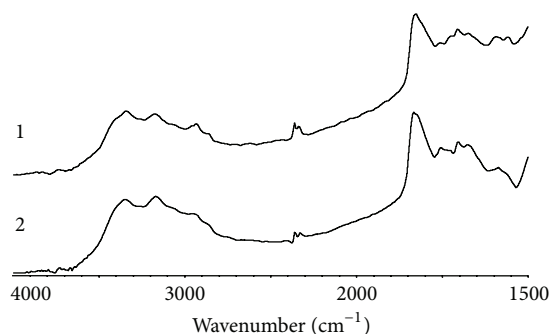


FIGURE 5: FTIR spectrum of arginine spot (trace 1) on a narrow band TLC plate. For comparison, a reference FTIR spectrum of pure arginine (trace 2) is also included.

distribution of alanine and arginine spots was probed by using FTIR microscope with spectral mapping technique and manifested by a 3D chromatogram. Experimental results demonstrate that alanine and arginine can be successfully separated by the narrow band TLC plate. Moreover, the FTIR spectra of the separated alanine and arginine spots on the narrow band TLC plate are roughly the same as the reference IR spectra of alanine and arginine. The present work demonstrates that TLC/FTIR technique is applicable in analysis complex mixtures.

## Conflict of Interests

The authors declare that there is no conflict of interests regarding the publication of this paper.

## Acknowledgment

This work is supported by the National Natural Science Foundation of China (51373003).

## References

- [1] M. Srivastava, Ed., *High-Performance Thin-Layer Chromatography (HPTLC)*, Springer, Heidelberg, Germany, 2011.
- [2] L. Y. He, Ed., *Method and Application of Planar Chromatography*, Chemical Industry Press, Beijing, China, 2005.
- [3] J. G. Wu, Ed., *Modern FTIR Spectroscopy Technology and Application*, Science and Technology Press, Beijing, China, 1994.
- [4] S. F. Weng, Ed., *Fourier Transform Infrared Spectrometer*, Chemical Industry Press, Beijing, China, 2nd edition, 2010.
- [5] R. N. McCoy and E. C. Fiebig, "Technique for obtaining infrared spectra of microgram amounts of compounds separated by thin layer chromatography," *Analytical Chemistry*, vol. 37, no. 4, pp. 593–595, 1965.
- [6] P. A. Sturm, R. M. Parkhurst, and W. A. Skinner, "Quantitative determination of individual tocopherols by thin layer chromatographic separation and spectrophotometry," *Analytical Chemistry*, vol. 38, no. 9, pp. 1244–1247, 1966.
- [7] C. J. Percival and P. R. Griffiths, "Direct measurement of the infrared spectra of compounds separated by thin-layer chromatography," *Analytical Chemistry*, vol. 47, pp. 154–156, 1975.
- [8] M. P. Fuller and P. R. Griffiths, "Diffuse reflectance measurements by infrared Fourier transform spectrometry," *Analytical Chemistry*, vol. 50, pp. 1906–1910, 1978.
- [9] M. P. Fuller and P. R. Griffiths, "Infrared microsampling by diffuse reflectance Fourier transform spectrometry," *Applied Spectroscopy*, vol. 34, no. 5, pp. 533–539, 1980.
- [10] G. E. Zuber, R. J. Warren, P. P. Begosh, and E. L. O'Donnell, "Direct analysis of thin-layer chromatography spots by diffuse reflectance Fourier transform infrared spectrometry," *Analytical Chemistry*, vol. 56, pp. 2935–2939, 1984.
- [11] L. B. Lloyd, R. C. Yeates, and E. M. Eyring, "Fourier transform infrared photoacoustic spectroscopy in thin-layer chromatography," *Analytical Chemistry*, vol. 54, pp. 549–552, 1982.
- [12] R. L. White, "Analysis of thin-layer chromatographic adsorbates by Fourier transform infrared photoacoustic spectroscopy," *Analytical Chemistry*, vol. 57, pp. 1819–1822, 1985.
- [13] N. D. Danielson, J. E. Katon, S. P. Bouffard, and Z. Zhu, "Zirconium oxide stationary phase for thin-layer chromatography with diffuse reflectance fourier transform infrared detection," *Analytical Chemistry*, vol. 64, no. 18, pp. 2183–2186, 1992.
- [14] S. P. Bouffard, J. E. Katon, A. J. Sommer, and N. D. Danielson, "Development of microchannel thin-layer chromatography with infrared microspectroscopic detection," *Analytical Chemistry*, vol. 66, no. 13, pp. 1937–1940, 1994.
- [15] W. He, R. Shanks, and G. Amarasinghe, "Analysis of additives in polymers by thin-layer chromatography coupled with Fourier transform-infrared microscopy," *Vibrational Spectroscopy*, vol. 30, no. 2, pp. 147–156, 2002.
- [16] W. He, G. Cheng, F. Zao, Y. Lin, J. Huang, and R. Shanks, "Separation and identification of multicomponent mixture by thin-layer chromatography coupled with Fourier transform-infrared microscopy," *Spectrochimica Acta A*, vol. 61, no. 8, pp. 1965–1970, 2005.
- [17] X. Liu, Q.-H. Pan, J. Ding et al., "Using barium fluoride fine particles as stationary phase for TLC/FTIR analysis," *Spectroscopy and Spectral Analysis*, vol. 31, no. 7, pp. 1767–1771, 2011.
- [18] Q. Zhu, X. Su, H. J. Wu et al., "The analysis for silver iodide fine particles of TLC/FTIR matrix," *Spectroscopy and Spectral Analysis*, vol. 32, no. 7, pp. 1790–1794, 2012.
- [19] W. Liu, H. J. Wu, X. P. Wang et al., "Preparation and application of barium fluoride particles as stationary phase for TLC-FTIR analysis," *Chemical Journal of Chinese Universities*, vol. 34, no. 6, pp. 1347–1352, 2013.
- [20] F. Wang and H. J. Wu, "Development of narrow-band TLC plates for TLC/FTIR analysis," *Analytical Methods*, vol. 5, pp. 4138–4144, 2013.



## Research Article

# Structure Characterization of [N-Phenylamino(2-boronphenyl)-R-methyl]phosphonic Acid by Vibrational Spectroscopy and Density Functional Theory Calculations

Natalia Piergies<sup>1</sup> and Edyta Proniewicz<sup>2</sup>

<sup>1</sup> Faculty of Chemistry, Jagiellonian University, Ulice Ingardena 3, 30-060 Krakow, Poland

<sup>2</sup> Faculty of Foundry Engineering, AGH University of Science and Technology, Ulice Reymonta 23, 30-059 Krakow, Poland

Correspondence should be addressed to Edyta Proniewicz; [proniewi@agh.edu.pl](mailto:proniewi@agh.edu.pl)

Received 2 September 2013; Accepted 23 November 2013; Published 23 January 2014

Academic Editor: Yizhuang Xu

Copyright © 2014 N. Piergies and E. Proniewicz. This is an open access article distributed under the Creative Commons Attribution License, which permits unrestricted use, distribution, and reproduction in any medium, provided the original work is properly cited.

We present the first Fourier-transform infrared absorption (FT-IR) and Fourier-transform Raman (FT-Raman) analysis of vibrational structure of [N-phenylamino(2-boronphenyl)-R-methyl]phosphonic acid ([PhN-(2-PhB(OH)<sub>2</sub>)-R-Me]PO<sub>3</sub>H<sub>2</sub>). Assignments of experimental wavenumbers are based on performed theoretical calculations using density functional theory (DFT). Theoretical calculations show that the most stable structure of the investigated molecule is dimer in *cis-trans* conformation created by a pair of intermolecular hydrogen bonds between the boron hydroxyl groups of two monomers.

## 1. Introduction

In recent years aminophosphonic acids gain the attention and interest of the researchers because of their diverse and interesting biological activities [1–4]. These compounds are defined as amino acid derivatives, in which the carboxylic acid group [–C(=O)OH] is replaced by the phosphonic acid moiety [–P(=O)(OH)<sub>2</sub>] [5]. Such modification inhibits the activity of certain enzymes by effective competition for the active site of the enzyme and by forming strong electrostatic binding [6]. Thus, the aminophosphonic acids found application as enzyme inhibitors [6–8] and medical [9, 10] and herbicidal agents [5].  $\alpha$ -Amino boronic acids also demonstrate high potential in medical chemistry [11, 12], especially as anticancer therapy agents [13], antibiotics [14], and enzymes inhibitors [15]. This is due to the boronic acid moiety ability to create hydrogen bonds and stable covalent bonds in the enzyme active side [12, 16].

The unique properties of the phosphonic and boronic acid groups cause that the amino acids analogues containing

these functional groups become very attractive molecular systems. Therefore, we present the first vibrational characteristic of [N-phenylamino(2-boronphenyl)-R-methyl]phosphonic acid ([PhN-(2-PhB(OH)<sub>2</sub>)-R-Me]PO<sub>3</sub>H<sub>2</sub>) (see Figure 1 for molecular structure) considered as potential protease and kinase inhibitor. We used Fourier-transform Raman spectroscopy to investigate the vibrations and structure of the abovementioned compound. Because the absorption infrared method gives complementary information to the Raman method, supports the Raman analysis, and helps to solve ambiguities during this analysis, the absorption infrared spectra are also examined. Both these methods are commonly employed in both experimental investigations [17–20] and theoretical calculations [21–23] to analyze and compare structures for a large number of conformers of the investigated compounds. Interpreting the Raman and absorption infrared spectra involves explaining spectral regions and wavenumbers based on likely vibrational modes. Such an understanding of a molecule's vibrational spectrum is essential for explaining the relation between the molecular

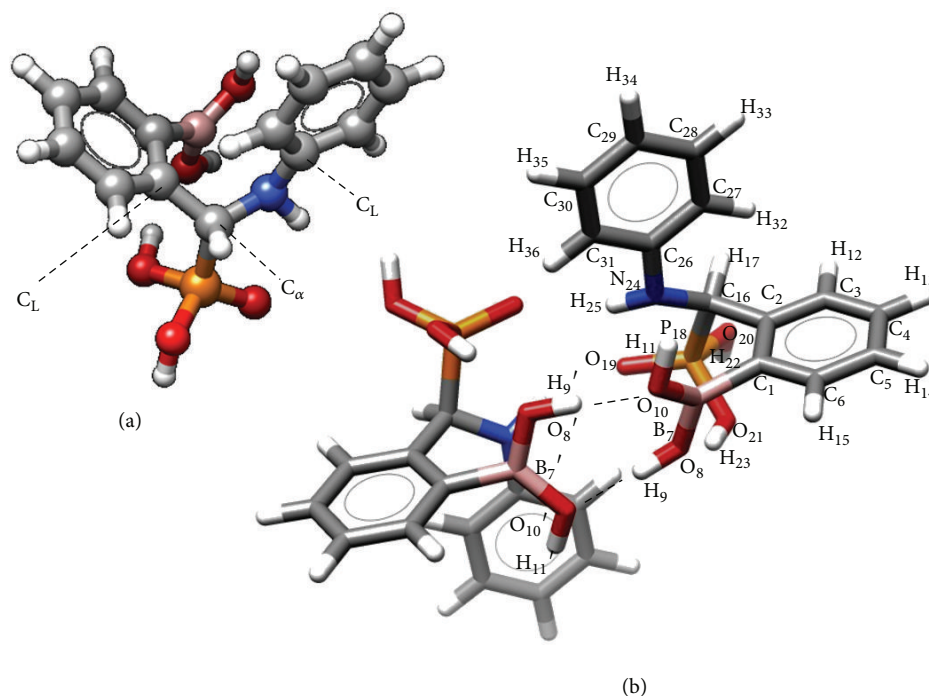


FIGURE 1: The molecular structure of [PhN-(2-PhB(OH)<sub>2</sub>)-R-Me]PO<sub>3</sub>H<sub>2</sub> monomer (a) and dimer structure (b) (where C<sub>L</sub> denotes carbon atom of the aromatic ring connected to the aliphatic chain).

structure and spectral response. To provide the definitive band assignments needed to generate vibrational spectra useful for structural analysis, we performed vibrational analysis using Density Functional Theory (DFT) calculations at the B3LYP/6-311G(d,p) level of theory. Our aim is to produce an extensive look-up table of infrared and Raman spectra that can make structure determination a fast and accurate process.

## 2. Materials and Methods

**2.1. [N-phenylamino(2-boronphenyl)-R-methyl]phosphonic Acid Synthesis.** The investigated compound was synthesized according to the previous published procedure [24]. Its purity and chemical structure were checked using <sup>1</sup>H, <sup>13</sup>C, <sup>31</sup>P, and <sup>11</sup>B NMR spectroscopy (Bruker Avance DRX 300 MHz spectrometer, Bruker Polska, Poznań) and ESI-MS (Bruker MicrOTOF-Q spectrometer, Bruker Polska, Poznań).

**2.2. FT-Raman Measurements.** A Nicolet spectrometer (model NXR 9650) equipped with a liquid-nitrogen-cooled germanium detector was used for the FT-Raman measurements of [PhN-(2-PhB(OH)<sub>2</sub>)-R-Me]PO<sub>3</sub>H<sub>2</sub> on a glass plate. The 1064 nm line from a continuous-wave Nd<sup>3+</sup>:YAG laser was used as an excitation source with a power output of 500 mW. During the measurements, 1000 scans were collected with a resolution of 4 cm<sup>-1</sup>.

**2.3. FT-IR Measurements.** FT-IR spectra were obtained for thin pellets containing about 1 mg of [PhN-(2-PhB(OH)<sub>2</sub>)-R-Me]PO<sub>3</sub>H<sub>2</sub> dispersed in 200 mg KBr at room temperature.

These measurements were carried out using a Bruker spectrometer (EQUINOX 55) equipped with a DT-GS detector in the range of 400–4000 cm<sup>-1</sup> with a Nernst rod as an excitation source.

**2.4. Theoretical Analysis.** To optimize the ground-state geometry of [PhN-(2-PhB(OH)<sub>2</sub>)-R-Me]PO<sub>3</sub>H<sub>2</sub> and to calculate their FT-Raman and FT-IR spectra, the Gaussian 03 suite was used [25]. Our earlier analysis of various types of *N*-benzylamino(boronphenyl) methylphosphonic acids [26] and a literature study for similar compounds [27, 28] noted that the most stable structure of the boronic acid derivatives is a cyclic dimer formed by a pair of intermolecular hydrogen bonds between the boron hydroxyl groups of two monomers. Based on previous experience, here we present the theoretical calculations for the most stable structure of the substituted phenylboronic acid dimer (Figure 1). We also performed calculations for the monomer (not shown) and compare its energy with the energy of the corresponding dimer. The calculated stabilization of the energy indicates that dimer is more stable than monomer ( $E_{\text{dimer}} = -1634029$  kcal/mol,  $E_{\text{monomer}} = -817006$  kcal/mol).

A DFT method with the B3LYP level of theory was employed to optimize the molecular structure of [PhN-(2-PhB(OH)<sub>2</sub>)-R-Me]PO<sub>3</sub>H<sub>2</sub>. The triple-split valence basis with a polarization function on heavy atoms and hydrogens (6-311G(d,p)) was applied as the basis set [29]. This type of basis was applied for the calculations of similar phenylboronic acid derivatives and provides reliable results [27, 28]. No imaginary wavenumbers were observed during optimization, which demonstrates that the calculated structure correspond

to energy minima on the potential energy surface for nuclear motion.

Theoretical Raman intensities were calculated by the Raint program, which uses the following relationship [30]:

$$I_i^R = 10^{-12} (\nu_0 - \nu_i)^4 \nu_i^{-1} S_i \quad (1)$$

in which  $I_i$  is given in arbitrary units,  $\nu_0$  is the laser excitation wavenumber [ $\text{cm}^{-1}$ ] ( $9398.5 \text{ cm}^{-1}$  for a Nd:YAG laser),  $\nu_i$  is the frequency of the normal mode obtained from the DFT calculation, and  $S_i$  is the Raman scattering activity of the normal mode.

The theoretical vibrational spectra were generated by the free GaussSum 0.8 software package [31]. The calculated wavenumbers were scaled by a scaling factor of 0.987, and the theoretical spectra were plotted by setting the full width at half maximum (FWHM) at  $11 \text{ cm}^{-1}$  (the average value of a typical FWHM for these compounds in the condensed phase with a 50%/50% Gaussian/Lorentzian band shape). This scaling factor and FWHM were fitted based on the comparison between the wavenumbers and shape of bands of theoretical and experimental spectra. This procedure was used in order to better reproduce the experimental results.

To obtain normal mode assignments for the calculated vibrational bands, the potential energy distribution (PED) for the optimized structures was determined with the freeware Gar2ped program [32] in conjunction with a visualization script.

### 3. Results and Discussion

**3.1. Geometric Structures.** The most stable structure of  $[\text{PhN}-(2-\text{PhB}(\text{OH})_2)-R-\text{Me}]\text{PO}_3\text{H}_2$  is a cyclic dimer formed by a pair of intermolecular hydrogen bonds between the boron hydroxyl groups of two monomers. Thus, the theoretical spectra presented are calculated for dimer. For this dimer specie, there are two possible conformers (*cis-trans* and *trans-cis*) depending on the positions of the hydrogen atoms bonded to the oxygen atom of the boronic group, whether they are directed away from (*trans*) or toward (*cis*) the phenylboronic ring. Our calculations show that the *cis-trans* conformation has the lowest energy; thus, it is the most stable. The molecular structure and numbering scheme of the atoms of the investigated compounds are given in Figure 1, while Table 1 lists some geometric parameters for this molecule.

The  $\text{O}_8-\text{B}_7-\text{O}_{10}$  and  $\text{O}_8'-\text{B}_7'-\text{O}_{10}'$  moieties in the presented dimer are almost perpendicular to the ring. This structure is promoted by possible interaction between nitrogen and boron atoms [33]. The hydrogen atoms of both boronic groups in the dimers ( $\text{H}_9$ ,  $\text{H}_{10}$ ,  $\text{H}_9'$ , and  $\text{H}_{10}'$ ) lie in the  $\text{O}-\text{B}-\text{O}$  plane (Figure 1). This could be explained on the basis of the oxygen lone-electron pairs having a resonance interaction with the empty p-orbital of the boron atom, forcing the hydrogen atoms to be in the  $\text{O}-\text{B}-\text{O}$  plane [34]. The calculated B–O and C–B bond lengths (Table 1) for  $[\text{PhN}-(2-\text{PhB}(\text{OH})_2)-R-\text{Me}]\text{PO}_3\text{H}_2$  are in good agreement with those present in the X-ray structure of phenylboronic ( $\text{B}-\text{O}$ :  $1.362 \text{ \AA}$ —*cis* H (atom H directed toward the phenylboronic ring),  $1.378 \text{ \AA}$ —*trans* H (atom H directed toward

TABLE 1: Select calculated bond lengths and angles of the  $[\text{PhN}-(2-\text{PhB}(\text{OH})_2)-R-\text{Me}]\text{PO}_3\text{H}_2$  dimer.

Bond	Bond length [Å]	Bond	Bond length [Å]	Angle	[°]
$\text{C}_1-\text{C}_2$	1.406	$\text{P}_{18}-\text{O}_{19}$	1.485	$\text{C}_1-\text{B}_7-\text{O}_8$	117.1
$\text{C}_2-\text{C}_3$	1.394	$\text{P}_{18}-\text{O}_{20}$	1.613	$\text{B}_7-\text{O}_8-\text{H}_9$	116.5
$\text{C}_3-\text{C}_4$	1.392	$\text{P}_{18}-\text{O}_{21}$	1.605	$\text{O}_8-\text{B}_7-\text{O}_{10}$	117.2
$\text{C}_4-\text{C}_5$	1.391	$\text{O}_{20}-\text{H}_{22}$	0.964	$\text{C}_1-\text{B}_7-\text{O}_{10}$	124.9
$\text{C}_5-\text{C}_6$	1.393	$\text{O}_{21}-\text{H}_{23}$	0.982	$\text{B}_7-\text{O}_{10}-\text{H}_{11}$	112.7
$\text{C}_6-\text{C}_1$	1.401	$\text{C}_{16}-\text{N}_{24}$	1.458	$\text{B}_7-\text{O}_{10}-\text{H}_9'$	114.4
$\text{C}_1-\text{B}_7$	1.575	$\text{N}_{24}-\text{H}_{25}$	1.020	$\text{B}_7'-\text{O}_{10}'-\text{H}_9$	114.4
$\text{B}_7-\text{O}_8$	1.371	$\text{N}_{24}-\text{C}_{26}$	1.410		
$\text{O}_8-\text{H}_9$	0.979	$\text{C}_{26}-\text{C}_{27}$	1.407		
$\text{H}_9-\text{O}_{10}'$	1.826	$\text{C}_{27}-\text{C}_{28}$	1.387		
$\text{B}_7-\text{O}_{10}$	1.382	$\text{C}_{28}-\text{C}_{29}$	1.396		
$\text{O}_{10}-\text{H}_{11}$	0.963	$\text{C}_{29}-\text{C}_{30}$	1.389		
$\text{O}_{10}-\text{H}_9'$	1.826	$\text{C}_{30}-\text{C}_{31}$	1.395		
$\text{C}_2-\text{C}_{16}$	1.524	$\text{C}_{31}-\text{C}_{26}$	1.402		
$\text{C}_{16}-\text{P}_{18}$	1.863				

the phenylboronic ring); C–B:  $1.568 \text{ \AA}$  [33] and pentafluorophenylboronic ( $\text{B}-\text{O}$ :  $1.362 \text{ \AA}$ —*cis* H,  $1.355 \text{ \AA}$ —*trans* H; C–B:  $1.579 \text{ \AA}$ ) acids [34]. The calculated  $\text{B}_7-\text{O}_8$  and  $\text{B}_7-\text{O}_{10}$  (Table 1) bonds distance ( $\sim 1.371 \text{ \AA}$ ) for the investigated compound indicates typical B–O length of phenylboronic acid derivatives which lie in the range of  $1.35\text{--}1.38 \text{ \AA}$  [33].

**3.2. FT-Raman, FT-IR, and DFT Studies.** Figure 2 shows the experimental (black traces) and theoretical (red traces) FT-Raman and FT-IR spectra of  $[\text{PhN}-(2-\text{PhB}(\text{OH})_2)-R-\text{Me}]\text{PO}_3\text{H}_2$  in the spectral range between  $3650$  and  $400 \text{ cm}^{-1}$ , whereas Table 2 summarizes the experimental and theoretical band wavenumbers with the calculated (DFT, B3LYP/6-311 G(d,p)) potential energy distribution (PED, in %) (the whole PED information is provided in Table S1 in Supplementary Material available online at <http://dx.doi.org/10.1155/2014/247237>). The given vibrational analysis is also based on our earlier investigations of  $[N\text{-benzylamino}(\text{boronphenyl})\text{methyl}]$  [26], fluoro- and formyl [35], and phenyl [36–38] analogues of phosphonic acids.

**Aromatic Vibrations.** The  $3069/3056$ ,  $1606$ ,  $1588$ ,  $1188$ ,  $1161$ ,  $1031$ ,  $1008/999$ ,  $775$ ,  $617$ , and  $490 \text{ cm}^{-1}$  spectral features due to the characteristic phenyl ring vibrations (see Table 2 for pre-cise bands assignment) dominate the  $[\text{PhN}-(2-\text{PhB}(\text{OH})_2)-R-\text{Me}]\text{PO}_3\text{H}_2$  Raman spectrum (Figure 2, the top black trace). The noticeable spectral shift to lower wavenumbers for the  $\nu_2$ ,  $\nu_{8a}$ , and  $\nu_{12}$  modes of the phenylboronic ring compared to that of phenyl reflects some redistribution of the  $\pi$ -electrons caused by the electron donor character of the boronic acid group (acceptor). Some of the ring bands are also observed in the corresponding FT-IR spectrum (at  $3058$ ,  $1604$ ,  $1590$ ,  $1177$ ,  $998/983$ , and  $777 \text{ cm}^{-1}$ ). These bands are associated with the  $\nu_2$ ,  $\nu_{8a}$ ,  $\nu_{8b}$ ,  $\nu_{9a}/\nu_{15}$ ,  $\nu_{12}$ , and  $\nu_{11}$

TABLE 2: The calculated wavenumbers and potential energy distribution (PED, %) for the FT-Raman and FT-IR spectra of [PhN-(2-PhB(OH)<sub>2</sub>)-R-Me]PO<sub>3</sub>H<sub>2</sub><sup>a</sup>.

Calc.	Wavenumbers/cm <sup>-1</sup>		Assignment
	FT-Raman	FT-IR	
	Exp.		B3LYP/6-311G(d,p) (PED %; >5%)
449	432	430	$\gamma_{as}(\phi)_B(31)$ , $\delta_{oop}(CC_L(C_\alpha)C)_{\phi B}$ , $\delta_s(C_\alpha PO_3)$ , $\delta_{p(bridge)}$
451	474		$\gamma_{as}(\phi)_B(29)$ , $\delta_{oop}(CC_L(C_\alpha)C)_{\phi B}$ , $\delta_s(C_\alpha PO_3)$ , $\gamma_{as(bridge)}$
499	490	491	$\delta_{p(bridge)}$ , $\gamma_{s(bridge)}$ , $\gamma_{as(bridge)}$ , $\delta_{oop}(CC_L(C_\alpha)C)_{\phi B}$
531		533	$\delta_{p(bridge)}$ , $\gamma_{s(bridge)}$ , $\gamma_{as(bridge)}$
553	543		$\delta_{p(bridge)}(48)$ , $\gamma_{s(bridge)}$ , $\gamma_{as(bridge)}$
581	591	591	$\delta_{p(bridge)}(36)$ , $\gamma_{s(bridge)}$ , $\gamma_{as(bridge)}$
627	617	617	$\delta_{as}(\phi)(34)$ , $\delta_{oop}(CBO_2)$ , $\gamma_{as(bridge)}$ , $\gamma_{s(bridge)}$
659	635	636	$\delta_{p(bridge)}(25)$ , $\gamma_{as(bridge)}$ , $\gamma_{s(bridge)}$
696		688	$\delta_{p(bridge)}(46)$ , $\gamma_{s(bridge)}$ , $\gamma_{as(bridge)}$
717		710	$\gamma_{as(bridge)}(32)$ , $\gamma_{s(bridge)}$ , $\delta_{p(bridge)}$
720	722		$\delta_{p(bridge)}(49)$ , $\gamma_{s(bridge)}$ , $\gamma_{as(bridge)}$
746	<b>745</b>	<b>742</b>	$\delta_{p(bridge)}(18)$ , $\delta_p(\phi)_B$ , $\gamma_{s(bridge)}$
793	775	777	$\delta_{oop}(CC_L(C_\alpha)C)_{\phi B}(36)$ , $\delta_p(\phi)_B$ , $\delta_{oop}(C_L C_B(OH)_2(B)C)_{\phi B}$
822	808	809	$\delta_{p(bridge)}(43)$ , $\gamma_{s(bridge)}$ , $\gamma_{as(bridge)}$
823	826	827	$\nu(PO)(12)$ , $\gamma_{as(bridge)}$
886	884	882	$\delta_{p(bridge)}(35)$ , $\gamma_{s(bridge)}$ , $\gamma_{as(bridge)}$
919	899	903	$\nu(PO)(30)$ , $\delta_{oop}(CC_L(C_\alpha)C)_{\phi B}$
924		924	$\nu(PO)(22)$ , $\delta_{p(bridge)}$
952	934		$\delta_{oop}(C_B(OH)_2 C(H)C)_{\phi B}(27)$ , $\delta_{oop}(C_L C(H)C)_{\phi B}$ , $\delta_{oop}(CC(H)C)_{\phi B}$ , $\gamma_{as}(\phi)_B$
987	999	983	$\delta_{oop}(CC(H)C)_{\phi B}(48)$ , $\delta_p(\phi)_B$
999	1008	998	$\delta_{trig}(\phi)(40)$ , $\delta_{p(bridge)}$ , $\rho_b(POH)$ , $\gamma_{s(bridge)}$
1036	1031	1021	$\nu(CC)_\phi(51)$
1045		1042	$\delta_{p(bridge)}(31)$ , $\nu(CC)_{\phi B}$ , $\gamma_{s(bridge)}$ , $\gamma_{as(bridge)}$
1084	1074	1073	$\nu(C_\alpha N)(14)$ , $\delta_{p(bridge)}$
1106		1090	$\gamma_{as(bridge)}(48)$ , $\gamma_{s(bridge)}$ , $\delta_{p(bridge)}$
1165	1161	1162	$\rho_r(CC(H)C)_\phi(58)$ , $\delta_{p(bridge)}$ , $\gamma_{s(bridge)}$
1171	1181	1177	$\rho_r(CC(H)C)_{\phi B}(60)$ , $\rho_r(C_L C(H)C)_{\phi B}$
1194	1188	1189	$\rho_r(C_L C(H)C)_\phi(34)$ , $\rho_r(CC(H)C)_\phi$
1216		1206	$\nu(P=O)(16)$ , $\rho_r(C_L C_\alpha(H)P)$ , $\rho_r(C_\alpha(H,P)N)$ , $\rho_r(C_L C_\alpha(H,P)N)$
1234		1227	$\nu(P=O)(46)$ , $\rho_r(C_L C_\alpha(H)P)$ , $\rho_r(C_\alpha(H,P)N)$ , $\rho_r(C_L C_\alpha(H,P)N)$
1244	1242		$\delta_{p(bridge)}(36)$ , $\gamma_{s(bridge)}$ , $\nu(P=O)$ , $\gamma_{as(bridge)}$
1271		1264	$\delta_{p(bridge)}(42)$ , $\gamma_{s(bridge)}$ , $\gamma_{as(bridge)}$
1286		1285	$\delta_{p(bridge)}(39)$ , $\gamma_{s(bridge)}$ , $\gamma_{as(bridge)}$
1346	1330	1330	$\delta_{p(bridge)}(26)$ , $\gamma_{s(bridge)}$ , $\rho_r(C_L C(H)C)_\phi$ , $\gamma_{as(bridge)}$
1349		1363	$\gamma_{as(bridge)}(38)$ , $\gamma_{s(bridge)}$ , $\nu(BO)$ , $\delta_{p(bridge)}$
1446	1428	1428	$\rho_r(CC(H)C)_\phi(36)$ , $\nu(CC)_\phi$ , $\rho_r(C_\alpha N(H)C_L)$
1450		1450	$\rho_r(CC(H)C)_{\phi B}(43)$ , $\nu(CC)_{\phi B}$ , $\nu(C_L C)_{\phi B}$
1510		1495	$\rho_r(CC(H)C)_\phi(28)$ , $\rho_r(C_L C(H)C)_\phi$ , $\nu(CC)_\phi$
1519	1509		$\rho_r(C_\alpha N(H)C_L)(50)$
1587	1588	1590	$\nu(CC)_{\phi B}(40)$ , $\nu(C_L C_B(OH)_2)_{\phi B}$ , $\rho_r(CC(H)C)_{\phi B}$
1620	1606	1604	$\nu(CC)_{\phi B}(30)$ , $\nu(C_L C)_{\phi B}$
1625		1635	$\nu(CC)_\phi(42)$ , $\delta_{as}(\phi)$
2938	2922	2924	$\nu(C_\alpha H)(99)$
2938		2957	$\nu(C_\alpha H)(99)$
3107	3059	3058	$\nu(CH)_{\phi B}(91)$

TABLE 2: Continued.

Calc.	Wavenumbers/cm <sup>-1</sup>		Assignment
	FT-Raman	FT-IR	
3145	3069		$\nu(\text{CH})_\phi$ (67), $\nu(\text{CH})_{\phi\text{B}}$
3405	3482		$\nu(\text{NH})$ (96)
3500	3503		$\nu(\text{OH})_{\text{BOHbridge}}$ (83), $\nu(\text{OH})_{\text{POH}}$

<sup>a</sup> Abbreviations:  $\nu$ : stretching;  $\rho_r$ : rocking;  $\delta$ : deformation;  $\gamma$ : torsion;  $p$ : puckering;  $\delta_{\text{trig}}$ : trigonal deformation;  $s$ : symmetric;  $as$ : antisymmetric;  $oop$ : out-of-plane vibrations;  $\phi$ : aromatic ring;  $\phi\text{B}$ : phenylboronic acid ring; bridge: hydrogen bonds [(HOBO)<sub>2</sub>];  $\text{C}_L$ : carbon atom of the aromatic ring connected to the aliphatic chain;  $\text{C}_\alpha$ : tetrahedral carbon atom; bold: vibrations related to band with Raman Intensity > 0.4 (%).

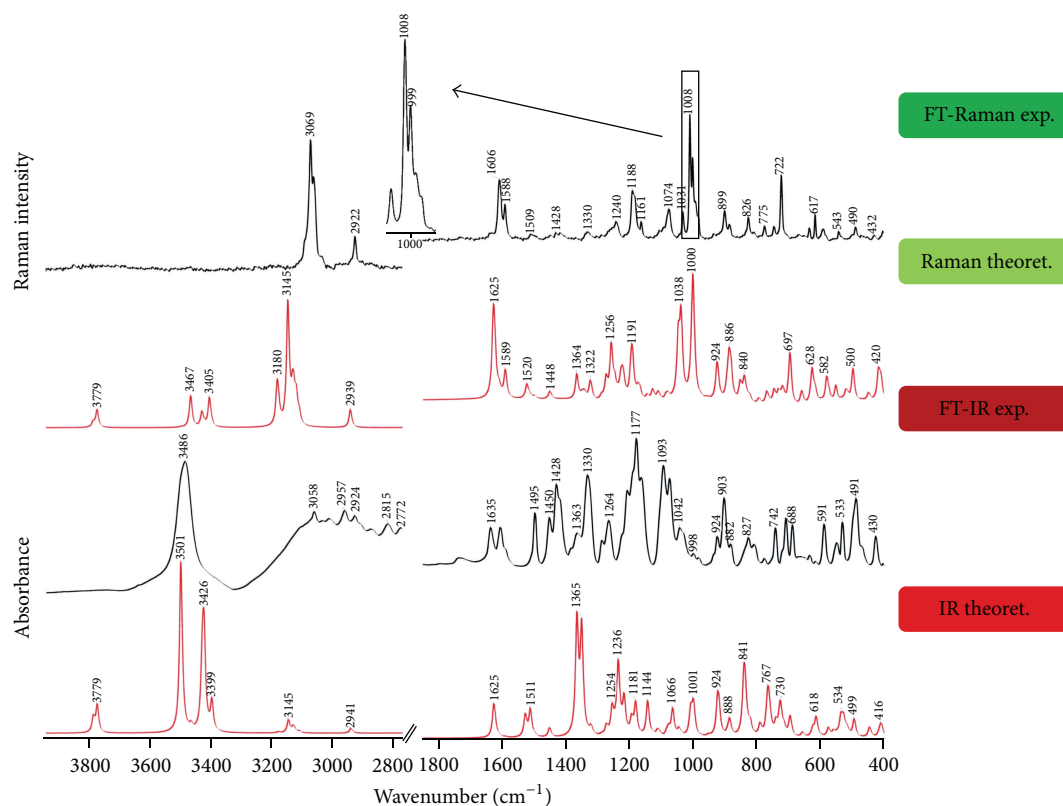


FIGURE 2: The experimental and theoretical FT-Raman and FT-IR spectra of [PhN-(2-PhB(OH)<sub>2</sub>)-R-Me]PO<sub>3</sub>H<sub>2</sub> in the spectral range of 3650–400 cm<sup>-1</sup>.

modes (according to the Wilson numbering scheme) [39], respectively. The other ring vibrations appear in the FT-IR spectrum as two medium absorbencies at 1495 [ $\nu_{19a}$ ] and 1450 cm<sup>-1</sup> [ $\nu_{19b}$ ].

**Boronic Acid Group Vibrations.** In the [PhN-(2-PhB(OH)<sub>2</sub>)-R-Me]PO<sub>3</sub>H<sub>2</sub> vibrational spectra, several moderate and weak bands due to the boronic acid group vibrations appear. From these, according to Erdogdu and Coworkers [40] and Ayyappan and Coworkers [41], the B–O stretching vibrations [ $\nu(\text{BO})$ ] are expected to be enhanced near 1453–1450, 1384, and 1369–1361 cm<sup>-1</sup>. Our calculations for dimer placed these vibrations at 1363–1349 cm<sup>-1</sup>. The bands allocated to the –BOH deformation vibrations [ $\delta(\text{BOH})$ ] appear in the spectral range of 1100–1000 cm<sup>-1</sup> [40, 41]. Our calculations indicated

that bands observed in these ranges are due to the deformation and torsion vibrations of the HOBO...H bridge coupled with the  $\nu(\text{C}_\alpha\text{N})$  mode [ $\delta/\gamma_{(\text{bridge})} + \nu(\text{NC}/\text{C}_\alpha\text{N})$ ]. Ayyappan and coworkers also suggested that bands assignable to the coupling of the B–C and B–O stretching vibrations [ $\nu(\text{BC}/\text{BO})$ ] are seen at 809–797 cm<sup>-1</sup>. However, the calculations performed for the [PhN-(2-PhB(OH)<sub>2</sub>)-R-Me]PO<sub>3</sub>H<sub>2</sub> dimer indicate that this band can be assigned to the  $\delta/\gamma_{(\text{bridge})}$  modes. Erdogdu and coworkers indicated that the  $\gamma(\text{OBCC})$  and  $\gamma(\text{HOBC}/\text{OBCC})$  vibrations appear in the range 740–580 cm<sup>-1</sup>. Our theoretical calculations provide evidence that the bands occurring in this spectral ranges are connected with torsion and deformation vibrations of the HOBO...H fragment. Additionally, the 540 cm<sup>-1</sup> band may be assigned to the torsion of the –HOBC–, –HOBH–, and –HOBO–



fragments [ $\gamma(\text{HOB(C)})/(\text{HOB(H)})/(\text{HOB(O)})$ ] [37, 38], whereas our calculations pointed out that the  $543\text{ cm}^{-1}$  bands are due to the torsion vibrations of  $\text{HOB(O)}\cdots\text{H}$  [ $\delta_{(\text{bridge})}$ ] and the deformation of  $\text{HOB(O)}\cdots\text{H}$  [ $\gamma_{(\text{bridge})}$ ]. The above discrepancies in the band assignments may be due to the fact that Erdogdu and coworkers and Ayyappan and coworkers presented results for phenylboronic acid derivative monomer, while we performed theoretical calculations for dimer.

Bearing in mind that the most stable structure of  $[\text{PhN}-(2\text{-PhB}(\text{OH})_2)\text{-R-Me}]\text{PO}_3\text{H}_2$  is a dimer formed by two hydrogen bonds between the boron hydroxyl groups of two monomers, the deformation and torsion vibrations of the  $\text{HOB(O)}\cdots\text{H}$  bridge are expected in the vibrational spectra. These vibrations are manifested by the  $1363\text{--}1330$ ,  $1286\text{--}1242$ ,  $1106\text{--}1090$ ,  $1074\text{--}1042$ ,  $886\text{--}882$ ,  $822\text{--}808$ ,  $746\text{--}732$ ,  $722\text{--}710$ ,  $659\text{--}635$ ,  $574\text{--}543$ ,  $533\text{--}522$ , and  $499\text{--}490\text{ cm}^{-1}$  spectral features.

**Phosphonate Group Vibrations.** The  $\text{-PO}_3\text{H}_2$  group gives rise to several vibrational bands. These appear in the  $1242\text{--}1206$ ,  $1008\text{--}998$ ,  $924\text{--}903$ ,  $827\text{--}823$ , and  $496\text{--}430\text{ cm}^{-1}$  spectral ranges. The  $1242$  and  $1206\text{ cm}^{-1}$  spectral features are primarily due to the  $\text{P=O}$  stretching vibrations [ $\nu(\text{P=O})$ ], whereas the  $924\text{--}903$  and  $827\text{--}823\text{ cm}^{-1}$  bands are assigned to the  $\text{P-O}$  stretching mode [ $\nu(\text{P-O})$ ]. The two other bands mentioned above, located at  $1010\text{--}990$  and  $496\text{--}430\text{ cm}^{-1}$ , are mainly due to the  $\rho_b(\text{POH})$  and  $\delta_s(\text{C}_\alpha\text{PO}_3)$  vibrations, respectively.

**Imine and Methine Groups Vibrations.** In the  $[\text{PhN}-(2\text{-PhB}(\text{OH})_2)\text{-R-Me}]\text{PO}_3\text{H}_2$  FT-IR spectrum, the broad, strong band due to the imine group vibrations is observed at  $3482\text{ cm}^{-1}$  [31]. This band is associated with the  $\text{N-H}$  stretching mode [ $\nu(\text{NH})$ ]. The broadness of this spectral feature can be explained by the formation of intermolecular and/or intramolecular hydrogen bonds between the  $\text{-PO}_3\text{H}_2$ ,  $\text{-NH-}$ , and  $\text{-BOH}$  groups. The  $\text{C-N}$  stretching vibrations [ $\nu(\text{C}_\alpha\text{N})$ ] are observed at around  $1074\text{ cm}^{-1}$ . The deformation modes of the  $\text{C}_\alpha\text{N(H)C}$  fragment are enhanced at  $1519\text{--}1509$  and  $1446\text{--}1428\text{ cm}^{-1}$ . In contrast, the rocking vibrations of the  $\text{C}_\alpha(\text{H,P})\text{NH}$  fragment contribute to the bands at  $1509$ ,  $1428$ , and  $1227\text{--}1206\text{ cm}^{-1}$ . The  $>\text{CH-}$  group's stretching vibrations exhibit also moderate spectral features in the high wavenumber range of the vibrational spectra (Table 2).

## 4. Conclusions

In this work, the  $[N\text{-phenylamino}(2\text{-boronphenyl})\text{-R-methyl}]\text{phosphonic acid}$  ( $[\text{PhN}-(2\text{-PhB}(\text{OH})_2)\text{-R-Me}]\text{PO}_3\text{H}_2$ ) was investigated using Fourier-transform infrared and Fourier-transform Raman methods. We briefly discussed the characteristic FT-Raman and absorption infrared bands that are crucial for understanding vibrational structures of the tilted compound.

In order to better understand the correlation between obtained spectral feature and the vibrational structure, the DFT calculations at the B3LYP; 6-311G(d,p) level using Gaussian'03, GaussSum 0.8, and GAR2PED softwares were performed.

Our theoretical and experimental considerations provide the description of the most stable structure of the investigated molecules which is a cyclic dimer, in the *cis-trans* conformation, formed by a pair of intermolecular hydrogen bonds between the boron hydroxyl groups of two monomers. Moreover, the spectral range of FT-IR and FT-Raman bands associated with the aromatic and aliphatic functional group vibrations of the molecule was characterized.

## Conflict of Interests

The authors declare that there is no conflict of interests regarding the publication of the paper.

## Acknowledgments

The authors are grateful to Professor P. Kafarski and Dr. A. Rydzewska for donation of samples. This work was supported by the National Science Center of the Polish Ministry of Science and Higher Education (Grants no. N N204 544339 to Edyta Proniewicz and no. 2011/03/N/ST4/00777 to Natalia Piergies and Edyta Proniewicz). Natalia Piergies gratefully acknowledges the Marian Smoluchowski Krakow Research Consortium: "Matter-Energy-Future" (KNOW) for financial support in the form of a scholarship. The authors kindly acknowledge the Academic Computer Center "Cyfronet" in Krakow for computational facilities and Dr. M. Andrzejak (Jagiellonian University) for the use of the visualization script.

## References

- [1] P. Kafarski, B. Lejczak, R. Tyka, L. Koba, E. Pliszcak, and P. Wieczorek, "Herbicidal activity of phosphonic, phosphinic, and phosphonous acid analogues of phenylglycine and phenylalanine," *Journal of Plant Growth Regulation*, vol. 14, no. 4, pp. 199–203, 1995.
- [2] E. Naydenova, M. Topashka-Ancheva, P. Todorov, T. Yordanova, and K. Troev, "Novel  $\alpha$ -aminophosphonic acids. Design, characterization, and biological activity," *Bioorganic and Medicinal Chemistry*, vol. 14, no. 7, pp. 2190–2196, 2006.
- [3] E. D. Naydenova, P. T. Todorov, and K. D. Troev, "Recent synthesis of aminophosphonic acids as potential biological importance," *Amino Acids*, vol. 38, no. 1, pp. 23–30, 2010.
- [4] A. Kraszewski and J. Stawinski, "H-phosphonates: versatile synthetic precursors to biologically active phosphorus compounds," *Pure and Applied Chemistry*, vol. 79, no. 12, pp. 2217–2227, 2007.
- [5] B. Lejczak and P. Kafarski, "Biological activity of aminophosphonic acids and their short peptides," *Topics in Heterocyclic Chemistry*, vol. 20, pp. 31–63, 2009.
- [6] M. Pawelczak, K. Nowak, and P. Kafarski, "Synthesis of phosphono dipeptides, inhibitors of cathepsin C," *Phosphorus, Sulfur and Silicon and Related Elements*, vol. 132, pp. 65–71, 1998.
- [7] M. E. Tanner, S. Vaganay, J. van Heijenoort, and D. Blanot, "Phosphinate inhibitors of the D-glutamic acid-adding enzyme of peptidoglycan biosynthesis," *Journal of Organic Chemistry*, vol. 61, no. 5, pp. 1756–1760, 1996.
- [8] M. Bubenik, R. Rej, N. Nguyen-Ba, G. Attardo, F. Ouellet, and L. Chan, "Novel nucleotide phosphonate analogues with potent



- antitumor activity," *Bioorganic and Medicinal Chemistry Letters*, vol. 12, no. 21, pp. 3063–3066, 2002.
- [9] J. Grembecka, A. Mucha, T. Cierpicki, and P. Kafarski, "The most potent organophosphorus inhibitors of leucine aminopeptidase. Structure-based design, chemistry, and activity," *Journal of Medicinal Chemistry*, vol. 46, no. 13, pp. 2641–2655, 2003.
- [10] R. Snoeck, A. Holý, C. Dewolf-Peeters, J. van den Oord, E. de Clercq, and G. Andrei, "Antivaccinia activities of acyclic nucleoside phosphonate derivatives in epithelial cells and organotypic cultures," *Antimicrobial Agents and Chemotherapy*, vol. 46, no. 11, pp. 3356–3361, 2002.
- [11] D. S. Matteson, "α-amido boronic acids: a synthetic challenge and their properties as serine protease inhibitors," *Medicinal Research Reviews*, vol. 28, no. 2, pp. 233–246, 2008.
- [12] P. C. Trippier and C. McGuigan, "Boronic acids in medicinal chemistry: anticancer, antibacterial and antiviral applications," *MedChemComm*, vol. 1, no. 3, pp. 183–198, 2010.
- [13] D. Chen, M. Frezza, S. Schmitt, J. Kanwar, and Q. P. Dou, "Bortezomib as the first proteasome inhibitor anticancer drug: current status and future perspectives," *Current Cancer Drug Targets*, vol. 11, no. 3, pp. 239–253, 2011.
- [14] A. M. Irving, C. M. Vogels, L. G. Nikolcheva et al., "Synthesis and antifungal and antibacterial bioactivity of cyclic diamines containing boronate esters," *New Journal of Chemistry*, vol. 27, no. 10, pp. 1419–1426, 2003.
- [15] W. Yang, X. Gao, and B. Wang, "Boronic acid compounds as potential pharmaceutical agents," *Medicinal Research Reviews*, vol. 23, no. 3, pp. 346–368, 2003.
- [16] T. Asano, H. Nakamura, Y. Uehara, and Y. Yamamoto, "Design, synthesis, and biological evaluation of aminoboronic acids as growth-factor receptor inhibitors of EGFR and VEGFR-1 tyrosine kinases," *ChemBioChem*, vol. 5, no. 4, pp. 483–490, 2004.
- [17] E. Podstawka-Proniewicz, M. Kosior, Y. Kim, K. Rolka, and L. M. Proniewicz, "Nociceptin and its natural and specifically-modified fragments: structural studies," *Biopolymers*, vol. 93, no. 12, pp. 1039–1054, 2010.
- [18] E. Podstawka-Proniewicz, D. Sobolewski, A. Prah, Y. Kim, and L. M. Proniewicz, "Structure and conformation of Arg8 vasopressin modified analogs," *Journal of Raman Spectroscopy*, vol. 43, no. 1, pp. 51–60, 2012.
- [19] E. Podstawka-Proniewicz, A. Kudelski, Y. Kim, and L. M. Proniewicz, "Adsorption of neurotensin-family peptides on SERS-active Ag substrates," *Journal of Raman Spectroscopy*, vol. 43, no. 9, pp. 1196–1203, 2012.
- [20] E. Proniewicz, D. Skořuba, A. Kudelski et al., "B2 bradykinin receptor antagonists: adsorption mechanism on electrochemically roughened Ag substrate," *Journal of Raman Spectroscopy*, vol. 44, no. 2, pp. 205–211, 2013.
- [21] E. Podstawka-Proniewicz, M. Andrzejak, P. Kafarski, Y. Kim, and L. M. Proniewicz, "Vibrational characterization of L-valine phosphonate dipeptides: FT-IR, FT-RS, and SERS spectroscopy studies and DFT calculations," *Journal of Raman Spectroscopy*, vol. 42, no. 5, pp. 958–979, 2011.
- [22] E. Podstawka-Proniewicz, N. Piergies, D. Skořuba, P. Kafarski, Y. Kim, and L. M. Proniewicz, "Vibrational characterization of L-leucine phosphonate analogues: FT-IR, FT-Raman, and SERS spectroscopy studies and DFT calculations," *The Journal of Physical Chemistry A*, vol. 115, no. 40, pp. 11067–11078, 2011.
- [23] E. Proniewicz, E. Pięta, A. Kudelski et al., "Vibrational and theoretical studies of the structure and adsorption mode of *m*-nitrophenyl α-guanidinomethylphosphonic acid analogues on silver surfaces," *The Journal of Physical Chemistry A*, vol. 117, no. 23, pp. 4963–4972, 2013.
- [24] P. Młynarz, A. Rydzewska, and Z. Pokładek, "Preparation of a novel group of hybrid compounds N-benzyl aminoborobenzylphosphonic and N,N'-ethylenedi(aminoborobenzylphosphonic) acids," *Journal of Organometallic Chemistry*, vol. 696, no. 2, pp. 457–460, 2011.
- [25] M. J. Frisch, G. W. Trucks, H. B. Schlegel et al., *Aussian03, Revision A. 1*, Gaussian Inc, Pittsburgh, Pa, USA, 2003.
- [26] N. Piergies, E. Proniewicz, A. Kudelski et al., "Fourier transform infrared and Raman and surface-enhanced Raman spectroscopy studies of a novel group of boron analogues of aminophosphonic acids," *The Journal of Physical Chemistry A*, vol. 116, no. 40, pp. 10004–10014, 2012.
- [27] M. K. Cyrański, A. Jezierska, P. Klimentowska, J. J. Panek, and A. Sporzyński, "Impact of intermolecular hydrogen bond on structural properties of phenylboronic acid: quantum chemical and X-ray study," *Journal of Physical Organic Chemistry*, vol. 21, no. 6, pp. 472–482, 2008.
- [28] A. Jezierska, J. J. Panek, G. Z. Zukowska, and A. Sporzyński, "A combined experimental and theoretical study of benzoxaborole derivatives by Raman and IR spectroscopy, static DFT, and first-principle molecular dynamics," *Journal of Physical Organic Chemistry*, vol. 23, no. 5, pp. 451–460, 2010.
- [29] F. Jensen, *Introduction to Computational Chemistry*, John Wiley and Sons, Chichester, UK, 2007.
- [30] D. Michalska and R. Wysockiński, "The prediction of Raman spectra of platinum(II) anticancer drugs by density functional theory," *Chemical Physics Letters*, vol. 403, no. 1–3, pp. 211–217, 2005.
- [31] N. M. O'Boyle and J. G. Vos, *GaussSum 0. 8*, Dublin City University, Dublin, Ireland, 2004, <http://gausssum.sourceforge.net>.
- [32] J. L. M. Martin and C. van Alsenoy, *Gar2ped*, University of Antwerp, Antwerp, Belgium, 1995.
- [33] D. G. Hall, *Boronic Acids. Preparation and Applications in Organic Synthesis, Medicine and Materials*, Wiley-VCH, Weinheim, Germany, 2011.
- [34] M. Kurt, "An experimental and theoretical study of molecular structure and vibrational spectra of pentafluorophenylboronic acid molecule by density functional theory and ab initio Hartree Fock calculations," *Journal of Molecular Structure*, vol. 874, no. 1–3, pp. 159–169, 2008.
- [35] N. Piergies, E. Proniewicz, Y. Ozaki, Y. Kim, and L. M. Proniewicz, "Influence of substituent type and position on the adsorption mechanism of phenylboronic acids: infrared, raman, and surface-enhanced raman spectroscopy studies," *The Journal of Physical Chemistry A*, vol. 117, no. 27, pp. 5693–5705.
- [36] E. Podstawka, R. Borszowska, M. Grabowska, M. Drg, P. Kafarski, and L. M. Proniewicz, "Investigation of molecular structures and adsorption mechanisms of phosphonodipeptides by surface-enhanced Raman, Raman, and infrared spectroscopies," *Surface Science*, vol. 599, no. 1–3, pp. 207–220, 2005.
- [37] E. Podstawka, A. Kudelski, and L. M. Proniewicz, "Adsorption mechanism of physiologically active L-phenylalanine phosphonodipeptide analogues: comparison of colloidal silver and macroscopic silver substrates," *Surface Science*, vol. 601, no. 21, pp. 4971–4983, 2007.
- [38] E. Podstawka, A. Kudelski, P. Kafarski, and L. M. Proniewicz, "Influence of aliphatic spacer group on adsorption mechanisms of phosphonate derivatives of L-phenylalanine: surface-enhanced Raman, Raman, and infrared studies," *Surface Science*, vol. 601, no. 19, pp. 4586–4597, 2007.

- [39] E. B. Wilson Jr., "The normal modes and frequencies of vibration of the regular plane hexagon model of the benzene molecule," *Physical Review*, vol. 45, no. 10, pp. 706–714, 1934.
- [40] Y. Erdogdu, M. Tahir Güllüoğlu, and M. Kurt, "DFT, FT-Raman, FT-IR and NMR studies of 2-fluorophenylboronic acid," *Journal of Raman Spectroscopy*, vol. 40, no. 11, pp. 1615–1623, 2009.
- [41] S. Ayyappan, N. Sundaraganesan, M. Kurt, T. R. Sertbakan, and M. Özdoğan, "Molecular structure, vibrational spectroscopic studies and NBO analysis of the 3,5-dichlorophenylboronic acid molecule by the density functional method," *Journal of Raman Spectroscopy*, vol. 41, no. 10, pp. 1379–1387, 2010.

## Research Article

# Synthesis and Characterization of CdS/TiO<sub>2</sub>-Montmorillonite Nanocomposite with Enhanced Visible-Light Absorption

Feng-shan Zhou, Dai-mei Chen, Bao-lin Cui, and Wei-heng Wang

*School of Materials Science and Technology, China University of Geosciences, Beijing 100083, China*

Correspondence should be addressed to Feng-shan Zhou; [zhoufs@cugb.edu.cn](mailto:zhoufs@cugb.edu.cn) and Dai-mei Chen; [chendaimei@cugb.edu.cn](mailto:chendaimei@cugb.edu.cn)

Received 4 October 2013; Accepted 14 December 2013; Published 20 January 2014

Academic Editor: Yizhuang Xu

Copyright © 2014 Feng-shan Zhou et al. This is an open access article distributed under the Creative Commons Attribution License, which permits unrestricted use, distribution, and reproduction in any medium, provided the original work is properly cited.

Sodium montmorillonite (MMT) was chosen as the carrier; a series of CdS/TiO<sub>2</sub>-MMT nanocomposites with enhanced visible-light absorption ability was prepared by hydrothermal synthesis method combination with semiconductor compound modification method. The samples are characterized by X-ray diffraction (XRD), X-ray photoelectron spectroscopy (XPS), and ultraviolet visible (UV-Vis) spectroscopy; the results showed that TiO<sub>2</sub> and CdS nanoparticles were loaded on the surface of montmorillonite uniformly. N<sub>2</sub> adsorption-desorption experiment showed that the specific surface area of TiO<sub>2</sub>/montmorillonite nanocomposite made by this method can reach 200 m<sup>2</sup>/g and pore-size distribution was from 4 to 6 nm; UV-Vis showed that the recombination of CdS and TiO<sub>2</sub> enhanced visible-light absorption ability of samples of TiO<sub>2</sub>/montmorillonite and visible-light absorption ability increase with the increased of the adsorption of CdS.

## 1. Introduction

The bentonite is a kind of clay mineral mainly consisting of montmorillonite (MMT); the crystal structure of MMT is 2:1 layered silicates [1]. Pillared clay is a new mineral that used the high temperature resistant pillared agent with positively charged replaced the exchangeable positive ions in the montmorillonite, bridging the crystal structure of 2:1 layered silicates and put them open, and formed a kind of “layered and columnar” structure of two-dimensional passage [2]. Ti-pillared clay (Ti-PILC) has pore structure, large specific surface area, and thermal stability. Therefore, they are being used in many applications such as the preparation of catalyst, catalyst carrier, molecular sieve, adsorbent, environmental protection material, ion exchanger, conductive material, storage material, and nanocomposites [3–5].

At present, the preparation methods of TiO<sub>2</sub> pillared clay are Ti inorganic salt hydrolysis [6] or Sol-Gel method of Ti alkoxides [1]. But the particle size of hydrated titanium ion gel particles [TiO(OH)<sub>x</sub>]<sup>mn+</sup> is only 1–2 nm, which is precursor of titanium oxide particles by the traditional method. The photocatalytic efficiency is relatively low; most of interlayer pores are micropores that hinder the contact between the

substrate and catalyst for undersized titanium oxide between Montmorillonite interlayer. Next, the band gap of TiO<sub>2</sub> is wider ( $E_g = 3.2$  eV) and the efficiency of water used is low for it only can be excited at near ultraviolet, in which the wavelength is equal to or less than 387 nm in the sunlight.

The structure of Ti-pillared montmorillonite, which is prepared by hydrothermal synthesis method, is exfoliated. Which make some TiO<sub>2</sub> particles adsorb on the surface of montmorillonite enhanced visible-light absorption ability of the Ti pillared montmorillonite by using semiconductor CdS that has visible-light absorption ability as a photosensitizer, to improve the visible-light catalytic ability of composite catalyst.

## 2. Experiment

### 2.1. Material

**2.1.1. Samples Purchased.** Natural MMT with the purity 98% is supplied from Zhejiang Sanding Co., Ltd., China. TiCl<sub>4</sub>, HCl, ethyl alcohol, and other chemical agents are purchased from Beijing Chemical Reagent Co., Ltd. And all the reagents used in the experiment were of analytical reagent grade.

TABLE 1: Specific surface area of CdS/TiO<sub>2</sub>-MMT.

Sample	BET specific surface area (m <sup>2</sup> /g)
CdS-MMT	40.7789
CdS/TiO <sub>2</sub> -MMT-0.5	212.1027
CdS/TiO <sub>2</sub> -MMT-1.0	203.5253
CdS/TiO <sub>2</sub> -MMT-2.0	198.4932
CdS/TiO <sub>2</sub> -MMT-4.0	173.7505

**2.1.2. Preparation of Ti Pillared Montmorillonite.** TiCl<sub>4</sub> was put into 6 mol/L HCl aqueous solution gradually; dilute the solution to Ti pillared solution ([Ti] = 0.82 mol/L, [HCl] = 0.74 mol/L), aged for 96 h. Next, Ti pillared solution was put into 0.2% (mass fraction) sodium montmorillonite suspension according to the molarity of Ti in clay 20 mmol/g. We washed the sample with deionized water until without Cl<sup>-</sup> after aged for 16 h, Centrifugal separation, put the produced sample into the aqueous solution and then put the solution into high pressure reactor, continuously hydrothermal treatment at 160°C for 72 h. At last, a denoted as TiO<sub>2</sub>-MMT sample was obtained after being centrifuged and washed.

**2.1.3. Preparation of CdS/TiO<sub>2</sub>-MMT.** The CdS precursor solution was obtained after CdAc<sub>2</sub>·2H<sub>2</sub>O and CS (NH<sub>2</sub>)<sub>2</sub> (the ratio of moles is 1:2) dissolved in 20 mL deionized water and ultrasonic processing for 5 min. Subsequently, the intensive mixed solution of TiO<sub>2</sub>-MMT and the above precursor solution with 60 mL deionized water were put into a 100 mL high pressure reactor. After hydrothermal treatment at 160°C for 12 h, the produced samples were filtered, washed with deionized water and absolute ethanol in turn, dried, ground and denoted by the names CdS/TiO<sub>2</sub>-MMT-0.5, CdS/TiO<sub>2</sub>-MMT-1, CdS/TiO<sub>2</sub>-MMT-2, and CdS/TiO<sub>2</sub>-MMT-4 according to different concentration of CdS.

**2.2. Characterization.** The X-ray powder diffraction (XRD) (D/MAX2000) was used to determine the crystallite size and identity of TiO<sub>2</sub> and CdS in the samples. The particle diameter was calculated by characteristic diffraction peaks. Nitrogen adsorption-desorption test used Model ASAP2400 physisorption apparatus by Micromeritics Instrument Co., Ltd., USA. Samples were calcined at 200°C for more than 4 h under vacuum 113 Pa. The surface areas of samples were determined by using BET equation (Table 1); the pore size distribution treated by using the BJH method, the surface element valence, and energy level of samples were characterized by X-ray photoelectron spectroscopy (XPS) in a Perkin-Elmer, USA. The instrument condition: Mg Kα (1253.6 eV) source is X-ray, power is 300.0 W, spot size is 0.8 mm<sup>2</sup>, the vacuum is 6.67 × 10<sup>-7</sup> Pa, pass energy is 187.0 eV and 23.5 eV, and the Cls (284.6 eV) is the internal marked standard. The UV-Vis diffuse reflectance spectra of samples in the 200–800 nm range were recorded using U-3010 UV-Vis spectrophotometer.

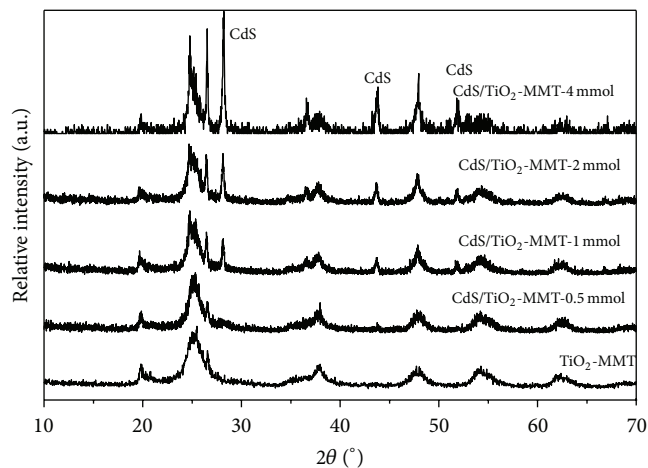
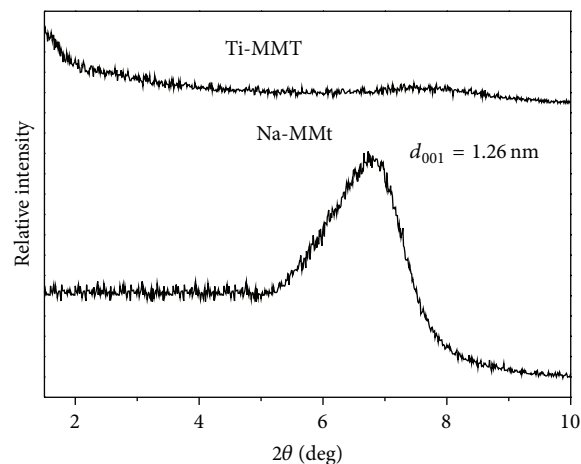
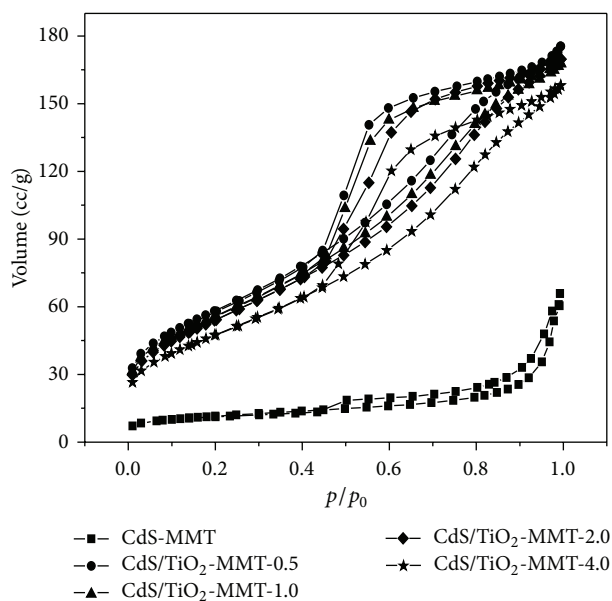
FIGURE 1: Large angle XRD spectra of CdS/TiO<sub>2</sub>-MMT (10°–70°).

FIGURE 2: Small angle XRD spectra of Na-MMT and Ti-MMT (1°–10°).

### 3. Results and Discussion

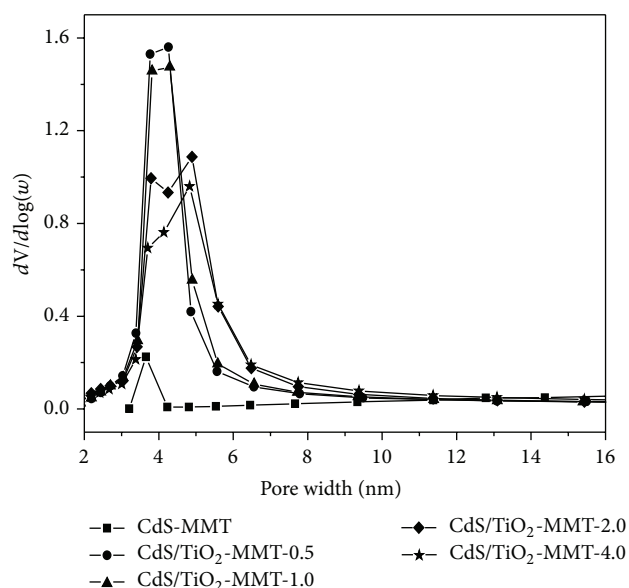
**3.1. XRD Characterization of CdS/TiO<sub>2</sub>-MMT.** The structure of the CdS/TiO<sub>2</sub>-MMT was investigated by using XRD, and the spectra are shown in Figure 1 (wide angle) and Figure 2 (low angle). It can be seen in Figure 1 that the characteristic diffraction peaks for anatase at 2θ values 25.3°, 37.8°, 47.7°, and 54.9° are observed from the XRD patterns of all the samples. The peaks appear at 28.0°, 36.9°, 43.7°, and 51.8° due to the cubic CdS particles. In addition, with the increase of CdS/MMT's concentration (mmol/g), the intensity of the peak was enhanced. These facts indicate that the CdS particles have been loaded on the surface of montmorillonite. The small angle XRD spectra of Na-MMT and Ti-MMT are shown in Figure 2. No obvious peak can be seen in the small angle XRD spectrum of Ti-MMT. The structure of Ti-MMT is called "delaminated" [7]; in other words, it is the mixture of TiO<sub>2</sub> particles and Ti-pillared montmorillonite (Ti-PILC),

FIGURE 3: Large angle XRD spectra of CdS/TiO<sub>2</sub>-MMT.

which has some TiO<sub>2</sub> in the interlayer while others on the surface of montmorillonite.

**3.2. Absorption Analysis of CdS/TiO<sub>2</sub>-MMT to N<sub>2</sub>.** The N<sub>2</sub> adsorption-desorption isotherm of CdS/TiO<sub>2</sub>-MMT is illustrated in Figure 3. It can be inferred that CdS/TiO<sub>2</sub>-MMT has a mesoporous structure due to the isotherm of CdS/TiO<sub>2</sub>-MMT with a prolate shape particularly, which states that most of the mesoporous in CdS/TiO<sub>2</sub>-MMT are formed by montmorillonite flake. As a consequence, CdS always gathers on the surface but difficultly enters into the interlayer of montmorillonite without titanium existing as the exchanger. When the reaction system obtains both titanium exchanger and cadmium sulfide precursor at the same time, it is easy for CdS to enter into the interlayer of montmorillonite because the titanium exchanger enlarges interlayer spacing of montmorillonite by squeezing into it. As a result, pillar structure mesoporous material with TiO<sub>2</sub> and CdS in the interlayer was obtained. As Figure 4 shows, the size of mesoporous in CdS/TiO<sub>2</sub>-MMT is concentrated among 4–6 nm, which declared CdS/TiO<sub>2</sub>-MMT with quite uniform mesoporous. It can be seen that the specific surface area decreases with the increase of CdS content, which may be a result of the mesoporous blocked with too much TiO<sub>2</sub> and CdS in the interlayer of montmorillonite being meanwhile too much TiO<sub>2</sub> and CdS gathered on the surface of montmorillonite perhaps is the other reason for the specific surface area reduction.

**3.3. XPS Characterization of CdS/TiO<sub>2</sub>-MMT.** The XPS spectra of Ti2p<sub>3/2</sub>(A), Cd3d<sub>5/2</sub>(B), and S2p(C) in CdS/TiO<sub>2</sub>-MMT-2 are shown, respectively, in Figure 5, and the XPS spectrum patterns were measured with binding energy Cls = 284.8 eV as the internal marked standard. The existence of Ti, Cd and S in CdS/TiO<sub>2</sub>-MMT-2 is illustrated in XPS

FIGURE 4: Pore size distribution of CdS/TiO<sub>2</sub>-MMT.

spectra. Firstly, the two peaks, which binding energy are respectively 458.99 eV and 464.80 eV, are attributed as Ti2p<sub>3/2</sub> and Ti2p<sub>1/2</sub> (Figure 5(a)); thus, the existence of Ti<sup>4+</sup> in TiO<sub>2</sub> is demonstrated. Secondly, the peaks of Cd3d<sub>5/2</sub> can be seen at 405.30 eV and 412.20 eV (Figure 5(b)) suggesting Cd<sup>2+</sup> in CdS. Thirdly, it can be seen that the peaks of S2p at 169.2 eV, which are thought to be the peaks of S within CdS. All the evidence shows clearly that CdS exists in CdS/TiO<sub>2</sub>-MMT sample.

**3.4. UV-Vis Absorption of CdS/TiO<sub>2</sub>-MMT.** Figure 6 shows UV-vis absorption spectra of the resulting CdS/TiO<sub>2</sub>-MMT samples. The visible-light absorption of the sample is enhanced obviously with the increase of CdS internal load. The absorption edge is in accordance with TiO<sub>2</sub>-MMT when lacking CdS. Then the absorption edge spectral shift to nearby 600 nm, in other words, accord with CdS-MMT. The reinforcement of visible-light absorption ability can contribute to the increase of visible-light catalytic activity of sample.

## 4. Conclusions

CdS/TiO<sub>2</sub>-MMT nanocomposite was prepared with the hydrothermal synthesis method, in which sodium montmorillonite was used as carrier and visible-light catalytic semiconductor CdS was used as photosensitizer. Both TiO<sub>2</sub> and CdS had been loaded on the surface of montmorillonite, which is demonstrated by the results of experiments. In the reaction system, with the increase of precursor CdAc<sub>2</sub>·2H<sub>2</sub>O, the CdS supported on the surface of montmorillonite is added; meanwhile the absorption edge of CdS/TiO<sub>2</sub>-MMT shift's to the direction of visible-light that enhanced the visible light absorption ability of CdS/TiO<sub>2</sub>-MMT.



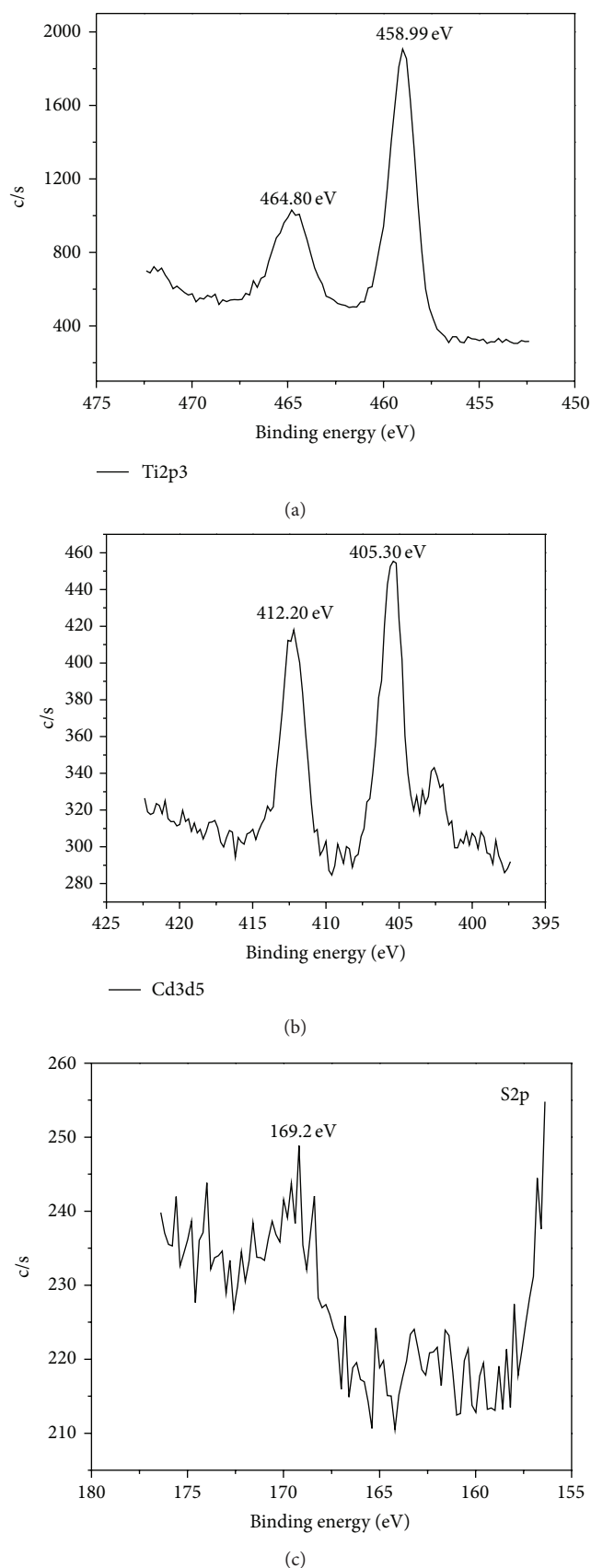


FIGURE 5: The XPS spectra of Ti2p3 (a), Cd3d5 (b), and S2p (c) in CdS/TiO<sub>2</sub>-MMT-2.

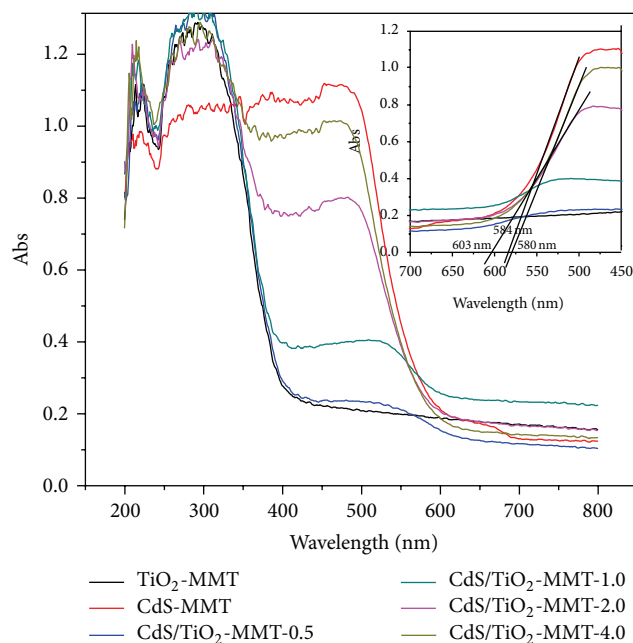


FIGURE 6: Ultraviolet visible-light absorption ability of CdS/TiO<sub>2</sub>-MMT.

## Disclosure

We confirm that the paper is authors owned work, and is original and unpublished, and is not being considered for publication elsewhere.

## Conflict of Interests

The authors declare that there is no conflict of interests regarding the publication of this paper.

## References

- [1] J. Sterte, "Synthesis and properties of titanium oxide crosslinked montmorillonite," *Clays and Clay Minerals*, vol. 34, no. 6, pp. 658–664, 1986.
- [2] Q. Lu, X. Lei, Z. Tang, and H. Liu, "Crystal structure and crystal chemistry of pillared clay mineral materials," *Geological Science and Technology Information*, vol. 20, no. 1, pp. 91–99, 2001.
- [3] J.-F. Qu, Y.-J. Zhao, J.-X. Ma et al., "Directly synthesis of titanium pillared clay from Ca-bentonites," *Journal of the Chinese Ceramic Society*, vol. 35, pp. 1104–1109, 2007.
- [4] J. L. Valverde, A. de Lucas, P. Sánchez, F. Dorado, and A. Romero, "Cation exchanged and impregnated Ti-pillared clays for selective catalytic reduction of NO<sub>x</sub> by propylene," *Applied Catalysis B*, vol. 43, no. 1, pp. 43–56, 2003.
- [5] C. Ooka, H. Yoshida, K. Suzuki, and T. Hattori, "Highly hydrophobic TiO<sub>2</sub> pillared clay for photocatalytic degradation of organic compounds in water," *Microporous and Mesoporous Materials*, vol. 67, no. 2-3, pp. 143–150, 2004.



- [6] S. Yamanaka, T. Nishihara, M. Hattori et al., "Preparation and properties of titania pillared clay," *Materials Chemistry and Physics*, vol. 17, pp. 87–101, 1987.
- [7] J. P. Chen, M. C. Hausladen, and R. T. Yang, "Delaminated  $\text{Fe}_2\text{O}_3$ -pillared clay: its preparation, characterization, and activities for selective catalytic reduction of No by  $\text{NH}_3$ ," *Journal of Catalysis*, vol. 151, no. 1, pp. 135–146, 1995.

## Research Article

# The Use of FTIR-ATR Spectrometry for Evaluation of Surgical Resection Margin in Colorectal Cancer: A Pilot Study of 56 Samples

Hongwei Yao,<sup>1</sup> Xueying Shi,<sup>2</sup> and Yuanfu Zhang<sup>3</sup>

<sup>1</sup> Department of General Surgery, Peking University Third Hospital, Beijing 100191, China

<sup>2</sup> Department of Pathology, School of Basic Medical Sciences, Peking University Third Hospital, Beijing 100191, China

<sup>3</sup> College of Chemistry and Molecular Engineering, State Key Laboratory of Rare Earth Material Chemistry and Application, Peking University, Beijing 100871, China

Correspondence should be addressed to Hongwei Yao; [yaohongwei@medmail.com.cn](mailto:yaohongwei@medmail.com.cn)

Received 6 September 2013; Revised 11 November 2013; Accepted 14 December 2013; Published 16 January 2014

Academic Editor: Yizhuang Xu

Copyright © 2014 Hongwei Yao et al. This is an open access article distributed under the Creative Commons Attribution License, which permits unrestricted use, distribution, and reproduction in any medium, provided the original work is properly cited.

Colorectal cancer is one of the most common malignancies in human, and it is also one of the most leading causes of cancer-related death. Recently, Fourier transform infrared (FTIR) spectrometry is considered to develop into a new method for cancer diagnosis. In this study, colorectal cancer and mucosa 1 cm, 2 cm, and 5 cm away from tumor were measured by FTIR spectroscopy. FTIR spectra of colorectal cancer and mucosa 1 cm away from tumor were different from those of mucosa 2 cm and 5 cm away from tumor. According to the analysis of FTIR spectrometry, the decrease of lipid and the increase of protein and nucleic acid were observed in the former two sites. FTIR spectrometry, therefore, may be developed into a rapid promising method for judging surgical resection margin of colorectal cancer.

## 1. Introduction

Colorectal cancer is a disease with a major worldwide burden. It is the fourth most common malignancy with 1.2 million people developing colorectal cancer annually, and it is also the third most common cause of cancer death in the world, responsible for 0.6 million deaths annually [1, 2]. Surgical resection is one of the most important methods in the treatment of colorectal cancer. The range of surgical removal was directly related to the postoperative recovery and long-term survival outcomes of the patient. If the resection range is too small, it may lead to tumor recurrence after operation and influence the patient's long-term survival. And a beyond range of resection may lead to longer duration of postoperative recovery, even surgical complications. Therefore the determination of resection range is one of the core issues in the operation, and the safety of the distal and proximal resection margins of bowel should be ensured. Intraoperative pathological examination of frozen section is the most common method for checking the cutting edge,

which usually takes about 40 minutes one time. For some patients difficult to diagnose, it may need to be taken for pathological examination several times in the operation. It will prolong the operation time and cause adverse effect on the recovery of patients after operation.

Fourier transform infrared (FTIR) spectrometry provides abundant information concerning the variation of biological tissues at molecular level, so this approach may be developed as a new method for cancer diagnosis [3–9]. Meanwhile, less time is needed for each FTIR measurement, which takes approximately one to three minutes. In this paper, we perform a pilot study on the determination of surgical resection margin during the operation of colorectal cancer by using FTIR spectroscopic method coupled with optical fiber and attenuated total reflection probe. The aim of the present study is to develop a new method of FTIR spectroscopy as an intraoperative, rapid, and nondestructive diagnosing tool, which could determine the safety of resection margins in the colorectal cancer surgery.

## 2. Materials and Methods

**2.1. Samples Collections.** The study was approved ethically by Institutional Review Board of Peking University Third Hospital. All fourteen patients were fully informed with written consent. Fourteen fresh colorectal cancer specimens of radical resection were obtained from the Department of General Surgery in Peking University Third Hospital. In the operation room fresh samples were collected within five minutes after the colorectal specimens were removed. In each specimen four sites of fresh samples were obtained, which were shown in Figure 1 and recorded as Part A (tumor sample), Part B (intestinal mucosa sample 1 cm away from the tumor), Part C (intestinal mucosa sample 2 cm away from the tumor), and Part D (intestinal mucosa sample 5 cm away from the tumor). Fifty-six fresh samples were collected in this study.

Each sample was divided into two parts, approximately  $0.5\text{ cm} \times 0.5\text{ cm}$  in size for each part. One was used for FTIR spectroscopic studies without any special sample premanagement. And the other part was processed as paraffin embedded blocks and sent to pathologists for pathological diagnosis.

**2.2. Instrument.** A WQF-660 FTIR spectrometer (Beijing Rayleigh Analytical Instrument Corporation, Beijing, China) equipped with a liquid nitrogen-cooled mercury cadmium telluride detector and an attenuated total reflectance (ATR) probe was used in this work. Freshly removed tissue was put on the ATR probe to collect FTIR spectrum. During the experiment, 32 scans were coadded to achieve an acceptable signal-to-noise ratio, with wavenumber ranging from  $4000\text{ cm}^{-1}$  to  $1000\text{ cm}^{-1}$ . All the spectra were recorded at a resolution of  $4\text{ cm}^{-1}$ .

**2.3. Data Processing and Statistics.** FTIR spectra were measured using OMNIC E.S.P. 5.0 software (Nicolet Instrument Co., Madison, WI, USA). The following FTIR parameters were obtained: peak positions, full width at half maximum, and intensities, from which the relative intensity ratios were calculated. The above peak parameters were analyzed by using SPSS (version 17.0, SPSS Inc., Chicago, IL, USA), and normal distribution tests were performed in all parameters. For the normal distributed parameters, paired  $t$ -test was adopted. For the nonnormal distributed parameters, Wilcoxon paired signed-rank test was performed.  $p \leq 0.05$  was considered statistically different.

## 3. Results and Discussion

**3.1. Pathological Results.** Pathological examinations with hematoxylin and eosin (H&E) staining were performed in all fifty-six samples. Adenocarcinomas were observed in all fourteen samples obtained in Part A and two samples in Part B. Adenocarcinomas were absent in the other twelve samples in Part B and all samples in Part C and Part D.

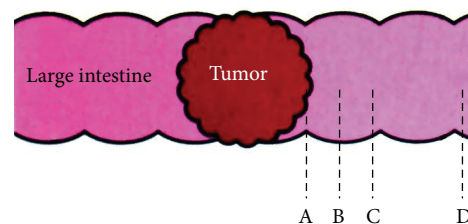


FIGURE 1: The schematic diagram of specimen of colorectal cancer removed and the samples obtained from four parts (Part A: tumor sample, Part B: intestinal mucosa sample 1 cm away from the tumor, Part C: intestinal mucosa sample 2 cm away from the tumor, and Part D: intestinal mucosa sample 5 cm away from the tumor).

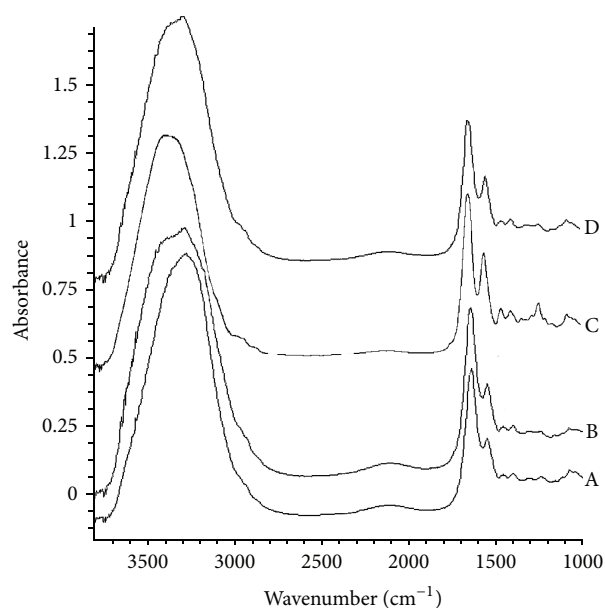


FIGURE 2: FTIR spectra of four samples from Parts A, B, C, and D, with wavenumber ranging from  $3800\text{ cm}^{-1}$  to  $1000\text{ cm}^{-1}$ .

TABLE 1: Preliminary assignments of Fourier transform infrared bands in colorectal cancer and mucosa.

Wavenumber/ $\text{cm}^{-1}$	Preliminary assignment
3275	$\nu_{\text{O-H}}, \nu_{\text{N-H}}$ (water, protein)
2925	$\nu_{\text{as}}, \text{CH}_3$ (lipid)
2855	$\nu_{\text{as}}, \text{CH}_2$
1740	$\nu_{\text{C=O}}$ (lipid)
1640	Amide I band (protein)
1550	Amide II band (protein)
1460	$\delta_{\text{C-H}}$ (lipid)
1400	$\delta_{\text{C-H}}, \delta_{\text{C-O-H}}$ (lipid)
1303	$\delta_{\text{C-H}}, \delta_{\text{C-O-H}}$ , and amide III band
1240	$\delta_{\text{as}}, \text{PO}_2^-$ (nucleic acid)
1160	$\nu_{\text{C-O}}, \delta_{\text{C-O-H}}$ , and $\delta_{\text{C-O-C}}$ (carbohydrate)
1120	$\nu_{\text{C-O}}, \delta_{\text{C-O-H}}$ , and $\delta_{\text{C-O-C}}$ (carbohydrate)
1083	$\nu_s \text{PO}_2^-$ (nucleic acid)

TABLE 2: FTIR spectrum comparisons of Parts A, B, C, and D (*t*-test results).

Variable	Part A		Part B		Part C		Part D		<i>t</i> ( <i>t'</i> )	<i>p</i>
	<i>n</i>	Mean $\pm$ SD	<i>n</i>	Mean $\pm$ SD	<i>n</i>	Mean $\pm$ SD	<i>n</i>	Mean $\pm$ SD		
<i>I</i> / <i>I</i>										
<i>I</i> <sub>1550</sub> / <i>I</i> <sub>1080</sub>	14	5.25 $\pm$ 1.26	14	5.43 $\pm$ 1.03	14	6.83 $\pm$ 1.34	14	6.56 $\pm$ 0.89	-2.631	0.001**
<i>I</i> <sub>1550</sub> / <i>I</i> <sub>1460</sub>	14	5.93 $\pm$ 1.42	14	5.60 $\pm$ 1.35	14	4.84 $\pm$ 1.08	14	4.67 $\pm$ 1.20	2.216	0.041*
<i>I</i> <sub>1080</sub> / <i>I</i> <sub>1460</sub>	14	1.08 $\pm$ 0.43	14	0.95 $\pm$ 0.33	14	0.65 $\pm$ 0.27	14	0.71 $\pm$ 0.22	2.095	0.036*

*I* stands for the intensity of band; \*  $p < 0.05$ ; \*\*  $p < 0.01$ .

TABLE 3: FTIR spectrum comparisons of Parts A, B, C, and D (*rank-sum* results).

Variable	Part A		Part B		Part C		Part D		<i>Z</i>	<i>p</i>
	<i>n</i>	Median	<i>n</i>	Median	<i>n</i>	Median	<i>n</i>	Median		
<i>P</i> /cm <sup>-1</sup>										
<i>P</i> <sub>2925</sub>	14	2918.3	14	2919.0	14	2927.2	14	2926.4	-2.358	0.023*
<i>P</i> <sub>1080</sub>	14	1083.80	14	1083.8	14	1079.9	14	1078.40	-2.179	0.032*
<i>I</i> / <i>I</i>										
<i>I</i> <sub>1740</sub> / <i>I</i> <sub>1460</sub>	14	0.42	14	0.44	14	0.55	14	0.51	-1.074	0.065

*P* stands for the peak position of band; *I* stands for the intensity of band; \*  $p < 0.05$ .

**3.2. Spectra Analysis.** There are 56 FTIR spectra obtained from 14 specimens. Four spectra of samples from one specimen were shown in Figure 2. In every spectrum, thirteen bands can be observed and the assignments of these bands are given in Table 1. After comparison, we found that the FTIR spectra from Part A of the 14 samples are similar to the corresponding FTIR spectra from Part B. FTIR spectra from Part C of the 14 samples are similar to the corresponding FTIR spectra from Part D. The differences between the four groups are shown in Tables 2 and 3.

**3.3. The Variation of Infrared Bands Related to Lipid Contents among Different Parts of the Specimen.** The vibration bands near 2925, 2855, 1740, 1460, and 1400 cm<sup>-1</sup> were all related to lipid in the samples. The peaks around 2925 cm<sup>-1</sup> in FTIR spectra of Part A and Part B undergo red shift in comparison with those in Part C and Part D ( $p = 0.023$ ). The relative intensity of the 1740 cm<sup>-1</sup> band to 1460 cm<sup>-1</sup> absorption peak decreased in the spectra of Part A and Part B than in those in Part C and Part D ( $p = 0.065$ ). The above results demonstrate that the lipid contents in Part A and Part B are less than those in Part C and Part D. According to the literature, the decrease of lipid bands in malignant part of tissues is related to the decrease of the content of fat. Two reasons may account for the decrease of fat in malignant tissues: normal tissues, including fat cells, are excluded by the proliferating malignant tissue in the growth of the tumor. Thus, less fat cells were found. The fat in the region of the malignant tissue is consumed because of the necessary increased nutritional and energy requirement in the development of the cancer [10].

**3.4. The Variation of Infrared Bands Related to Protein among Different Parts of the Specimen.** 1640 cm<sup>-1</sup> absorption peak belongs to amide I band of protein and H-O-H deformation

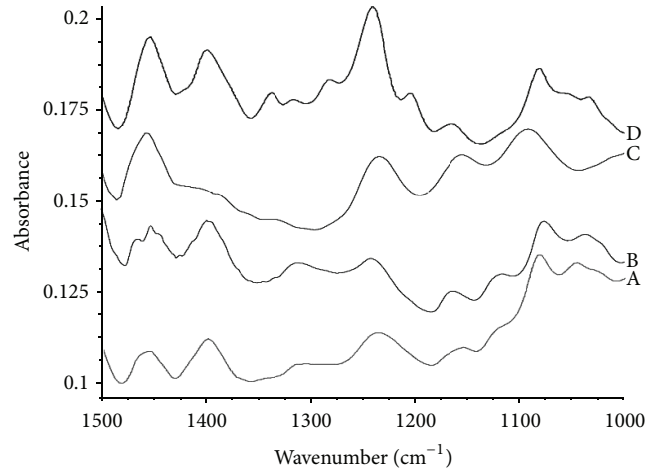


FIGURE 3: FTIR spectra of four samples from Parts A, B, C, and D, with wavenumber ranging from 1500 cm<sup>-1</sup> to 1000 cm<sup>-1</sup>.

vibration of water. 1550 cm<sup>-1</sup> absorption peak arises from N-H bending and C-N stretching (amide II band) in proteins which may be related to the  $\alpha$ -helix substructure of the protein. The relative intensity of the 1550 cm<sup>-1</sup> band to 1080 cm<sup>-1</sup> absorption peak decreases in the malignant tissue ( $p = 0.001$ ). This may be caused by the increase of the nucleic acid or the decrease of the  $\alpha$ -helix substructure of the protein in Part A and Part B. The ratio of the intensity of 1550 cm<sup>-1</sup> peak to 1460 cm<sup>-1</sup> peak was much higher in the spectra of Parts A and B than that in parts C and D ( $p = 0.041$ ). This means that more protein is contained in the malignant tissue, which is produced from the faster cell metabolism [11].

**3.5. The Variation of Infrared Bands Related to Nucleic Acid among Different Parts of the Specimen.** 1240 cm<sup>-1</sup> band

belongs to the symmetric P=O stretching band ( $\nu_s(\text{P=O})$ ).  $1080\text{ cm}^{-1}$  peak is assigned to the P–O–C stretching band ( $\nu(\text{P–O–C})$ ). Blue shift of the  $1080\text{ cm}^{-1}$  peak is observed in the spectra of Parts A and B in comparison with that in parts C and D ( $p = 0.032$ ). The cell division during the reproduction of the tumor proceeds in an abnormal way and the structure of the nucleic acid may change. Thus the position of  $1080\text{ cm}^{-1}$  peak in the spectra of Parts A and B undergoes blue shift. As shown in Figure 3, the ratio of the intensity of  $1080\text{ cm}^{-1}$  peak to  $1460\text{ cm}^{-1}$  peak was higher in the spectra of Parts A and B than that in Parts C and D ( $p = 0.036$ ). This means that the relative content of nucleic acid to lipid increases in Parts A and B than that in Parts C and D. The reason is that tumor cell proliferation is faster in the malignant tissue; thus more nucleic acid is produced [12].

#### 4. Conclusions

It can be concluded that FTIR spectra of colorectal cancer and mucosa 1 cm away from tumor were different from those of mucosa 2 cm and 5 cm away from tumor. FTIR spectra of colorectal cancer and mucosa 1 cm away from tumor were different from those of mucosa 2 cm and 5 cm away from tumor. According to the analysis of FTIR spectrometry, the decrease of lipid and the increase of protein and nucleic acid were observed in tumor and tumor surrounding area within 1 cm. FTIR spectrometry, therefore, may be developed into a rapid promising method for judging surgical resection margin of colorectal cancer.

#### Conflict of Interests

The authors declare that there is no conflict of interests regarding the publication of this paper.

#### Acknowledgment

This work was supported by the Foundation of Beijing Excellent Talent Training Project (Project no. 2010D009001000-005).

#### References

- [1] A. Jemal, F. Bray, M. M. Center, J. Ferlay, E. Ward, and D. Forman, "Global cancer statistics," *CA Cancer Journal for Clinicians*, vol. 61, no. 2, pp. 69–90, 2011.
- [2] R. Siegel, D. Naishadham, and A. Jemal, "Cancer statistics," *A Cancer Journal for Clinicians*, vol. 63, no. 1, pp. 11–30, 2013.
- [3] M. J. Walsh, M. J. German, M. Singh et al., "IR microspectroscopy: potential applications in cervical cancer screening," *Cancer Letters*, vol. 246, no. 1-2, pp. 1–11, 2007.
- [4] J.-G. Wu, Y.-Z. Xu, C.-W. Sun et al., "Distinguishing malignant from normal oral tissues using FTIR fiber-optic techniques," *Biopolymers*, vol. 62, no. 4, pp. 185–192, 2001.
- [5] C. Petibois and G. Dél  ris, "Chemical mapping of tumor progression by FT-IR imaging: towards molecular histopathology," *Trends in Biotechnology*, vol. 24, no. 10, pp. 455–462, 2006.
- [6] H.-W. Yao, Y.-Q. Liu, W. Fu, X.-Y. Shi, Y.-F. Zhang, and Y.-Z. Xu, "Initial research on Fourier transform infrared spectroscopy for the diagnosis of colon neoplasms," *Spectroscopy and Spectral Analysis*, vol. 31, no. 2, pp. 297–301, 2011.
- [7] N. Fujioka, Y. Morimoto, T. Arai, and M. Kikuchi, "Discrimination between normal and malignant human gastric tissues by Fourier transform infrared spectroscopy," *Cancer Detection and Prevention*, vol. 28, no. 1, pp. 32–36, 2004.
- [8] Q.-B. Li, X.-J. Sun, Y.-Z. Xu et al., "Diagnosis of gastric inflammation and malignancy in endoscopic biopsies based on fourier transform infrared spectroscopy," *Clinical Chemistry*, vol. 51, no. 2, pp. 346–350, 2005.
- [9] X.-X. Gao, H.-W. Yao, J.-K. Du et al., "Study on malignant and normal rectum tissues using IR and  $^1\text{H}$  and  $^{31}\text{P}$  NMR spectroscopy," *Spectroscopy and Spectral Analysis*, vol. 29, no. 4, pp. 969–973, 2009.
- [10] H. H. Mantsch and D. Chapman, *Infrared Spectroscopy of Biomolecules*, Wiley-Liss, New York, NY, USA, 1996.
- [11] D. Naumann, "FT-infrared and FT-Raman spectroscopy in biomedical research," in *Infrared and Raman Spectroscopy of Biological Materials*, practical Spectroscopy, H.-U. Gremlich and B. Yan, Eds., Marcel Dekker, New York, NY, USA, 2001.
- [12] S. C. Van't Westeinde and R. J. Van Klaveren, "Screening and early detection of lung cancer," *Cancer Journal*, vol. 17, no. 1, pp. 3–10, 2011.



## Research Article

# Assessment of the Inhibitory Effect of Rifampicin on Amyloid Formation of Hen Egg White Lysozyme: Thioflavin T Fluorescence Assay versus FTIR Difference Spectroscopy

Gang Ma, Hong Zhang, Jianhua Guo, Xiaodan Zeng, Xiaoqian Hu, and Wenying Hao

*Key Laboratory of Medicinal Chemistry and Molecular Diagnosis of Ministry of Education,  
College of Chemistry and Environmental Science, Hebei University, Baoding 071002, China*

Correspondence should be addressed to Gang Ma; [gma.hbu@gmail.com](mailto:gma.hbu@gmail.com)

Received 6 September 2013; Revised 31 October 2013; Accepted 14 December 2013; Published 6 January 2014

Academic Editor: Yizhuang Xu

Copyright © 2014 Gang Ma et al. This is an open access article distributed under the Creative Commons Attribution License, which permits unrestricted use, distribution, and reproduction in any medium, provided the original work is properly cited.

The inhibitory effect of rifampicin on the amyloid formation of hen egg white lysozyme was assessed with both Thioflavin T (ThT) fluorescence assay and Fourier transform infrared (FTIR) difference spectroscopy. We reveal that ThT fluorescence assay gives a false positive result due to rifampicin interference, while FTIR difference spectroscopy provides a reliable assessment. With FTIR, we show that rifampicin only has marginally inhibitory effect. We then propose that FTIR difference spectroscopy can potentially be a convenient method for inhibitor screening in amyloid study.

## 1. Introduction

Amyloid aggregates are insoluble protein aggregates with the characteristic cross- $\beta$  structure and fibrous morphology [1]. In vivo, amyloid deposition is a pathological hallmark of more than 40 neurodegenerative, systemic, and nonsystemic diseases [2]. These human diseases, collectively termed as amyloid diseases, include some well-known disorders such as Alzheimer's disease, Parkinson's disease, and Type II diabetes. Each of these diseases is associated with amyloid fibrillation of one unique type of protein or peptide [2]. The apparent linkage between amyloid formation and amyloid disease makes designing and developing molecular interventions into amyloid formation an attractive strategy to prevent and treat amyloid diseases [3].

Amyloid formation is a rather complex protein aggregation process. The aggregation kinetic curve usually follows a typical sigmoidal function featuring a lag phase, a growth phase, and an equilibrium phase [4]. Furthermore, there can be oligomeric intermediates in diverse sizes and morphologies. These intermediate oligomers have been referred to in numerous ways as amorphous aggregates, protofibrils, prefibrillar aggregates, globulomers, and annular protofibrils [5]. Both mature fibril and nonfibrillar oligomers have been

hypothesized to be the possible pathogenic agents in amyloid diseases [3].

As amyloid fibril has been hypothesized to be one of the pathogenic agents in amyloid diseases [3], searching molecules that can inhibit amyloid fibrillation has been one of the major research efforts in the field of amyloid research. Rifampicin is an antibiotic which has been found to be able to inhibit amyloid formation of numerous proteins such as amyloid- $\beta$ ,  $\alpha$ -synuclein, islet amyloid polypeptide (IAPP), and hen egg white lysozyme (HEWL) [6–9]. However, the general picture of the inhibitory effect of rifampicin on amyloid formation has been challenged in recent years. Meng et al. reported that rifampicin in fact had no inhibitory effect on the amyloid formation of IAPP, contrary to previous observation [10]. They demonstrated that the apparent inhibitory effect was simply due to the false positive result of Thioflavin T (ThT) fluorescence assay caused by rifampicin interference. The discovery by Meng et al. clearly demonstrates that the effect of rifampicin on the amyloid formation is a rather complicated issue and there is no general answer with respect to the actual role of rifampicin during amyloid formation. In this study, we would like to reexamine the inhibitory effect of rifampicin on the amyloid fibrillation of HEWL by using HEWL as a model amyloidogenic system. HEWL is not

a protein which is directly relevant to amyloid disease, yet it is a widely used model protein in amyloid study due to its low cost. Our aim in this study is threefold. (1) Can rifampicin really inhibit the amyloid formation of HEWL? (2) Does rifampicin interfere with ThT assay in the HEWL system? (3) If the ThT assay is problematic in inhibitor screening, can we find another convenient way to accurately assess the effect of rifampicin?

## 2. Material and Methods

**2.1. Materials.** Hen egg white lysozyme (HEWL) with a purity of  $\geq 90\%$  (catalog number L6876) was obtained from Sigma-Aldrich (Saint Louis, USA). Deuterium oxide ( $D_2O$ ) with  $>99.8\%$  purity was obtained from J&K Chemical (Beijing, China). Sodium chloride with  $>99\%$  purity was obtained from Sigma-Aldrich. Deuterium chloride (DCl) (35% by weight in  $D_2O$ ) was obtained from Sigma-Aldrich. Sodium azide ( $NaN_3$ ) with a purity of 99% was purchased from Tianjin Chemical Plant (Tianjin, China). Rifampicin was obtained from Yuanye (Shanghai, China). All materials are used without further purification.

**2.2. Sample Preparations.** HEWL solution in  $D_2O$  (pD = 2) containing 140 mM NaCl and 200 ppm  $NaN_3$  was used for fibrillation study. Solution pH was adjusted using DCl solution in  $D_2O$  to reach a pH meter reading of 1.6 (pD = pH reading + 0.4). The HEWL solution was first passed through a  $0.22 \mu m$  filter before incubation. Rifampicin was first dissolved into  $D_2O$  (pD = 2) to make a concentrated solution of 7 mM. This solution was then used to make HEWL-rifampicin mixture solution. In this study, the concentration of HEWL was 5 mg/mL and the concentration of rifampicin was  $400 \mu M$ . The concentration of HEWL was determined by weighing and the concentration of rifampicin was determined with UV-Vis spectroscopy with the reported extinction coefficient of  $28000 M^{-1} \cdot cm^{-1}$  at 334 nm [11]. The HEWL and HEWL-rifampicin solutions in sealed glass vials were incubated in a thermoshaker at  $62^\circ C$  without agitation. Whenever necessary, aliquots will be taken out of the incubation vial for ThT fluorescence, Fourier transform infrared (FTIR), and atomic force microscopy (AFM) characterizations. Care was always taken to avoid light exposure to the incubation vials.

**2.3. ThT Fluorescence Assay.** ThT fluorescence assay was performed with a Hitachi F-7000 fluorescence spectrophotometer. An excitation wavelength of 450 nm with a slit width of 5 nm and an emission wavelength of 486 nm with a slit width of 10 nm were used. The voltage of photomultiplier tube was set to 700 V. The concentration of ThT solution is  $10 \mu M$ . The buffer is 20 mM phosphate buffer at pH = 7.4. The assay was performed ex situ. To measure fibrillation kinetics, aliquots of HEWL incubation solutions without or with rifampicin were taken out of the incubation vial at different time-points and were subjected to the assay immediately. For each measurement,  $40 \mu L$  of incubation solution was added into  $960 \mu L$  of ThT solution in a 1.0 cm quartz cuvette. The solution in the cuvette was shaken first before running

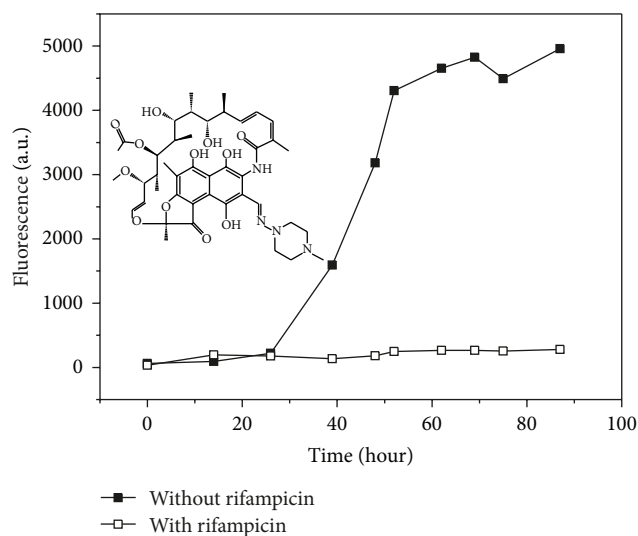


FIGURE 1: Effect of rifampicin on the fibrillation of HEWL by ThT fluorescence assay. Inset: molecular structure of rifampicin.

each acquisition. For rifampicin interference experiment,  $40 \mu L$  of incubation solution was added into  $960 \mu L$  of ThT solution in a 1.0 cm quartz cuvette first to obtain an initial ThT fluorescence reading at 486 nm. Then  $1.5 \mu L$  of 7 mM rifampicin solution was injected into the above solution and the change of ThT fluorescence reading at 486 nm over time was recorded.

**2.4. AFM Measurement.** All the AFM images were taken on dried samples in air with NT-MDT Solver P47 Scanning Probe Microscope (Zelenograd, Russia) in tapping mode. A  $90 \mu m \times 90 \mu m$  scanner was used throughout the AFM experiment. The silicon cantilevers were purchased from NT-MDT. The cantilever has a resonance frequency of 100 kHz and a nominal force constant of 3 N/m. The samples for AFM measurement were prepared using the following method:  $10 \mu L$  incubation solution was diluted 100 times with deionized water (Millipore, Billerica, USA) and then  $100 \mu L$  of the diluted solution was dropped onto freshly cleaved mica. After 10 min waiting time, the protein solution was rinsed off with deionized water. The mica surface was then left dry under ambient condition.

**2.5. FTIR Measurement.** The FTIR spectra were obtained at room temperature with a Bruker Vertex 70 FTIR spectrometer (Bruker, Germany) equipped with a DLaTGS detector. The sample compartment was constantly purged with dry air from a home-made purge system to minimize water vapor interference. A demountable liquid cell with a pair of  $CaF_2$  windows and a  $50 \mu m$  spacer was utilized. Spectra were collected with a spectral resolution of  $4 cm^{-1}$  and 128 scans. FTIR data processing was performed with OPUS software (Bruker, Germany). Prior hydrogen-deuterium (H/D) exchange on the HEWL was not performed before incubation in order to minimize structural perturbation on the protein. When HEWL in  $D_2O$  solution was incubated at  $62^\circ C$ ,

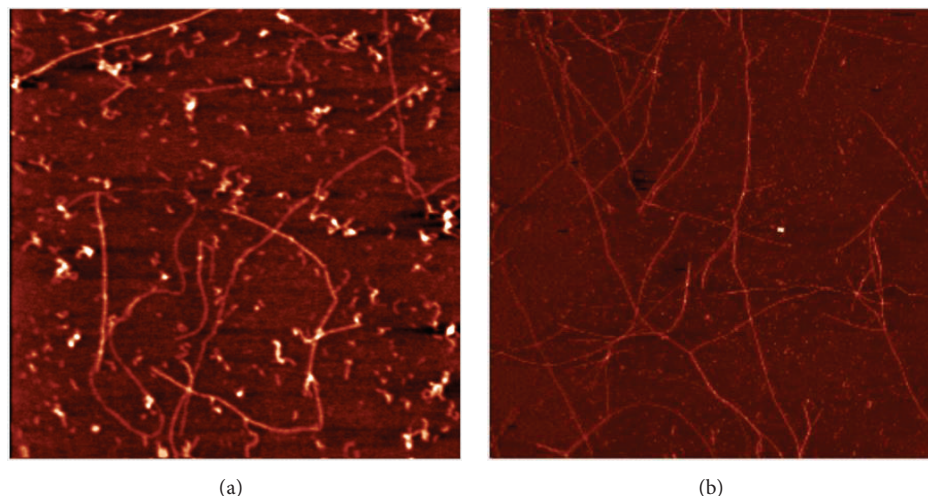


FIGURE 2: AFM characterization of HEWL fibrillation (a) without rifampicin in the incubation solution and (b) with rifampicin in the incubation solution. Scan size:  $5\ \mu\text{m} \times 5\ \mu\text{m}$ .

the peptide backbone became fully deuterated during the lag phase as evidenced by the disappearance of the amide I band at  $1540\ \text{cm}^{-1}$  after 5 h incubation [12]. Residual  $\text{H}_2\text{O}$  in the overwhelming  $\text{D}_2\text{O}$  forms HOD and has negligible effect on the spectral analysis in the amide I region.

### 3. Results and Discussion

We first use ThT fluorescence assay to investigate the inhibitory effect of rifampicin on the amyloid formation of HEWL. The ThT assay is the standard method to quantify the growth of fibrillar aggregates during amyloid formation [13, 14]. ThT, as an extrinsic fluorescent probe molecule, once binding to amyloid fibrils, gives a characteristic fluorescent emission at  $\sim 480\ \text{nm}$  with  $\sim 440\ \text{nm}$  excitation. The intensity of ThT fluorescence is hypothesized to be proportional to the amount of amyloid fibrils. We here perform a comparative study on HEWL fibrillation without and with the presence of rifampicin in the incubation solution at  $\text{pD} = 2$  and  $62^\circ\text{C}$  with the ThT assay. The heat and acidic condition are the standard conditions to induce fibril formation of HEWL [15]. At selected time-points, aliquots of incubation solution were taken out of the incubation vial for fluorescence measurements. The ThT assay results of this comparative study are shown in Figure 1. The fibrillation kinetic curve of HEWL without the influence of rifampicin shows a typical sigmoidal shape, featuring a lag phase, a growth phase, and an equilibrium phase. However, the fibrillation kinetic curve of HEWL under the influence of rifampicin is basically at the baseline level. A simple comparison between the two kinetic curves clearly suggests that rifampicin completely inhibited the fibrillation of HEWL under the current experimental conditions.

As already mentioned above, Meng et al. have shown that rifampicin could interfere with ThT assay. In fact, Hudson et al. also pointed out that ThT assay could be biased by exogenous compounds [16]. Therefore, to confirm the inhibitory

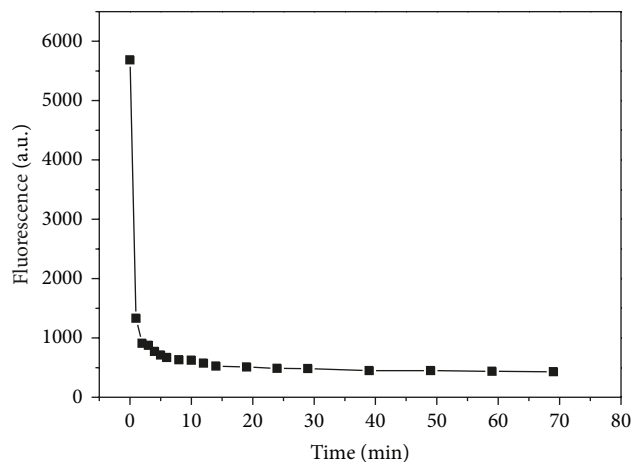


FIGURE 3: Fluorescence intensity decay of ThT upon the addition of rifampicin.

effect of rifampicin observed in the above ThT fluorescence investigation, we characterized the HEWL incubation solutions without and with rifampicin using AFM to see whether there are fibrillar aggregates present or not. Figure 2 gives the AFM results for HEWL incubation solutions with and without rifampicin. Surprisingly, on both of the samples, extensive presence of fibrillar aggregates was observed under AFM. This means that the AFM results do not support the conclusion that we drew based on ThT assay.

To explore the cause of the above conflicting evidences from ThT assay and AFM study, we performed the following experiments with fluorescence spectroscopy. We first added ThT into the solution containing HEWL fibrils and obtained the initial ThT fluorescence reading. Then, we added rifampicin into the above mixture and began to monitor ThT fluorescence decay over time. As shown in Figure 3, upon addition of rifampicin, there is an instant drop in ThT

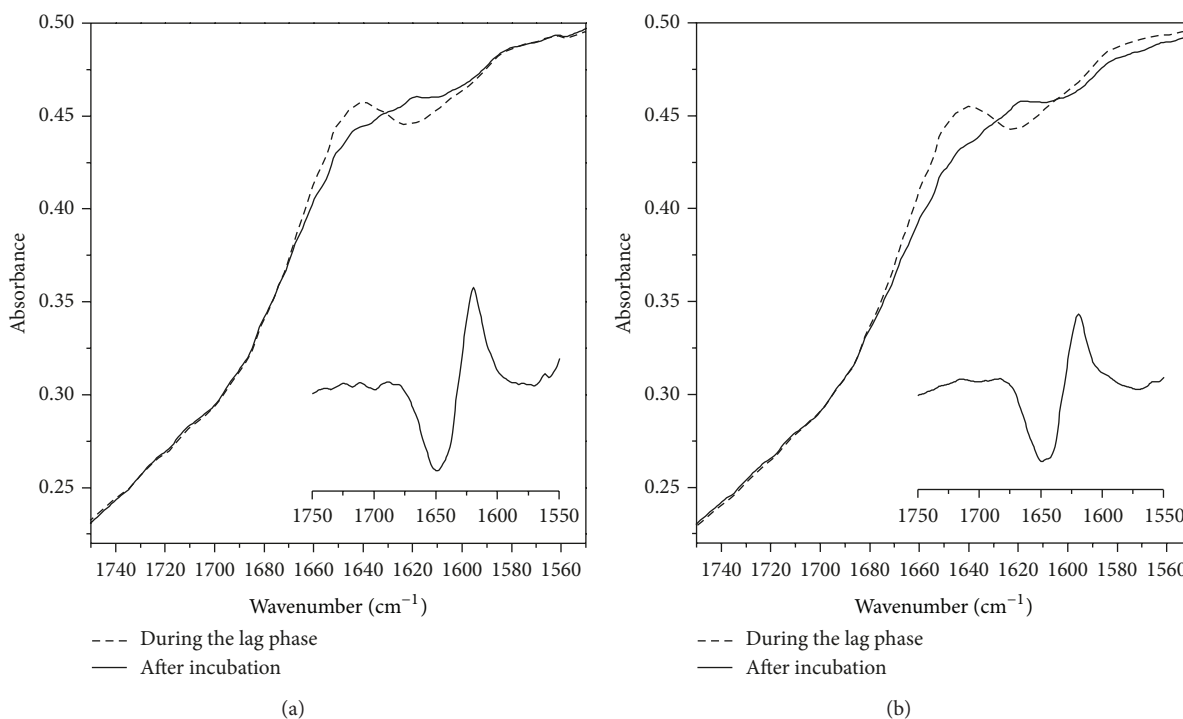


FIGURE 4: FTIR results for the inhibitory effect of rifampicin on HEWL fibrillation (a) without rifampicin in the incubation solution and (b) with rifampicin in the incubation solution. Dash line: raw spectrum taken during the lag phase; solid line: raw spectrum taken at the end of incubation. Inset: difference spectrum.

fluorescence intensity. Obviously, the presence of rifampicin interferes with ThT assay. The exact cause of this ThT intensity drop surely deserves future investigations, but it should be due to either quenching effect or rifampicin competition against ThT on available binding sites. Because of the interference of rifampicin, ThT assay cannot be used as a reliable method to evaluate the actual effect of rifampicin on HEWL fibrillation.

As ThT assay could give misleading false positive results, it is beneficial to search for alternative convenient methods for inhibitor screening. We would like to explore the feasibility of FTIR difference spectroscopy as an alternative inhibitor screening method. FTIR is a conformation sensitive technique due to the fact that each protein secondary structure has its unique infrared absorption in the  $1700\text{--}1600\text{ cm}^{-1}$  amide I region [17]. This means that the growth of cross- $\beta$  structure during amyloid formation can be easily monitored and quantified with FTIR difference spectroscopy. In addition, as FTIR is a label free method and directly detects the  $\beta$ -sheet structures, it is basically immune to the interference of exogenous compounds such as rifampicin.

We performed two sets of FTIR measurements under identical conditions to explore the exact effect of rifampicin on the amyloid formation of HEWL. Figure 4(a) gives the raw spectra of HEWL incubation solution without the rifampicin presence taken during the lag phase and at the end of incubation. The difference spectrum between the two raw

spectra is also shown in the inset. It is obtained by subtracting the FTIR spectrum of the incubation solution taken during the lag phase (i.e., at 5 h time-point) from that taken at the end of incubation (i.e., at 90 h time-point). The existence of the  $1618\text{ cm}^{-1}$  peak in the difference spectrum is a direct indicator for the presence of amyloid fibril [12]. The intensity of this peak is directly proportional to the amount of HEWL fibril. Figure 4(b) gives the raw spectra of HEWL incubation solution with the rifampicin presence taken during the lag phase and at the end of incubation. The difference spectrum between the two raw spectra is also shown in the inset. The existence of the  $1618\text{ cm}^{-1}$  peak shows that there is amyloid fibril presence even under the influence of rifampicin. This observation is consistent with the observation in the AFM study but contrary to the false positive result from ThT assay. Furthermore, we found that the intensity of the  $1618\text{ cm}^{-1}$  fibril peak in the difference spectrum in Figure 4(b) is only slightly lower than that of the control shown in Figure 4(a). This supports the argument that rifampicin only marginally inhibits the amyloid formation of HEWL.

Clearly, Figure 4 gives a proof-of-concept example to support the proposal that FTIR difference spectroscopy can be used as an alternative inhibitor screening method. Certainly the FTIR assay used here still needs further optimizations in future studies. For example, the current transmission mode FTIR spectroscopy can be replaced with attenuate total reflection (ATR) mode FTIR spectroscopy. This can make



sample handling and spectral subtraction more user-friendly. In addition, a high throughput FTIR accessory needs to be developed to make large-scale screening feasible.

#### 4. Conclusions

In conclusion, we evaluated the inhibitory effect of rifampicin on the amyloid formation of hen egg white lysozyme (HEWL) with both ThT fluorescence assay and FTIR difference spectroscopy. Our results indicate that ThT assay is not a reliable assessment method as rifampicin interferes with such assay. Unlike ThT assay, FTIR difference spectroscopy directly monitors the growth of  $\beta$ -sheet structures during amyloid formation; thus, can be an accurate approach to evaluate the effect of rifampicin. With FTIR difference spectroscopy, we showed that rifampicin only had marginally inhibitory effect. We then proposed that FTIR difference spectroscopy can potentially be used as a convenient method for inhibitor screening in amyloid study.

#### Conflict of Interests

The authors declare that there is no conflict of interests regarding the publication of this paper.

#### Acknowledgments

The authors gratefully acknowledge the financial support from the National Natural Science Foundation of China (no. 21075027), the Natural Science Foundation of Hebei Province (no. B2011201082), the Key Project of Chinese Ministry of Education (no. 211014), and the Specialized Research Fund for the Doctoral Program of Higher Education (20121301110003).

#### References

- [1] M. R. Sawaya, S. Sambashivan, R. Nelson et al., "Atomic structures of amyloid cross- $\beta$  spines reveal varied steric zippers," *Nature*, vol. 447, no. 7143, pp. 453–457, 2007.
- [2] F. Chiti and C. M. Dobson, "Protein misfolding, functional amyloid, and human disease," *Annual Review of Biochemistry*, vol. 75, pp. 333–366, 2006.
- [3] P. T. Lansbury and H. A. Lashuel, "A century-old debate on protein aggregation and neurodegeneration enters the clinic," *Nature*, vol. 443, no. 7113, pp. 774–779, 2006.
- [4] J. D. Harper and P. T. Lansbury Jr., "Models of amyloid seeding in Alzheimer's disease and scrapie: mechanistic truths and physiological consequences of the time-dependent solubility of amyloid proteins," *Annual Review of Biochemistry*, vol. 66, pp. 385–407, 1997.
- [5] C. G. Glabe, "Structural classification of toxic amyloid oligomers," *The Journal of Biological Chemistry*, vol. 283, no. 44, pp. 29639–29643, 2008.
- [6] T. Tomiyama, S. Asano, Y. Suwa et al., "Rifampicin prevents the aggregation and neurotoxicity of amyloid  $\beta$  protein in vitro," *Biochemical and Biophysical Research Communications*, vol. 204, no. 1, pp. 76–83, 1994.
- [7] J. Li, M. Zhu, S. Rajamani, V. N. Uversky, and A. L. Fink, "Rifampicin inhibits  $\alpha$ -synuclein fibrillation and disaggregates fibrils," *Chemistry and Biology*, vol. 11, no. 11, pp. 1513–1521, 2004.
- [8] J. J. Meier, R. Kayed, C.-Y. Lin et al., "Inhibition of human IAPP fibril formation does not prevent  $\beta$ -cell death: evidence for distinct actions of oligomers and fibrils of human IAPP," *American Journal of Physiology: Endocrinology and Metabolism*, vol. 291, no. 6, pp. E1317–E1324, 2006.
- [9] V. H. Lieu, J. W. Wu, S. S.-S. Wang, and C.-H. Wu, "Inhibition of amyloid fibrillization of hen egg-white lysozymes by rifampicin and p-benzoquinone," *Biotechnology Progress*, vol. 23, no. 3, pp. 698–706, 2007.
- [10] F. Meng, P. Marek, K. J. Potter, C. B. Verchere, and D. P. Raleigh, "Rifampicin does not prevent amyloid fibril formation by human islet amyloid polypeptide but does inhibit fibril thioflavin-T interactions: implications for mechanistic studies of  $\beta$ -cell death," *Biochemistry*, vol. 47, no. 22, pp. 6016–6024, 2008.
- [11] K. P. Kumar and D. Chatterji, "Resonance energy transfer study on the proximity relationship between GTP binding site and the rifampicin binding site of *Escherichia coli* RNA polymerase," *Biochemistry*, vol. 29, no. 2, pp. 317–322, 1990.
- [12] Y. Zou, Y. Li, W. Hao, X. Hu, and G. Ma, "Parallel  $\beta$ -sheet fibril and antiparallel  $\beta$ -sheet oligomer: new insights into amyloid formation of hen egg white lysozyme under heat and acidic condition from ftir spectroscopy," *The Journal of Physical Chemistry B*, vol. 117, pp. 4003–4013, 2013.
- [13] H. LeVine III, "Quantification of  $\beta$ -sheet amyloid fibril structures with thioflavin T," *Methods in Enzymology*, vol. 309, pp. 274–284, 1999.
- [14] L. P. Jameson, N. W. Smith, and S. V. Dzyuba, "Dye-binding assays for evaluation of the effects of small molecule inhibitors on amyloid (a $\beta$ ) self-assembly," *ACS Chemical Neuroscience*, vol. 3, pp. 807–819, 2012.
- [15] R. Mishra, K. Sörgjerd, S. Nyström, A. Nordigården, Y.-C. Yu, and P. Hammarström, "Lysozyme amyloidogenesis is accelerated by specific nicking and fragmentation but decelerated by intact protein binding and conversion," *Journal of Molecular Biology*, vol. 366, no. 3, pp. 1029–1044, 2007.
- [16] S. A. Hudson, H. Ecroyd, T. W. Kee, and J. A. Carver, "The thioflavin T fluorescence assay for amyloid fibril detection can be biased by the presence of exogenous compounds," *FEBS Journal*, vol. 276, no. 20, pp. 5960–5972, 2009.
- [17] A. Barth and C. Zscherp, "What vibrations tell us about proteins," *Quarterly Reviews of Biophysics*, vol. 35, no. 4, pp. 369–430, 2002.



## Research Article

# The In Situ Polymerization and Characterization of PA6/LiCl Composites

Dandan Sun, Jiang Li, Qinghua Pan, Chaowei Hao, and Guoqiao Lai

Key Laboratory of Organosilicon Chemistry and Material Technology Ministry of Education, Hangzhou Normal University, Hangzhou 310012, China

Correspondence should be addressed to Chaowei Hao; [cwhao@hznu.edu.cn](mailto:cwhao@hznu.edu.cn)

Received 5 October 2013; Accepted 23 November 2013

Academic Editor: Yizhuang Xu

Copyright © 2013 Dandan Sun et al. This is an open access article distributed under the Creative Commons Attribution License, which permits unrestricted use, distribution, and reproduction in any medium, provided the original work is properly cited.

PA6/LiCl composites were synthesized by in situ anionic polymerization based on the interaction between the inorganic salts and PA6. Sodium hydroxide as initiator and N-acetylcaprolactam as activator were used in the preparation of PA6/LiCl composites with variety of LiCl content. X-ray diffraction (XRD) and differential scanning calorimeter (DSC) testing results showed that both of degree of crystallinity and melting temperature of the composites were decreased under the influence of LiCl. And the  $\gamma$  crystal phase proportion increased with increasing the LiCl content to appropriate amount.

## 1. Introduction

Polyamide is general thermoplastic resin with repeat amide groups—[NHCO]—on the molecular main chain, and it is commonly known as nylon. PA6 is a very common and important polymer material used in different fields ranging from textile and carpet production to special technical applications. The intramolecular polar amide group of PA6 can be found in hydrogen bond, increasing the intermolecular forces, and exhibiting relatively high strength, good toughness, chemical and abrasion resistance, and so forth. Nowadays, superfine fibers have attracted more and more attention from people for occupying the special properties, and the research on the superfine fibers is developing quickly [1]. However, the plenty of hydrogen bonding between chains in PA6, quickly crystal capacity, high crystallinity, and chain defects in the crystal lattice restrict the molecular arrangement and orientation, which hinders the achievement of higher DR during the PA6 spinning and the processing of the superfine fiber.

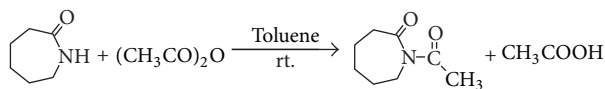
The studying emphasis of PA6 is always focusing on the modification in order to change the properties of polymer and be suitable for more applications [2–5]. There are many modification methods, which in general can be divided into blending, in situ polymerization, and copolymerization. As for in situ polymerization of PA6 composite, the acquired

composites are prepared by adding the modifier (polymer or inorganic particles) to the caprolactam molten monomer, then adding sodium hydroxide as initiator to open the ring, and introducing N-acetylcaprolactam as activators to a high-polymerization rate [6, 7]. This paper introduced the modification of PA6 and prepared a series of PA6/lithium chloride composite via in situ anionic polymerization. The characterization of the composites was carried out by FT-IR, NMR, DSC, and X-ray analysis methods.

## 2. Materials and Methods

**2.1. Materials.** Caprolactam, AR, Aladdin Chemistry Co., Ltd.; Sodium hydroxide, AR, Aladdin Chemistry Co., Ltd.; lithium chloride, AR, Tianjin University Chemical Reagent Factory; acetic anhydride, Shanghai Lingfeng Chemical Reagent Co., Ltd.

**2.2. The Preparation of N-Acetylcaprolactam (CCL).** N-Acetylcaprolactam can increase the electronegativity of amido bond and improve the amide carbonyl activity of caprolactam anion. Toluene was used as solvent in the preparation; the ratio of acetic anhydride and caprolactam was 1.2:1, then heating reflux for 2 h and extracting the unreacted acetic anhydride and the acetic acid with distilled water. The synthesis of CCL was shown in Scheme 1.



SCHEME 1: Synthesis of N-acetylcaprolactam.

**2.3. Synthesis of LiCl/PA6 Composites.** Lithium chloride which acted as modifier can interact with carbonyl group in caprolactam monomer and dissolve into the monomer, which means the well dispersed of modifier in the polymer composites. The experimental process was as follows: firstly, adding certain amount of caprolactam in a three-flask bottle and heating to 130°C under vacuum for 30 minutes to remove moisture and impurity in the system; secondly, quickly putting certain amount of lithium chloride into the bottle, keeping up the vacuum, and heating to 135°C at the same time until lithium chloride dissolved completely; thirdly, adding catalyzer sodium hydroxide into the melt mixture and heating to 140°C; fourthly, after catalyzing for 15 minutes, adding the activator (CCL) into the bottle fast; finally, pouring the melt mixture into a mold preheated at 180°C until the polymerization finished.

### 3. Results and Discussion

**3.1. The Characterization of N-Acetylcaprolactam (CCL).** The products were characterized by FT-IR and NMR, as shown in Figures 1 and 2.  $^1\text{H-NMR}$  ( $\text{CDCl}_3$ ,  $\delta$ ): 2.49 (S, 3H,  $-\text{CH}_3$ ), 2.73 (T, 2H,  $-\text{CH}_2-$ ), 3.89 (T, 2H,  $-\text{CH}_2-$ ); IR ( $\text{cm}^{-1}$ , film) 2933 ( $-\text{CH}_2-$ ), 1696 ( $\text{C=O}$ ).

**3.2. XRD Analysis of PA6/LiCl Composite.** PA6 was a multicrystal phase polymer; the crystallization behavior including crystallinity, crystal structure, size, and distribution of spherulite had decisive influence on the physical properties of nylon product. As a result, controlling the appropriate crystalline state was very important for PA6 product to obtain excellent performance. Under different crystallization conditions, different formation of the hydrogen bond structure forming is different, which led to different spherulite structure. PA6 mainly had two stable crystal structures  $\alpha$  and  $\gamma$  [8],  $\gamma$ -form can improve the degree of deformation, and  $\alpha$ -form has strong stability. During PA6 spinning process,  $\gamma$ -form could improve the deformation degree and benefit to prepare the superfine denier fiber.

The XRD patterns in Figure 3 showed that the samples of PA6 and the composites displayed characteristic peaks at scattering angles of 20.0° and 23.60° [9], corresponding to the reflections of the crystalline planes (200) and combined (002)/(202), respectively, which was corresponding to monoclinic  $\alpha$ -phase morphology. The peak position of the composites had a slight displacement compared with PA6, which implied that the lattice dimension of PA6 changed with the addition of lithium chloride. It was interesting that the composite had obvious diffraction peak at about 21.4°, which corresponded to the  $\gamma$ -form of PA6.

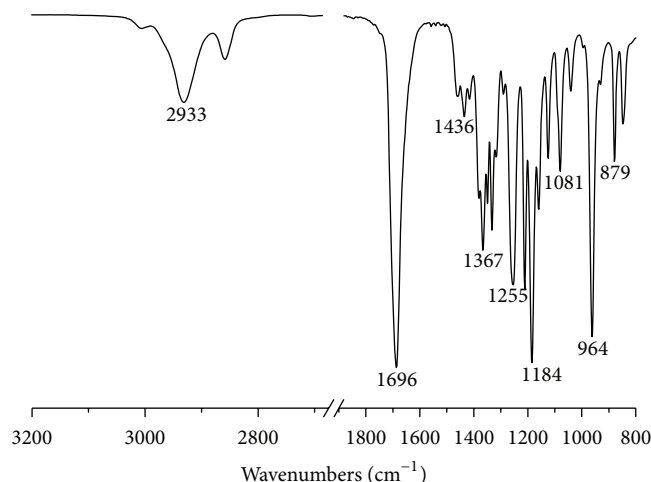


FIGURE 1: FT-IR spectrum of N-acetylcaprolactam.

TABLE 1: The XRD parameters of the PA6/LiCl composites.

Sample	HKL	$2\theta/^\circ$	A	$A\alpha_1/A\alpha_2$ (%)	$A\gamma/A\alpha$ (%)
0%	200	20.3	620.5		
	100	21.8	126.4	48.6	6.7
	002 + 202	23.5	1276.0		
0.1%	200	20.3	453.3		
	100	21.6	213.0	34.2	11.9
	002 + 202	23.6	1327.1		
0.3%	200	20.2	268.1		
	100	21.4	176.5	90.0	31.2
	002 + 202	23.6	297.7		
0.5%	200	20.3	99.0		
	100	21.6	171.1	30.7	40.6
	002 + 202	23.7	322.2		
1.0%	200	20.4	581.8		
	100	21.8	171.2	70.9	12.2
	002 + 202	23.8	820.7		

As can be seen from Table 1, compared with pure PA6, both the two diffraction angles in PA6/LiCl composites became larger, which could be due to the destruction effect of lithium chloride molecule on the hydrogen bonding between the PA6 chains. Comparing the proportion of  $\alpha$ -form of PA6 and the composites, we could find that the content of  $\alpha$ -form reduced with increasing content of lithium chloride. Variation trend of the  $\gamma$ -crystal form also can be seen from Figure 3. With increasing content of lithium chloride, the intensity of  $\gamma$ -form crystal diffraction peak increased first and then decreased, which illustrated that the proportion of PA6  $\gamma$ -form crystal phase increased with lithium chloride content increasing in a certain range.

**3.3. DSC Analysis of PA6/LiCl Composite.** Figure 4 showed the heating curves after erasing thermal history of nylon and composites. In the process of constant heating rate, the melting temperature linear declined with the increasement

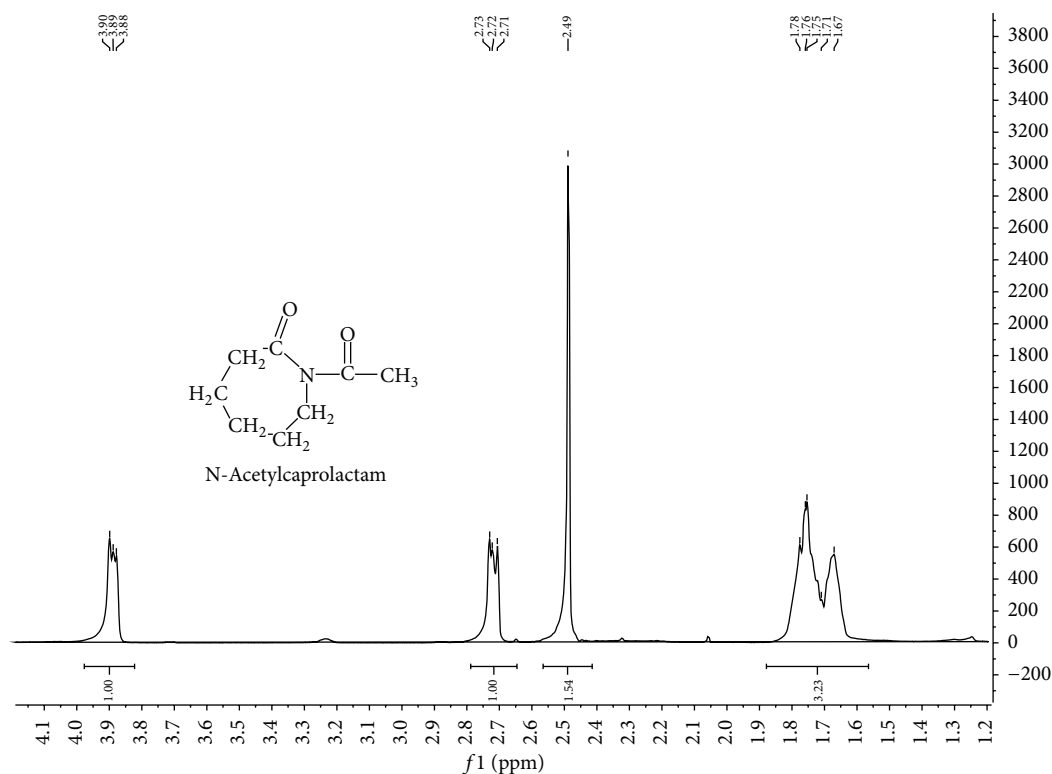
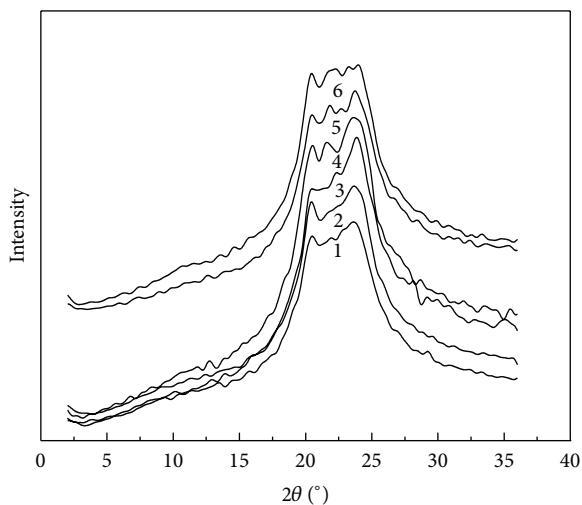
FIGURE 2:  $^1\text{H}$ -NMR spectrum of N-acetylcaprolactam.

FIGURE 3: Wide angle X-ray diffraction patterns of LiCl/PA6 composites with different LiCl content: (1) 0.0%; (2) 0.1%; (3) 0.3%; (4) 0.5%; (5) 1.0%; (6) 2.0%.

of lithium chloride content. When the content reached 2%, the melting temperature declined to nearly  $20^\circ\text{C}$  compared with that of PA6. Both the pure PA6 and the PA6/LiCl composites had multiple melting peaks, which may be due to the different degree of crystallinity and crystal perfection. Higher temperature crystallization peak corresponded to a perfect crystal melting, while the low temperature peak was the low degree of crystal perfection [10, 11]. With the addition

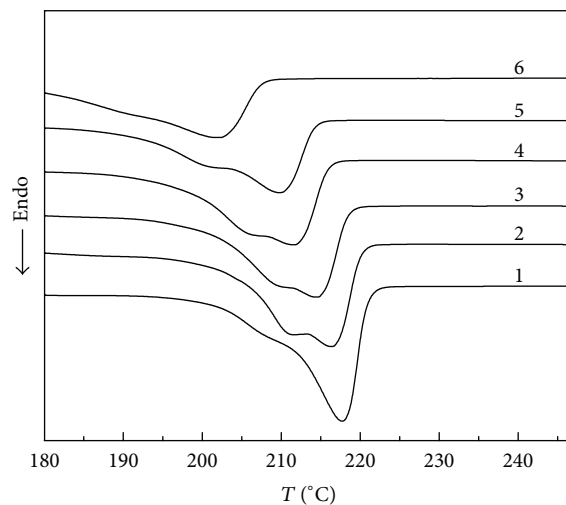


FIGURE 4: The second heating process of the PA6/LiCl composites with different LiCl content: (1) 0.0%; (2) 0.1%; (3) 0.3%; (4) 0.5%; (5) 1.0%; (6) 2.0%.

of lithium chloride, lithium ion could form six membered ring-structure via complexing interaction with PA6 molecule, which reduced molecular chain migration rate and the degree of crystal perfection.

#### 4. Conclusions

We prepared the PA6/LiCl composites via in situ anionic polymerization. IR and NMR result confirmed the successful

synthesis of N-acetylcaprolactam which acted as activator. DSC and X-ray results showed that the  $\gamma$ -crystal phase proportion in composites increased with increasing the LiCl content to appropriate amount. While  $\gamma$ -form could improve the degree of deformation, which implied that the preparation of superfine fiber for PA6 became easily during the spinning.

## Acknowledgments

This work was financially supported by the Major Science and Technology Projects of Science and Technology Department of Zhejiang Province (Contract Grant no. 2010C11043) and funded by National High Technology Research and Development Program 863 (2010AA03A406).

## References

- [1] R. Wang and D. S. Zhang, *Process and Application of the Superfine Fibers*, China Textile & Apparel Press, Zhejiang, China, 2007.
- [2] V. N. Dougnac, B. C. Peoples, and R. Quijada, "The effect of nanospheres on the permeability of PA6/SiO<sub>2</sub> nanocomposites," *Polymer International*, vol. 60, no. 11, pp. 1600–1606, 2011.
- [3] C. Z. Liao and S. C. Tjong, "Mechanical and thermal behaviour of polyamide 6/silicon carbide nanocomposites toughened with maleated styrene-ethylene-butylene-styrene elastomer," *Fatigue and Fracture of Engineering Materials and Structures*, vol. 35, no. 1, pp. 56–63, 2012.
- [4] B. Huang, D. Li, Z. Li, X. Li, and W. Zhou, "Reactive compatibilization of PA 6/ABS blends by ethylene-acrylate-glycidyl methacrylate copolymer," *Journal of Applied Polymer Science*, vol. 122, no. 1, pp. 586–592, 2011.
- [5] G. Rusu and E. Rusu, "Anionic nylon 6/TiO<sub>2</sub> composite materials: effects of TiO<sub>2</sub> filler on the thermal and mechanical behavior of the composites," *Polymer Composites*, vol. 33, no. 9, pp. 1557–1569, 2012.
- [6] O. Monticelli, S. Bocchini, A. Frache, E. S. Cozza, O. Cavalleri, and L. Prati, "Simple method for the preparation of composites based on PA6 and partially exfoliated graphite," *Journal of Nanomaterials*, vol. 2012, Article ID 938962, 5 pages, 2012.
- [7] Z. Xu and C. Gao, "In situ polymerization approach to graphene-reinforced nylon-6 composites," *Macromolecules*, vol. 43, no. 16, pp. 6716–6723, 2010.
- [8] H. Arimoto, M. Ishibashi, M. Hirai et al., "Crystal structure of the  $\gamma$  form of nylon6," *Journal of Polymer Science*, vol. 3, no. 1, pp. 317–326, 1965.
- [9] M. I. Kohan, *Nylon Plastics Handbook*, Hanser, New York, NY, USA, 1995.
- [10] S. Yue, W. Gong, N. Qi, B. Wang, W. Zhou, and Y. Zhu, "Effect of the dispersion of organic rectorite on the nonisothermal crystallization kinetics and melting behaviors of nylon 6 nanocomposites," *Journal of Applied Polymer Science*, vol. 110, no. 5, pp. 3149–3155, 2008.
- [11] L. Cui, Q. Fu, C.-J. Chang, and J.-T. Yeh, "The effect of poly(vinyl alcohol) hydrolysis on the properties of its blends with nylon 6," *Polymer Engineering and Science*, vol. 49, no. 8, pp. 1553–1561, 2009.

## Research Article

# A Promising Material by Using Residue Waste from Bisphenol A Manufacturing to Prepare Fluid-Loss-Control Additive in Oil Well Drilling Fluid

Zhi-Lei Zhang,<sup>1</sup> Feng-Shan Zhou,<sup>1</sup> Yi-He Zhang,<sup>1</sup> Hong-Wei Huang,<sup>1</sup> Ji-Wu Shang,<sup>1</sup> Li Yu,<sup>1</sup> Hong-Zhen Wang,<sup>2</sup> and Wang-Shu Tong<sup>1</sup>

<sup>1</sup> National Laboratory of Mineral Materials, School of Materials Science and Technology, China University of Geosciences, Beijing 100083, China

<sup>2</sup> Institute of Chemistry, Chinese Academy of Sciences, Beijing 100190, China

Correspondence should be addressed to Feng-Shan Zhou; [zhoufs@cugb.edu.cn](mailto:zhoufs@cugb.edu.cn) and Yi-He Zhang; [zhangyihe@cugb.edu.cn](mailto:zhangyihe@cugb.edu.cn)

Received 5 September 2013; Accepted 21 October 2013

Academic Editor: Yizhuang Xu

Copyright © 2013 Zhi-Lei Zhang et al. This is an open access article distributed under the Creative Commons Attribution License, which permits unrestricted use, distribution, and reproduction in any medium, provided the original work is properly cited.

The residues mixture from Bisphenol A manufacturing process was analyzed. Fourier transform infrared (FTIR) spectroscopy, gas chromatography-mass spectrometry (GC-MS), and nuclear magnetic resonance (NMR) were used to characterize the residues. The results indicated that the residues were complex mixture of several molecules. 3-(2-Hydroxyphenyl)-1,1,3-trimethyl-2,3-dihydro-1H-inden-5-ol and phenol were the main components of the residues. The technical feasibility of using it as phenol replacement in fluid-loss-control additive production was also investigated. The fluid-loss-control capacity of the novel additive was systematically investigated. It was discovered that the well fluid-loss performance of the prepared additive can be achieved, especially at high temperature.

## 1. Introduction

Bisphenol A (BPA) is an organic compound with two phenolic hydroxyl groups [1]. Generally, it is synthesized by condensation of phenol with acetone [2–4]. For reactions involving the substitution of a proton in an aromatic ring, both the rate of reaction and the equilibrium distribution of products are influenced by the density of electrons at the centre of reaction [5]. However, due to the high reactivity of the system, many byproducts can be produced and are present in the reaction mixture. For example, a crude product stream consisted of 41% BPA, 36.2% ortho,para-isomer, 1.1% ortho,ortho-isomer, 14.2% phenol, 3.5% chromane, 0.05% flavan, and 12% of unidentified compounds [6]. The formulas of some by-products are shown in Figure 1. After numerous and diverse purification processes, the impurities (such as the excess phenol, cyclic dimmers derived from BPA, chroman-based compounds, spirobiindane compounds, and the like)

were separated from BPA and finally formed the complex residue compound.

Being an important industrial chemical, BPA has been widely used [7, 8], and the demand for BPA production has increased [1]. With the growing production of BPA [9], there will be more and more residues from the BPA industry. It is predicted that there will be over  $50 \times 10^3$  ton residues produced annually in China. According to European Waste Catalogue (EWC), the residues are absolute hazardous (07 01 08\*). So, appropriate disposal and recycling of the residues are necessary for environmental protection and public health. The residues are generally burned as a means of disposal. Because the incineration technology is not qualified; treatment and recycling of the residues in China have been a thorny problem. The previous researches mainly concentrated on the treatment of the by-products and recovery of the useful phenol [10–12]. Hence, it is imperative to develop methods to utilize the industry waste. So far, there have



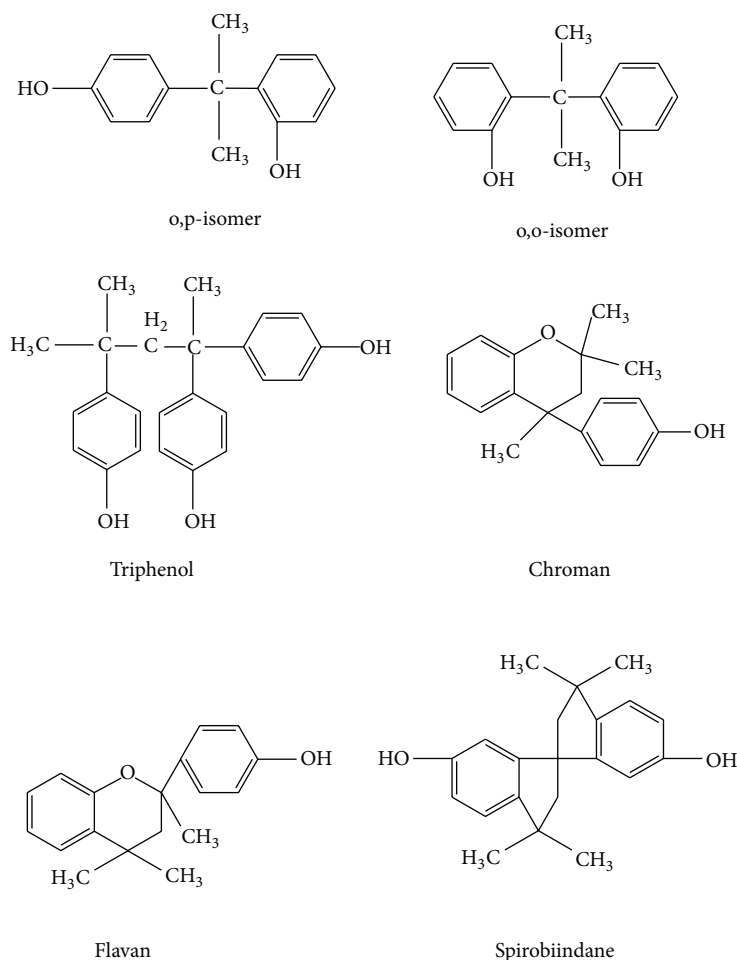


FIGURE 1: Formulas of the impurities.

only been relatively limited researches in this respect. The residues have been used in furan no-bake foundry binders and phenolic-based foundry shell resin formulations [13].

The petroleum drilling fluids, more commonly known as drilling muds, are complex chemical systems necessary for oil development. Among other functions, a drilling mud needs to create a thin low-permeability cake that protects permeable production formations. Fluid-loss-control additives form filter cakes surrounding the well bore to retard the loss of drilling fluid into permeable formations [14–17]. It has been common practice in the oil well drilling industry to employ starches, starch derivatives, cellulose derivatives, and water-soluble gums to reduce the filtrate volume of water base muds. Although these materials reduce the fluid loss of drilling muds, they are not thermally stable. Generally, water-soluble sulfonated phenolic condensate is obtained from the reaction of phenol, formaldehyde, and anhydrous sodium sulfite [18]. As a drilling mud additive, it has good fluid-loss-control performance and resistance to high temperature [19]. However, when the treated muds are subjected to extreme thermal environments, such products should be further modified to enhance the properties. And with raw material prices, the commercial pressure of competition is also growing. Utilization of waste materials for modification

or substitution of primary resources has been a widespread concern [20–22]. Phenol has an ortho-para directing activation group, hydroxyl. It could be condensed and sulfonated to produce a fluid-loss-control additive under the presence of formaldehyde and sodium sulfite. Although there are many complicate components coexisting in the residues, most of them have the activation group hydroxyl and could react like phenol. The condensation polymerization by using this kind of residues is more likely a copolycondensation. The resultant products will have the same essential functional group as the products from condensation and sulfonation by using phenol. So, it is feasible by using the residues to displace phenol as a raw material to produce fluid-loss-control additive.

The purpose of this study was to confirm the components of the residue mixture and evaluate the technical feasibility of using it as phenol replacement in fluid-loss-control additive production.

## 2. Experimental Details

**2.1. Materials.** The residues mixtures were obtained from Nanjing Zunyu Chemical Co., Ltd., China. It was obvious that the waste material was shiny black solid (Figure 2(a)). It was

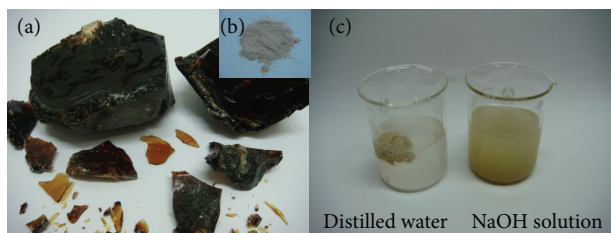


FIGURE 2: Comparison between the residues before (a) and after (b) grinding and the dispersion in distilled water and NaOH solution (c).

highly brittle, and the powder (Figure 2(b)) could be obtained after grinding. And then, the powder was stirring under the refluxing temperature in distilled water and sodium hydroxide (NaOH) solution for an hour, respectively. In Figure 2(c), the dispersion of the powder was markedly different. In distilled water, the powder was gathering into a mass slowly, but it dispersed well in the NaOH solution. The raw bentonite was obtained from Dagang Oilfield (Group) Co., Ltd., Tianjin, China. The sulfonated methyl phenolic resin obtained from the Third Exploration Company of Tarim Petroleum Exploration and Development Headquarters was marked as  $M_1$  and obtained from Derun Chemical Co., Ltd., Binzhou, China, and was marked as  $M_2$ . Sulfonated lignite obtained from Hairong Industry & Trade Co., Ltd., Korla, China, and Beijing Institute of Exploration Engineering was marked as  $M_3$  and  $M_4$ , respectively. All the chemicals such as phenol, formaldehyde, sodium sulfite, sodium bisulfite, sodium hydroxide, sodium chloride, acetone, and cyclohexane were analytical grade and obtained from Beijing Chemical Plant, China. A homemade column chromatograph with a length and width of 40 cm and 3 mm, respectively, packed with silica gel (ZCX.H, 200–300 mesh size, Branch of Qingdao Haiyang Chemical Plant, China) was used in the study. Standard HSGF254 HPTLC plates (100 × 25 mm) were purchased from Yantai Chemical Industry Research Institute, China.

**2.2. Methods.** FTIR was conducted on the residues on a Perkin-Elmer SP100 FTIR spectrometer by the KBr disc technique. It was operated in the ATR (attenuated total reflectance) mode, and 32 scans were collected at a resolution of  $4\text{ cm}^{-1}$ .

An Agilent Technologies 7890A gas chromatograph equipped with the Agilent 5975C mass spectrometer (Agilent 7890A/5975C GC-MS System) was used to identify the organic compositions. The system was operated at  $40^\circ\text{C}$  for 1 min and then up to  $300^\circ\text{C}$  at a ramping rate of  $10^\circ\text{C}/\text{min}$  and held for 5 min. One  $\mu\text{L}$  of the samples was injected in split mode with a split ratio of 10:1. An Agilent J&W column, with 30 m in length, 0.25 mm internal diameter, and 0.25  $\mu\text{m}$  film thicknesses was adopted in the separation system. High-purity helium was the carrier gas and introduced at a constant rate of 1.4 mL/min.

The eluent used in the column chromatography experiment was an acetone/cyclohexane (1/5, v/v) mixture which was determined by previous thin-layer chromatography

experiments. The materials obtained by column chromatography were dried at  $50^\circ\text{C}$  for 24 h in a vacuum oven to a constant weight. Nuclear magnetic resonance spectra ( $^1\text{H-NMR}$ , 400 MHz) were acquired on a Bruker-400 spectrometer with the 1 mm TXI micro liter probe using deuterated chloroform as the solvent.

The fresh-water base mud containing 50 g/L of sodium bentonite was prepared by mixing the raw bentonite and fresh water at a certain ratio, stirring for 15 min at a high speed of 10,000 rpm and aging for 24 h at room temperature. The testing mud was obtained with an addition of fluid-loss-control agents and/or sodium chloride into the base mud.

The fluid-loss-control properties of the muds, including API filtrate volume (i.e.,  $\text{FL}_{\text{API}}$ ) and high-temperature/high-pressure filtrate volume (i.e.,  $\text{FL}_{\text{HTHP}}$ ), were determined according to American Petroleum Institute (API) specifications and Chinese SY/T5621-93 specifications, respectively. In this test process, a ZNS-2A medium-pressure and GGS42-2 high-pressure filtration apparatus (made by Qingdao Haitongda Special Instruments Co., Ltd., China) were used. Figure 3 shows the schematic of the filtration apparatus. The rheological parameters, such as apparent viscosity (AV), plastic viscosity (PV), and yield point (YP), were determined by a ZNN-D6 rotating viscometer.

**2.3. Preparation of Fluid-Loss-Control Additive RPF.** A 3-neck flask with a stirrer, thermometer, and reflux condenser was charged with the residues, formaldehyde water solution (37% w/w), sodium hydroxide, and water. The mixture was heated slowly to a certain temperature. After stirring for about an hour, a second portion of formaldehyde water solution, sodium hydroxide and water was added into the mixture with sodium sulfite and sodium bisulfite. After synthesis, the production was pan-dried at  $70^\circ\text{C}$  and then crushed into powders over 80 mesh sieve for use in mud tests. The nomenclature of this fluid-loss-control additive is designated as RPF here. And the PF was prepared using phenol to replace the residues. Furthermore, there are very little by-products produced from this process which is environmentally green.

**2.4. Orthogonal Array Experimental Design.** In the present study, an L25 (56) orthogonal array (OA) was used to investigate the effect of formulas and parameters. The orthogonal array was listed in Table 1, and the data analysis was carried out through the range analysis. After the orthogonal experiments and subsequent data analysis, the magnitudes were reflected.

### 3. Results and Discussion

**3.1. Spectroscopy Analysis.** The infrared spectrum of the residues with the characteristic hydroxyl group stretching band at  $3424\text{ cm}^{-1}$  can be observed in Figure 4. The hydroxyl group band in the residues and RPF does not as strong as that in the PF. This could be attributed to the complex components of the residues and RPF. The absorption peaks at  $2962\text{ cm}^{-1}$  and  $1468\text{ cm}^{-1}$  can be assigned to the vibrational modes of methyl and/or methylene. The peaks at  $1605\text{ cm}^{-1}$

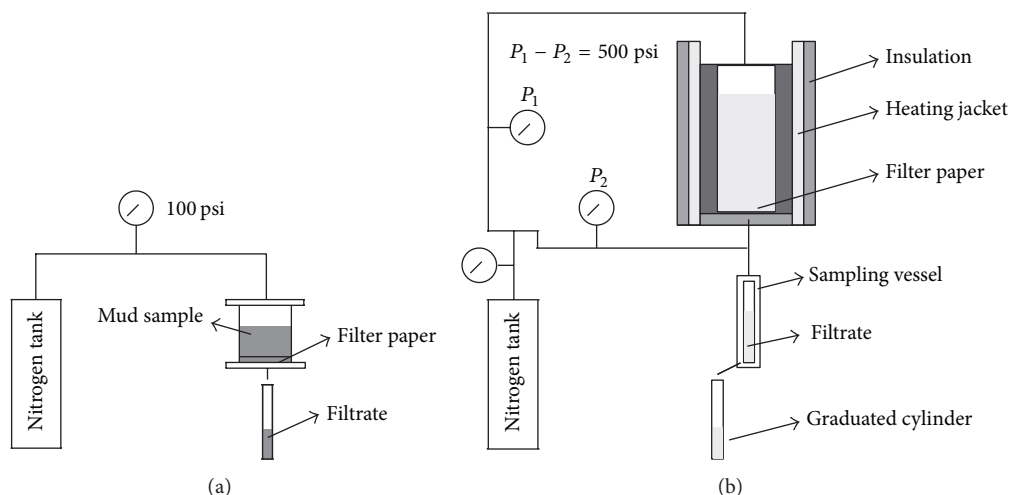


FIGURE 3: Schematic of the API (a) and HTHP (b) filtration test apparatus.

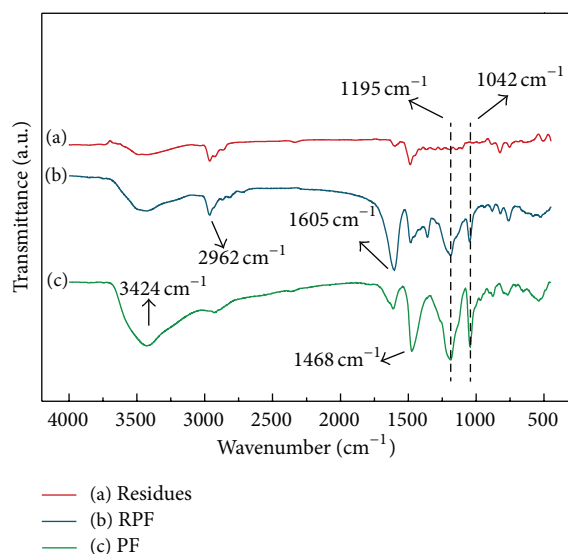


FIGURE 4: FTIR spectra of the residues, RPF, and PF.

corresponded to the carbon-carbon double bond stretching vibration of the benzene ring skeleton. An observable sulfonate group antisymmetric stretching vibration band at  $1195\text{ cm}^{-1}$  and a carbon-sulfur bond stretching band at  $1042\text{ cm}^{-1}$  can be found in the spectrum of RPF and PF but not in the spectrum of the residues. This feature is considered to be characteristic of the sulfonation reaction.

Gas chromatography-mass spectrometry (GC-MS) is used to isolate and determine the organic molecules. The chromatogram of residues is depicted in Figure 5(a). Separation and peak profiles are accomplished in 30 min and several components can be isolated. The component contents (with the retention time of 6.8 min, 8.8 min, 14.0 min, 21.5 min, and 22.9 min) are 34.5%, 7.6%, 5.6%, 24.6%, and 6.4%, respectively (Table 2). Figures 5(b), 5(c), 5(d), 5(e), and 5(f) show the partial mass spectra of these five constituents

TABLE 1: Levels and factors affecting the fluid-loss properties.

Levels	Factors					
	A ( $^{\circ}\text{C}$ ) <sup>a</sup>	B <sup>b</sup>	C <sup>c</sup>	D <sup>d</sup>	E (mL) <sup>e</sup>	F (h) <sup>f</sup>
1	60	2.77	17.12	3.61	29.7	3
2	70	1.39	5.71	2.71	39.6	4
3	80	0.93	3.42	1.80	49.5	5
4	90	0.69	2.45	1.20	59.4	6
5	100	0.56	1.90	0.90	69.3	7

<sup>a</sup>A: reaction temperature.

<sup>b</sup>B: mass ratio of residue to formaldehyde.

<sup>c</sup>C: mass ratio of residue to catalyst.

<sup>d</sup>D: mass ratio of residue to sulfonating agent.

<sup>e</sup>E: amount of water.

<sup>f</sup>F: reaction time.

TABLE 2: GC/MS results of the residues.

Peak	Retention time (min)	Assignments	Molecular ion	Content (%)
1 <sup>#</sup>	6.8	Phenol	94.0	34.5
2 <sup>#</sup>	21.5	A <sup>a</sup>	268.0	24.6
3 <sup>#</sup>	8.8	Undecane	156.0	7.6
4 <sup>#</sup>	14.0	B <sup>b</sup>	174.0	5.6
5 <sup>#</sup>	22.9	C <sup>c</sup>	268.0	6.4

<sup>a</sup>A: 3-(2-hydroxyphenyl)-1,1,3-trimethyl-2,3-dihydro-1H-inden-5-ol.

<sup>b</sup>B: 1,5,7-trimethyl-1,2,3,4-tetrahydronaphthalene.

<sup>c</sup>C: 3-(4-hydroxyphenyl)-1,1,3-trimethyl-2,3-dihydro-1H-inden-5-ol.

marked as 1<sup>#</sup>, 2<sup>#</sup>, 3<sup>#</sup>, 4<sup>#</sup>, and 5<sup>#</sup>. The molecular ions in the two main components, 1<sup>#</sup> and 2<sup>#</sup>, have  $m/z$  values of 94 and 268, respectively, suggesting that number 1 is phenol, number 2 is 3-(2-hydroxyphenyl)-1,1,3-trimethyl-2,3-dihydro-1H-inden-5-ol. Phenol has already been used to produce phenolic resin and sulfonated phenolic resin. Number 2 has two phenolic hydroxyl groups, so it could condense with formaldehyde as well.

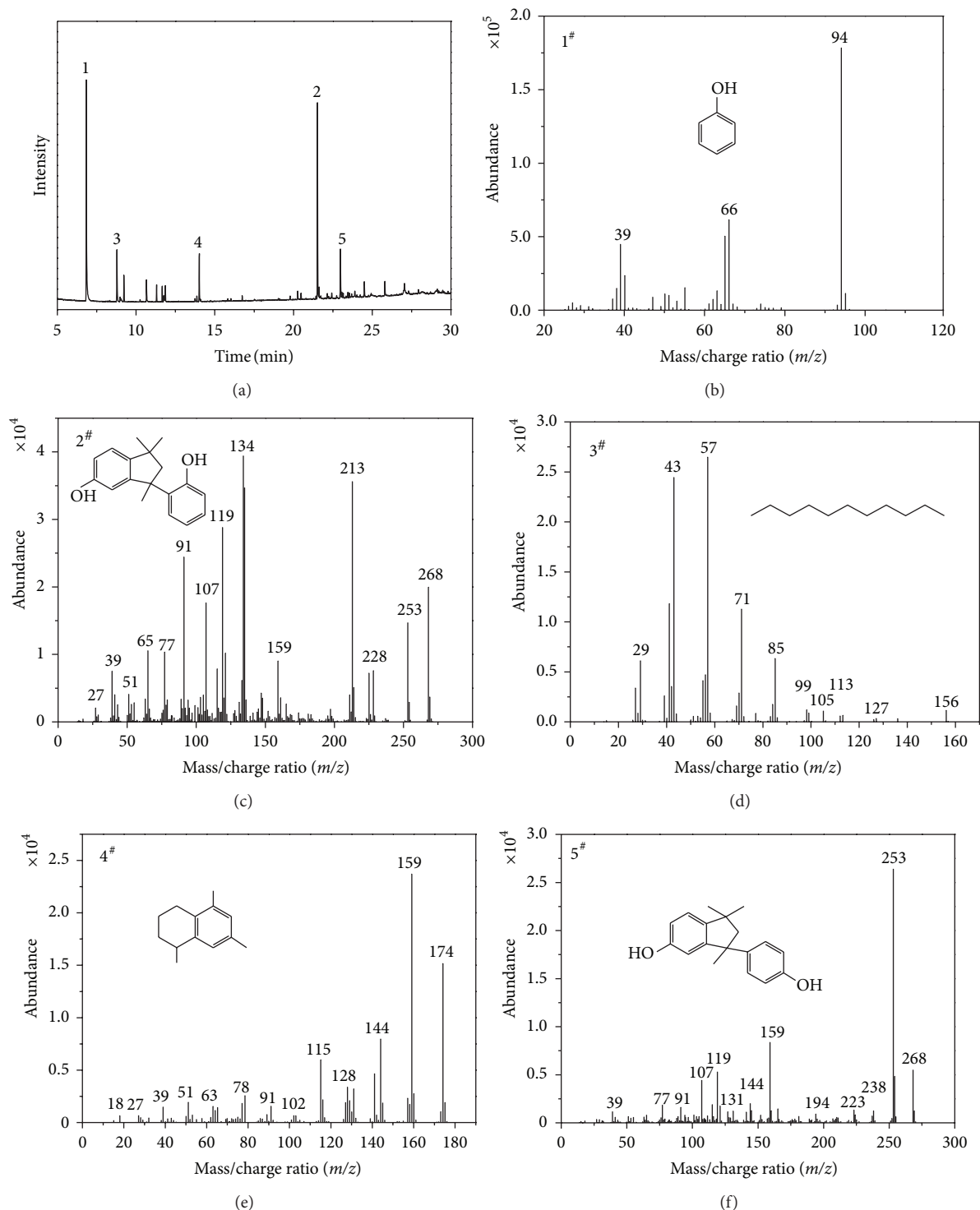


FIGURE 5: Chromatogram of the residues (a) and mass spectra of the five components from the residues (peaks 1–5 in the chromatogram) at different retention times of (b) 6.8 min, (c) 21.5 min, (d) 8.8 min, (e) 14.0 min, and (f) 22.9 min.

There are many components in the residues. Some of the components have little content, similar structures, and polarity. Hence, it is difficult to separate the components absolutely. In our column chromatography experiments, there are five components obtained and the two main components are further identified by  $^1\text{H}$  NMR and the results are in

agreement with those from GC-MS. As shown in Figure 6(a), the signal at 5.051 ppm corresponds to the hydroxyl group (1). In the region of 6.8–7.3 ppm, there are signals assigned to the aromatic protons (2, 3, and 4). Hence, compounds number 1 is indeed phenol, also known as carboic acid. In Figure 6(b), the resonance at 5.388 ppm corresponds to

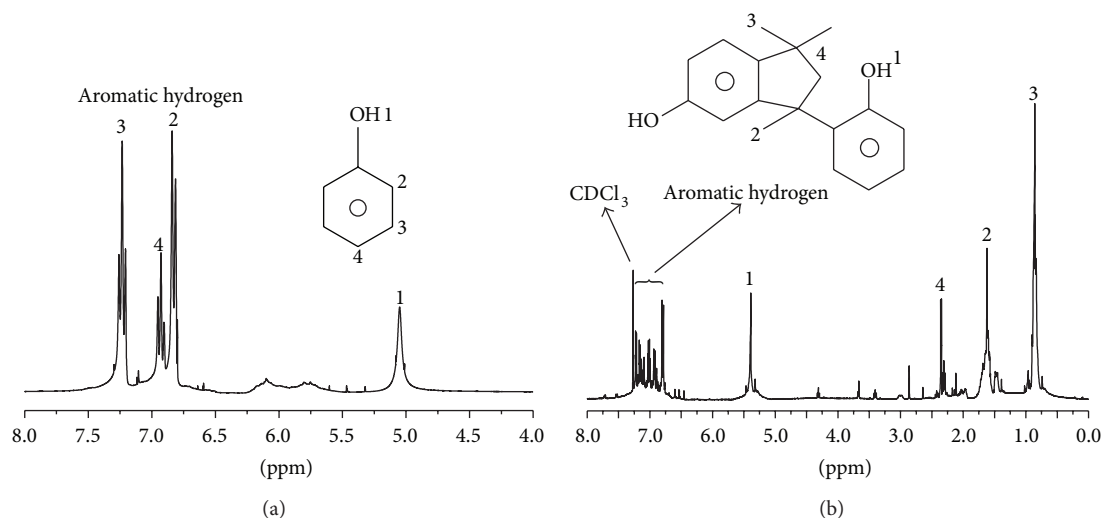


FIGURE 6: Proton nuclear magnetic resonance spectrum acquired from the two main components of the residues.

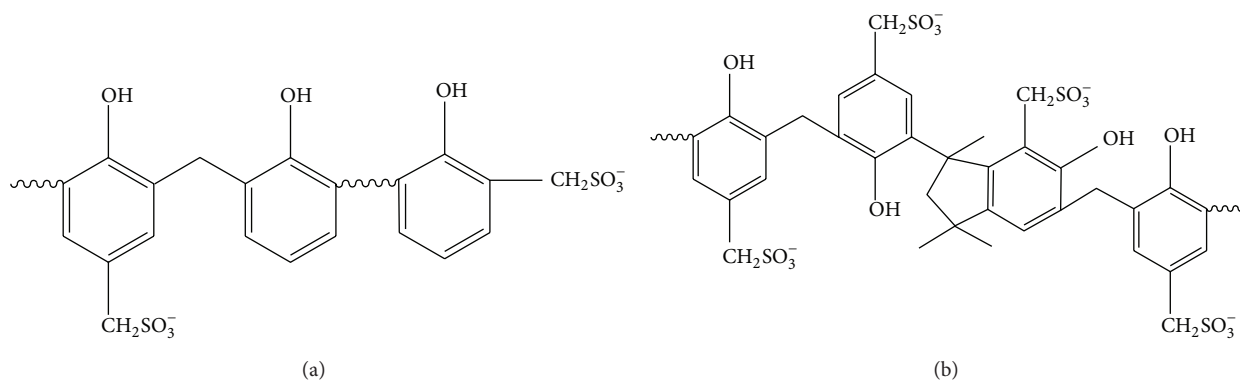


FIGURE 7: Structural representation of PF and RPF.

the hydroxyl group (1). The signals at 1.619 ppm, 0.858 ppm, and 2.346 ppm arise from protons 2, 3, and 4, respectively. In the region of 6.683–7.267 ppm, there are signals assigned to the aromatic protons and deuterated chloroform. Thus, number 2 is identified to be 3-(2-hydroxyphenyl)-1,1,3-trimethyl-2,3-dihydro-1H-inden-5-ol.

Hydroxyl is an ortho-para directing group. Due to the reactive positions, these two components could be condensed and sulfonated under the presence of formaldehyde and sodium sulfite. The simple schematic diagrams of the production were shown in Figure 7; (a) was PF and (b) was RPF. This is not the real structure but a possible structure that imaged to illustrating the condensation polymerization and the sulfonation reaction. The real structure of the reaction products will be more complex. The other components do not play a major role in this study because of the relatively tiny amount or the absence of active functional group.

**3.2. Effect of Formulas and Parameters on Filtration Properties.** There are two important parameters in range analysis:  $K_{ij}$  and  $R_i$ .  $K_{ij}$  is defined as the sum of the evaluation indexes of all levels ( $j = 1, 2, 3, 4$ ) in each factor ( $i = A, B, C, D$ ).

$K'_{ij}$  (mean value of  $K_{ij}$ ) is used to determine the optimal level and the optimal combination of factors. The optimal level for each factor could be obtained when  $K'_{ij}$  is the largest.  $R_i$  is defined as the range between the maximum and minimum value of  $K'_{ij}$  and is used for evaluating the importance of the factors [23]. According to the OA25 matrix, twenty-five experiments were carried out and their filtrate volume results were shown in Table 3. This table shows that the range of  $FL_{API}$  was from 10 mL to 30 mL and the range of  $FL_{HTHP}$  was from 50 mL to 138 mL. The mean values of  $K$  ( $K'_{ij}$ ) for different factors at different levels in the range analysis were shown in Table 4. As mentioned, for each factor, the higher mean value ( $K'_{ij}$ ) indicates the larger effect on filtration loss.

As shown in Table 4, for API filtrate properties,  $K'_{ij}$  was the lowest at these combinations  $A_4B_4C_2D_5E_3F_1$ , and, for HTHP properties,  $K'_{ij}$  was the lowest at  $A_1B_2C_5D_3E_4F_1$ . Compared with the range values of different factors ( $R_i$ ), the factors' levels of significance are as follows: for API,  $C$  (6.10) >  $B$  (4.20),  $F$  (4.20) >  $A$  (3.70) >  $D$  (3.48) >  $E$  (3.12); for HTHP,  $A$  (31.20),  $B$  (31.20) >  $E$  (27.60) >  $C$  (26.00) >  $D$  (19.60) >  $F$  (16.00).



TABLE 3:  $FL_{API}$  and  $FL_{HTHP}$  in OA25 matrix.

Trial number	Factors						Results	
	A	B	C	D	E	F	$FL_{API}$ (mL)	$FL_{HTHP}$ (mL)
1	1	1	1	1	1	1	22	78
2	1	2	2	2	2	2	23	72
3	1	3	3	3	3	3	24	60
4	1	4	4	4	4	4	20	72
5	1	5	5	5	5	5	20	90
6	2	1	2	3	4	5	19	72
7	2	2	3	4	5	1	27	92
8	2	3	4	5	1	2	22	100
9	2	4	5	1	2	3	25	126
10	2	5	1	2	3	4	30	138
11	3	1	3	5	2	4	26	110
12	3	2	4	1	3	5	23	104
13	3	3	5	2	4	1	18	50
14	3	4	1	3	5	2	26	124
15	3	5	2	4	1	3	26	116
16	4	1	4	2	5	3	20	74
17	4	2	5	3	1	4	22	56
18	4	3	1	4	2	5	26	104
19	4	4	2	5	3	1	10	86
20	4	5	3	1	4	3	27	108
21	5	1	5	4	3	2	21	60
22	5	2	1	5	4	3	25	68
23	5	3	2	1	5	4	20	90
24	5	4	3	2	1	5	25	112
25	5	5	4	3	2	1	24	96

TABLE 4: Range analysis data of the  $FL_{API}$  and  $FL_{HTHP}$ .

Value name	A	B	C	D	E	F
$FL_{API}$						
$K'_1$	21.80	21.78	25.80	23.40	23.40	20.30
$K'_2$	24.70	24.00	19.70	23.30	24.80	23.10
$K'_3$	23.90	22.10	25.80	23.10	21.68	24.50
$K'_4$	21.00	21.20	21.80	24.08	22.00	23.60
$K'_5$	23.08	25.40	21.38	20.60	22.60	22.70
R	3.70	4.20	6.10	3.48	3.12	4.20
$FL_{HTHP}$						
$K'_1$	74.40	78.80	102.40	101.20	92.40	80.40
$K'_2$	105.60	78.40	87.20	89.20	101.60	89.00
$K'_3$	100.80	80.80	96.40	81.60	89.60	92.00
$K'_4$	85.60	104.00	89.20	88.80	74.00	93.20
$K'_5$	85.20	109.60	76.40	90.80	94.00	96.40
R	31.20	31.20	26.00	19.60	27.60	16.00

**3.3. Filtration Properties.** According to the optimal conditions shown above, we have changed and modified the experiment conditions and parameters and finally prepared the fluid-loss-control additive RPF and PF. As a fluid-loss-control additive, RPF and PF could improve the properties of drilling fluid. Series of fresh-water and salt-water mud

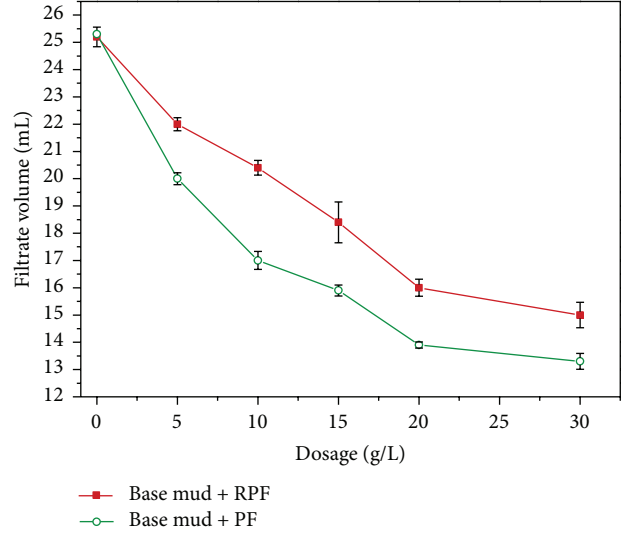


FIGURE 8: The effect of RPF and PF concentration on the API filtration loss of fresh water mud.

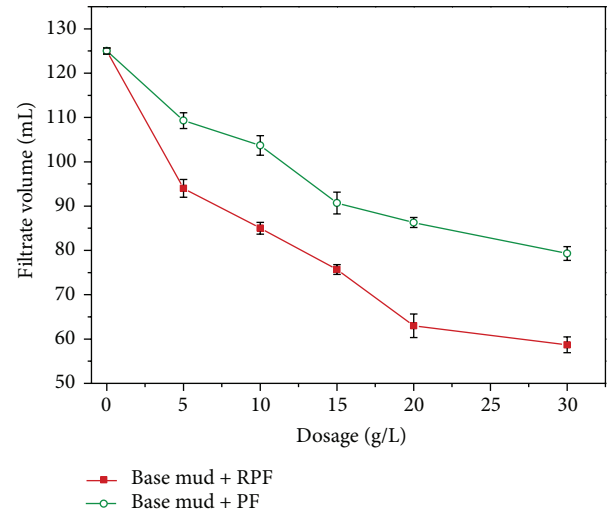


FIGURE 9: The effect of RPF and PF concentration on the HTHP filtration loss of fresh water mud.

formulations were prepared, and the filtrate volumes were measured. To probe into the effect of dosage of the fluid-loss-control additive on filtration properties, test of API filtration, and HTHP filtration were performed. From Figures 8 and 9, it can be observed that the fluid-loss volumes decreased with more additives used. These additives dispersed into the base mud and then could be adsorbed onto the clay surface under the action of hydrogen bond between the hydroxyl and the clay surface [24]. So, there exists a saturated adsorption amount. When the additive addition was over dose, the excess additives have little influence on filtration properties. As shown in Figures 8 and 9, when the concentration of the additive was higher than 20 g/L, the fluid-loss volumes decreased slowly.

From the analysis shown in Figures 5 and 6 and the possible structure of the product shown in Figure 7, it was expected that RPF would have better HTHP filtrate properties than PF. Segmental motion of molecular chain is dependence on temperature. The higher the temperature is, the more intense the segmental motion is. When the segmental motion is intense enough, molecular repulsion will be stronger than attraction and the molecular chain breaks. This was called degradation. There are two situations when polymer degrades; the molecular weight of the additive decreases and the amount of functional group of the additive decreases. These situations would cause the fluid-loss-control performance deterioration. Polymer will degrade at high temperatures, but the degree of the degradation is different because of the different molecular structure. If there are more aromatic groups in the molecular chain, the chain segments are bigger, and the temperature needs to be higher to make the segments motion. 3-(2-Hydroxyphenyl)-1,1,3-trimethyl-2,3-dihydro-1H-inden-5-ol and phenol are the main components in the residues. Phenol condensation polymer is endowed well HTHP fluid-loss-control performance by introducing benzene ring into the molecular structure. 3-(2-Hydroxyphenyl)-1,1,3-trimethyl-2,3-dihydro-1H-inden-5-ol has the activation group hydroxyl, and the molecular structure is more rigid than phenol. So, the resultant additives will have well HTHP fluid-loss-control performance by using these residues.

There are two competitive factors that affect the fluid-loss-control performance of RPF. (1) The components in the residue are complex, and some of them do not have the essential reactive group. These components cannot participate in the reaction and have no effect to improve the HTHP performance. (2) Most of the components in the residue are aromatic derivative, and they have the same reactive group like phenol. These components have the essential functional group as fluid-loss-control additives. Meanwhile, the side chain of the RPF molecular is bigger by introducing these aromatic derivatives into the condensation reaction as the constitutional unit than introducing phenol. The bigger side chain provides RPF better thermostability.

It can be seen in Figure 9 that the HTHP fluid-loss-control performance of RPF is better than PF. This can be explained as, in the fresh water mud, the thermo stability of the molecular chain is more important for the HTHP performance than the amount of the functional groups. The positive effect of the rigid molecular structure of the aromatic derivatives is more than the negative effect of the inactive components. This is why fewer components in residue could result in better HTHP fluid-loss-control performance in fresh water mud of RPF than that of PF.

To show the stability of RPF as a fluid-loss-control additive in saline solutions, filtration loss test of 20 g/L additive in 50 g/L bentonite mud with 40 g/L NaCl was performed. It is important to have additive for drilling mud that are stable in saline environments. Without additive, bentonite mud would lose its fluid-loss-control properties. According to the DLVO theory, it is thought to be explained as that the electrolyte solutions will compress the electrostatic double layer, affect hydration and coagulation stability of clays, and lead to

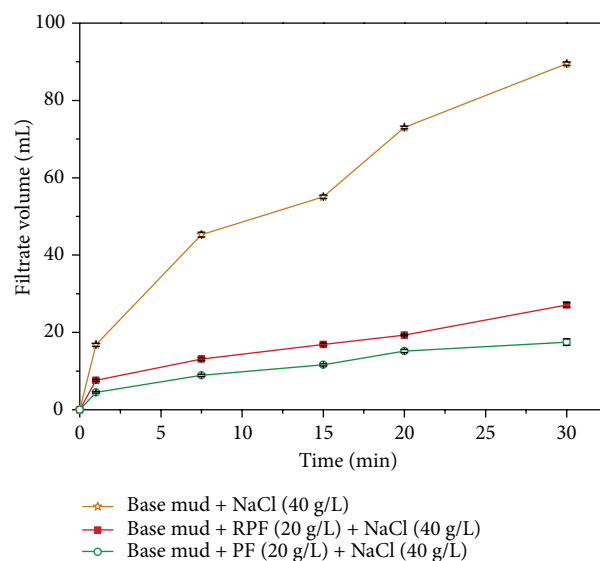


FIGURE 10: API filtration loss of RPF and PF in base mud and NaCl (40 g/L) solutions.

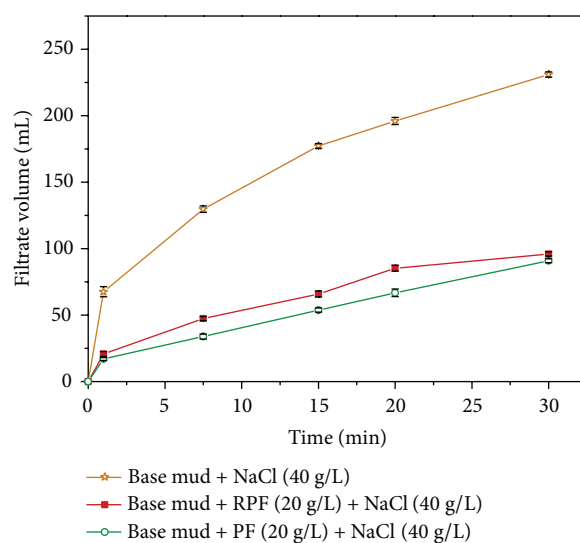


FIGURE 11: HTHP filtration loss of RPF and PF in base mud and NaCl (40 g/L) solutions.

the dehydration of the additives. Therefore, salt resistance additives should have enough adsorbing groups to connect with the clay surface and enough hydration groups to control the free water, and the hydration groups should be insensitive to electrolyte. The RPF have phenolic hydroxyl groups as the adsorbing groups and sulfonate groups as the hydration groups which have been proved to have well salt resistance [25]. RPF was expected to have salt resistance like PF. From the experiments data shown in Figures 10 and 11, unlike the expected results, RPF took a relatively poor effect compared with PF. It might be caused by the less active ingredient content. In the presence of salt solutions, the content of sulfonate groups plays the major role of the salt resistance. There are some inactive components in the residues, which

TABLE 5: Properties of RPF compared to commercial fluid-loss-control additives.

Fluid-loss-control additive <sup>a</sup>	AV (mPa·s)	PV (mPa·s)	YP (Pa)	FL <sub>API</sub> (mL)	FL <sub>HTHP</sub> (mL)
RPF	21.5	12.0	9.5	16.0	62.0
M <sub>1</sub>	20.5	7.0	13.5	16.0	88.0
M <sub>2</sub>	17.5	7.0	10.5	10.0	64.0
M <sub>3</sub>	13.5	9.0	4.5	11.0	66.0
M <sub>4</sub>	14.0	8.0	6.0	12.0	72.0

<sup>a</sup>The dosage of fluid-loss-control additive was 20 g/L.

could not participate in the sulfonation reaction. However, from the experiment results shown in Figure 9, it is obvious that although the effective component is less, the HTHP performance is still better.

For comparison, the properties of RPF and some commercial fluid-loss-control additives were shown in Table 5. It can be seen that the API filtrate volume of RPF is 16 mL and the HTHP filtrate volume of RPF is 62 mL. Through the comparison, it reveals that the HTHP performance of RPF is better than these commercial products. The viscosity of RPF is higher, and the yield point is in the middle.

## 4. Conclusion

The residue wastes produced from the BPA industry were complex compounds. Phenol and 3-(2-hydroxyphenyl)-1,1,3-trimethyl-2,3-dihydro-1H-inden-5-ol were the two main components of the residues. The fluid-loss-control additive produced using the residues showed better HTHP fluid-loss-control performance than some commercial products. This study indicates that the residues have potential application in fluid-loss-control additive manufacture. Using it to substitute phenol will improve the high temperature performance and endow the additive with significant cost advantage.

## Conflict of Interests

All the authors declare that they have no conflict of interests.

## Disclai mes

The paper is authors owned work, is original and unpublished, and is not being considered for publication elsewhere.

## Acknowledgments

This work is jointly supported by the Special fund of co-construction of Beijing Education Committee and the Fundamental Research Funds for the Central Universities no. 2652013062.

## References

- [1] W. T. Tsai, "Human health risk on environmental exposure to Bisphenol-A: a review," *Journal of Environmental Science and Health*, vol. 24, no. 2, pp. 225–255, 2006.
- [2] P. Michele and C. Giuseppe, Braz. Pedido PI BR, 7, 903, 483, 1979.
- [3] V. N. Sheemol, I. R. Unni, and C. Gopinathan, "Catalysis by heteropoly acids: formation of bisphenol A from phenol and acetone," *Indian Journal of Chemical Technology*, vol. 8, no. 4, pp. 298–300, 2001.
- [4] A. E. Donald, B. R. Lawrence, C. Ye-mon, and J. R. Lawrence, *Upflow Fixed Bed Reactor With Packing Elements*, WO Patent, 1997.
- [5] C. D. Nenitescu, *Chimie Organica*, vol. 2, p. 47, 1980.
- [6] Z. N. Verkhovskaya, M. Ya. Klimenko, L. B. Vystavkina et al., "Composition of the by-products of diphenylolpropane synthesis and their recovery," *Neftpererab Nefekhim*, vol. 5, pp. 34–35, 1973.
- [7] A. V. Krishnan, P. Stathis, S. F. Permeth, L. Tokes, and D. Feldman, "Bisphenol-A: an estrogenic substance is released from polycarbonate flasks during autoclaving," *Endocrinology*, vol. 132, no. 6, pp. 2279–2286, 1993.
- [8] C. A. Staples, P. B. Dorn, G. M. Klecka, S. T. O'Block, and L. R. Harris, "A review of the environmental fate, effects, and exposures of bisphenol A," *Chemosphere*, vol. 36, no. 10, pp. 2149–2173, 1998.
- [9] F. Jiao, X. Sun, and Z. Pang, "Production and market analysis of Bisphenol A," *Chemistry & Industry*, vol. 26, pp. 21–33, 2008.
- [10] S. Evitt, C. Chi, M. S. Lee, and D. Palmer, *Process For Recovering Phenol From A BPA Waste Stream*, 2010.
- [11] J. C. Carnahan, *Phenol Recovery From Bisphenol-A Waste Streams*, 1981.
- [12] S. J. Shafer, J. Pressman, and J. L. Lee, *Method For Recovering Material Values From Bisphenol Tars*, 2001.
- [13] K. K. Chang, M. C. Clingerman, M. L. Lott, and J. T. Schneider, *Use of Bisphenol A tar in furan No-bake Foundry Binders*, 1999.
- [14] P. L. Moore, *Drilling Practices Manual*, The Petroleum Publishing, Tulsa, Oklahoma, 1974.
- [15] C. L. William and J. P. Gary, *Standard Handbook of Petroleum & Natural Gas Engineering*, Gulf Professional Publishing, Houston, Tex, USA, 2nd edition, 1996.
- [16] A. D. Patel, E. Stamatkis, and E. Davids, U.S. Patent 6, 247, 543, 2001.
- [17] J. McDermott, *Drilling Mud and Fluid Additives*, Noyes Data Corp, London, UK, 1973.
- [18] K. C. Hsu and Y. F. Lee, "Water-soluble sulfonated phenolic resins. I. Synthesis," *Journal of Applied Polymer Science*, vol. 57, pp. 1419–1537, 1995.
- [19] J. J. M. Nahm and D. A. Rowe, U.S. Patent 3, 956, 140, 1976.
- [20] S. Rukzon and P. Chindaprasirt, "Utilization of bagasse ash in high-strength concrete," *Materials and Design*, vol. 34, pp. 45–50, 2012.
- [21] W. Wang and G. Huang, "Characterisation and utilization of natural coconut fibres composites," *Materials and Design*, vol. 30, no. 7, pp. 2741–2744, 2009.
- [22] H. Y. Aruntas, M. Gürüb, M. Dayı, and T. İlker, "Utilization of waste marble dust as an additive in cement production," *Materials & Design*, vol. 31, no. 8, pp. 4039–4042, 2010.
- [23] C. Chuanwen, S. Feng, L. Yuguo, and W. Shuyun, "Orthogonal analysis for perovskite structure microwave dielectric ceramic

thin films fabricated by the RF magnetron-sputtering method,” *Journal of Materials Science*, vol. 21, no. 4, pp. 349–354, 2010.

- [24] D. J. Greenland, “Adsorption of polyvinyl alcohols by montmorillonite,” *Journal of Colloid Science*, vol. 18, no. 7, pp. 647–664, 1963.
- [25] U. P. Strauss and Y. P. Leung, “Volume changes as a criterion for site binding of counterions by polyelectrolytes,” *Journal of the American Chemical Society*, vol. 87, no. 7, pp. 1476–1480, 1965.

## Research Article

# Analysis of a Benzamide/Cholesterol Mixture by Using TLC/FTIR Technique

**Xiaokun Fan,<sup>1,2</sup> Ran Guo,<sup>2</sup> Jia-jia Shi,<sup>1,2</sup> Haijun Wu,<sup>3</sup> Anqi He,<sup>2</sup> Yongju Wei,<sup>1</sup> Cuige Liu,<sup>1</sup> Shifu Weng,<sup>2</sup> Zhanlan Yang,<sup>2</sup> Yizhuang Xu,<sup>2</sup> Isao Noda,<sup>4</sup> and Jinguang Wu<sup>2</sup>**

<sup>1</sup> College of Chemistry and Material Science, Hebei Normal University, Shijiazhuang 050024, China

<sup>2</sup> College of Chemistry and Molecular Engineering, Peking University, Beijing 100871, China

<sup>3</sup> Mongolia Medical College, Inner Mongolia University for the Nationalities, Tongliao 028000, China

<sup>4</sup> Department of Materials Science and Engineering, University of Delaware, Newark, DE 19716, USA

Correspondence should be addressed to Yizhuang Xu; xyz@pku.edu.cn

Received 6 September 2013; Accepted 22 November 2013

Academic Editor: Edyta Proniewicz

Copyright © 2013 Xiaokun Fan et al. This is an open access article distributed under the Creative Commons Attribution License, which permits unrestricted use, distribution, and reproduction in any medium, provided the original work is properly cited.

We applied TLC/FTIR coupled with a mapping technique to analyze a cholesterol/benzamide mixture. Narrow-band TLC plates by using AgI as a stationary phase were used to separate benzamide and cholesterol. The distribution of cholesterol and benzamide spots was manifested by 3D chromatogram. Benzamide and cholesterol can be successfully separated by the narrow-band TLC plate. Moreover, characteristic bands of benzamide and cholesterol can be identified from their FTIR spectra. In addition, the FTIR spectra of the separated benzamide and cholesterol spots on the narrow band TLC plate are roughly the same as the corresponding reference IR spectra.

## 1. Introduction

Thin-layer chromatography (TLC) is one of the most versatile and widely used separation methods. The concept of TLC is simple, and samples usually require only minimal pretreatment [1–3]. TLC continues to feature a broad range of applications, such as analysis of pharmaceuticals, herbal medicines and dietary supplements, biological and clinical samples, foods and beverages, environmental pollutants, and many other chemicals. Although TLC exhibits advantages in the separation of mixtures, there is a limitation in identifying separated unknown components. In most TLC experiments, separated samples are identified by color, UV-Vis absorbance, or fluorescence signals. However, it becomes difficult to detect samples that have neither UV-Vis absorbance nor fluorescence signals. Spraying visualization reagents on TLC plate is helpful sometimes. However, the utility of visualization reagents for unknown TLC spot identification is somewhat limited, since the selected visualization reagents may not be suitable for every substance with a broad range of molecular structures present in the sample. FTIR spectroscopy [4, 5]

is a universal tool that can identify various organic compounds or metal complexes with organic ligands, even if the separated substance lacks color, UV-Vis absorbance, or fluorescence signals. Additionally, FTIR spectrum provides abundant information relevant to functional groups of separated substances. Moreover, it might be possible to recognize unknown separated spots directly on TLC plate based on their FTIR spectra. Nowadays, the progress on FTIR spectrometer instrumentation provides additional opportunity for the development of TLC/FTIR technique. For example, the development of FTIR spectrometer with a microscope attachment makes it convenient to acquire FTIR spectra even on each tiny separated sample spot on a TLC plate. In addition, the advancement on mapping/imaging techniques enables us to obtain FTIR spectra of every microregion on a TLC plate automatically. Thus, it has become possible to perform TLC/FTIR analysis in a quick and convenient manner.

As a matter of fact, great efforts have been made to develop TLC/IR technique for about 50 years. In the 1960s, TLC/IR analysis was carried out via solvent elution transfer approach [6, 7]. In this approach, suitable solvents were used



to dissolve each separated sample spot so that the analytes can be transferred out of the TLC plate. After removing the solvent by vaporization, IR spectrum of the obtained sample is recorded. The procedure is tedious and time-consuming, and the analysis is under a risk of sample loss and contamination. In 1975, Griffiths et al. [8–10] published a pioneering work on the development of *in situ* TLC/IR technique. This approach is quick, convenient, and free of the risk of sample loss, since FTIR spectrum is directly obtained from the separated sample spot on a TLC plate. Subsequently, Griffiths et al. [9, 10], Zuber et al. [11], Lloyd et al. [12], and White [13] adopted various spectral techniques to develop a more practical *in situ* TLC/IR technique. However, the biggest problem of the *in situ* TLC/FTIR is that traditional TLC stationary phases, such as silica and alumina, exhibit strong background absorption that can bring about significant interference to sample identification. To solve the problem, Danielson et al. proposed to use zirconium oxide that has no absorbance in mid-IR region as a new stationary phase for TLC/FTIR analysis [14, 15]. However, considerable amount of water was adsorbed on zirconium oxide and brought about severe interference in the measurement of FTIR spectra. Consequently, the problem of interference from stationary phase is not adequately addressed. Further development of the *in situ* TLC/FTIR technique has been mainly inhibited by the problem of strong background absorbency of stationary phase. As a matter of fact, there has been surprisingly few papers [16, 17] relevant to TLC/FTIR published around the world during the past decade.

To break the bottleneck of the TLC/FTIR method, we proposed to use IR-transparent, insoluble inorganic salt particles as novel stationary phases for TLC/FTIR analysis. The reason for this approach is that inorganic salt is transparent for infrared light, thereby removing the interference caused by IR absorption from stationary phase. The inorganic salt should be insoluble so that the risk of stationary phase being destroyed by mobile phase can be avoided. In addition, significant efforts have been made to control the size of the inorganic salt particles to be around 100 nm. The reasons are as follows. (1) Decreasing the size of stationary phase particles alleviates the effect of light scattering so that the quality of the corresponding FTIR spectra can be improved. (2) As the size of the particles of stationary phase decreases, the efficiency of TLC separation is enhanced. (3) Decreasing the size of the inorganic salt particle results in increasing the specific area of the stationary phase. Thus, more analytic molecules are allowed to be adsorbed on the surface of the stationary phase. This advantage is helpful in alleviating the overloading problem and improving the sensitivity of detection of separated sample by using FTIR measurement.

Based on the above consideration, a systematic work on the TLC/FTIR analysis using inorganic salts has been conducted in our laboratory [18–20]. Our experiments showed that barium fluoride and silver iodide particles may be used as new effective stationary phases for TLC/FTIR analysis. In further experiment, we realized that the thorough removal of the adsorbed water is very important for successful TLC/FTIR analysis. Barium fluoride particles tend to retain significant amount of adsorbed water, while it is much easier to remove

adsorbed water completely for silver iodide particles. Thus, we focus on the TLC/FTIR studies by using AgI particles as stationary phase.

In parallel, we have made considerable effort to develop a new approach to prepare TLC plates. In the traditional way of the preparation of TLC plate, polymeric adhesive is utilized to bind stationary phase particles together. However, polymeric adhesive has strong absorbance in IR region and brings about significant interference in the FTIR detection. To solve this problem, we develop an approach called “settlement volatilization method” to prepare TLC plates without polymeric adhesive.

Recently, we propose a new technique to prepare narrowband TLC plates [21]. The advantages of the narrowband TLC are as follows. (1) The preparation time is much reduced in comparison with that of the previous preparation of a TLC plate by using “settlement volatilization method.” (2) The usage of stationary phase in narrowband TLC plates decreases by about one order of magnitude in comparison with that of traditional TLC plates. This is very important for using expensive material (e.g., AgI particles) as a stationary phase. (3) The sensitivity of detection of a separated sample spot increases significantly by using narrowband TLC plates because the area of the separated spots is significantly reduced.

The application of TLC/FTIR techniques in our previous work was limited to simply separating and identifying mixtures of pigments. We notice that analysis of colorless mixture is one of the advantages of the TLC/FTIR approach. In the present work, a narrowband TLC plate by using AgI as stationary phase was utilized to analyze a mixture of benzamide and cholesterol. In addition, FTIR microscope with a mapping technique capability was used to reveal the distribution of colorless cholesterol and benzamide band on the narrowband TLC plate.

## 2. Experimental

**2.1. Reagents.** All reagents are of AR grade. Ethanol, chloroform, normal heptane, benzamide, cholesterol, hydrofluoric acid, and silver nitrate were obtained from Beijing Chemical Factory. Potassium iodide was a product of Sinopharm Chemical Reagent Co., Ltd.

Silver iodide was synthesized by a reaction between silver nitrate and potassium iodide. The experimental details of the preparation of silver iodide particles can be found in our previous work [19]. The diameters of the silver iodide particles are around 100 nm.

**2.2. Apparatus.** A Thermo-Fischer Nicolet iN10 MX FTIR spectrometer equipped with an IR microscope was used in the experiments.

### 2.3. Procedures

**2.3.1. Preparation of Mixed Sample Solutions.** 0.100 g benzamide was dissolved in 10.0 mL ethanol to prepare a 1 wt% benzamide solution. Similarly, 1% cholesterol solution was

prepared by dissolving 0.100 g cholesterol in 10.0 mL chloroform.

A mixed solution sample was prepared by mixing equal volumes of 1% cholesterol solution and 1% benzamide solution.

**2.4. Narrowband TLC Analysis.** We prepared narrowband TLC plate to conduct the experiment. The preparation process of the narrowband TLC plates is described in detail in our previous work [21].

The sample solution was manually spotted at one end of narrowband TLC plate by using a 0.3 mm glass capillary in diameter. After evaporation of the solvent, the narrowband TLC plate was developed by using an ethanol/heptane mixture as a mobile phase (the volume ratio between heptane and ethanol is 9 : 1). The typical development time was about 20–30 minutes.

**2.5. In Situ TLC-FTIR Detection.** Narrowband TLC plate after separation was dried at 100°C in a vacuum oven to remove residual mobile phase. Then, TLC plates were examined directly by using the FTIR microscope. To reveal the distribution of the cholesterol and benzamide spots on the narrowband TLC plate, FTIR mapping technique under linear scan mode was utilized. That is, FTIR spectrum of every tiny region on TLC plate ( $100\ \mu\text{m} \times 100\ \mu\text{m}$ ) is obtained sequentially along the direction of the diffusion of mobile phase. All the spectra were recorded under reflection mode at a resolution of  $16\ \text{cm}^{-1}$  and 16 scans were coadded. To improve the signal-to-noise ratio, reflect spectrum from gold mirror was used as background spectrum.

3D chromatogram that is utilized to reveal the distribution of cholesterol and benzamide spots was generated via a program written in our lab by using the software of MATLAB.

### 3. Results and Discussion

After separating cholesterol and benzamide, the photograph of narrowband TLC plate is shown in Figure 1. Since both cholesterol and benzamide are colorless substances, no separated sample spot can be observed. However, the separated cholesterol and benzamide spots can be successfully identified by using FTIR spectroscopic method. In this experiment, FT-IR spectrum of each tiny region on the narrowband TLC plate is sequentially recorded. The obtained FT-IR spectra are organized along the direction of the diffusion of mobile phase so that a 3D chromatogram (the first dimension is wavenumber from FTIR spectrum, the second dimension is migration distance, and the third dimension is absorbance) is constructed. The 3D chromatogram is manifested via a contour map mode. As shown in Figure 2, two separated spots can be clearly visualized in the 3D chromatogram. Typical FTIR spectra of the two spots, which are obtained by slicing the 3D chromatogram, are shown as trace 1 in Figures 3 and 4. Carbonyl band around  $1670\ \text{cm}^{-1}$  can be found in trace 1 of Figure 3 of the lower spot. These results suggest that the corresponding spot is benzamide spot. On the other hand, OH stretching band around  $3400\ \text{cm}^{-1}$  and C–H stretching



FIGURE 1: A photograph of the narrowband TLC plate after separation of cholesterol and benzamide mixtures (the width of the narrowband is 3 mm).

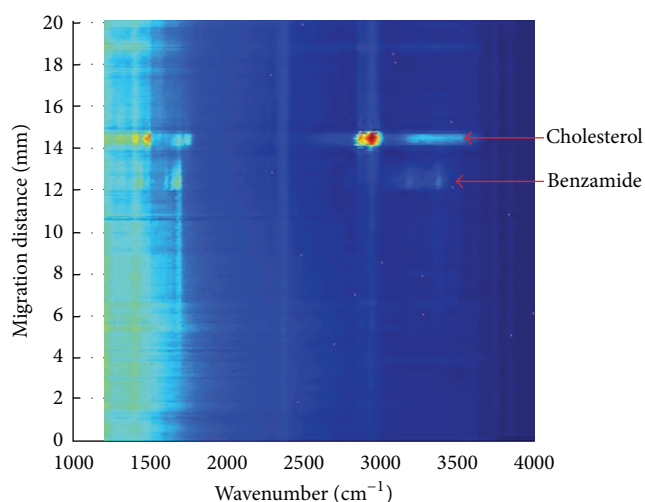


FIGURE 2: 3D chromatogram to characterize the distribution of the cholesterol and benzamide spots on a narrowband TLC plate.

band around  $2900\ \text{cm}^{-1}$  are observable in trace 1 of Figure 4. This result suggests that the corresponding spot is cholesterol spot.

To confirm that the above two spots are from benzamide and cholesterol, we recorded the reference FTIR spectra of benzamide and cholesterol via the following experiments: about  $0.1\ \mu\text{L}$  of ethanol solution containing 1% benzamide only and  $0.1\ \mu\text{L}$  of ethanol solution containing 1% cholesterol only were manually spotted on two TLC plates. After evaporation of solvent, the TLC plate was developed by using a mixture of ethanol and normal heptane (the volume ratio of normal heptane and ethanol is 9:1) as mobile phases. Afterwards, the two plates were dried at 100°C in a vacuum oven to remove residual mobile phase. We use FTIR microscope mapping technique to locate benzamide and

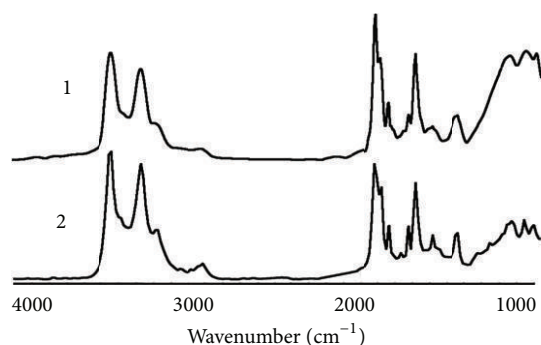


FIGURE 3: FTIR spectrum of benzamide spot (trace 1) on a narrow-band TLC plate. For comparison, a reference FTIR spectrum of pure benzamide (trace 2) is also included.

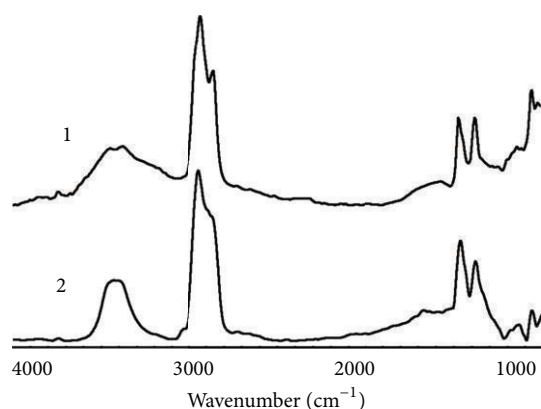


FIGURE 4: FTIR spectrum of cholesterol spot (trace 1) on a narrow-band TLC plate. For comparison, a reference FTIR spectrum (trace 2) of pure cholesterol is also included.

cholesterol spots on the two narrowband TLC plates. Then, we collected FTIR spectra on the benzamide and cholesterol spots. The obtained FTIR spectra are used as reference spectra and shown as trace 2 in Figures 3 and 4. As demonstrated in Figures 3 and 4, FTIR spectra of upper and lower spots are almost the same as the reference spectra of cholesterol and benzamide. This result confirms that the separated spots shown in Figure 2 are indeed cholesterol and benzamide.

#### 4. Conclusion

In this work, we use narrowband TLC plates by using AgI as stationary phase to separate benzamide and cholesterol. Then, the distribution of benzamide and cholesterol spots was probed by using FTIR microscope with spectral mapping technique and manifested by 3D chromatogram. Experimental results demonstrate that benzamide and cholesterol can be successfully separated by the narrowband TLC plate. In addition, characteristic band of benzamide and cholesterol can be identified from their FTIR spectra. Moreover, the FTIR spectrum of the separated benzamide and cholesterol spots on the narrowband TLC plate are roughly the same as the reference IR spectra of pure benzamide and cholesterol.

The present work demonstrates that TLC/FTIR technique is applicable in analysis of complex mixtures.

#### Conflict of Interests

The authors declare that there is no conflict of interests regarding the publication of this paper.

#### Acknowledgment

Financial support from the National Natural Science Foundation of China (51373003) is gratefully acknowledged.

#### References

- [1] M. Srivastava, Ed., *High-Performance Thin-Layer Chromatography (HPTLC)*, Springer, Heidelberg, Germany, 2011.
- [2] L. Y. He, Ed., *Method and Application of Planar Chromatography*, Chemical Industry Press, Beijing, China, 2005.
- [3] J. Sherma, "Planar chromatography," *Analytical Chemistry*, vol. 82, no. 12, pp. 4895–4910, 2010.
- [4] J. G. Wu, Ed., *Modern FTIR Spectroscopy Technology and Application*, Science and Technology Press, Beijing, China, 1994.
- [5] S. F. Weng, Ed., *Fourier Transform Infrared Spectrometer*, Chemical Industry Press, Beijing, 2nd edition, 2010.
- [6] R. N. McCoy and E. C. Fiebig, "Technique for obtaining infrared spectra of microgram amounts of compounds separated by thin layer chromatography," *Analytical Chemistry*, vol. 37, pp. 593–595, 1965.
- [7] P. A. Sturm, "Quantitative determination of individual tocopherols by thin layer chromatographic separation and spectrophotometry," *Analytical Chemistry*, vol. 38, no. 9, pp. 1244–1247, 1966.
- [8] C. J. Percival and P. R. Griffiths, "Direct measurement of the infrared spectra of compounds separated by thin-layer chromatography," *Analytical Chemistry*, vol. 47, no. 1, pp. 154–156, 1975.
- [9] M. P. Fuller and P. R. Griffiths, "Diffuse reflectance measurements by infrared fourier transform spectrometry," *Analytical Chemistry*, vol. 50, no. 13, pp. 1906–1910, 1978.
- [10] M. P. Fuller and P. R. Griffiths, "Infrared microsampling by diffuse reflectance Fourier transform spectrometry," *Applied Spectroscopy*, vol. 34, pp. 533–539, 1980.
- [11] G. E. Zuber, R. J. Warren, P. P. Begosh, and E. L. O'Donnell, "Direct analysis of thin-layer chromatography spots by diffuse reflectance fourier transform infrared spectrometry," *Analytical Chemistry*, vol. 56, no. 14, pp. 2935–2939, 1984.
- [12] L. B. Lloyd, R. C. Yeates, and E. M. Eyring, "Fourier transform infrared photoacoustic spectroscopy in thin-layer chromatography," *Analytical Chemistry*, vol. 54, no. 3, pp. 549–552, 1982.
- [13] R. L. White, "Analysis of thin-layer chromatographic adsorbates by Fourier transform infrared photoacoustic spectroscopy," *Analytical Chemistry*, vol. 57, no. 9, pp. 1819–1822, 1985.
- [14] N. D. Danielson, J. E. Katon, S. P. Bouffard, and Z. Zhu, "Zirconium oxide stationary phase for thin-layer chromatography with diffuse reflectance fourier transform infrared detection," *Analytical Chemistry*, vol. 64, no. 18, pp. 2183–2186, 1992.

- [15] S. P. Bouffard, J. E. Katon, A. J. Sommer, and N. D. Danielson, "Development of microchannel thin-layer chromatography with infrared microspectroscopic detection," *Analytical Chemistry*, vol. 66, no. 13, pp. 1937–1940, 1994.
- [16] W. He, R. Shanks, and G. Amarasinghe, "Analysis of additives in polymers by thin-layer chromatography coupled with Fourier transform-infrared microscopy," *Vibrational Spectroscopy*, vol. 30, no. 2, pp. 147–156, 2002.
- [17] W. He, G. Cheng, F. Zao, Y. Lin, J. Huang, and R. Shanks, "Separation and identification of multicomponent mixture by thin-layer chromatography coupled with Fourier transform-infrared microscopy," *Spectrochimica Acta Part A*, vol. 61, no. 8, pp. 1965–1970, 2005.
- [18] X. Liu, Q.-H. Pan, J. Ding et al., "Using barium fluoride fine particles as stationary phase for TLC/FTIR analysis," *Spectroscopy and Spectral Analysis*, vol. 31, no. 7, pp. 1767–1771, 2011.
- [19] Q. Zhu, X. Su, H. J. Wu et al., "The analysis for silver iodide fine particles of TLC/FTIR matrix," *Spectroscopy and Spectral Analysis*, vol. 32, no. 7, pp. 1790–1794, 2012.
- [20] W. Liu, H. J. Wu, X. P. Wang et al., "Preparation and application of barium fluoride particles as stationary phase for TLC-FTIR analysis," *Chemical Journal of Chinese Universities*, vol. 34, no. 6, pp. 1347–1352, 2013.
- [21] F. Wang and H. J. Wu, "Development of narrow-band TLC plates for TLC/FTIR analysis," *Analytical Methods*, vol. 5, pp. 4138–4144, 2013.



## Research Article

# Fluorescent Properties of Hymecromone and Fluorimetric Analysis of Hymecromone in Compound Dantong Capsule

Huanhuan Zhi,<sup>1,2</sup> Jingdan Wang,<sup>2</sup> Shujing Wang,<sup>2</sup> and Yongju Wei<sup>1,2</sup>

<sup>1</sup> College of Life Science, Hebei Normal University, Shijiazhuang 050024, China

<sup>2</sup> College of Chemistry and Material Science, Hebei Normal University, Shijiazhuang 050024, China

Correspondence should be addressed to Yongju Wei; weiyju@126.com

Received 5 September 2013; Accepted 21 October 2013

Academic Editor: Yizhuang Xu

Copyright © 2013 Huanhuan Zhi et al. This is an open access article distributed under the Creative Commons Attribution License, which permits unrestricted use, distribution, and reproduction in any medium, provided the original work is properly cited.

Fluorescence spectra of hymecromone (4MU) aqueous solutions are investigated at different pHs. Two fluorescent species of 4MU, neutral molecular form and anion form, are considered to be the main fluorescent forms. Quantum yields of the two forms are measured to be 0.74 at pH 5.98 and 0.95 at pH 9.75, respectively. The ionization constant of 7-hydroxyl proton of 4MU is determined to be  $pK_a = 7.85 \pm 0.03$  by a pH-fluorescence method. Addition of methanol into 4MU aqueous solution leads to a blue shift of maximum emission wavelength from 445 nm to 380 nm, and a decrease in fluorescence intensity. 3D fluorescence spectra of Chinese patent drug Compound Dantong Capsule (CDC) and its four component herbal drugs are also investigated. Based on their fluorescent properties, a novel fluorimetric method is proposed for the selective determination of 4MU in CDC without preseparation. The new method is suitable for the routine quality evaluation of CDC.

## 1. Introduction

Coumarins, both natural and synthetic, are of interest because of their multiple biological and photodynamic activities. They are extensively used as medicine and analytical reagent [1–7]. Hymecromone (4-Methyl-7-hydroxycoumarin, 7-Hydroxy-4-methylcoumarin, 4-Methylumbelliferone, abbreviated as 4MU) is a synthetic coumarin compound. It is claimed that 4MU and its derivatives or metal complexes possess diverse pharmacological properties, such as antiviral [8], antifungal and antioxidative [9], anticancer [10–13], anticoagulant, and spasmolytic activities [14, 15]. The fluorescence of 4MU had been observed early [16], a water-soluble polymeric fluorescent probe for measurement of near-neutral pH was synthesized based on the fluorescent properties of 4MU [17], and the effect of pH on fluorescence was restudied recently [18]; however, no comprehensive and detailed fluorescence spectra and quantum yield have been found in the literature.

Compound Dantong Capsule (CDC, also named Fufang Dantong Capsule) is a Chinese proprietary medicine [19]. It is effective in cure cholecystitis, cholangitis, intercurrent infection of gallbladder, and biliary tract concretion [19, 20].

The chemical composition of CDC includes 4MU (also named Dantong) and four kinds of Chinese herbal medicines, including *Herba Isodonis Lophanthoidis* (Xihuangcao), *Herba Artemisiae Scopariae* (Yinchen), *Herba Andrographis* (Chuanxinlian), and *Rhei Radix et Rhizoma* (Dahuang). The content of 4MU is one of the main quality indexes of CDC [21]. Earlier, the spectrophotometric method was applied for the determination of 4MU in CDC according to the absorbance of 4MU at 372 nm [19]. Later, since the interference of coexistent components, high performance liquid chromatographic methods (HPLC) were developed for the determination of 4MU in CDC [21–23]. So far, no fluorimetric method was reported for the determination of 4MU in CDC and other medicinal samples.

Fluorimetry has been recognized as one of the most useful analytical methods owing to its high sensitivity, good selectivity, simplicity, speediness, and low cost. It can be suitable for analysis of some complex samples such as traditional Chinese medicine containing a fluorescent component, especially in the case of a routine analysis. Three-dimensional fluorescence spectra (3D fluorescent fingerprint) have been used in our lab for qualitative identification of Chinese herbal medicines



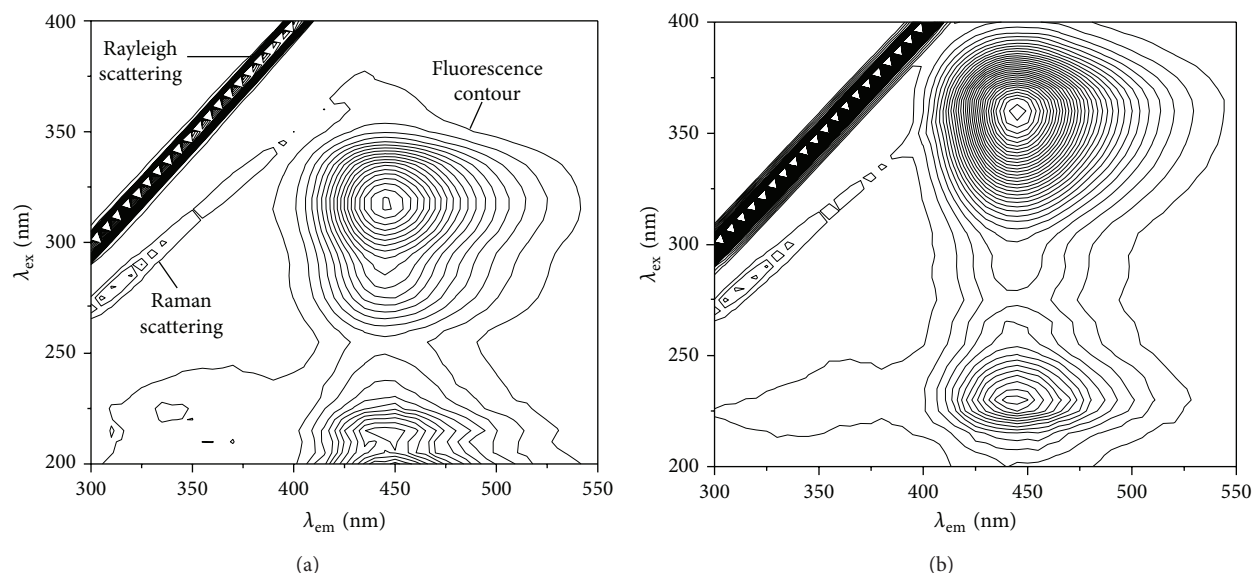


FIGURE 1: 3D fluorescence spectra of 4MU aqueous solution at different pH.  $c_{4MU}$ : 18.5 ng mL<sup>-1</sup>. (a) pH 5.98; (b) pH 9.75. Contour interval:  $R$ .

[24]. Moreover, a number of fluorimetric methods have been developed for quantitative determination of active components in medicinal materials, such as paeonol in *Cynanchi Paniculati Radix* (Xuchangqing) [25], camptothecin in common *Camptotheca* fruit (Xishuguo) [26], and arctiin in *Arctii Fructus* (Niubangzi) [27]. In this study, the fluorescent properties of 4MU are investigated, and its quantum yield and 7-hydroxyl proton ionization constant are measured. The fluorescent properties of CDC and its four consisting Chinese herbal medicines are also studied. Based on the spectral differences between 4MU and other components in CDC, a fluorimetric method is proposed for the determination of 4MU in CDC sample without preseparation.

## 2. Experimental

**2.1. Apparatus.** Fluorescence measurements were performed on a Hitachi (Tokyo, Japan) F-7000 spectrofluorimeter equipped with a xenon lamp, 1 cm quartz cell, and a UV-29 filter placed into the emission light path to remove secondary spectrum. The excitation and emission slits (band pass) 5 nm/5 nm were used throughout the work. Absorption spectra were recorded using a Shimadzu (Kyoto, Japan) UV-2501PC recording spectrophotometer with 1 cm quartz cell. An Orion (Beverly, USA) 868 pH/ISE meter was used for pH measurement.

**2.2. Chemicals and Materials.** Hymecromone (4MU, serial no. 100241-200503, a reagent for quantitative analysis, molecular weight: 176.17) and Chinese herbal medicine (comparison drug for qualitative identification) Xihuangcao (serial no. 121488-200501), Yinchen (serial no. 120950-200305), Chuanxinlian (serial no. 121082-200302), and Dahuang (serial no. 120984-200301) were purchased from the National Institute for the Control of Pharmaceuticals and Biological Products of China (Beijing, China). 4MU stock solution was

prepared by dissolving 3.61 mg reagent in 100 mL methanol (TEDIA, HPLC grade) and diluted to appropriate concentration with methanol as needed. Compound Dantong Capsule (CDC, product lot no. 100601) was produced by National Tsing Hua Pharmaceutical Co., Ltd. Hubei-day Saint, China. Quinine bisulphate (HPLC grade) was acquired from J&K Scientific Ltd. (Beijing, China); its solution was prepared by dissolving 391.47 mg reagent in 500 mL 0.05 mol L<sup>-1</sup> H<sub>2</sub>SO<sub>4</sub> and diluted to appropriate concentration with 0.05 mol L<sup>-1</sup> H<sub>2</sub>SO<sub>4</sub> when it was used. Britton-Robinson buffer solution was a mixture of phosphoric acid, boric acid, and acetic acid (each 0.02 mol L<sup>-1</sup>) and adjusted to an appropriate pH by addition of 0.1 mol L<sup>-1</sup> NaOH solution. All the buffer chemicals were of analytical grade. The water used throughout the study was doubly-deionized and verified to be free from fluorescence.

**2.3. General Procedure for Spectral Measurement.** A series of 10 mL volumetric flasks was added appropriate amount of 4MU or CDC and buffer solutions. The mixtures were diluted to the mark with water and mixed well. Fluorescence or absorption spectra were measured at room temperature. Meanwhile, Raman scattering of water at excitation wavelength of 350 nm was measured (expressed as  $R$ , for calibration of 3D fluorescence spectra) [24].

**2.4. Determination of Ionization Constant.** A number of solutions containing the same concentration of weak acid HB and different pH were prepared. Fluorescence intensity  $F$  and pH of each solution were measured. Then the ionization constant  $pK_a$  was calculated according to the following equation [28]:

$$pK_a = pH - \lg \frac{F_{HB} - F}{F - F_B}, \quad (1)$$

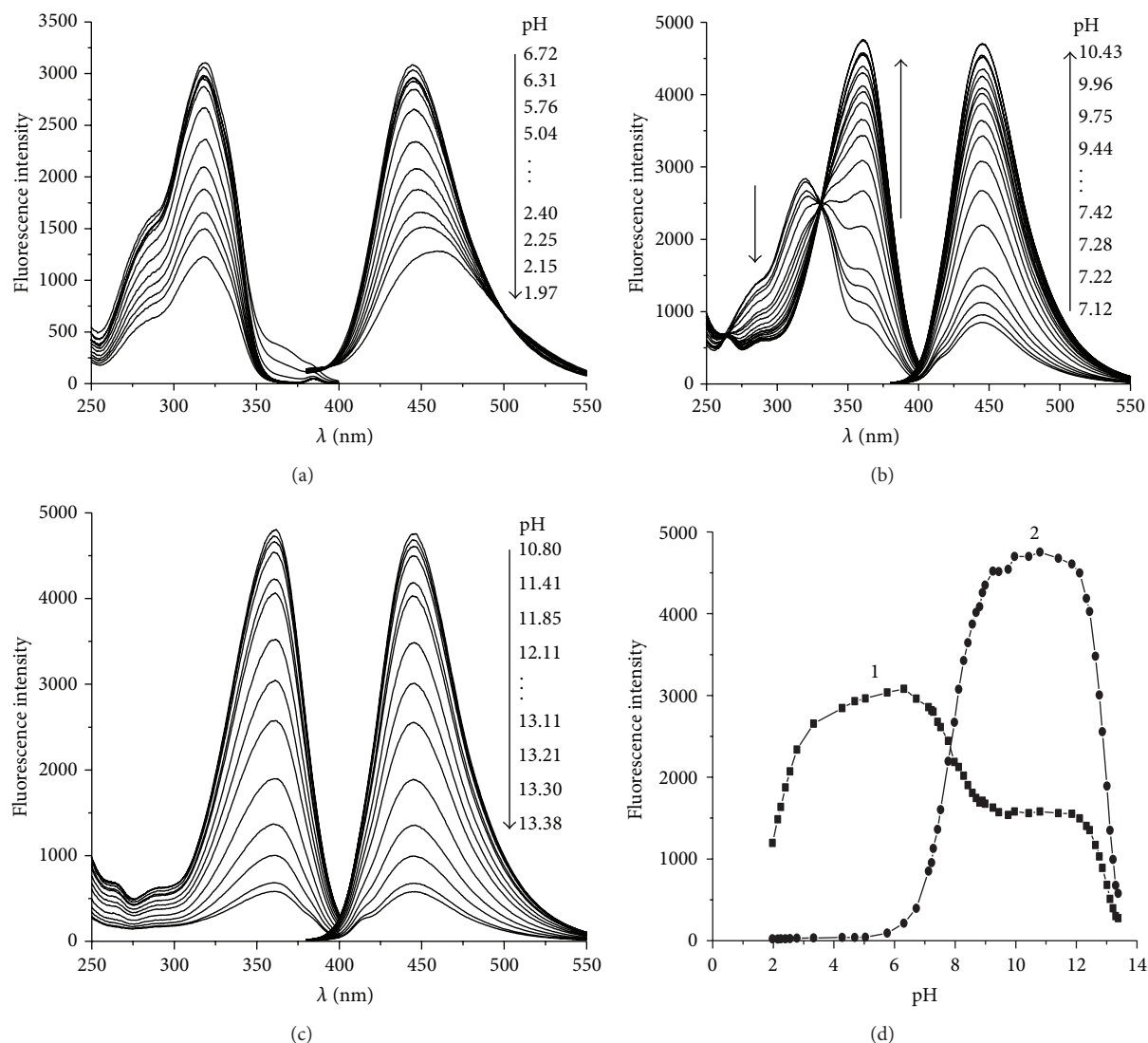


FIGURE 2: (a), (b) and (c) Fluorescence excitation and emission spectra of 4MU at different pH and (d) relationship between fluorescence intensity and pH.  $c_{4MU}$ :  $18.5 \text{ ng mL}^{-1}$ ;  $\lambda_{ex}/\lambda_{em}$ : (a) and (d(1)):  $320 \text{ nm}/445 \text{ nm}$ , (b), (c) and (d(2)):  $360 \text{ nm}/445 \text{ nm}$ .

where  $F_{HB}$  and  $F_B$  were the fluorescence intensity of HB and its conjugate base B; they can be measured at sufficient acidic pH where all HB species exist in the neutral molecular form and at sufficient alkaline pH where all HB species exist in the anion form, respectively.

**2.5. Measurement of Fluorescence Quantum Yield.** Quinine bisulphate was used as a reference (quantum yield 0.55 at excitation wavelength of  $313 \text{ nm}$ ) in measuring quantum yield of 4MU. For the measurement, quinine bisulphate and 4MU solutions were prepared in proper concentration so that the absorbance ( $A$ ) of the two solutions was similar and not larger than 0.05. Absorption and fluorescence spectra were recorded, and then quantum yields were calculated according to the following equation [28, 29]:

$$Y_u = Y_r \cdot \frac{F_u}{F_r} \cdot \frac{A_r}{A_u}, \quad (2)$$

where  $Y_u$  and  $Y_r$  were the fluorescence quantum yield of unknown and the reference,  $F_u$  and  $F_r$  were the integral fluorescence intensity of unknown and reference solutions, and  $A_u$  and  $A_r$  were the absorbance of unknown and reference solutions at their excitation wavelengths, respectively.

**2.6. Sample Preparation.** Dissolve  $9.21 \text{ mg}$  CDC powder in  $100 \text{ mL}$  methanol and dilute to  $0.921 \mu\text{g mL}^{-1}$  with methanol as sample solution.

### 3. Results and Discussion

#### 3.1. Fluorescence Properties of 4MU

**3.1.1. 3D Fluorescence Spectra of 4MU.** 3D (three-dimensional) fluorescence spectra of solvent blank and 4MU aqueous solutions at pH 5.98 and at pH 9.75 were measured as shown in Figure 1. The spectra indicated that the solvent used in

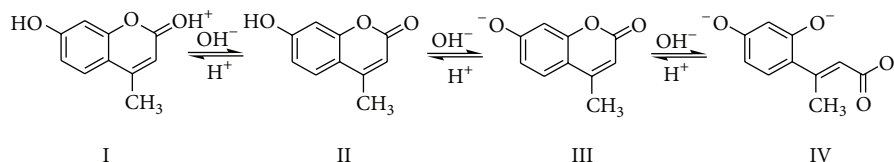


FIGURE 3: Proton ionization and hydrolysis process of 4MU.

this study was basically no fluorescence. 4MU can produce strong fluorescence in near neutral condition with maximum excitation wavelength ( $\lambda_{\text{ex}}$ ) of 320 nm and maximum emission wavelength ( $\lambda_{\text{em}}$ ) of 445 nm, while in weak alkaline condition, the fluorescence intensity enhanced,  $\lambda_{\text{ex}}$  red shifted from 320 nm to 360 nm, but  $\lambda_{\text{em}}$  remained constant. Figure 1 revealed that pH has an important influence on fluorescence.

**3.1.2. Effect of pH on Fluorescence.** As shown in Figure 2, effect of pH on fluorescence excitation and emission spectra of 4MU at various pHs were studied. In acidic conditions (pH 1.97–6.72), along with the decrease in pH, fluorescence intensity declined,  $\lambda_{\text{ex}}$  centered at 320 nm, and  $\lambda_{\text{em}}$  red shifted slightly from 445 nm to 455 nm. In the range of pH 7.12–10.43, along with the increase in pH, fluorescence emission at 445 nm enhanced, but the excitation band centered at 320 nm declined, meanwhile a new excitation band centered at 360 nm emerged and an iso-fluorescence point [30] formed at 330 nm. In the range of pH 10.80–13.38, along with the increase in pH, fluorescence emission at 445 nm gradually quenched while  $\lambda_{\text{ex}}$  and  $\lambda_{\text{em}}$  remained constant.

The relationship between pH and fluorescence intensity was summarized in Figure 2(d).

The variation of fluorescence spectra implies that the solution equilibrium or molecular structure of 4MU changed along with the change in pH. According to Figure 2, we suppose that the proton dissociation and hydrolysis process of 4MU is as shown in Figure 3.

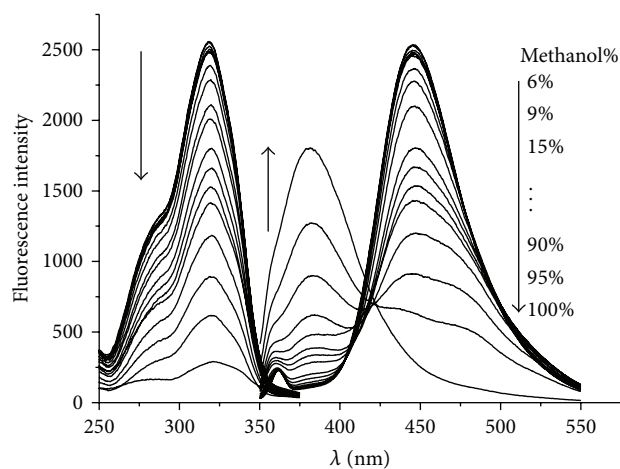
The structure of 4MU contains a benzene ring (linked with 7-OH) and a lactonic ring (include lactone bond and 2-C=O). In strong acid conditions, the 2-carbonyl oxygen protonated [28, 30] to form a cationic species (type I), leading to a decrease in fluorescence intensity and a red shift in emission wavelength. In near neutral conditions (pH 4.0–7.0), 4MU exist mainly as molecular form (type II) which have strong fluorescence with  $\lambda_{\text{ex}}$  of 320 nm and  $\lambda_{\text{em}}$  of 445 nm. In weak alkaline conditions (pH 9.0–12.0), 7-hydroxyl proton dissociated and 4MU exist mainly as anion form (type III) which have stronger fluorescence with  $\lambda_{\text{ex}}$  of 360 nm and  $\lambda_{\text{em}}$  of 445 nm. In strong alkaline conditions (pH > 12.0), the hydrolysis of lactone bond take place [28, 31], leading to a fluorescence quenching.

**3.1.3. Ionization Constant of 7-Hydroxyl Proton.** With the above discussion, ionization constant of 7-OH proton can be determined in suitable conditions. Using the pH-fluorescence method described in Section 2.4, the ionization constant of 7-hydroxyl proton was determined to be  $\text{p}K_a = 7.85 \pm 0.03$  (Table 1).

TABLE 1: Determination of ionization constant of 4MU.

pH	$F$	$\lg[(F_{\text{HB}} - F)/(F - F_{\text{B}})]^*$	$\text{p}K_a$	Average $\text{p}K_a$
7.52	1601	−0.30	7.82	$7.85 \pm 0.03$
7.77	2195	−0.07	7.84	
7.98	2672	0.11	7.87	
8.12	3074	0.26	7.86	
8.28	3427	0.41	7.87	

\*  $F_{\text{HB}} = 21.18$ ,  $F_{\text{B}} = 4753$ .

FIGURE 4: Fluorescence spectra of 4MU in aqueous solutions containing different amounts of methanol.  $c_{4\text{MU}}: 18.5 \text{ ng mL}^{-1}$ ; pH: 5.98;  $\lambda_{\text{ex}}/\lambda_{\text{em}}: 320 \text{ nm}/445 \text{ nm}$ .

In addition, according to the relationship between fluorescence intensity and pH, we can graphically estimate the ionization constant. In Figure 2(d), the abscissa of the intersection of curve (a) and curve (b) is about 7.85, which is just the  $\text{p}K_a$ .

The ionization constant determined above is close to the ionization constant of umbelliferone;  $\text{p}K_a = 7.61 \pm 0.03$  [28]. The little difference between the two constants reflects the impact of 4-methyl on the acidity of 7-hydroxyl proton.

**3.1.4. Effect of Solvent on Fluorescence.** Solvent polarity usually has a profound effect on the emission spectral properties of fluorophores and further influences the sensitivity of a fluorimetric method. Figure 4 shows the fluorescence spectra of 4MU in aqueous solutions containing different amounts of methanol. Along with the increase percentage of methanol, fluorescence emission band centered at 445 nm gradually

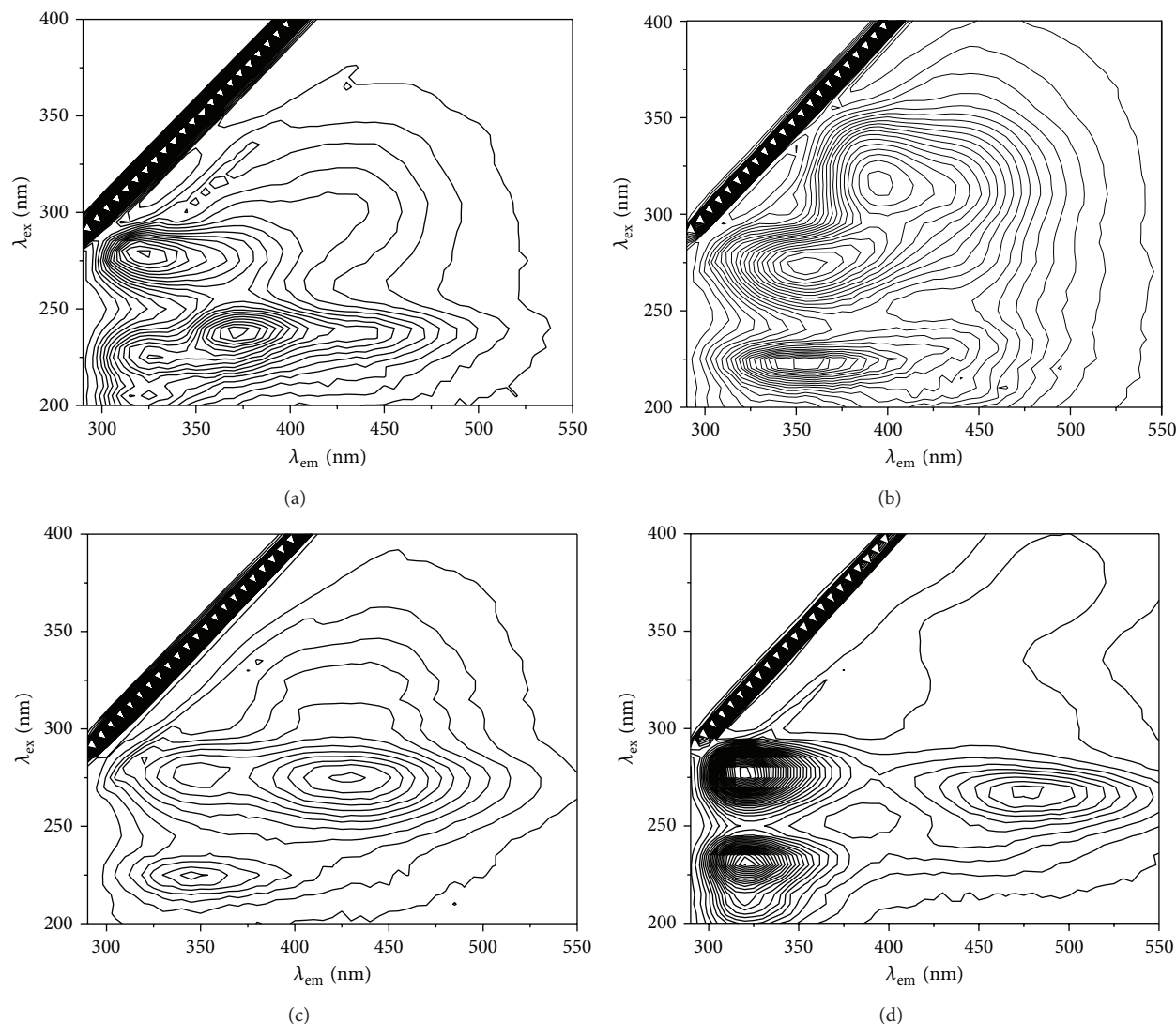


FIGURE 5: 3D fluorescence spectra of four kinds of Chinese herbal medicines in CDC. (a) Xihuangcao,  $c$ :  $400 \mu\text{g mL}^{-1}$ ; (b) Yinchen,  $c$ :  $400 \mu\text{g mL}^{-1}$ ; (c) Chuanxinlian,  $c$ :  $400 \mu\text{g mL}^{-1}$ ; (d) Dahuang,  $c$ :  $100 \mu\text{g mL}^{-1}$ . Contour interval:  $R$ .

declined, while a new emission band centered at 380 nm emerged. When the percentage of methanol reached 100%, the  $\lambda_{\text{em}}$  blue shifted to 380 nm; however, the fluorescence intensity was less than that in aqueous solutions. Therefore, we choose water as the appropriate solvent in establishing a fluorimetric method in the following study, and control the methanol percentage in aqueous solution no more than 20% to obtain sensitive and stable fluorescence.

**3.1.5. Measurement of Fluorescence Quantum Yield of 4MU.** Using the method described in Section 2.5, quantum yields of 4MU in near neutral (pH 5.98) and weak alkaline (pH 9.75) conditions were measured, as shown in Table 2. In near neutral solution, 4MU exist as molecular form; its quantum yield at excitation wavelength 320 nm was measured to be 0.74. In weak alkaline solution, 4MU exist as anion form; its quantum yield at excitation wavelength 360 nm was measured to be 0.95. These results indicate that 4MU is

an excellent fluorophore. A fluorimetric method for determination of 4MU in Chinese patent drug should be very sensitive either in near neutral or in weak alkaline conditions.

### 3.2. Determination of 4MU in Compound Dantong Capsule

**3.2.1. 3D Fluorescence Spectra of Four Kinds of Chinese Herbal Medicines in CDC.** The key point for developing a fluorimetric method is to understand the fluorescent properties of the analyte and other components in the sample, then find a way to avoid interference of the coexistent components on the fluorescence of the analyte. For these reason, 3D fluorescence spectra of four kinds of Chinese herbal materials in CDC were measured and shown in Figure 5.

From Figure 5 we showed that all the four kinds of Chinese herbal medicines contain fluorescent components. The interference of these components on the fluorescence of 4MU seems to be a serious problem. However, we noted



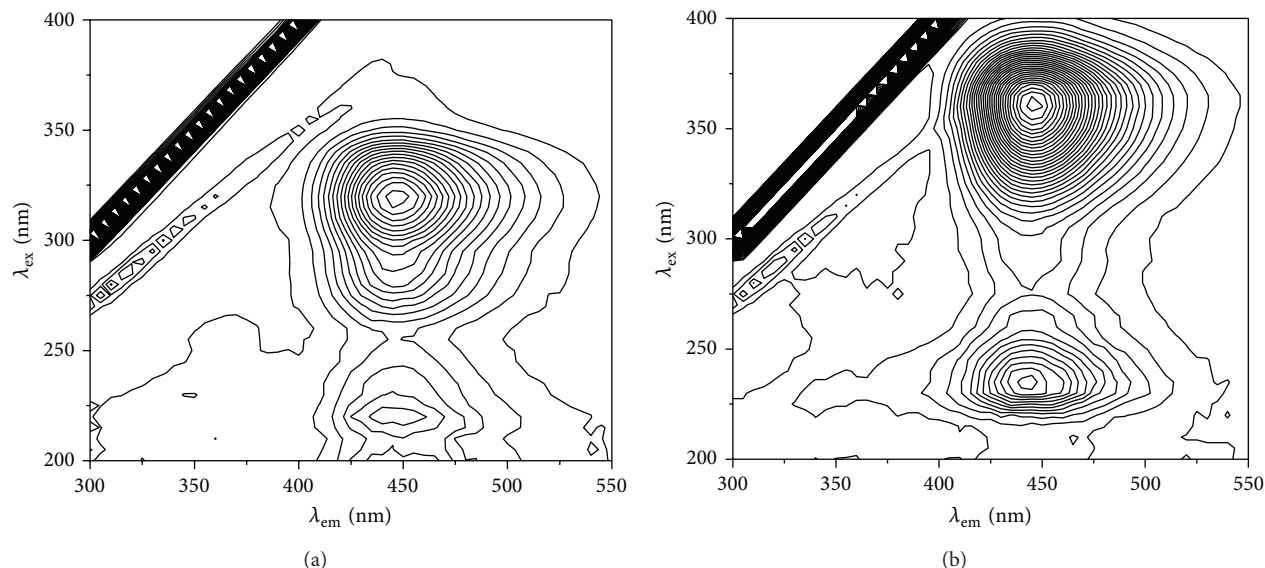


FIGURE 6: 3D fluorescence spectra of CDC solution at different pH.  $c_{\text{CDC}}: 55.3 \text{ ng mL}^{-1}$ . (a) pH 5.85; (b) pH 9.22. Contour interval:  $R$ .

TABLE 2: Measurement of fluorescence quantum yield of 4MU in different condition.

$\lambda_{\text{ex}}/\text{nm}$	Quinine bisulphate			4MU (pH 5.98)			4MU (pH 9.75)		
	$A$	$F^*$	$Y$	$A$	$F^*$	$Y$	$A$	$F^*$	$Y$
313	0.0365	105566	0.55	0.0440	178748	0.77			
320	0.0391	104878	0.51	0.0488	190213	0.74			
350	0.0411	123457	0.57				0.0440	220646	0.95
360	0.0320	95986	0.57				0.0481	239780	0.95

$F^*$  wavelength range of integral fluorescence intensity: 380 nm~600 nm.

that the concentrations of these herbal medicines in Figure 5 ( $400 \mu\text{g mL}^{-1} \sim 100 \mu\text{g mL}^{-1}$ ) were much higher than the concentration of 4MU in Figure 1 ( $18.5 \text{ ng mL}^{-1}$ ). So, whether these herbal medicines in CDC interfere with the fluorescence of 4MU should be considered further from the view point of concentration.

**3.2.2. 3D Fluorescence Spectra of CDC.** Figure 6 shows the 3D fluorescence spectra of CDC dilute solutions at pH 5.85 and at pH 9.22. Comparing Figure 6 to Figure 1, we figured out that the two pictures are basically the same. The fluorescence peaks presented in Figure 5 are not emerged in Figure 6. This result indicated that the fluorescence of those four herbal medicines in CDC is too weak to be seen, either because of their low concentration or due to their poor luminous ability. So, we can conclude that the coexistent components in CDC do not interfere with the fluorescence of 4MU. The content of 4MU in CDC can be determined simply by a fluorimetric method.

From Figures 6 and 2, we also know that the fluorimetric method may be performed at near neutral or at weak alkaline pH. For simplicity, we prefer the method to be performed at near neutral pH so that the fluorescence intensity of CDC water solution can be measured directly without using a buffer solution.

**3.2.3. Determination of 4MU in CDC by a Standard Curve Method.** A series of standard aqueous solutions containing different amounts of 4MU, from  $1.55$  to  $31.0 \text{ ng mL}^{-1}$ , were prepared. Fluorescence spectra, as shown in Figure 7(a), and fluorescence intensity at measuring wavelength of  $\lambda_{\text{ex}}/\lambda_{\text{em}} = 320 \text{ nm}/445 \text{ nm}$  of each solution were measured. A linear calibration curve of fluorescence intensity against concentration was plotted, as shown in Figure 7(b). The regression equation obtained was  $I_F = 5.5 + 104.1c \text{ (ng mL}^{-1}\text{)}$ , with correlation coefficient  $R = 0.9998$  ( $n = 13$ ).

A number of solutions containing different amounts of CDC were prepared and their fluorescence intensities at wavelength of  $\lambda_{\text{ex}}/\lambda_{\text{em}} = 320 \text{ nm}/445 \text{ nm}$  were recorded. Using the calibration curve, the 4MU content in CDC sample was determined to be  $33.35 \pm 0.10\%$ , as shown in Table 3.

**3.2.4. Determination of 4MU in CDC by a Standard Addition Method.** As shown in Figure 8, a standard addition method was employed to verify the result obtained above. The regression equation obtained was  $I_F = 636.9 + 105.3c \text{ (ng mL}^{-1}\text{)}$ , with correlation coefficient  $R = 0.9998$  ( $n = 5$ ). The content of 4MU in CDC sample was calculated to be  $33.3\%$ , which was coincident with the result obtained by standard curve method.



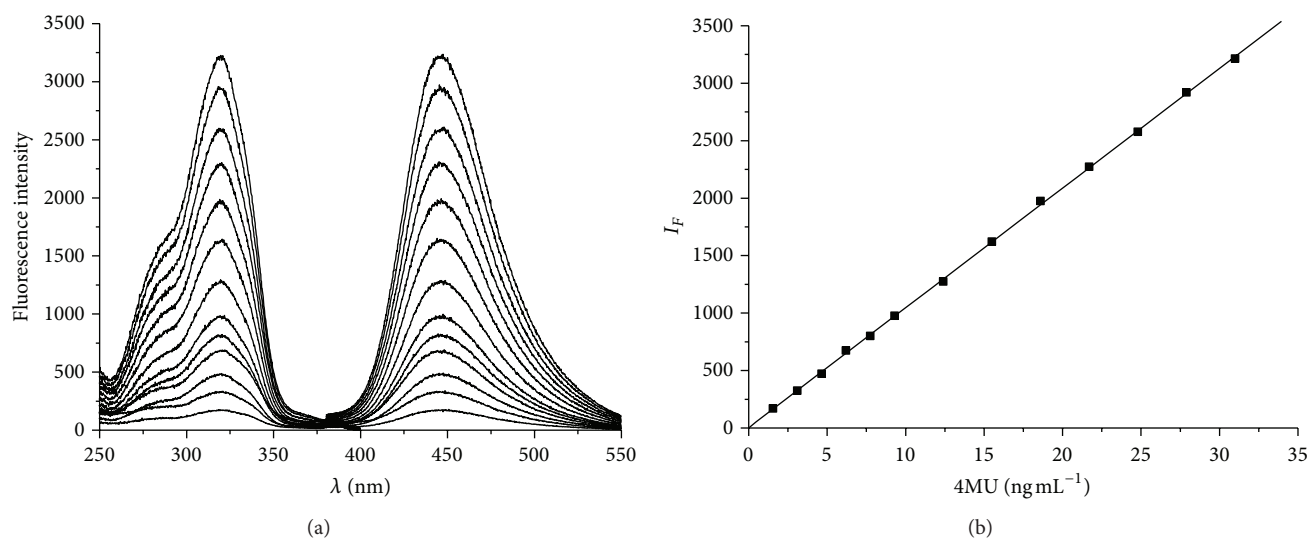


FIGURE 7: (a) Fluorescence spectra of 4MU in different concentrations; (b) plot of fluorescence intensity versus concentration. pH: 5.98;  $\lambda_{\text{ex}}/\lambda_{\text{em}}$ : 320 nm/445 nm.

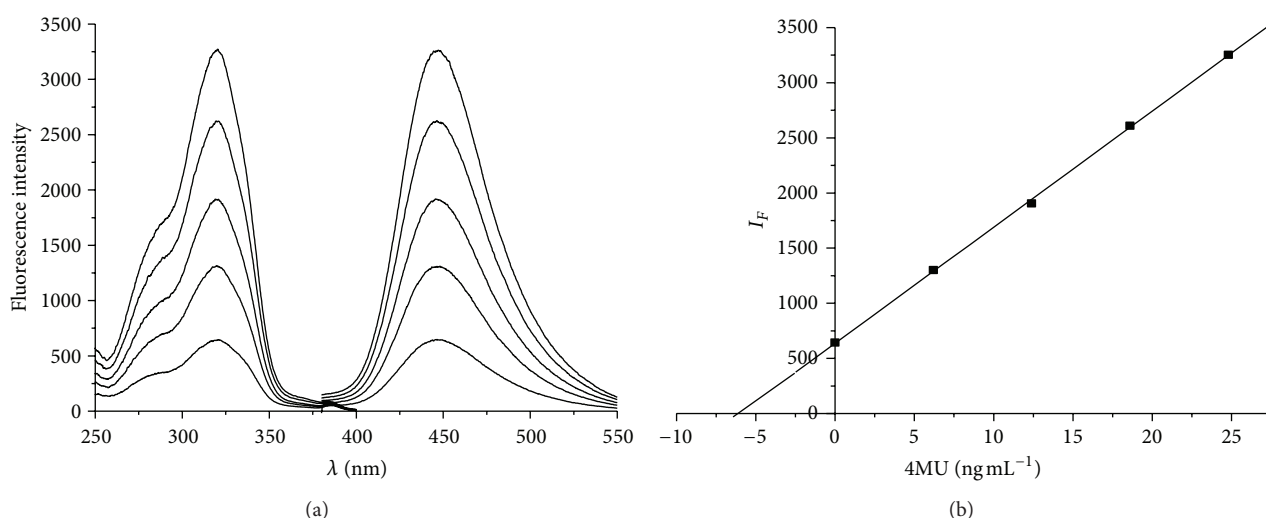


FIGURE 8: (a) Fluorescence spectra and (b) plot of fluorescence intensity *versus* concentration of a standard addition method for the determination of 4MU in CDC sample. pH: 5.98;  $\lambda_{\text{ex}}/\lambda_{\text{em}}$ : 320 nm/445 nm.

TABLE 3: Determination of 4MU in CDC by standard curve method.

No.	1	2	3	4	5
CDC added (V/mL)	0.20	0.40	0.60	0.80	1.00
Fluorescence intensity ( $I_F$ )	643.5	1285	1924	2561	3217
4MU determined ( $\text{ng mL}^{-1}$ )	6.13	12.3	18.4	24.5	30.8
4MU content in CDC (%)	33.3	33.4	33.3	33.3	33.5
Average content (%)	$33.4 \pm 0.1$				

According to the CDC drug label, the content of 4MU in CDC is 100 mg per grain (0.3 g). It is evident that the analytical result of this method agrees with the drug label.

#### 4. Conclusion

Hymecromone (4MU) is an excellent fluorophore. Acidity and solvent have important influence on its fluorescence. In near neutral aqueous solutions, 4MU exist mainly as neutral molecular form which can be produced strong fluorescence at 445 nm. In weak alkaline solutions, 4MU exist mainly as anion form which can be produced stronger fluorescence at 445 nm. In methanol solution, the fluorescence peak at 445 nm blue shifted to 380 nm and the fluorescence intensity declined in a certain extent. There is a good linear relationship between fluorescent intensity and 4MU concentration. The 3D fluorescence spectra of Chinese patent drug CDC dilute solutions are very similar to the 3D fluorescence spectra of 4MU, indicating that the main fluorescent component in

CDC is 4MU. The coexistent components in CDC do not interfere with the fluorescence of 4MU because of their low concentration or poor luminous ability. So, the content of 4MU in CDC can be determined simply by fluorimetric method without preseparation.

## Abbreviations

CDC: Compound Dantong Capsule (Fufang Dantong Capsule)

$\lambda_{\text{ex}}$ : Maximum excitation wavelength

$\lambda_{\text{em}}$ : Maximum emission wavelength.

## Conflict of Interests

The authors declare that they have no conflict of interests.

## Acknowledgment

This work was supported by the National Natural Science Foundation of China (nos. 20675025, 20975029, and 81173496).

## References

- [1] Z. Zhou, N. Li, and A. Tong, "A new coumarin-based fluorescence turn-on chemodosimeter for  $\text{Cu}^{2+}$  in water," *Analytica Chimica Acta*, vol. 702, no. 1, pp. 81–86, 2011.
- [2] L. Y. Wang, H. H. Li, and D. R. Cao, "A new photoresponsive coumarin-derived Schiff base: chemosensor selectively for  $\text{Al}^{3+}$  and  $\text{Fe}^{3+}$  and fluorescence "turn-on" under room light," *Sensors and Actuators B*, vol. 181, pp. 749–755, 2013.
- [3] K. Li, N. Li, X. Chen, and A. Tong, "A ratiometric fluorescent chemodosimeter for  $\text{Cu}(\text{II})$  in water with high selectivity and sensitivity," *Analytica Chimica Acta*, vol. 712, pp. 115–119, 2012.
- [4] H. X. Xu, X. Q. Wang, C. L. Zhang, Y. P. Wu, and Z. P. Liu, "Coumarin-hydrazone based high selective fluorescence sensor for copper(II) detection in aqueous solution," *Inorganic Chemistry Communications*, vol. 34, pp. 8–11, 2013.
- [5] X. B. Huang, Y. Dong, Q. W. Huang, and Y. X. Cheng, "Hydrogen bond induced fluorescence recovery of coumarin-based sensor system," *Tetrahedron Letters*, vol. 54, pp. 3822–3825, 2013.
- [6] N. Chattopadhyay, A. Mallick, and S. Sengupta, "Photophysical studies of 7-hydroxy-4-methyl-8-(4'-methylpiperazin-1'-yl) methylcoumarin: a new fluorescent chemosensor for zinc and nickel ions in water," *Journal of Photochemistry and Photobiology A*, vol. 177, no. 1, pp. 55–60, 2006.
- [7] P. Mladěnka, K. Macáková, L. Zatloukalová et al., "In vitro interactions of coumarins with iron," *Biochimie*, vol. 92, no. 9, pp. 1108–1114, 2010.
- [8] M. Mazzei, E. Nieddu, M. Miele et al., "Activity of Mannich bases of 7-hydroxycoumarin against Flaviviridae," *Bioorganic and Medicinal Chemistry*, vol. 16, no. 5, pp. 2591–2605, 2008.
- [9] B. Sarkanj, M. Molnar, M. Cacic, and L. Gille, "4-Methyl-7-hydroxycoumarin antifungal and antioxidant activity enhancement by substitution with thiosemicarbazide and thiazolidinone moieties," *Food Chemistry*, vol. 139, pp. 488–495, 2013.
- [10] H. Morohashi, A. Kon, M. Nakai et al., "Study of hyaluronan synthase inhibitor, 4-methylumbelliferone derivatives on human pancreatic cancer cell (KPI-NL)," *Biochemical and Biophysical Research Communications*, vol. 345, no. 4, pp. 1454–1459, 2006.
- [11] S. S. Bhattacharyya, S. Paul, S. K. Mandal, A. Banerjee, N. Boujedaini, and A. R. Khuda-Bukhsh, "A synthetic coumarin (4-Methyl-7 hydroxy coumarin) has anti-cancer potentials against DMBA-induced skin cancer in mice," *European Journal of Pharmacology*, vol. 614, no. 1–3, pp. 128–136, 2009.
- [12] K. Harada, H. Kubo, Y. Tomigahara et al., "Coumarins as novel  $17\beta$ -hydroxysteroid dehydrogenase type 3 inhibitors for potential treatment of prostate cancer," *Bioorganic and Medicinal Chemistry Letters*, vol. 20, no. 1, pp. 272–275, 2010.
- [13] A. Kultti, S. Pasonen-Seppänen, M. Jauhiainen et al., "4-Methylumbelliferone inhibits hyaluronan synthesis by depletion of cellular UDP-glucuronic acid and downregulation of hyaluronan synthase 2 and 3," *Experimental Cell Research*, vol. 315, no. 11, pp. 1914–1923, 2009.
- [14] I. P. Kostova, I. I. Manolov, I. N. Nicolova, and N. D. Danchev, "New metal complexes of 4-methyl-7-hydroxycoumarin sodium salt and their pharmacological activity," *Il Farmaco*, vol. 56, no. 9, pp. 707–713, 2001.
- [15] I. Kostova, I. Manolov, I. Nicolova, S. Konstantinov, and M. Karaivanova, "New lanthanide complexes of 4-methyl-7-hydroxycoumarin and their pharmacological activity," *European Journal of Medicinal Chemistry*, vol. 36, no. 4, pp. 339–347, 2001.
- [16] L. D. Li and G. Z. Jin, "Luminescence properties of 4-Methyl-7-hydroxy-coumarin," *Chinese Journal of Analytical Chemistry*, vol. 22, no. 5, pp. 440–444, 1994.
- [17] S. Dong, H. Ma, X. Li, M. Sun, and X. Duan, "Synthesis of a new water-soluble polymeric probe and its fluorescent properties for ratiometric measurement of near-neutral pH," *Analytical Letters*, vol. 37, no. 14, pp. 2937–2948, 2004.
- [18] I. Jones, J. Hamilton, R. Srivastava, and P. Galloway, "Effect of neutral and acid pH on the fluorescence of 4-methylumbelliferone and the implications for dry blood spot assays," *Molecular Genetics and Metabolism*, vol. 108, no. 2, article S51, 2013.
- [19] Pharmacopoeia Committee of Chinese Ministry of Health, *Traditional Chinese Medicine Drugs Preparation*, vol. 5, 1991.
- [20] A. Abate, V. Dimartino, P. Spina et al., "Hymecromone in the treatment of motor disorders of the bile ducts: a multicenter, double-blind, placebo-controlled clinical study," *Drugs under Experimental and Clinical Research*, vol. 27, no. 5–6, pp. 223–231, 2001.
- [21] L. Zhang, B. Y. Li, and A. L. Yang, "Studies on the quality standard for Compound Dantong Capsule," *Tianjin Pharmacy*, vol. 16, no. 5, pp. 15–17, 2004.
- [22] L. Zhang and J. Zhu, "Determination of the content and dissolution of hymecromone in Compound Dantong Capsules by HPLC," *Traditional Chinese Drug Research & Clinical Pharmacology*, vol. 17, no. 3, pp. 222–224, 2006.
- [23] L. R. Zheng, D. Liang, and Y. Chen, "Determination of 7-hydroxy-4-methylcoumarin in Compound Dantong Capsule by HPLC," *Pharmaceutical and Clinical Research*, vol. 16, no. 4, pp. 333–334, 2008.
- [24] Y. J. Wei, *3D Fluorescent Fingerprint of Chinese Herbal Medicine*, Science Press, Beijing, China, 2012.
- [25] F. Yang, C. G. Liu, and Y. J. Wei, "Fluorimetric analysis of paeonol in Chinese herbal medicine Cynanchi Paniculati Radix by aluminum ion-sensitized fluorescence," *Acta Pharmaceutica Sinica B*, vol. 2, no. 3, pp. 294–299, 2012.

- [26] L. P. Wang and Y. J. Wei, "Fluorimetric analysis of camptothecin in Chinese herbal medicine common Camptotheca fruit," *Acta Pharmaceutica Sinica*, vol. 47, no. 10, pp. 1370–1374, 2012.
- [27] S. J. Wang, Q. Zhang, L. P. Wang, and Y. J. Wei, "Fluorescent properties of arctiin and arctigenin and fluorimetric analysis of arctiin in traditional Chinese medicine Arctii Fructus," *Journal of Instrumental Analysis*, vol. 33, 2014.
- [28] J. Zhang, C. Liu, and Y. Wei, "Fluorescence quantum yield and ionization constant of umbelliferone," *Huaxue Tongbao*, vol. 74, no. 10, pp. 957–960, 2011.
- [29] J. G. Xu and Z. B. Wang, *Fluorimetry*, Science Press, Beijing, China, 3rd edition, 2007.
- [30] C. G. Liu, Y. Z. Xu, Y. J. Wei et al., "Fluorescence spectra and protonation of ofloxacin," *Spectroscopy and Spectral Analysis*, vol. 25, no. 4, pp. 584–587, 2005.
- [31] L. Y. Kong, *Coumarin Chemistry*, Chemical Industry Press, Beijing, China, 1st edition, 2008.

## Research Article

# Preparation and Characterization of Lanthanum Carbonate Octahydrate for the Treatment of Hyperphosphatemia

Anqi He,<sup>1</sup> Fengshan Zhou,<sup>2</sup> Fang Ye,<sup>3</sup> Ying Zhang,<sup>1,4</sup> Xiren He,<sup>5</sup>  
Xin Zhang,<sup>1,6</sup> Ran Guo,<sup>1</sup> Xing Zhao,<sup>5</sup> Yan Sun,<sup>1,7</sup> Ming Huang,<sup>3</sup>  
Qin Li,<sup>4</sup> Zhanlan Yang,<sup>1</sup> Yizhuang Xu,<sup>1</sup> and Jinguang Wu<sup>1</sup>

<sup>1</sup> College of Chemistry and Molecular Engineering, Peking University, Beijing 100871, China

<sup>2</sup> School of Materials Science and Technology, China University of Geosciences, Beijing 100083, China

<sup>3</sup> Beijing Coway Pharm. Co. Ltd., Beijing 100094, China

<sup>4</sup> School of Medicine, Henan University, Kaifeng 471003, China

<sup>5</sup> Tianjin Cenway Pharm. Co. Ltd., Tianjin 300480, China

<sup>6</sup> College of Pharmacy, Liaoning University of Traditional Chinese Medicine, Shenyang 11660, China

<sup>7</sup> College of Chemistry and Material Science, Hebei Normal University, Shijiazhuang 050024, China

Correspondence should be addressed to Fengshan Zhou; zhoufs@pku.edu.cn and Yizhuang Xu; xyz@pku.edu.cn

Received 6 September 2013; Accepted 15 October 2013

Academic Editor: Isao Noda

Copyright © 2013 Anqi He et al. This is an open access article distributed under the Creative Commons Attribution License, which permits unrestricted use, distribution, and reproduction in any medium, provided the original work is properly cited.

We proposed a new approach to prepare lanthanum carbonate via reactions between lanthanum chloride and  $\text{NaHCO}_3$ . In the reaction, small amount of  $\text{NaHCO}_3$  solution was firstly added to the acidic lanthanum chloride solution to generate lanthanum carbonate nuclei and then  $\text{NaHCO}_3$  is added to the lanthanum chloride at a constant speed. This approach makes both precipitation reaction and neutralization reaction take place simultaneously. Consequently, lanthanum carbonate is produced at low pH environment (pH below 4.0) so that the risk of generating lanthanum carbonate hydroxide is reduced. The product of the above reaction is validated by EDTA titration, elemental analysis, and XRD characterization. In addition, we established a FTIR spectroscopic method to identify  $\text{La}(\text{OH})\text{CO}_3$  from  $\text{La}_2(\text{CO}_3)_2 \cdot 8\text{H}_2\text{O}$ . Lanthanum carbonate exhibits considerable ability to bind phosphate.

## 1. Introduction

Hyperphosphatemia is a complication of end stage renal failure. In healthy adults, the average daily intake of phosphate is around 1000–1500 mg, which is balanced by faecal and urinary outputs [1]. For patients with renal failure, however, the phosphate excretion ability of kidneys is reduced significantly. Consequently, the concentration of phosphate in the blood increases, leading to hyperphosphatemia [2]. Hyperphosphatemia causes secondary hyperparathyroidism, renal osteodystrophy, and other diseases. Moreover, high concentration of phosphate in serum results in the formation of calcium phosphate precipitates. Large amount of calcium phosphate precipitates deposited in blood vessels may lead to fetal cardiovascular and cerebrovascular problems in end stage renal failure patients [3].

Current treatment of hyperphosphatemia involves dietary phosphate restrictions, dialysis, and taking phosphate binder and vitamin D [3]. Most dietary phosphate is derived from protein, and the phosphate content has an almost linear correlation with protein intake. Dialysis patients have a higher dietary protein requirement than healthy persons [4]. It is difficult to rely on dietary restrictions to achieve control of phosphate. Moreover, dialysis provides inadequate removal of phosphate in serum. Therefore, renal failure patients have to take phosphate binders [5].

The use of phosphate binder began in the early 1970s [5] and the earliest phosphate binders are aluminum-based compounds. The drug is highly effective and cheap [1]. However, aluminum may accumulate in bone, brain, heart, and liver, causing aluminum toxicity in long-term use [6, 7]. Later, a calcium-based phosphate binder was developed.

However, the efficacy of the calcium-based drug turned out to be lower than that of the aluminum-based compound. Moreover, calcium-based phosphate binder can cause hypercalcaemia and gastrointestinal adverse effects [2]. Therefore, ideal phosphate binders that are safe and highly effective in binding phosphate are needed [6].

Lanthanum carbonate is an ideal phosphate binder. It prevents the adsorption of dietary phosphate by forming insoluble lanthanum phosphate. It has been reported that lanthanum carbonate binds phosphate optimally at pH 3–5, while retaining binding activity at pH 1–7 [8, 9]. *In vitro* studies suggest that the efficacy of lanthanum phosphate is comparable to that of aluminium compounds in binding with phosphate [1]. The FDA has approved that lanthanum carbonate can be utilized as a phosphate binder for renal failure patients.

Concerning the preparation of lanthanum carbonate, there are several approaches reported in the literature [10, 11]. However, these methods have unresolved problems. For example, it has been reported that lanthanum carbonate can be prepared by a reaction between  $\text{Na}_2\text{CO}_3$  and  $\text{LaCl}_3$  in aqueous solutions. We notice that lanthanum ion possesses strong ability to bind hydroxide ion when the pH value of the aqueous solution is high. On the other hand, the pH value of an aqueous solution of  $\text{Na}_2\text{CO}_3$  is rather high. As a result, the reaction between  $\text{Na}_2\text{CO}_3$  and  $\text{LaCl}_3$  may produce undesirable  $\text{La}(\text{OH})\text{CO}_3$  as a side product with lanthanum carbonate.

Although it has been reported that  $\text{La}(\text{OH})\text{CO}_3$  can bind phosphate [12],  $\text{La}(\text{OH})\text{CO}_3$  has not been approved by the FDA for the treatment of hyperphosphatemia. It has not been elucidated whether the  $\text{La}(\text{OH})\text{CO}_3$  is safe in medical practice.

In this paper, we proposed a new approach to prepare lanthanum carbonate via reactions between  $\text{NaHCO}_3$  and  $\text{LaCl}_3$  in aqueous solution under low pH environment. In addition, the prepared lanthanum carbonate was characterized by using FTIR, XRD, elemental analysis, and titration methods. The ability of the lanthanum carbonate in binding phosphate was validated by spectrometric methods.

## 2. Experimental

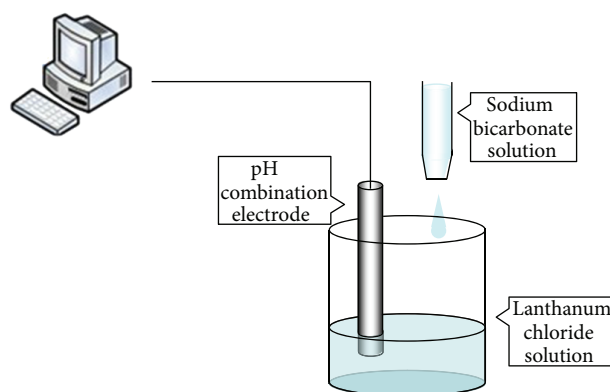
**2.1. Reagents.** Lanthanum oxide (99.999% purity) was purchased from Jiaton technology company.

Hydrochloric acid (37 wt%, AR), sodium bicarbonate (AR), disodium salt of EDTA (AR), acetic acid (AR), and sodium acetate (AR) were purchased from Beijing Chemical Plant.

Zinc oxide (reference materials) was purchased from Beijing Institute of Chemical Reagents.

**2.2. Instrument.** Elemental analyses (C, H, N) were performed on an Elementar Vario EL elemental analyzer.

X-ray powder diffraction (XRD) data were recorded on a Rigaku D/Max-2000 diffractometer at 40 kV, 100 mA for  $\text{Cu K}\alpha$ .



SCHEME 1: Schematic diagram of the experimental setup on the reaction between lanthanum chloride and sodium bicarbonate.

FTIR spectra of  $\text{La}_2(\text{CO}_3)_3 \cdot 8\text{H}_2\text{O}$  and  $\text{La}(\text{OH})\text{CO}_3$  were collected on a Thermo-Fisher Nicolet iN10 MX FTIR spectrometer equipped with an IR microscope. The spectra were recorded under transmission mode at a resolution of  $8\text{ cm}^{-1}$  and 64 scans were coadded.

Other FTIR spectra were recorded on a Fourier Transform Nicolet 6700 by using KBr pellets method. The spectra were recorded under transmission mode at a resolution of  $2\text{ cm}^{-1}$  and 16 scans were coadded.

Quantitative analysis of phosphate was performed by using spectrophotometry ( $\lambda = 700\text{ nm}$ ) on a PE Lambda 35 UV-Vis spectrophotometer.

### 2.3. Preparation

**2.3.1. Preparation of Lanthanum Carbonate.** Lanthanum chloride was prepared via a reaction between lanthanum oxide and HCl solution. The initial concentration of  $\text{La}^{3+}$  was 1 mol/L and the initial pH value of the solution was below zero.  $\text{NaHCO}_3$  was dissolved in deionized water, and the concentration of  $\text{NaHCO}_3$  of the obtained solution was 1 mol/L.

Lanthanum carbonate was prepared by adding  $\text{NaHCO}_3$  solution into an aqueous solution of lanthanum chloride under stirring. Description and discussion on the experimental conditions in detail can be found in Section 3. During the reaction, the pH values of the reactive environment were measured by using a combination electrode. The data were converted into digital signal and collected into a desktop computer via a cluster communication port (Scheme 1).

**2.3.2. Preparation of Lanthanum Carbonate Hydroxide.** The obtained lanthanum carbonate was suspended in deionized water and the mixture was refluxed for 15 hours. Afterwards, the product was obtained via a filtration process.

**2.4. Chemical Analysis of the Samples.** The  $\text{La}^{3+}$  content of the samples was measured by using EDTA titration. The concentration of the EDTA solution was calibrated by using zinc oxide.



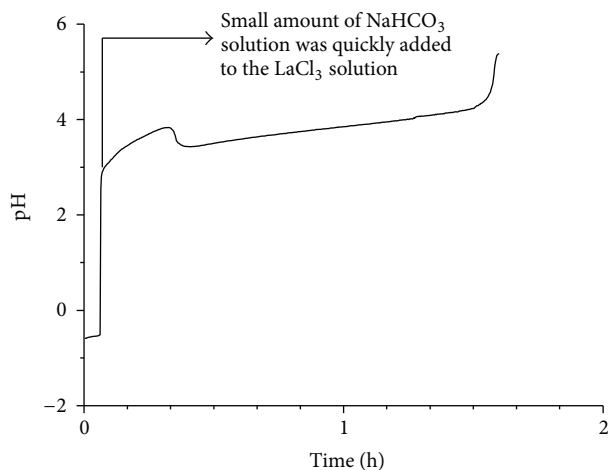
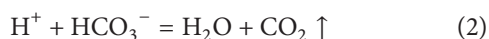
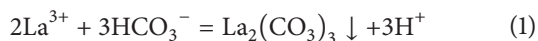


FIGURE 1: Variation of pH value as a function of time when  $\text{NaHCO}_3$  solution is added to  $\text{LaCl}_3$  solution at a rate of 0.2 mL/s.

### 3. Results and Discussion

When the sodium bicarbonate solution is added to the lanthanum chloride solution, the following two reactions cooccur in the system:



Reaction (1) is a precipitation reaction between  $\text{HCO}_3^-$  and  $\text{La}^{3+}$  and the products of the reaction are  $\text{La}_2(\text{CO}_3)_3$  precipitates and proton. Reaction (2) is a neutralization reaction between  $\text{HCO}_3^-$  and  $\text{H}^+$ . The precipitation reaction cannot be initiated without lanthanum carbonate nuclei being in the system while the acid-based neutralization reaction takes place as long as  $\text{H}^+$  and  $\text{HCO}_3^-$  cooccur in the system. If the  $\text{NaHCO}_3$  solution was slowly added to the lanthanum chloride solution, the precipitation reaction cannot be initiated since no lanthanum carbonate nuclei occur in the system. As a result, only the neutralization reaction takes place in the system. Thus, the pH value of the system increases monotonically as more  $\text{NaHCO}_3$  solution is added. As a result, lanthanum carbonate is prepared at high-pH environment and the risk of producing lanthanum carbonate hydroxide increases considerably.

Herein, we propose an alternative approach to prepare lanthanum carbonate at lower pH environment. The approach is composed of three steps: (1) preparation of lanthanum carbonate nuclei, (2) preparation of lanthanum carbonate, and (3) termination of the reaction.

In the first step, small amount of  $\text{NaHCO}_3$  solution was quickly added to the lanthanum chloride solution. The concentration of  $\text{NaHCO}_3$  in the local regions is high enough so that lanthanum carbonate precipitates are formed. The produced lanthanum carbonate can be used as nuclei center and hence the bottleneck of the lack of lanthanum carbonate nuclei is removed. During the reaction, the variation of pH value is monitored and shown in Figure 1. When aqueous solution of  $\text{NaHCO}_3$  was quickly added, the pH value

jumped around 3. In the meantime, white precipitates of lanthanum carbonate appeared. Since  $\text{H}^+$  was released from the precipitation reaction between  $\text{La}^{3+}$  and  $\text{HCO}_3^-$ , the decrease of pH can be observed in Figure 1. If no more  $\text{NaHCO}_3$  was added, the produced lanthanum carbonate can be dissolved completely by the acid produced from the reaction. To preserve the lanthanum carbonate nuclei,  $\text{NaHCO}_3$  solution was introduced into the system by using a ZDJ-400 multifunctional titrimer so that the injecting rate can be accurately controlled. The speed of injection of  $\text{NaHCO}_3$  solution was kept at 0.2 mL/s. During this process, more and more lanthanum carbonate precipitates were produced, while the pH value almost remained invariant. The reason for this phenomenon is that  $\text{NaHCO}_3$  plays a dual role in the system. On the one hand,  $\text{NaHCO}_3$  reacts with  $\text{La}^{3+}$  to produce lanthanum carbonate together with  $\text{H}^+$ . On the other hand,  $\text{NaHCO}_3$  acts as a base that can neutralize  $\text{H}^+$ . Since both precipitation reaction and neutralization reaction cooccur in the system, a dynamic equilibration on the concentration of  $\text{H}^+$  is established and the pH value remains a constant during the reaction. It should be pointed out that the reaction is carried out at lower pH environment (pH is below 4.0) and the risk of producing  $\text{La}(\text{OH})\text{CO}_3$  is significantly reduced.

When  $\text{La}^{3+}$  in the solution is completely consumed by the reaction, the precipitating reaction cannot be performed any more. However, the neutralization reaction can still be carried out. As a result, the pH value of the system jumped to 6 (Figure 1). To confirm that  $\text{La}^{3+}$  is used up at this moment, we collected small amount of supernatant from the system and added several drops of  $\text{NaOH}$  solution (1 mol/L), and no  $\text{La}(\text{OH})_3$  precipitate was observed, confirming that  $\text{La}^{3+}$  is completely consumed. Therefore, the reaction was stopped and the precipitate was collected as sample I.

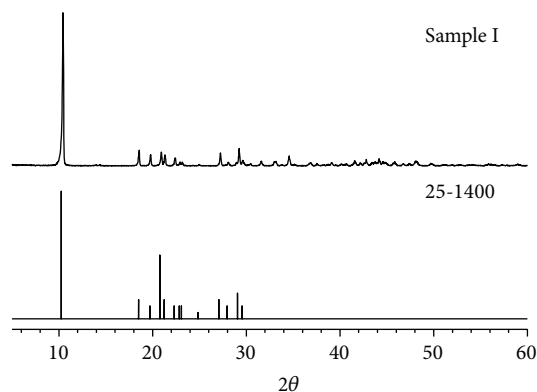
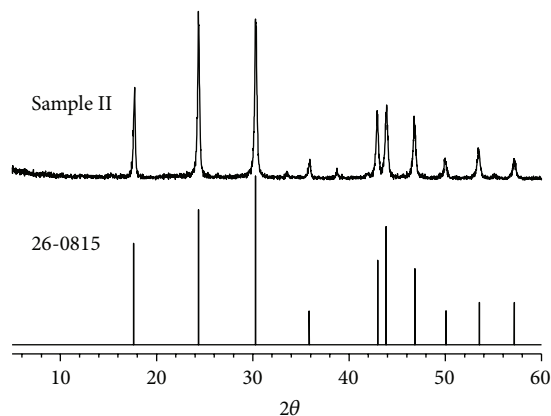
The sample I was characterized by using XRD and the result is shown in Figure 2. The XRD pattern of the product matches with the  $\text{La}_2(\text{CO}_3)_3 \cdot 8\text{H}_2\text{O}$  in ICDD PDF2-2004 database (card number: 25-1400) with a matching degree of 92.0%. This result indicated that the product of the above reaction is  $\text{La}_2(\text{CO}_3)_3 \cdot 8\text{H}_2\text{O}$ .

The sample I was added to deionized water and the mixture was refluxed for 15 hours. Afterwards, the product was obtained after a filtration process and denoted as sample II. XRD pattern of sample II is shown in Figure 3. The XRD pattern matches with the  $\text{La}(\text{OH})\text{CO}_3$  in ICDD PDF2-2004 database (card number: 26-0815) with a matching degree of 95.7%. Thus, the product is proved to be  $\text{La}(\text{OH})\text{CO}_3$ .

Titration and elemental analysis results provide additional experimental evidence to support that the two samples are  $\text{La}_2(\text{CO}_3)_3 \cdot 8\text{H}_2\text{O}$  and  $\text{La}(\text{OH})\text{CO}_3$ , respectively. The contents of lanthanum in the two samples were measured by EDTA titration. The contents of carbon were obtained by elemental analysis. The results of the above analysis are summarized in Table 1. Good agreement is found between the theoretical content and experimental results. From the chemical formula, we find that lanthanum carbonate and lanthanum carbonate hydroxide show significant difference on the molar ratio between carbon and lanthanum (denoted by  $n_c/n_{\text{La}^{3+}}$ ). If the prepared sample is  $\text{La}_2(\text{CO}_3)_3$ , the  $n_c/n_{\text{La}^{3+}}$

TABLE I: Results on the chemical analysis of sample I and sample II.

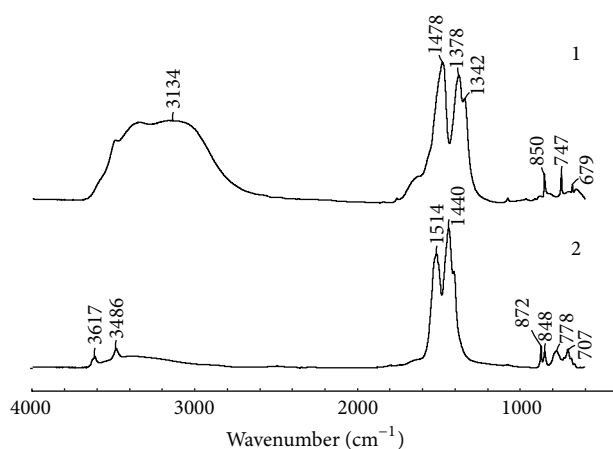
	Content of lanthanum		Content of carbon		$n_c/n_{La^{3+}}$
	Experimental value ( $\times 10^{-3}$ mol/g)	Theoretical value ( $\times 10^{-3}$ mol/g)	Experimental value ( $\times 10^{-3}$ mol/g)	Theoretical value ( $\times 10^{-3}$ mol/g)	
Sample I	3.293	3.322	4.98	4.98	1.52
Sample II	4.388	4.631	4.75	4.63	1.08

FIGURE 2: The XRD patterns of sample I and standard  $La_2(CO_3)_3 \cdot 8H_2O$  from ICDD PDF2-2004 (card number: 25-1400). Match degree: 92.0%.FIGURE 3: The XRD patterns of sample II and standard  $La(OH)CO_3$  from ICDD PDF2-2004 (card number: 26-0815). Match degree: 95.7%.

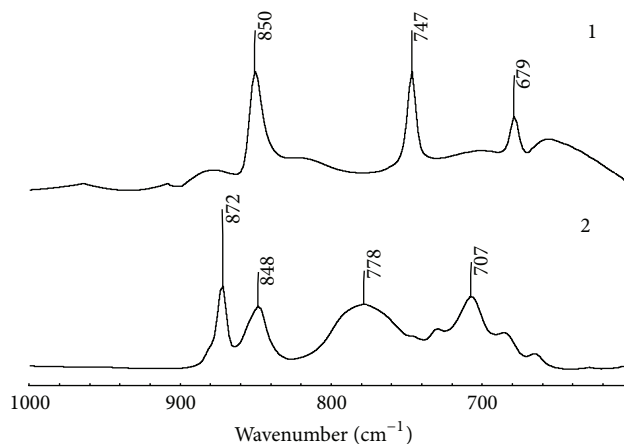
should be  $3/2 = 1.5$ . If the sample was  $La(OH)CO_3$ , the  $n_c/n_{La^{3+}}$  should be  $1/1 = 1$ . The  $n_c/n_{La^{3+}}$  values for sample I and sample II are 1.52 and 1.08 (Table 1), confirming that the products are lanthanum carbonate and lanthanum carbonate hydroxide, respectively.

Based upon the above result, we used the FTIR spectroscopic method to establish a rapid and reliable approach to identify lanthanum carbonate and lanthanum carbonate hydroxide.

FTIR spectrum of  $La_2(CO_3)_3 \cdot 8H_2O$  is given in Figure 4. For comparison, FTIR spectrum of  $La(OH)CO_3$  is also shown. Significant difference between the spectrum of  $La_2(CO_3)_3 \cdot 8H_2O$  and that of  $La(OH)CO_3$  can be clearly



(a)



(b)

FIGURE 4: (a) FTIR spectra of  $La_2(CO_3)_3 \cdot 8H_2O$  (line 1) and  $La(OH)CO_3$  (line 2). (b) FTIR spectra of  $La_2(CO_3)_3 \cdot 8H_2O$  (line 1) and  $La(OH)CO_3$  (line 2) in the fingerprint region ( $1000-600\text{ cm}^{-1}$ ).

observed in the fingerprint region ( $1000-600\text{ cm}^{-1}$ ).  $La_2(CO_3)_3 \cdot 8H_2O$  has sharp peaks at  $850\text{ cm}^{-1}$ ,  $747\text{ cm}^{-1}$ , and  $679\text{ cm}^{-1}$ , while  $La(OH)CO_3$  has absorption peaks at  $872\text{ cm}^{-1}$ ,  $848\text{ cm}^{-1}$ ,  $778\text{ cm}^{-1}$ , and  $707\text{ cm}^{-1}$ . The above dramatically different spectral features make it possible to detect  $La(OH)CO_3$  impurity in lanthanum carbonates. Here, different amount of  $La(OH)CO_3$  was mixed with  $La_2(CO_3)_3 \cdot 8H_2O$ , and FTIR spectra of the mixtures were collected by using KBr pellets method. Characteristic peak of  $La(OH)CO_3$  at  $872\text{ cm}^{-1}$  can be observed when 5 wt% of  $La(OH)CO_3$  was mixed with  $La_2(CO_3)_3 \cdot 8H_2O$  (Figure 5). To improve the sensitivity of the FTIR method, second

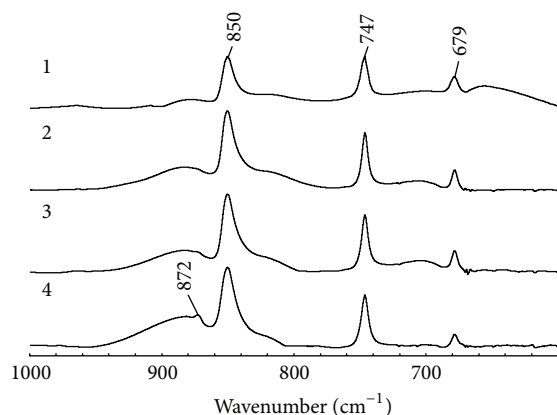


FIGURE 5: FTIR spectra of  $\text{La}_2(\text{CO}_3)_3 \cdot 8\text{H}_2\text{O}$  (line 1),  $\text{La}_2(\text{CO}_3)_3 \cdot 8\text{H}_2\text{O}$  containing 1 wt%  $\text{La}(\text{OH})\text{CO}_3$  (line 2),  $\text{La}_2(\text{CO}_3)_3 \cdot 8\text{H}_2\text{O}$  containing 2 wt%  $\text{La}(\text{OH})\text{CO}_3$  (line 3), and  $\text{La}_2(\text{CO}_3)_3 \cdot 8\text{H}_2\text{O}$  containing 5 wt%  $\text{La}(\text{OH})\text{CO}_3$  (line 4) in the fingerprint region (1000–600  $\text{cm}^{-1}$ ).

derivative spectra were utilized. In this case, characteristic peak of  $\text{La}(\text{OH})\text{CO}_3$  at 872  $\text{cm}^{-1}$  can be identified even if only 1 wt% of  $\text{La}(\text{OH})\text{CO}_3$  was mixed with  $\text{La}_2(\text{CO}_3)_3 \cdot 8\text{H}_2\text{O}$  (Figure 6).

To characterize the ability of lanthanum carbonate to bind phosphate, the following experiment was conducted: 0.2 g  $\text{KH}_2\text{PO}_4$  was dissolved in  $\text{CH}_3\text{COOH}-\text{CH}_3\text{COONa}$  solution (the concentrations of  $\text{CH}_3\text{COOH}$  and  $\text{CH}_3\text{COONa}$  are both 1 mol/L) so that 100.0 mL  $\text{KH}_2\text{PO}_4$  solution whose pH value is around 4.7 was prepared. 0.5 g  $\text{La}_2(\text{CO}_3)_3 \cdot 8\text{H}_2\text{O}$  was added to the phosphate solution. Enough stirring was applied on the suspension. During the experiment, phosphate can be adsorbed by lanthanide carbonate so that the concentration of phosphate is decreased with time. To monitor the decay of the concentration of phosphate, small amount of supernatant was collected at different time and the concentration of phosphate in the supernatant was analyzed by using the Mo-Sb antispectrophotometric method. Figure 7 shows the variation of the concentration of phosphate in the solution as a function of time. 50% phosphate is removed from the solution within 30 min and more than 95% phosphate is adsorbed by lanthanum carbonate within 120 min. Considering the fact that food stays in the stomach for 4 hours, lanthanum carbonate is enough to bind most phosphate.

#### 4. Conclusion

We proposed a new approach to prepare lanthanum carbonate via reactions between lanthanum chloride and  $\text{NaHCO}_3$ . In the reaction, small amount of  $\text{NaHCO}_3$  solution was quickly added to the acidic lanthanum chloride solution to generate lanthanum carbonate nuclei. As a result, both precipitation reaction and neutralization reaction take place simultaneously. Lanthanum carbonate is produced at low pH environment (pH below 4.0) so that the risk of generating lanthanum carbonate hydroxide is significantly reduced. EDTA titration, elemental analysis, and XRD characterization confirm that  $\text{La}_2(\text{CO}_3)_3 \cdot 8\text{H}_2\text{O}$  are obtained

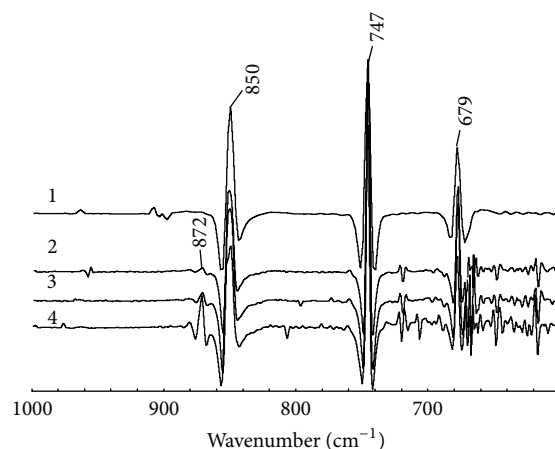


FIGURE 6: Second derivative FTIR spectra of  $\text{La}_2(\text{CO}_3)_3 \cdot 8\text{H}_2\text{O}$  (line 1),  $\text{La}_2(\text{CO}_3)_3 \cdot 8\text{H}_2\text{O}$  containing 1 wt%  $\text{La}(\text{OH})\text{CO}_3$  (line 2),  $\text{La}_2(\text{CO}_3)_3 \cdot 8\text{H}_2\text{O}$  containing 2 wt%  $\text{La}(\text{OH})\text{CO}_3$  (line 3), and  $\text{La}_2(\text{CO}_3)_3 \cdot 8\text{H}_2\text{O}$  containing 5 wt%  $\text{La}(\text{OH})\text{CO}_3$  (line 4) in the fingerprint region (1000–600  $\text{cm}^{-1}$ ).

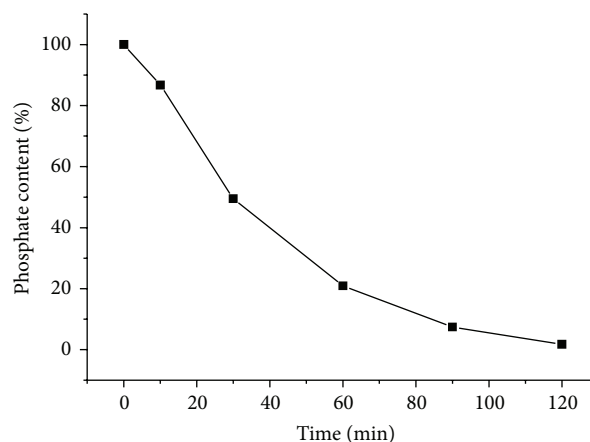


FIGURE 7: Variation of the concentration of phosphate in the supernatant as a function of time.

by using the above method. In addition, we established a method to identify  $\text{La}(\text{OH})\text{CO}_3$  from  $\text{La}_2(\text{CO}_3)_3 \cdot 8\text{H}_2\text{O}$ . Small amount of  $\text{La}(\text{OH})\text{CO}_3$  can be identified from  $\text{La}(\text{OH})\text{CO}_3/\text{La}_2(\text{CO}_3)_3 \cdot 8\text{H}_2\text{O}$  mixture even if the content of  $\text{La}(\text{OH})\text{CO}_3$  is only 1 wt%. Lanthanum carbonate exhibits a considerable ability to bind phosphate.

#### Conflict of Interests

The authors declare that there is no conflict of interests regarding the publication of this paper.

#### Acknowledgment

This work is supported by the National Natural Science Foundation of China (51373003).

## References

- [1] F. Albaaj and A. J. Hutchison, "Hyperphosphataemia in renal failure: causes, consequences and current management," *Drugs*, vol. 63, no. 6, pp. 577–596, 2003.
- [2] T. Plagemann, A. Prenzler, and T. Mittendorf, "Considerations about the effectiveness and cost effectiveness of therapies in the treatment of hyperphosphataemia," *Health Economics Review*, vol. 1, no. 1, pp. 1–9, 2011.
- [3] J. J. Schucker and K. E. Ward, "Hyperphosphatemia and phosphate binders," *American Journal of Health-System Pharmacy*, vol. 62, no. 22, pp. 2355–2361, 2005.
- [4] D. D. Freitas, R. L. Donne, and A. J. Hutchison, "Lanthanum carbonate—a first line phosphate binder?" *Current Opinion in Nephrology & Hypertension*, vol. 13, no. 6, pp. 403–409, 2004.
- [5] J. A. Coladonato, "Control of hyperphosphatemia among patients with ESRD," *Journal of the American Society of Nephrology*, vol. 16, no. 11, pp. S107–S114, 2005.
- [6] M. Tonelli, N. Pannu, and B. Manns, "Oral phosphate binders in patients with kidney failure," *New England Journal of Medicine*, vol. 362, no. 14, pp. 1212–1324, 2010.
- [7] H. H. Malluche and H. Mawad, "Management of hyperphosphataemia of chronic kidney disease: lessons from the past and future directions," *Nephrology Dialysis Transplantation*, vol. 17, no. 7, pp. 1170–1175, 2002.
- [8] S. P. Fricker, "The therapeutic application of lanthanides," *Chemical Society Reviews*, vol. 35, no. 6, pp. 524–533, 2006.
- [9] B. A. Murrer and N. A. Powell, "Pharmaceutical composition containing selected lanthanum carbonate hydrates," Patent US 5968976, 1999.
- [10] B. A. Murrey and N. A. Powell, "Pharmaceutical composition containing selected lanthanum carbonate hydrates," Patent CN 96193918.4, 1996.
- [11] P. Jeevanandam, Y. Koltypin, O. Palchik, and A. Gedanken, "Synthesis of morphologically controlled lanthanum carbonate particles using ultrasound irradiation," *Journal of Materials Chemistry*, vol. 11, no. 3, pp. 869–873, 2001.
- [12] J. C. Ferdinando and D. Gilmour, "Method of treating hyperphosphataemia using lanthanum hydroxyl carbonate," Patent CN 200580030985.1, 27 7 2005.

## Research Article

# Spectroscopic and Gas Chromatographic Studies of Pigments and Binders in Gdańsk Paintings of the 17th Century

Justyna Olszewska-Świetlik,<sup>1</sup> Bożena Szmelter-Fausek,<sup>1</sup>  
Ewa Pięta,<sup>2</sup> and Edyta Proniewicz<sup>2,3</sup>

<sup>1</sup> Department of Painting Technologies and Techniques, Nicolaus Copernicus University in Toruń, Ulica Sienkiewicza 30/32, 87-100 Toruń, Poland

<sup>2</sup> Faculty of Chemistry, Jagiellonian University, Ulica Ingardena 3, 30-060 Kraków, Poland

<sup>3</sup> Faculty of Foundry Engineering, AGH University of Science and Technology, Ulica Reymonta 23, 30-059 Krakow, Poland

Correspondence should be addressed to Justyna Olszewska-Świetlik; justyna.olszewska-swietlik@umk.pl

Received 5 September 2013; Accepted 30 October 2013

Academic Editor: Yizhuang Xu

Copyright © 2013 Justyna Olszewska-Świetlik et al. This is an open access article distributed under the Creative Commons Attribution License, which permits unrestricted use, distribution, and reproduction in any medium, provided the original work is properly cited.

This work presents spectroscopic (optical microscopy, OM; micro-Raman, Raman; and Fourier-transform adsorption infrared, FT-IR) and gas chromatographic studies of two famous panel paintings from the Gdańsk artists of the 17th century Golden Age, “Servilius Appius” by Isaac van den Blocke and “Allegory of Wealth” probably by Anton Möller. Application of the aforementioned methods allowed us to identify pigments and binders used in the panel paintings. In particular, it was determined that the yellow pigment used by both artists is lead-tin yellow type I ( $2\text{PbO}\cdot\text{SnO}_2$ ), the white pigment is lead (II) carbonate hydroxide ( $2\text{PbCO}_3\cdot\text{Pb}(\text{OH})_2$ ), and the ground layer material consist of chalk ( $\text{CaCO}_3$ ). The analysis showed also that in the case of “Allegory of Wealth,” the red layer consists not only of cinnabar ( $\text{HgS}$ ) but also of lead-tin yellow type I.

## 1. Introduction

Several documentary sources from the 17th century give recipes on how to paint, prepare grounds, and use colors for particular parts of the painting [1–4]. For example, De Mayerne pronounced that the quality of the materials used is essential not only for the ground layer but also for the paint layer. He recommended putting two different ground layers on the support. The first ground layer consisted of a very thin chalk-glue [ $\text{CaCO}_3$ —a white pigment used as a painting ground since antiquity [5]] that he polished. Then, he applied a second layer of lead (II) carbonate hydroxide [ $(\text{PbCO}_3)_2\cdot\text{Pb}(\text{OH})_2$ —a synthetic pigment produced since antiquity using an acidic organic compound on metallic lead [6, 7] with umber [ $\text{Fe}_2\text{O}_3\cdot\text{H}_2\text{O} + \text{MgO} + \text{Al}_2\text{O}_3$ ] [1]. Lead (II) carbonate hydroxide, lead-tin yellow [light (type I)— $\text{Pb}_2\text{SnO}_4$  and dark (type II)— $\text{Pb}(\text{Sn}, \text{Si})\text{O}_3$ ], yellow ochre [ $\text{Fe}_2\text{O}_3\cdot\text{H}_2\text{O}$ ], vermilion [ $\text{HgS}$ , a synthetic equivalent of cinnabar [8]], red lead [minimum,  $\text{Pb}_3\text{O}_4$ ], carmine (organic red—carminic acid),

iron oxide red [ $\text{Fe}_2\text{O}_3$ ], natural azurite [ $\text{Cu}_3(\text{CO}_3)_2(\text{OH})_2$ ], smalte [ $\text{CoO}\cdot n\text{K}_2\text{SiO}_3$ ], natural malachite [ $\text{Cu}_2\text{CO}_3(\text{OH})_2$ ], copper green [ $\text{Cu}(\text{CH}_3\text{COO})_2$ ], and charcoal were the most common pigments used in the 17th century [8]. Massicot [ $\text{PbO}$ ], schüttgelb (yellow lake pigment—organic pigments from many different sources), and orpiment [ $\text{As}_2\text{S}_3$ ] were also mentioned in the documentary sources from this period [1–4]. However, the later literature noted that lead-tin yellow was incorrectly identified as massicot [9, 10]. For example, De Mayerne suggested using massicot (in fact lead-tin yellow), yellow ochre, and schüttgelb to paint lighted and shaded surfaces, as well as transition from light to shade [1–4].

Despite progress in the field of instrumental analysis, identification of some of the pigments present in the painting layers, especially lead-tin yellow, is not always a simple task. Depending on the method of preparation, two types of lead-tin yellow can be obtained (type I and type II).

Recipes for lead-tin yellow are given in the Bolognese Paper *Segreti per colori* from the XVth century: “272. To



make yellow glass for paternosters or beads. Take of lead 1 lb., of tin 2 lbs., melt and calcine them, and make glass for paternosters.” and “273. To make giallolino for painting. Take 2 lbs. of this calcined lead and tin, that is 2 lbs. of this glass for paternosters, 2.5 lbs. of minimum, and 0.5 lb. of sand from Val d’Arno pounded very fine; put it into a furnace and let it fine itself and the color will be perfect” [11]. According to a different recipe, lead-tin yellow was obtained by heating approximately 3 parts of the oxide, lead dioxide, or most often minimum with 1 part of tin oxide [10, 12–14].

Lead-tin yellow type I occurs more frequently in art than does lead-tin yellow type II. This pigment was widely applied from antiquity to the first half of the 18th century [15]. Its early use was characteristic in Northern Europe. However, from the second half of the XVth century, it was identified in paintings from several European schools. For example, lead-tin yellow type I was found in the paintings of the Netherlandish artists Master of the Saint Bartholomew (1475–1510) and Gerard David (1460–1523), the Flemish artist Anthony van Dyck (1599–1641), and the Dutch artists Hendrick ter Brugghen (1588–1629) and Meindert Hobbema (1638–1709), whose works are in the National Gallery in London [7]. In works from the Polish collections, lead-tin yellow type I, in trace amounts, was identified in the Dutch triptych “*The Last Judgement*” (1473) by Hans Memling (1435–1494) (the National Museum in Gdańsk) [16].

Lead-tin yellow type II was obtained from lead glass, according to the procedure given in the Bolognese Paper [10, 12–14]. This type of yellow was used more often in the southern schools of painting, and the earliest example was identified in the paintings of Giotto di Bondone (1266–1377) and Jacopo di Cione (1325–1399) [7]. In the second half of the XVth century in Italy, lead-tin yellow type II was replaced by lead-tin yellow type I [7]. Examples include works by Moretto da Brescia (1498–1555) and Paolo Veronese (1528–1588) from the collections of the National Gallery in London, in which lead-tin yellow type I was identified by X-Ray Diffraction analysis [16].

During the 16th and 17th centuries, Gdańsk was a wealthy seaport and merchant city. Many artists, including immigrants from the Netherlands, lived in Gdańsk and composed their works of art that influenced the native Gdańsk artists. One of the families that settled in Gdańsk was the van den Blocke family from Mechelen (Flanders). They took up construction, ornamental masonry, and painting. Isaac van den Blocke was a painter and gained a reputation as a splendid artist for the Main Town Hall in Gdańsk (1606–1609) [17].

The second outstanding Gdańsk artist is Anton Möller, who arrived in Gdańsk from Królewiec. Möller’s art was influenced by Netherlandish and German painters. His famous work is “*The Last Judgement*” (1602–1603) from Arthus Court in Gdańsk.

Both artists are best known for Biblical themes and allegorical compositions that are often compared to the art of Flanders and the Netherlands.

The main aim of the analysis presented in this work was to supplement the data on the type of lead-tin yellow pigment used in the Gdańsk paintings in the first half of the XVIIth century, using the two example paintings “*Servilius*



FIGURE 1: “*Servilius Appius*” (1608–1609) by Isaac van den Blocke and a cross-section of sample (SA): SA.1—white ground layer/underpainting and SA.2—yellow painting layer.



FIGURE 2: “*Allegory of Wealth*” (c. 1600) by Anton Möller and a cross-section of sample (AW): AW.1—white ground layer/underpainting, AW.2—red painting layer, and AW.3—yellow painting layer.

*Appius*” by Isaac van den Blocke (Figure 1) and “*Allegory of Wealth*,” most likely by Anton Möller (Figure 2). This work is important because the examination of the type of lead-tin yellow in a greater number of paintings will contribute to a full view of the technologies and techniques that were used and the types of materials in the paintings in different regions of Europe. The second goal of the research was to gain analytical information on the inorganic and organic materials used for grounds, painting layers, and varnishes in both paintings to better understand and characterize their

painting technique. It was important to identify the pigments, how complex the binding media mixtures used for the layers were, and if the paintings show any characteristic features related to certain schools of painting. The obtained data were also important to better plan the sustainable conservation of the paintings. The present research is the first spectroscopic investigation of the Gdańsk 17th century paintings. Until now, the Gdańsk 17th century paintings have been studied only by art historians.

"*Servilius Appius*" (1608-1609) was painted for the Red Chamber in the Main Town Hall in Gdańsk (now The Gdańsk History Museum). Isaac van den Blocke placed more emphasis on the political and administrative content of this painting than on its artistic value. The theme of the painting was directed to the city council and warned against conflicts. It emphasizes cooperation as an important virtue for governance [18]. Blocke mainly used yellow colors in particular parts of garments, that is, collars and clothing finishing.

"*Allegory of Wealth*" (1600) is part of an allegorical cycle, along with the two paintings known as "*The Model of the World and the Gdańsk Citizens*" and "*Allegory of Pride*." The paintings point out vices of the citizens of Gdańsk. The author mainly painted with yellow color in detail such as shoes or ornaments on the textiles of robes.

A multidisciplinary approach was undertaken to accomplish these goals. Optical microscopy (OM), gas chromatography (GC), Fourier-transform absorption infrared (FT-IR), and micro-Raman (Raman) analysis answered questions regarding the type of lead-tin yellow or the particular pigments and binders used in paintings of this type.

## 2. Materials and Methods

**2.1. Samples.** Two samples were taken from yellow parts of the paintings: the yellow vest from "*Servilius Appius*" by Isaac van den Blocke (SA) and the yellow shoe from "*Allegory of Wealth*" by Anton Möller (AW). The cross-sections were prepared by setting the samples in resin and polishing the sample.

**2.2. Optical Microscopy Measurements.** OM measurements were carried out using a Nikon Optiphot-2 (NIKON INC., USA) conventional reflected light microscope.

**2.3. Micro-Raman Measurements.** The micro-Raman spectra of selected layers were recorded using an InVia spectrometer (Renishaw, England). This spectrometer was equipped with a diode laser emitting at 785.0 nm and a CCD detector. The laser power at the output was set at 30 mW. All spectra were acquired with a spectral resolution of 4 cm<sup>-1</sup> in the 100 to 3200 cm<sup>-1</sup> spectral range. Depending upon the signal to noise ratio (S/N), 4 to 16 scans were collected.

**2.4. Fourier-Transform Absorption Infrared Measurements.** The FT-IR spectra of SA and AW samples (ground, underpainting, painting layer, and varnish) were obtained with a Bruker Optics Alpha ATR FTIR spectrometer in the spectral

range of 4000–500 cm<sup>-1</sup> (Jadwiga W. Łukaszewicz, Wiesława Topolska, Department for Conservation and Restoration of Architectonic Elements and Details, The Institute for the Study, Restoration and Conservation of Cultural Heritage, Nicolaus Copernicus University in Toruń, Poland).

**2.5. Gas Chromatography Measurements.** Samples were decomposed to separate binders on the column. First, a 2 M methanolic KOH solution was used, followed by methylation with methyl chloroformate (MCF) and the hexane extraction of methyl esters of saturated fatty acids and dicarboxylic acids such as azelaic acid.

For these measurements, a Hewlett Packard 6890 Chromatograph equipped with a 30 m HP5 capillary column and flame ionization detector FID was used. The separation was performed in a programmable temperature furnace (Grzegorz Jaworski, Department of Painting Technologies and Techniques, The Institute for the Study, Restoration and Conservation of Cultural Heritage, Nicolaus Copernicus University in Toruń, Poland).

The obtained chromatograms were interpreted qualitatively by comparing the chromatograms of the reference binder, such as linseed oil and casein. From the chromatogram integration results, the ratios between acids were determined, that is, Az/Pa, Pa/St, and Pa/My, where Az, Pa, St, and My denote azelaic, palmitic, stearic, and myristic acids, respectively. Unfortunately, due to the small amount of sample taken from the painting "*Allegory of Wealth*," it was not possible to measure the binding media of the selected layers in the AW sample. Consequently, the measurements were performed on a sample that included all layers.

Before the GC analysis was performed, a complementary microchemical saponification test was performed with the samples to verify the presence of oil in the particular layers.

## 3. Results and Discussion

**3.1. Vibrational Analysis.** Analysis of a cross-section of SA (inset in Figure 1) and AW (inset in Figure 2) samples by optical microscopy and micro-Raman spectroscopy (Figures 3 and 4) revealed that the samples are multilayered and have two and three layers, respectively. The SA sample consisted of the following layers: SA.1—white ground layer/underpainting and SA.2—yellow painting layer (see Table 1); in contrast, the AW sample displayed the following layers: AW.1—white ground layer/underpainting, AW.2—red painting layer, and AW.3—yellow painting layer (see Table 1). Each Raman spectrum from the individual cross-section shows unique bands due to particular pigments. The spectral analysis of these bands was based on the spectral databases of pigments [19–40].

Raman analysis of the SA.1 layer (Figure 3) identified a mixture of pigments in this layer that yield a spectrum with strong bands from chalk (at 1087 and 278 cm<sup>-1</sup>) and lead (II) carbonate hydroxide (at 1054 cm<sup>-1</sup>). The presence of lead (II) carbonate hydroxide in the SA.1 layer is a consequence of mixing the ground layer with the very thin layer of underpainting. The Raman spectrum of the yellow painting

TABLE 1: Stratigraphy and results of the measurements of pigments and binders of a cross-section of the SA and AW samples.

No.	Layer	Detected pigments and binders		
		Micro-Raman	FT-IR	GC
SA				
2	Yellow painting layer	Lead-tin yellow type I (2PbO·SnO <sub>2</sub> ), chalk (CaCO <sub>3</sub> ), lead (II) carbonate hydroxide (2PbCO <sub>3</sub> ·Pb(OH) <sub>2</sub> )	Oil, protein, carbonates	Linseed oil
1	white ground layer/ underpainting			Linseed oil, casein
AW				
3	Yellow painting layer	Lead-tin yellow type I (2PbO·SnO <sub>2</sub> ),	Casein	Linseed oil, casein
2	Red painting layer	Cinnabar (HgS)		
1	White ground layer/ underpainting	Chalk (CaCO <sub>3</sub> ), lead (II) carbonate hydroxide (2PbCO <sub>3</sub> ·Pb(OH) <sub>2</sub> )	Casein, gluten glue, carbonates	

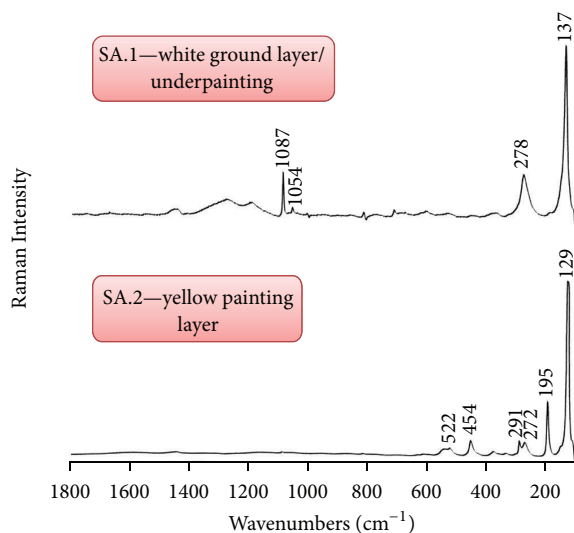


FIGURE 3: Micro-Raman spectra of the cross-section layers of “Servilius Appius” (SA).

layer (Figure 3, SA.2 layer) exhibited a prominent 129, spectral feature, and less intense bands at 195, 272, 291, 454, and  $522\text{ cm}^{-1}$ . All of these bands were attributed to lead-tin yellow type I.

The Raman spectrum of the AW.1 layer (Figure 4), similar to the Raman spectrum of the SA.1 layer, is characterized by bands due to the mixture of pigments, such as chalk (at  $1088\text{ cm}^{-1}$ ), lead (II) carbonate hydroxide (at  $1052\text{ cm}^{-1}$ ), and red pigment cinnabar (vermillion, at 252, 282, and  $342\text{ cm}^{-1}$ ). Due to the historical context of the art, bands attributed to cinnabar should not be observed in the AW.1 layer. These

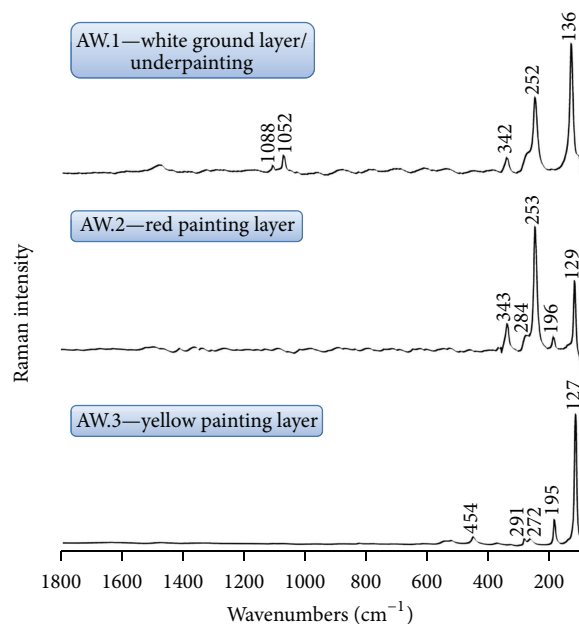


FIGURE 4: Micro-Raman spectra of the cross-section layers of “Allegory of Wealth” (AW).

results are most likely due to contamination of the sample during embedding in the resin block or displacement of some grains of these pigments from the previous painting layer. The OM and microchemical analyses revealed chalk, charcoal, and lead white in the AW.1 layer. The red painting layer (Figure 4, AW.2 layer) also contains vermillion, as is evident from the presence of the same spectral features as mentioned in the previous cases (layer AW.1). Similar to the Raman spectrum of the SA.2 layer, the AW.3 layer spectrum exhibited bands that corresponded to lead-tin yellow type I (at 127, 195, 272, 291, 454, and  $524\text{ cm}^{-1}$ ).

It should also be noted that both SA.1 and AW.1 spectra contain Raman band at  $\sim 137\text{ cm}^{-1}$  which could not be uniquely assigned to any of pigments. This is due to the fact that there are no additional observed spectral features. Consequently, we could only suppose that this Raman signal arising from the lead tin yellow type I or II.

The identification of varnishes and binding media is one of the most complicated issues for scientists and art conservators. The chemical composition of these materials should be analyzed using spectroscopic and chromatographic techniques such as FT-IR and GC. Figure 5 presents the FT-IR spectra of the sample from the investigated panel paintings, whereas Figure 6 shows their GC chromatograms. The binding media identified in the SA and AW samples based on the FT-IR spectra are linseed oil and protein [20, 23]. Hence, the observed fatty acids and ester bands in the FT-IR spectra may be explained by the use of drying oils in the preparation of the binder. Briefly, in the IR spectra of the SA and AW samples (Figure 5), the  $3349\text{ cm}^{-1}$  band due to the O–H bond stretch reveals the presence of the alcoholic groups in the analyzed samples. The  $\sim 2926$  and  $2855\text{ cm}^{-1}$  spectral features correspond to the C–H bond



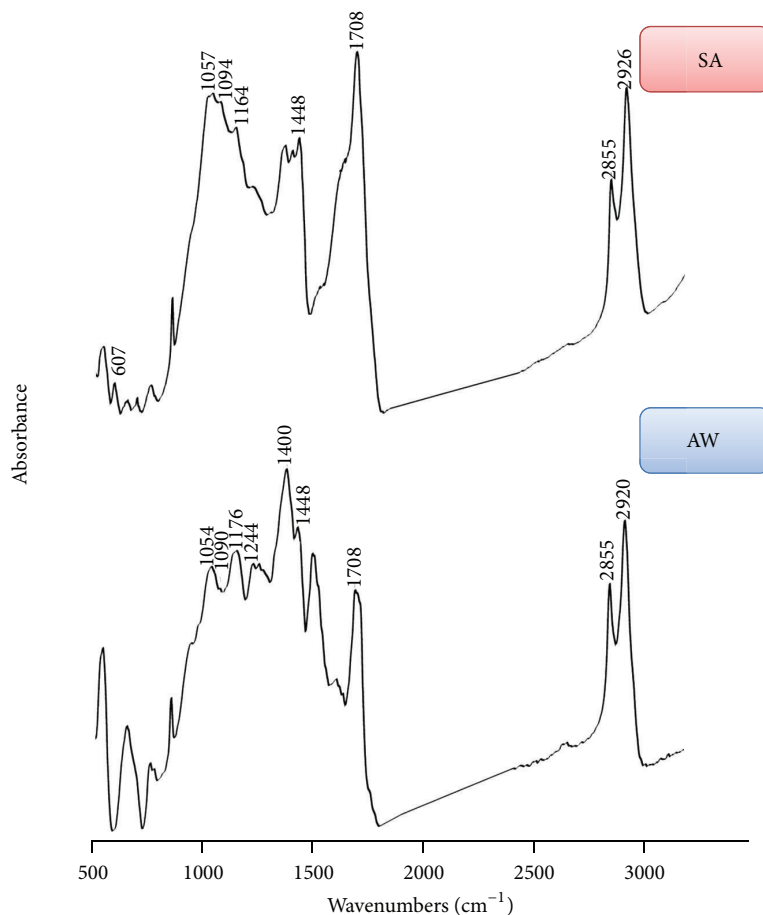


FIGURE 5: FT-IR spectra of sample taken from “Servilius Appius” (SA) and “Allegory of Wealth” (AW).

stretches of the hydrocarbon chains (fatty acids and proteins). The broad intense band with a maximum at  $1708\text{ cm}^{-1}$  and a shoulder at  $1658\text{ cm}^{-1}$  is due to the stretching vibrations of the  $\text{C}=\text{O}$  groups of resin acids and the  $\text{C}=\text{CH}_2$  olefin groups, respectively. Oils and proteins are represented by the characteristic  $1448\text{ cm}^{-1}$  band (deformations of  $\text{C}-\text{H}$  in  $-\text{CH}_2-$  and  $-\text{CH}_3$  groups), whereas the  $878$  and  $674\text{ cm}^{-1}$  Raman signals are only assignable to linseed oil. The  $1245$ ,  $\sim 1170$ , and  $\sim 1090\text{ cm}^{-1}$  spectral features suggest the presence of an ester group. The protein media as an animal glue also shows characteristic protein vibrations, such as the amide I ( $1658\text{ cm}^{-1}$ ) and amide II ( $1549\text{ cm}^{-1}$ ) bands and the aromatic amino acids ring modes ( $1514$ ,  $1605\text{ cm}^{-1}$ ). In the fingerprint spectral region, the  $1448$ ,  $1378$ ,  $1164$ ,  $1094$ , and  $1057\text{ cm}^{-1}$  bands may indicate the presence of a triterpenoid resin of dammar. In addition, chalk exhibits typical calcium carbonate bands such as the antisymmetric stretching vibration of  $\text{CO}_3^{2-}$  ( $1416$  and  $710\text{ cm}^{-1}$ ). The presence of the carbonate bands suggests the existence of calcium carbonate bound with calcite in the ground layer and lead (II) carbonate hydroxide in the painting layer and the underpainting.

The type of binding medium used in the investigated panel paintings was also determined using gas chromatography. The chromatograms of the SA (Figure 6, top trace) and

AW (Figure 6, bottom trace) samples indicate the following acids: palmitic—Pa, stearic—St, myristic—My, and azelaic—Az. From the results of the integration of the chromatograms, the ratios between the acids can be determined (Pa/St, Az/Pa, Pa/My, Pa—palmitic, St—stearic, Az—azelaic, and My—myristic). The ratios of the painting layer to the SA sample are assignable to linseed oil: Pa/St = 1,92, Az/Pa = 0,26, and Pa/My = 10,37. The presence of this binder was confirmed by GC and FTIR analysis and the microchemical test. The saponification test also confirmed the presence of oil.

For the ground layer with underpainting, the ratios were Pa/St = 2,28, Az/Pa = 0,19, and Pa/My = 5,64, which suggests that the binder composition is most likely casein and linseed oil. This result was also confirmed by FT-IR analysis. The GC analysis of the painting layers with the ground of the AW sample assigned the following ratios: Pa/St = 4,10, Pa/My = 3,92, and Az/Pa = 0,46, indicating that the binder composition is most likely linseed oil and casein. The microchemical test of saponification of the sample confirmed the presence of oil in the painting layer and underpainting. The FT-IR analysis also confirmed the analyzed binders.

The GC chromatogram of the SA sample (Figure 6, top trace) confirmed the results of the FT-IR analysis (Figure 5, top trace) and revealed linseed oil in the painting layer with underpainting and casein and linseed oil in the ground layer.

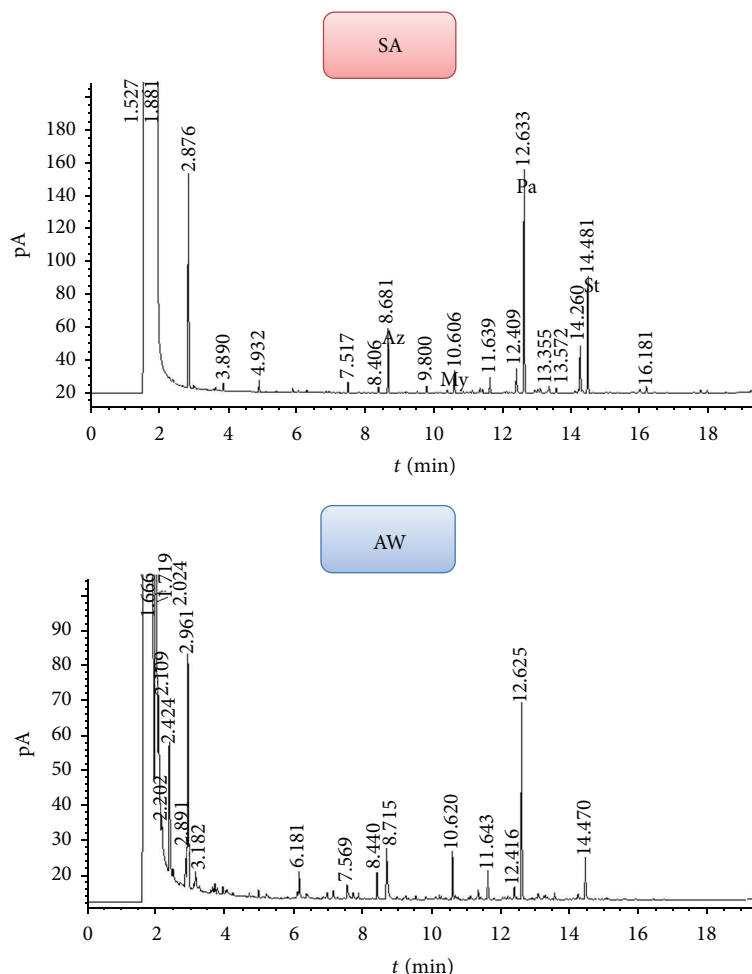


FIGURE 6: GC chromatogram of “Servilius Appius” (SA) (the integration of the peaks calculated ratios of acids: Pa/St = 1,92; Az/Pa = 0,26; Pa/My = 10,37; Pa—palmitic acid, St—stearic acid, Az—azelaic acid, and My—myristic acid) and “Allegory of Wealth” (AW) (the integration of the peaks calculated ratios of acids: Pa/St = 4,10; Pa/My = 3,92; Az/Pa = 0,38).

The presence of casein and linseed oil was also found in the AW sample (Figure 6, bottom trace), which was confirmed by FT-IR analysis (Figure 5, bottom trace).

#### 4. Conclusions

The analyzed paint samples originated from the panel paintings “*Servilius Appius*” and “*Allegory of Wealth*.” An interdisciplinary approach was used for the investigation of these samples to obtain information about their complex structure and to gain knowledge of the traditional painting techniques and the related technological sources. The OM, micro-Raman, FT-IR, and GC analytical techniques, which characterize all of the usual classes of inorganic pigments and organic binding media from the same microsample were used. The analysis of the binder was necessary to characterize the painting and plan its consolidation.

The performed analysis identified differences between the techniques used. For example, chalk, lead (II) carbonate hydroxide, and lead-tin yellow type I were used in “*Servilius*

*Appius*,” whereas chalk, lead (II) carbonate hydroxide, lead-tin yellow I, and cinnabar (vermilion) were used in “*Allegory of Wealth*.” Blocke painted with oil colors on a white ground that contained chalk and casein and on an underpainting of lead (II) carbonate hydroxide and linseed oil. He used lead-tin yellow type I as a yellow pigment. Möller painted with oil colors on a white chalk-glue-casein ground and an underpainting of lead (II) carbonate hydroxide was then applied. The yellow layer containing lead-tin yellow type I was applied to a red layer of cinnabar (vermilion).

FTIR and GC identified the composition of the binding media. The results were completed by micro-Raman analysis.

The obtained results have been compared with the FT-IR data (Figure 5). Due to the small amount of sample, it was not possible to obtain FT-IR spectra from each layer. The combination of RS and FT-IR spectroscopy proved to be complementary in the identification of pigments.

The vibrational analysis of the two panel paintings shows that artists of this period were familiar with using pigments such as lead-tin yellow type I or lead (II) carbonate hydroxide and the same ground layer material chalk. These similarities



suggest that both of these paintings were created under the influence of the same school or culture.

## Conflict of Interests

The authors declare that there is no conflict of interests regarding the publication of the paper.

## Acknowledgment

This work was supported by the Polish National Science Center of the Ministry of Science and Higher Education (Grant no. N N204 370340 to J. O.-Ś.).

## References

- [1] T. T. de Mayerne, "Pictoria, sculptoria, tinctoria et quae subalternarum atrium spectantia," in *Quellen für Maltechnik während der Renaissance und deren Folgezeit (XVI.XVIII. Jahrhundert) in Italien, Spanien, den Niederlanden, Deutschland, Frankreich und England, nebst dem de Mayerne Manuskript*, E. Berger, Ed., p. 98, Callwey, München, Germany, 1901.
- [2] C. van Mander and H. Floerke, *Das Leben der niederländischen und deutschen Maler*, vol. 2, George Müller, München, Germany, 1906.
- [3] C. van Mander, *Het Schilder-Boeck*, Martinus Nijhoff Publishers, The Hague, The Netherlands, 1916.
- [4] M. Roznerska, *Paintings Techniques of "Small Netherlands Masters" of XVII Century*, Nicolaus Copernicus University, Toruń, Poland, 1991.
- [5] I. M. Bell, R. J. H. Clark, P. J. Gibbs, and Christopher Ingold Laboratories, *Raman Spectroscopic Library of Natural and Synthetic Pigments*, University College London, Department of Chemistry, 2010, <http://www.chem.ucl.ac.uk/resources/raman/index.html>.
- [6] T. D. Chaplin, R. J. H. Clark, A. McKay, and S. Pugh, "Raman spectroscopic analysis of selected astronomical and cartographic folios from the early 13th century Islamic 'Book of Curiosities of the Sciences and Marvels for the Eyes,'" *Journal of Raman Spectroscopy*, vol. 37, no. 8, pp. 865–877, 2006.
- [7] N. Eastaugh, V. Walsh, T. D. Chaplin, and R. Siddall, *The Pigment Compendium: A Dictionary of Historical Pigments*, Elsevier Science, Oxford, UK, 2004.
- [8] J. Olszewska-Świetlik, *Painting Technology and Technique of Selected Modern Epitaphs from the St. Mary's Church in Gdańsk*, Nicolaus Copernicus University, Toruń, Poland, 2009.
- [9] R. Jacobi, "Über den in der Malerei verwendeten gelben Farbstoff der alten Meister," *Angewandte Chemie*, vol. 54, pp. 28–29, 1941.
- [10] H. Kühn, "Lead-tin-yellow," *Studies in Conservation*, vol. 13, pp. 7–33, 1968.
- [11] M. Merrifield, *Original Treatises on the Arts of Painting*, vol. 2, Dover, New York, NY, USA, 1967.
- [12] Z. Brochwicz and J. Rauchfleisch, *Application of X-Ray Spectroscopy to Identification of Inorganic Pigments, Library of Museology and Preservation of Monuments*, vol. 34, Warsaw, Poland, 1973.
- [13] P. Rudniewski, *Pigments and Their Identification*, vol. 13, Academy of Fine Arts, Warsaw, Poland, 1994.
- [14] Z. Kaszowska, *Advantages and Limitations of Analytical Techniques Used in Technological Studies of Gothic Panel Paintings*, WKiRDS ASP, Kraków, Poland, 2010.
- [15] A. Deneckere, M. Leeflang, M. Bloem et al., "The use of mobile Raman spectroscopy to compare three full-page miniatures from the breviary of Arnold of Egmond," *Spectrochimica Acta A*, vol. 83, no. 1, pp. 194–199, 2011.
- [16] K. Higgitt, M. Spring, and D. Saunders, *Pigment-Medium Interactions in Oil Paint Films Containing Red Lead or Lead-Tin-Yellow*, vol. 24, National Gallery Technical Bulletin, 2003.
- [17] J. Tylicki, *The Netherlands Origin of the van den Blocke Family*, vol. 71, Biuletyn Historii Sztuki, 2009.
- [18] J. Pałubicki, *Gdańsk Painters. Painters, Glaziers, Graphic Artists, and Engravers in Modern Gdańsk Archival Materials*, vol. 2, The National Museum in Gdańsk, Gdańsk, Poland, 2009.
- [19] T. Grzybkowska, *Aurea Porta of the Republic of Poland*, vol. 2, The National Museum in Gdańsk, Gdańsk, Poland, 1997.
- [20] P. Vandenabeele, B. Wehling, L. Moens, H. Edwards, M. de Reu, and G. van Hooydonk, "Analysis with micro-Raman spectroscopy of natural organic binding media and varnishes used in art," *Analytica Chimica Acta*, vol. 407, no. 1–2, pp. 261–274, 2000.
- [21] M. Abdel-Ghani, H. G. M. Edwards, B. Stern, and R. Janaway, "Characterization of paint and varnish on a medieval Coptic-Byzantine icon: novel usage of dammar resin," *Spectrochimica Acta A*, vol. 73, no. 3, pp. 566–575, 2009.
- [22] P. Vandenabeele, M. Ortega-Avilès, D. T. Castelleros, and L. Moens, "Raman spectroscopic analysis of Mexican natural artists' materials," *Spectrochimica Acta A*, vol. 68, no. 4, pp. 1085–1088, 2007.
- [23] C. Daher, C. Paris, A.-S. le Hô, L. Bellot-Gurlet, and J.-P. Échard, "A joint use of Raman and infrared spectroscopies for the identification of natural organic media used in ancient varnishes," *Journal of Raman Spectroscopy*, vol. 41, no. 11, pp. 1494–1499, 2010.
- [24] L. Burgio and R. J. H. Clark, "Library of FT-Raman spectra of pigments, minerals, pigment media and varnishes, and supplement to existing library of Raman spectra of pigments with visible excitation," *Spectrochimica Acta A*, vol. 57, no. 7, pp. 1491–1521, 2001.
- [25] I. M. Bell, R. J. H. Clark, and P. J. Gibbs, "Raman spectroscopic library of natural and synthetic pigments (pre-~ 1850 AD)," *Spectrochimica Acta A*, vol. 53, no. 12, pp. 2159–2179, 1997.
- [26] A. Nevin, I. Osticioli, D. Anglos, A. Burnstock, S. Cather, and E. Castellucci, "Raman spectra of proteinaceous materials used in paintings: a multivariate analytical approach for classification and identification," *Analytical Chemistry*, vol. 79, no. 16, pp. 6143–6151, 2007.
- [27] T. R. Ravindran, A. K. Arora, S. Ramya, R. V. Subba Rao, and B. Raj, "Raman spectroscopic study of medieval Indian art of 17th century," *Journal of Raman Spectroscopy*, vol. 42, no. 4, pp. 803–807, 2011.
- [28] A. Nevin, D. Comelli, I. Osticioli et al., "Multi-photon excitation fluorescence and third-harmonic generation microscopy measurements combined with confocal Raman microscopy for the analysis of layered samples of varnished oil films," *Applied Physics A*, vol. 100, no. 3, pp. 599–606, 2010.
- [29] P. Vandenabeele, F. Verpoort, and L. Moens, "Non-destructive analysis of paintings using fourier transform Raman spectroscopy with fibre optics," *Journal of Raman Spectroscopy*, vol. 32, no. 4, pp. 263–269, 2001.

- [30] K. Castro, M. Pérez-Alonso, M. D. Rodríguez-Laso, L. A. Fernández, and J. M. Madariaga, "On-line FT-Raman and dispersive Raman spectra database of artists' materials (e-VISART database)," *Analytical and Bioanalytical Chemistry*, vol. 382, pp. 248–285, 2005.
- [31] V. S. F. Muralha, L. Burgio, and R. J. H. Clark, "Raman spectroscopy analysis of pigments on 16-17th c. Persian manuscripts," *Spectrochimica Acta A*, vol. 92, pp. 21–28, 2012.
- [32] A. Deneckere, F.-P. Hocquet, A. Born et al., "Direct analysis of the central panel of the so-called Wyts triptych after Jan van Eyck," *Journal of Raman Spectroscopy*, vol. 41, no. 11, pp. 1500–1509, 2010.
- [33] J. Zuo, X. Zhao, R. Wu, G. Du, C. Xu, and C. Wang, "Analysis of the pigments on painted pottery figurines from the Han Dynasty's Yangling Tombs by Raman microscopy," *Journal of Raman Spectroscopy*, vol. 34, no. 2, pp. 121–125, 2003.
- [34] M. Hanesch, "Raman spectroscopy of iron oxides and (oxy)hydroxides at low laser power and possible applications in environmental magnetic studies," *Geophysical Journal International*, vol. 177, no. 3, pp. 941–948, 2009.
- [35] C. Pelosi, G. Agresti, U. Santamaria, and E. Mattei, "Artificial yellow pigments: production and characterization through spectroscopic methods of analysis," *E-Preservation Science*, vol. 7, pp. 108–115, 2010.
- [36] R. J. H. Clark, L. Cridland, B. M. Kariuki, K. D. M. Harris, and R. Withnall, "Synthesis, structural characterisation and Raman spectroscopy of the inorganic pigments lead tin yellow types I and II and lead antimonate yellow: their identification on medieval paintings and manuscripts," *Journal of the Chemical Society*, no. 16, pp. 2577–2582, 1995.
- [37] I. Borgia, B. G. Brunetti, C. Miliani, C. Ricci, C. Seccaroni, and A. Sgamellotti, "The combined use of lead-tin yellow type I and II on a canvas painting by Pietro Perugino," *Journal of Cultural Heritage*, vol. 8, no. 1, pp. 65–68, 2007.
- [38] C. Sandalinas and S. Ruiz-Moreno, "Lead-tin-antimony yellow: historical manufacture, molecular characterization and identification in seventeenth-century Italian painting," *Studies in Conservation*, vol. 49, no. 1, pp. 41–52, 2004.
- [39] H. G. M. Edwards, D. W. Farwell, E. M. Newton, F. R. Perez, and S. J. Villar, "Raman spectroscopic studies of a 13th century polychrome statue: identification of a "forgotten" pigment," *Journal of Raman Spectroscopy*, vol. 31, no. 5, pp. 407–413, 2000.
- [40] R. J. Meilunas, J. G. Bentsen, and A. Steinberg, "Analysis of aged paint binders by FTIR spectroscopy," *Studies in Conservation*, vol. 35, pp. 33–51, 1990.

## Research Article

# Improved Extended Multiplicative Scatter Correction Algorithm Applied in Blood Glucose Noninvasive Measurement with FT-IR Spectroscopy

**Qingbo Li, Qishuo Gao, and Guangjun Zhang**

*School of Instrumentation Science and Optoelectronics Engineering, Precision Optomechatronics Technology Key Laboratory of Education Ministry, Beihang University, Xueyuan Road No. 37, Haidian District, Beijing 100191, China*

Correspondence should be addressed to Guangjun Zhang; [qbleebuaa@buaa.edu.cn](mailto:qbleebuaa@buaa.edu.cn)

Received 4 September 2013; Accepted 12 October 2013

Academic Editor: Yizhuang Xu

Copyright © 2013 Qingbo Li et al. This is an open access article distributed under the Creative Commons Attribution License, which permits unrestricted use, distribution, and reproduction in any medium, provided the original work is properly cited.

In order to improve the predictive accuracy of human blood glucose quantitative analysis model with fourier transform infrared (FT-IR) spectroscopy, this paper uses a method named improved extended multiplicative scatter correction (Im-EMSC), which can effectively eliminate the scattering effects caused by human body strong scattering. The principal components of the differential spectra are used instead of the pure spectra of the analytes in this algorithm. Calibrate the unwanted physical characteristic through the shape of the curve of principal components, and extract the original glucose concentration information. Im-EMSC can efficiently remove most of the pathlength difference and baseline shift influences. Firstly, Im-EMSC is used as a preprocessing method, and then partial least squares (PLS) regression method is adopted to establish a quantitative analysis model. In this paper, the result of Im-EMSC is compared with those popular scattering correction algorithms of multiplicative scatter correction (MSC) and extended multiplicative scatter correction (EMSC) preprocessing methods. Experimental results show that the prediction accuracy has been greatly improved with Im-EMSC method, which is helpful for human noninvasive glucose concentration detection technology.

## 1. Introduction

Diabetes and its complications have been a heavy burden on the society. According to the International Diabetes Federation (IDF) latest statistics, there are 371 million individuals with diabetes worldwide in 2012 [1]. The control of blood glucose levels relies on blood glucose measurement. The tradition finger-prick way to measure blood glucose level is painful, potentially dangerous, and expensive to operate. In the last decades, many noninvasive methods [2–7] have been studied to measure blood glucose level.

Optical methods have been developed into the most powerful optical techniques of biomedical research and clinical application in noninvasive approaches for glucose monitoring in the last twenty years [8]. This noninvasive glucose measurement eliminates the painful pricking experience, risk of infection, and damage to finger tissue. The optical measurement of blood glucose is based on the light magnitude absorbed by glucose in blood at glucose absorption peaks, but

the measurement accuracy is still a barrier due to the weak signal from blood and interference of other blood components [9]. The mid-infrared (MIR) spectroscopy method is one of the most promising optical approaches. The absorption of glucose can be less influenced by other substances in mid-infrared region, with the narrow absorption peak [10], which makes it more easy to extract the glucose concentration information from the blood spectra. But because of the human body strong scattering effect, nonlinear relationship exists between glucose concentration and absorbance spectra [11, 12]. In order to successfully use FT-IR spectroscopy technique in noninvasive blood glucose measurement, the calibration model must provide a stable and predictive capacity. Therefore, it is important to eliminate the human body strong scattering impact and improve the robustness of the model. An improved extended multiplicative scatter correction (Im-EMSC) method is used to effectively solve these problems in this paper.

## 2. Experiment

**2.1. Experimental Instrument.** An attenuated total reflectance (ATR) accessory linked to a Thermo Nicolet 6700 FT-IR spectrometer, produced in the United States, was used. The ATR accessory was made of ZnSe crystal. The FT-IR spectrometer is equipped with a liquid nitrogen-cooled mercury cadmium telluride detector. The scanning range is 400~4000  $\text{cm}^{-1}$ , with 16 scan times, a resolution of 4  $\text{cm}^{-1}$ , and a gain of 1.

The reagent used is oral glucose powder produced by Peking University Third Hospital in Beijing, China.

**2.2. Acquisition of FT-IR Spectra.** Experiment procedure is described here. A healthy volunteer had been fasting for 8 h before this experiment began. The measurement site is the middle finger of right hand, which was in close contact with the cleaned ATR crystal in the experiment. Then he drank 100 mL water with 75 g glucose within 5 minutes; in succession the FT-IR spectra were collected from the finger every 12 minutes after cleaning the finger. At the time of sampling, the measurement position, measurement pressure, and the psychology of the volunteer were kept invariable as far as possible. In the meantime the corresponding blood glucose reference values were measured by the OneTouch Ultra 2 blood glucose meter produced by Johnson and Johnson Company, USA.

The experiment took 3 hours and a total of 17 FT-IR spectra were collected, including 11 spectra acquired in the first day with a glucose concentration range of 91.8~140.4 mg/dL and 6 spectra acquired in the second day with a glucose concentration range of 97.2~142.2 mg/dL.

## 3. Theory

**3.1. Im-EMSC Algorithm.** Stark and Martens developed multiplicative scatter correction (MSC) into the extended multiplicative scatter correction (EMSC) in 1989 [13]. The EMSC method employs the pure spectra of the analytes and interference effects to improve the optical pathlength estimation. Then, it is possible to reduce or eliminate the pathlength difference due to human body strong scattering in the preprocessing stage [14]. However, EMSC cannot be widely used due to a lack of the pure spectrum of chemical matter. In this paper, an improved EMSC (Im-EMSC) has been adopted. For this method, the principal components of the differential spectra are used instead of the pure spectrum of the interested analytes. Consequently, the scattering effects are corrected without any pure spectrum information.

The algorithm principle is as follows [15, 16].

The infrared spectral analysis is based on Lambert Beer's law [17]; under ideal conditions, the absorbance data  $Z_{i,\text{chem}}$  can be seen as a sum of the contributions from the different chemical constituents with spectra  $K = \{k_j, j = 1, 2, \dots, J\}$  and concentrations  $c_i = \{c_{ij}, j = 1, 2, \dots, J\}$ :

$$Z_{i,\text{chem}} = c_{i,1}k_1 + \dots + c_{i,j}k_j + \dots + c_{i,J}k_J. \quad (1)$$

Actually, there is a certain translation and rotation relationship between the measured spectra and the ideal spectra, taking into account that the scattering coefficients at all wavelengths are not the same; EMSC method expresses the measured spectra as follows:

$$Z_i \approx a_i I_r + b_i Z_{i,\text{chem}} + d_i \lambda + e_i \lambda^2, \quad (2)$$

where  $Z_i$  is a measured spectrum,  $Z_{i,\text{chem}}$  is ideal spectrum,  $I_r$  is identity matrix,  $\lambda$  is the wavelength, and  $a_i, b_i, d_i$ , and  $e_i$  are scalar parameters obtained by calibration.

So the equation can be rewritten as follows:

$$Z_i \approx a_i I_r + b_i (c_{i,1}k_1 + \dots + c_{i,j}k_j + \dots + c_{i,J}k_J) + d_i \lambda + e_i \lambda^2. \quad (3)$$

Spectrum (1)  $Z_{i,\text{chem}}$  may be rewritten as a deviation from a reference spectrum  $m$ , which could be, for example, the average of a set of empirical spectra as follows:

$$Z_{i,\text{chem}} = m + \Delta c_{i,1}k_1 + \dots + \Delta c_{i,j}k_j + \dots + \Delta c_{i,J}k_J. \quad (4)$$

In (4),  $\Delta c_{i,j}$  represents the deviations in the analyte and interference concentration compared with that of the reference sample.

Define the differential spectrum matrix  $Z_{\text{dif}}$ :

$$Z_{\text{dif}} = Z_i - m, \quad (5)$$

where  $Z_{\text{dif}}$  can be processed by principal components analysis (PCA); each load of the components can represent a specific factor. Then revoice  $Z_{\text{dif}}$  as follows:

$$Z_{\text{dif}} = t_1 p'_1 + t_2 p'_2 + \dots + t_j p'_j, \quad (6)$$

where  $p'_j$  is the principal component and  $t_j$  is the coefficient of the principal components.

Select the numbers of  $J$  as needed; these principal components not only contain the concentration differential information, but also include the different physical aspects (optical pathlength, the surface state, etc.). Determine the principal components that represent concentration information and physical characteristics through the shape of the curve of principal components. Calibrate the unwanted physical characteristic according to the actual needs and highlight information of the chemical concentration. Replace  $Z_{i,\text{chem}}$  by  $Z_{\text{dif}}$  and combine (3) and (6); then

$$Z_i = a_i I_r + b_i m + h_{i,1} p'_1 + h_{i,2} p'_2 + \dots + d_i \lambda + e_i \lambda^2 + \varepsilon_i, \quad (7)$$

where  $h_{i,j} = b_i t_j$ .

Let  $M = [I_r; m; p; \lambda; \lambda^2]$ , and let  $V_i = [a_i, b_i, h_i, d_i, e_i]$ ; construct calibration models using a multivariate linear calibration method such as PLS. The unnecessary principal components are defined as the interference factors and the left are defined as the effective factors. Correction spectrum can be obtained by subtracting the interference factors.

**3.2. Software.** The scattering correction algorithms and all the calculations were implemented in Matlab 2011 b.

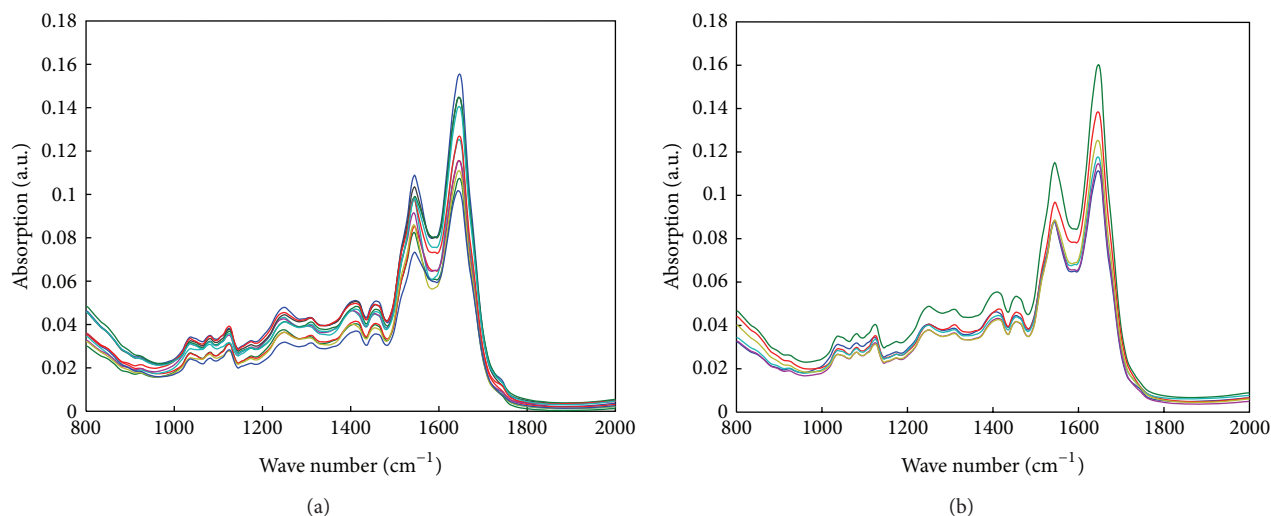


FIGURE 1: (a) The original spectra of the training set and (b) the original spectra of the test set.

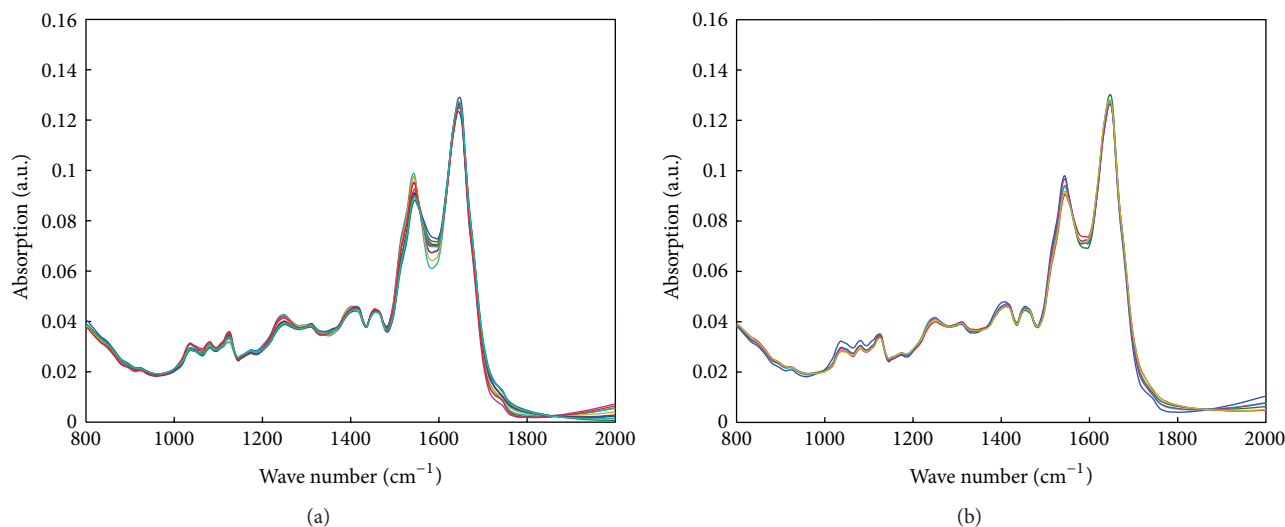


FIGURE 2: (a) The corrected spectra of the training set by Im-EMSC and (b) the corrected spectra of the test set by Im-EMSC.

## 4. Results and Discussion

**4.1. Model Selection and Comparison.** Two data sets were prepared. One is training set, consisting of 11 spectra acquired in the first day. The other is test set, consisting of the rest 6 spectra acquired in the second day. The wavelength region of 800–2000  $\text{cm}^{-1}$  was selected for calibration and predication. The original spectra are shown in Figure 1.

In this paper, the raw spectra were corrected by Im-EMSC first. The corrected spectra are shown in Figure 2.

Figure 2 shows the preprocessed spectra by Im-EMSC. All the spectra were normalized to an average estimated baseline level and an average estimated pathlength level. The variability in the spectra was much smaller.

PLS regression was constructed. Prediction results of the test set are shown in Table 1. Figure 3 gives the detailed comparison of the three preprocessing methods: Im-EMSC, EMSC, and MSC.

**4.2. Analysis of Experimental Results.** The predicted results of PLS regression after preprocessing by three methods are displayed in Table 1. RMSEP denotes the predictive accuracy of the calibration model.  $R$  denotes the correlation coefficient.

Table 1 shows that the best preprocessing method for scattering correction is Im-EMSC. Compared with the results from original data, RMSEP decreases from 9.3 mg/dL to 8.8 mg/dL. The predication accuracy increases by 5.4%. In addition,  $R$  increases from 0.86 to 0.95. The success of Im-EMSC is attributed to its avoiding of the request of matter pure spectrum, which limits the use of EMSC.

Because MSC and EMSC generated the overcorrection phenomenon, the prediction accuracy reduced in the experiment. As far as the methods of EMSC and MSC are concerned, scattering effects are assumed as a shift in the baseline and the average spectrum is used as a reference spectrum to eliminate the shift in the algorithm [18]. When



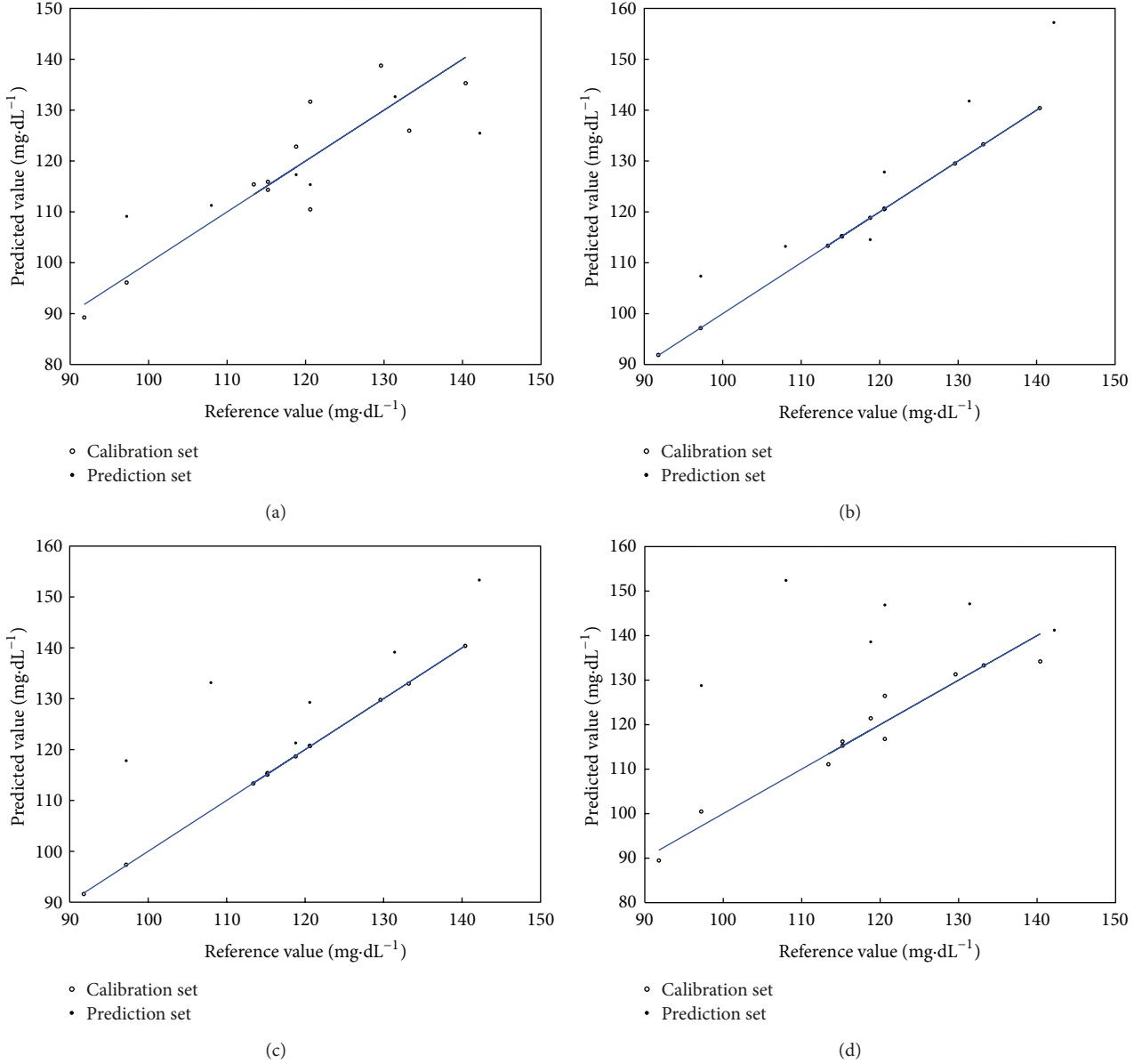


FIGURE 3: Distribution of predication results with different preprocessing methods. (a) The distribution of predication results of original spectra, (b) the distribution of predication results of the spectra preprocessed by Im-EMSC, (c) the distribution of predication results of the spectra preprocessed by Im-EMSC, and (d) the distribution of predication results of the spectra preprocessed by MSC.

TABLE 1: Prediction results of the test set with different preprocessing methods.

Preprocessing method	Principal components number	Root mean square error of prediction (RMSEP mg/dL)	Correlation coefficient ( $R$ )
Original	9	9.3	0.86
Im-EMSC	8	8.8	0.95
EMSC	11	15.1	0.85
MSC	5	26.8	0.34

the range of the concentrations of an interesting target is large, sometimes the actual chemical absorption information

is corrected as a baseline shift. The spectra with smaller concentrations information are overcorrected, which result in the low predication accuracy.

## 5. Conclusions

Due to human body strong scattering, the optical pathlength difference and baseline shift exist in blood glucose noninvasive measurement. In order to solve the problems and increase the predication accuracy, an appropriate method must be adopted in the preprocessing stage. Im-EMSC takes account of the wavelength effects, and simultaneously the principal components are used instead of a prior knowledge

about the analytes information. The scattering effects are absolutely corrected without any pure spectrum information. Im-EMSC is promising because it can raise the model prediction capability and robustness in human blood glucose noninvasive measurement using FT-IR spectroscopy.

## Conflict of Interests

The authors declare that there is no conflict of interests regarding the publication of this paper.

## Acknowledgment

This work is supported by Programs for Changjiang Scholars and Innovative Research Team (PCSIRT) in the University of China (IRT0705).

## References

- [1] International Diabetes Federation, *The IDF Diabetes Atlas*, International Diabetes Federation, 5th edition, 2012.
- [2] S. F. Malin, T. L. Ruchti, T. B. Blank, S. N. Thennadil, and S. L. Monfre, "Noninvasive prediction of glucose by near-infrared diffuse reflectance spectroscopy," *Clinical Chemistry*, vol. 45, no. 9, pp. 1651–1658, 1999.
- [3] S.-J. Yeh, C. F. Hanna, and O. S. Khalil, "Monitoring blood glucose changes in cutaneous tissue by temperature-modulated localized reflectance measurements," *Clinical Chemistry*, vol. 49, no. 6, pp. 924–934, 2003.
- [4] K. Maruo, M. Tsurugi, J. Chin et al., "Noninvasive blood glucose assay using a newly developed near-infrared system," *IEEE Journal on Selected Topics in Quantum Electronics*, vol. 9, no. 2, pp. 322–330, 2003.
- [5] I. A. Vitkin and R. C. N. Studinski, "Polarization preservation in diffusive scattering from in vivo turbid biological media: effects of tissue optical absorption in the exact backscattering direction," *Optics Communications*, vol. 190, no. 1–6, pp. 37–43, 2001.
- [6] A. M. K. Enejder, T.-W. Koo, J. Oh et al., "Blood analysis by Raman spectroscopy," *Optics Letters*, vol. 27, no. 22, pp. 2004–2006, 2002.
- [7] R. O. Esenaliev, K. V. Larin, I. V. Larina, and M. Motamedi, "Noninvasive monitoring of glucose concentration with optical coherence tomography," *Optics Letters*, vol. 26, no. 13, pp. 992–994, 2001.
- [8] N. S. Oliver, C. Toumazou, A. E. G. Cass, and D. G. Johnston, "Glucose sensors: a review of current and emerging technology," *Diabetic Medicine*, vol. 26, no. 3, pp. 197–210, 2009.
- [9] C.-F. So, K.-S. Choi, T. K. S. Wong, and J. W. Y. Chung, "Recent advances in noninvasive glucose monitoring," *Medical Devices*, vol. 5, pp. 45–52, 2012.
- [10] G. Li, M. Zhou, H.-J. Wu, and L. Lin, "The research status and development of noninvasive glucose optical measurements," *Spectroscopy and Spectral Analysis*, vol. 30, no. 10, pp. 2744–2747, 2010.
- [11] K. Kim, J.-M. Lee, and I.-B. Lee, "A novel multivariate regression approach based on kernel partial least squares with orthogonal signal correction," *Chemometrics and Intelligent Laboratory Systems*, vol. 79, no. 1–2, pp. 22–30, 2005.
- [12] X.-Y. Zhang, Q.-B. Li, and G.-J. Zhang, "Modified robust continuum regression by net analyte signal to improve prediction performance for data with outliers," *Chemometrics and Intelligent Laboratory Systems*, vol. 107, no. 2, pp. 333–342, 2011.
- [13] C. E. Miller and T. Naes, "A pathlength correction method for near-infrared spectroscopy," *Applied Spectroscopy*, vol. 44, no. 5, pp. 895–898, 1990.
- [14] H. Martens, J. P. Nielsen, and S. B. Engelsen, "Light scattering and light absorbance separated by extended multiplicative signal correction. Application to near-infrared transmission analysis of powder mixtures," *Analytical Chemistry*, vol. 75, no. 3, pp. 394–404, 2003.
- [15] H. Martens, S. W. Bruun, I. Adt, G. D. Sockalingum, and A. Kohler, "Pre-processing in biochemometrics: correction for path-length and temperature effects of water in FTIR biospectroscopy by EMSC," *Journal of Chemometrics*, vol. 20, no. 8–10, pp. 402–417, 2006.
- [16] Q.-X. Zhang, G.-J. Zhang, and Q.-B. Li, "A path-length correction method on biochemical parameter nondestructive measuring of folium," *Spectroscopy and Spectral Analysis*, vol. 30, no. 5, pp. 1310–1314, 2010.
- [17] H. Martens and E. Stark, "Extended multiplicative signal correction and spectral interference subtraction: new preprocessing methods for near infrared spectroscopy," *Journal of Pharmaceutical and Biomedical Analysis*, vol. 9, no. 8, pp. 625–635, 1991.
- [18] Q.-X. Zhang, Q.-B. Li, and G.-J. Zhang, "Scattering impact analysis and correction for leaf biochemical parameter estimation using Vis-NIR spectroscopy," *Spectroscopy*, vol. 26, no. 7, pp. 28–39, 2011.

## Research Article

# Effect of Nitric Acid on the Low Fluorescing Performance of Drilling Fluid Lubricant Based Animal and Vegetable Oils

Feng-shan Zhou,<sup>1</sup> Zheng-qiang Xiong,<sup>1,2</sup> Bao-lin Cui,<sup>1</sup> Feng-bao Liu,<sup>1,3</sup>  
Guang-huan Li,<sup>4</sup> Jin-ran Wei,<sup>4</sup> and Hua Cui<sup>4</sup>

<sup>1</sup> School of Materials Science and Technology, China University of Geosciences, Beijing 100083, China

<sup>2</sup> Beijing Institute of Exploration Engineering, Beijing 100083, China

<sup>3</sup> Tabei Exploratory & Development Department, PetroChina Tarim Oilfield Company, Korla 841000, China

<sup>4</sup> Drilling Fluid Technology Service Company, CNPC Bohai Drilling Engineering Ltd., Tianjin 300280, China

Correspondence should be addressed to Feng-shan Zhou; zhoufs@cugb.edu.cn

Received 5 September 2013; Accepted 21 October 2013

Academic Editor: Yizhuang Xu

Copyright © 2013 Feng-shan Zhou et al. This is an open access article distributed under the Creative Commons Attribution License, which permits unrestricted use, distribution, and reproduction in any medium, provided the original work is properly cited.

After synthesis of mixed fatty acid triethanolamine ester surfactant based on animal and vegetable mixed oils, the reaction solution was added into 4% (wt/wt) liquid nitric acid or 9% (wt/wt) solid nitric acid as eliminating fluorescent agent continuing to react from 1 to 2 hours. The low fluorescence lubricant named E167 for drilling fluid was prepared, in which maximum fluorescence intensity ( $F_{\max}$ ) was less than 10 in three-dimensional fluorescence spectra of excitation wavelength range. When the E167 was added into fresh water based drilling fluid at the dosage of 0.5% (wt/wt), the sticking coefficient reduced rate ( $\Delta K_f$ ) is 78% and the extreme pressure (E-P) friction coefficient reduced rate ( $\Delta f$ ) is 79%. In the case of 4% brine mud with 0.5% (wt/wt) E167 in it, the  $\Delta K_f$  and  $\Delta f$  are 75% and 62%, respectively. After the hot rolling ageing test  $180^\circ\text{C} \times 16\text{ h}$  with the E167 was added into fresh water based drilling fluid at the dosage of 1% (wt/wt), the  $\Delta K_f$  and  $\Delta f$  are greater than 70%, which shows a much better lubrication properties of strong resistance to high temperature. The fresh water based drilling fluid which contains 1% (wt/wt) E167 is almost nonfoaming even after hot rolling ageing  $120^\circ\text{C} \times 16\text{ h}$ .

## 1. Introduction

In the process of oil and gas drilling, in order to reduce the friction between drilling string and borehole, drilling string and casing, together with reducing the drill string torque and tripping resistance, lubricant often need to be added, thus avoiding sticking accident and improving the drilling speed.

The most commonly used liquid lubricants for drilling fluid are mineral oils and vegetable oils. The mineral oils are difficult to biodegrade, which causes serious pollution problems to the environment, and the high grade of fluorescence is unfavorable for geological logging. In the case of vegetable oils, with properties of low toxicity, good biodegradability, resource renewability, and low fluorescence level, it is a kind of lubricant for environment friendly using as drilling fluid with promising application [1–7].

There are at least three problems in unmodified vegetable oils [8–12]: (1) the vegetable oils have low thermal stability

in the process of hydrolysis, which are easy to saponify in alkaline environment, producing bubble of anion surfactant; (2) the adsorption consumption of water-soluble anion surfactant in the debris and borehole formation is larger than that of oil-soluble fat, which means that the consumption of lubricant after saponification is faster; namely, the lubricant after saponification is not durable; (3) with poor oxidation stability, the oil is easy to deteriorate resulting in stinking of drilling fluid, reducing and even losing the lubricating property. Therefore, chemical modification of vegetable oil is needed. The methods involved include hydrogenation [13], esterification [14, 15], and epoxidation [16].

The esterification modification of oil is studied in this paper using mixed oil as raw material, and the unsaturated bond of oil molecule was broken in the presence of nitric acid, and then a kind of low fluorescence lubricant with excellent lubricity was obtained.

## 2. Preparation and Performance Evaluation of Low Fluorescence Lubricant

**2.1. Materials and Apparatus.** The animal oil and vegetable oil were purchased, and solid nitric acid was prepared in our group. The purity of acid catalyst, triethanolamine, and nitric acid is all CP and GC for n-hexane.

The apparatus for measuring the adhesion coefficient was received Qingdao Haitongda Special Instruments Company; extreme pressure (E-P) lubrication device, OFI, USA; F-4600 fluorescence spectrophotometer, Hitachi, Japan; ZNN-D6S-six speed rotational viscometer and ZNS-2A-Low Pressure Filter Press, Qing Dao Haitongda Special Instruments Company; Infrared Spectrometer, Spectrum 100, Perkin Elmer, USA.

**2.2. Preparation of Low Fluorescence Lubricant E167.** Certain amounts of animal oil, vegetable oil, and acid catalyst were added into a three-necked flask equipped with a magnetic stirring bar, thermometer, and reflux condenser. The mixture was heated to corresponding temperature under stirring in given time, obtaining the ordinary lubricants without eliminating fluorescence. Then, the right amount of agent for eliminating fluorescence was added and the reaction continues for a certain time. Then, the target product was obtained.

**2.3. Evaluation of Fluorescence Properties.** At present, the UV visual for grading analysis method is commonly used for evaluating the fluorescent of drilling fluid lubricant. However, the method has the following problems [17]. (1) The wavelength emitted from UV lamp is around 365 nm, which is not enough to excite the fluorescence with wavelength lower than 365 nm. (2) Technically, it is difficult to accurately distinguish the fluorescence below 7 grades, using fluorescence logging instrument for naked-eye observation. (3) This method is only qualitative, but not quantitative, and with poor reproducibility. Therefore, according to the method described in patent by Patel [18], the fluorescence intensity of the lubricant  $F_{\max}$  was quantitatively measured by the three-dimensional fluorescence spectroscopy, and the three-dimensional fluorescence spectra were obtained according to the optimal excitation wavelength and emission wavelength of EM. Methods and parameters are as follows: mix the test sample with n-hexane according to the mass ratio 1:400 and then measure the fluorescence properties with fluorescence spectrophotometer; both excitation and emission slit widths were fixed at 2.5 nm, and scan rate was selected at  $1200 \text{ nm min}^{-1}$  and PMT voltage at 700 V.

**2.4. Evaluation of Lubricity.** The adhesion coefficient reduced rate ( $\Delta K_f$ ) and lubrication coefficient reduced rate ( $\Delta f$ ) are evaluation indicators of lubricity. The evaluation methods are according to drilling fluid liquid lubricant technical indicators Q/SY 1088-2007 [19].

**2.5. The Evaluation of Rheological Properties.** The rheological parameters apparent viscosity (AV), plastic viscosity (PV),

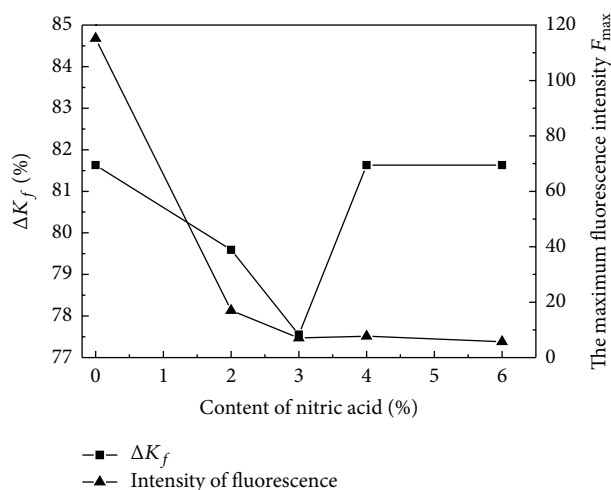


FIGURE 1

yield point (YP), and filtration at the room temperature ( $FL_{API}$ ) were investigated according to the first part of the field testing of drilling GB-T 16783.1-2006 [20].

**2.6. Evaluation of Foamability.** The method of foamability evaluation was performed referring to the technical requirements and analytical methods of drilling fluid lubricant Q/SY TZ 0022-2000 [21].

## 3. Results and Discussion

**3.1. The Mechanism of Eliminating Fluorescence.** Concentrated nitric acid in the reaction system decomposed nitrogen dioxide, with which the nitration reaction of unsaturated bond on the vegetable oil molecular chain occurred at high temperature [22]. The mechanism of reaction was proposed (see Figure 1).

According to the theory of fluorescence spectroscopy, the main functional groups of fluorescence are double bond, conjugated double bonds, benzene, and fused ring structure with  $\pi$  electron, wherein the benzene and fused ring structure have strong fluorescence emission property [23]. Therefore, after the oxidation of double bonds on the molecular chain of vegetable oil, the amount of  $\pi$  bond decreases and the fluorescence intensity of lubricant is weakened.

With cheap and strong oxidation characteristics, the nitric acid was chosen as the fluorescent eliminating agent, which broke the  $\pi$  bond of double bonds and reduced the fluorescence level, and then the low fluorescence lubricant was obtained.

### 3.2. The Optimization of Eliminating the Fluorescence

**3.2.1. Effect of Nitric Acid Content on Properties of Low Fluorescence Lubricant.** At a certain temperature, fixing the amount of lubricants, the liquid nitric acid was changed to react for 1 h, and the effect of nitric acid content on properties of low fluorescence lubricant was shown in Figure 2.

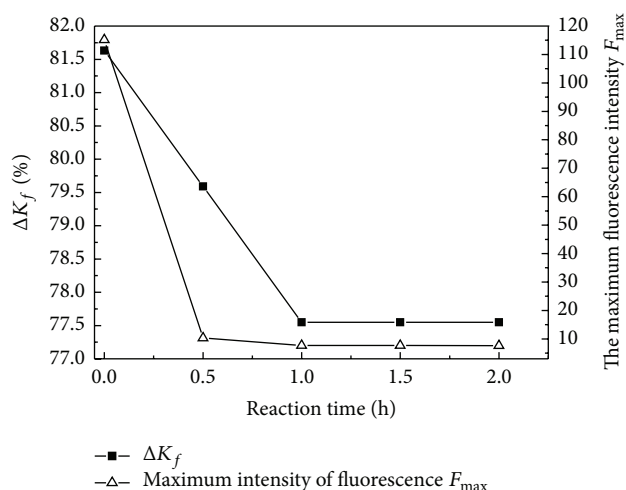


FIGURE 2: Effect of nitric acid content on properties of low fluorescence lubricant.

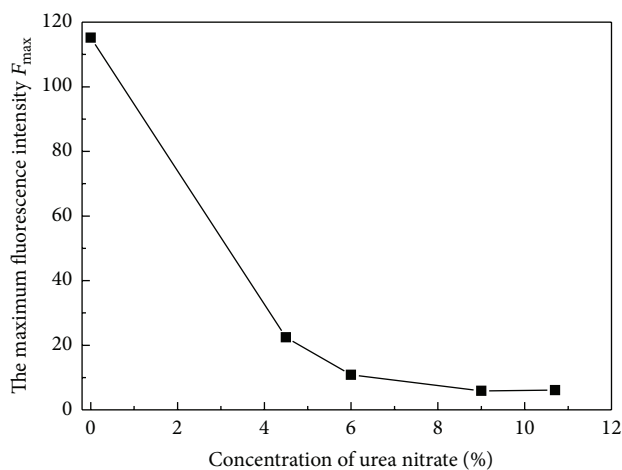


FIGURE 3: Effect of reaction time on performance of low fluorescence lubricant.

It can be seen from Figure 2 that the maximum fluorescence intensity of low fluorescence lubricant decreases gradually with the increase of nitric acid content, while the  $\Delta K_f$  decreases first and then increases. When the dosage of nitric acid is 4% (wt/wt), the fluorescence properties showed the lowest maximum fluorescence intensity ( $F_{\max}$  7.725) and high value of  $\Delta K_f$  (81.63%). So 4% of nitric acid content is chosen.

**3.2.2. Effect of Reaction Time on Performance of Low Fluorescence Lubricant.** At high temperature, the effect of reaction time on properties of low fluorescence lubricant was investigated after adding 4% of liquid nitric acid.

It can be seen in Figure 3 that the performance of low fluorescence lubricant presents regular changes with time changing. The value of  $\Delta K_f$  reduced to remain changeless after 77.55%, while the maximum fluorescence intensity decreased in larger in half an hour and then changed little after one hour.

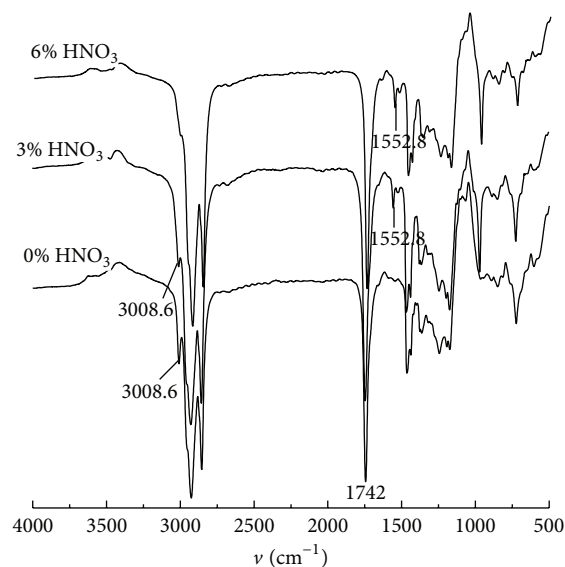


FIGURE 4: Effect of urea nitrate content on the maximum fluorescence intensity of low fluorescing lubricant.

As the reaction time increased, the unsaturated bonds were oxidated, then a part of the molecular chain was broken into small molecular compounds, leading to a reduction of the lubrication performance, and the fluorescence of lubricant intensity decreased meanwhile. In consideration of the fact that the value of  $\Delta K_f$  is 77.55% after 1 hour, the reaction time for eliminating fluorescence was 1 hour.

**3.2.3. Influence of Urea Nitrate Amount on the Maximum Fluorescence Intensity of Low Fluorescing Lubricant.** There is danger of using nitric acid liquid operating at high temperature; hence, it is necessary to use urea nitrate for instead. At the same conditions, the effect of urea nitrate content on performance of low fluorescence lubricant was also investigated at fixed reaction time (1 hour).

As shown in Figure 4, the value of the maximum fluorescence intensity reduced with the urea nitrate content increasing. The intensity value decreased to 5.871 when the amount of urea nitrate was increased to 9%. The low fluorescence lubricant produced by urea nitrate is with high freezing point and obvious particle, and it is easy to adhere to beaker. However, that produced by liquid nitrate does not have these disadvantages. Even so, the liquid urea nitrate is easy to store and use, and is of low cost as well. Whether using urea nitrate or liquid nitric acid as the fluorescent eliminating agent depends on the manufacturer.

**3.2.4. The Effect of Eliminating Fluorescence Reaction on the Structure of Lubricant.** The low fluorescence lubricants prepared with different dosages of nitric acid (reaction time 1 h) were characterized by FTIR, and the results were demonstrated in Figure 5.

It can be seen that characteristic peak at  $1742\text{ cm}^{-1}$  is related to stretching vibration of carbonyl ( $\text{C}=\text{O}$ ) for ester group. The peak at  $3008.6\text{ cm}^{-1}$  was assigned to  $=\text{C}-\text{H}$  and



TABLE 1: Fluorescence characteristics of lubricant before and after elimination of fluorescence.

Lubricant	The maximum fluorescence intensity $F_{\max}$	Corresponding EX (nm)	Corresponding EM (nm)
E167	7.725	258	332.0
Ordinary lubricant	115.2	300	385.6

The fluorescence grades of E167 are 2-3.

TABLE 2: Rheology variation of fresh water mud before and after adding E167.

Experimental condition	Content of E167 (%)	AV (mPa·s)	PV (mPa·s)	YP (Pa)	FL <sub>API</sub> (mL)
Room temperature	0	10.5	6	4.3	19.2
	0.5	11.5	6	5.7	18.4
	1.0	12.5	6	6.2	16.8
150°C × 16 h	0	17.0	8	9.1	26.0
	0.5	17.7	8	9.8	24.0
	1.0	18.0	8	10.1	24.0
180°C × 16 h	0	18.0	7	5.1	24.0
	0.5	19.0	8	10.5	26.0
	1.0	17.3	8	7.4	24.0

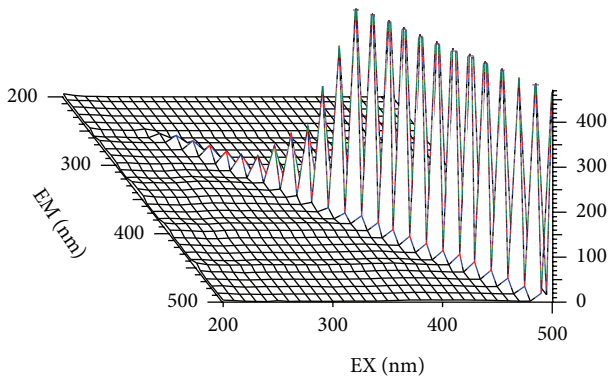


FIGURE 5: FTIR spectra of low fluorescing lubricant with different amount of nitric acid.

the  $1552\text{ cm}^{-1}$  peak was related to stretching vibration of  $-\text{C}-\text{NO}_2$ . The peak at  $3008.6\text{ cm}^{-1}$  was obvious without nitric acid, which decreased with the increase of nitric acid content, and the stretching vibration of  $-\text{NO}_2$  at  $1552\text{ cm}^{-1}$  occurred simultaneously. When the nitrate concentration is 6%, the peak at  $3008.6\text{ cm}^{-1}$  is not obvious. The variation of peaks in the spectra illustrated that the nitration reaction took place with  $\text{C}=\text{C}$  bond broken and  $\text{C}-\text{NO}_2$  formation.

**3.2.5. Effect of Elimination of Fluorescent Reaction on the Fluorescence Characteristics of Lubricant.** Table 1 demonstrated the fluorescence characteristics of lubricant before and after elimination of fluorescence, which showed that the maximum fluorescence intensity, the corresponding optimal excitation and emission wavelength are changed.

Figures 6 and 7 are 3D fluorescence spectra of E167 and ordinary lubricant, respectively. Comparing Figures 6 and 7, the ordinary lubricant shows fluorescence peak curve in three-dimensional map without nitrate. However, the fluorescence intensity peak of E167 was not presented on the

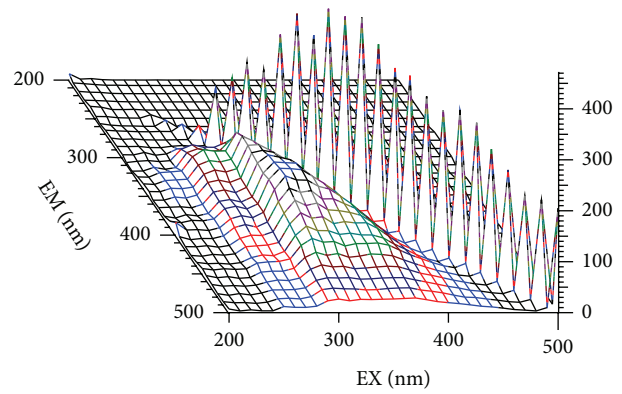


FIGURE 6: 3D fluorescence spectra of E167.

map after eliminating fluorescence. The results illustrated that the low fluorescing lubricant E167 prepared by reacting 4% liquid nitric acid for 1 hour has low intensity of fluorescence. The strong peaks on the diagonal were produced by the instrument itself, which cannot be avoided when the scan ranges of both EX and MX were set at 200–500 nm.

### 3.3. The Comprehensive Performance Evaluation of E167

**3.3.1. Rheological Properties.** Adding E167 into fresh water based mud and brine based mud, respectively, the rheological properties of E167 in 5.2% bentonite fresh water based mud (Weifang, Shandong) and 4% brine based mud systems were measured and the results were shown in Tables 2 and 3.

It can be seen from Table 2, in fresh water based mud, that both the apparent viscosity and yield point increased slightly, and the filter loss of API decreased mildly after adding into E167.

As shown in Table 3, in brine based mud, the same regularity was obtained: both the apparent viscosity and

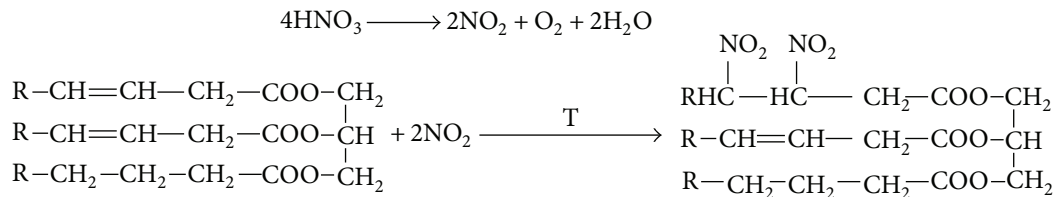


FIGURE 7: 3D fluorescence spectra of ordinary lubricant.

TABLE 3: Rheology variation of brine mud before and after adding E167.

Experimental condition	Content of E167 (%)	AV (mPa·s)	PV (mPa·s)	YP (Pa)	FL <sub>API</sub> (mL)
Room temperature	0	4.5	2	2.4	66
	0.5	4.8	3	2.2	66
	1.0	5.0	3	2.4	68
150°C × 16 h	0	3.5	3	1.0	104
	0.5	3.7	3	1.2	96
	1.0	4.0	3	1.4	86
180°C × 16 h	0	3.7	2	1.0	112
	0.5	4.0	2	2.4	106
	1.0	4.3	3	1.2	94

TABLE 4: Foaming rate of E167 at different conditions.

Sample	Experimental condition	Foaming rate (%)
Distilled water + 0.5% X-E167	Room temperature	3.3
Fresh water mud + 1.0% X-E167	Room temperature	6.7
Fresh water mud + 1.0% X-E167	Thermal ageing 120°C × 16 h	5.0
Fresh water mud + 1.0% X-E167	Thermal ageing 150°C × 16 h	43.3

Fresh water mud is mixed with 3.7% bentonite and distilled water (Chifeng Tianyu), pH = 9, AV = 8–9 mPa·s.

yield point increased slightly, and the filter loss of API decreased, meaning that the addition of E167 had no impact on rheological properties of the drilling fluid.

**3.3.2. Foamability.** The foaming performance at room temperature and thermal ageing at high temperature were evaluated after adding the E167 into fresh water based mud system. The methods of determining thermal ageing foaming rate are as follows: add 2.00 g sample into 400 mL fresh water based mud and put it into the aging tank after stirring 5 min. The mixture was thermal aged for 16 h at setting temperature, mixing with glass rod and then taking 300 mL mixture which was stirred for 5 min at 10000 r/min speed. After tiring, put the 300 mL mixture into 500 mL cylinder in 10 s, read the total volume at 30 s, and then calculate the foaming rate according to the formula.

Table 4 showed that, at the dosage of 1%, the E167 had weak foamability after thermal ageing for 16 h at 120°C, while the foaming was strong with the same time of hot rolling at 150°C. That is because the fat was hydrolyzed to form fatty acid at high temperature and then reacted with bases to form anionic surfactant sodium carboxylate, causing the enhancement of foaming capacity.

**3.3.3. Lubricity.** Adding E167 into 5.2% bentonite fresh water based mud (Weifang, Shandong) and 4% brine based mud successively, the lubricity and salt resistance were investigated as shown in Table 5.

It can be seen from the table that the E167 has good lubricant performance. In case of changing conditions, such as thermal aged at 180°C for 16 h and even in the 4% brine based mud, the values of  $\Delta K_f$  and  $\Delta f$  changed a little, which means that the E167 with good lubricity has relatively good temperature resistance and salt resistance.

**3.3.4. Comparison of Properties with Other Low Fluorescence Lubricants.** We selected two kinds of oil based low fluorescence lubricant with comprehensive performance on scene as a contrast sample, which were from Shengli Oilfield (S-WD) and Tarim Oilfield (T-YS), respectively. The properties of lubrication, fluorescence, and foaming rate were determined as shown in Table 6.

Compared with commercially available excellent products, the low fluorescence lubricant E167 prepared in this work has outstanding properties. Moreover, the comprehensive foaming performance after thermal ageing was superior to the contrast sample.

TABLE 5: The evaluation of lubricity for E167.

Type of mud	Content of E167 (%)	$\Delta K_f$ (%)	$\Delta f$ (%)	Testing condition
Fresh water mud	0.5	77.55	79.14	At room temperature
	1.0	77.55	76.82	At room temperature
	1.0	71.33	70.27	Thermal ageing $180^\circ\text{C} \times 16\text{ h}$ and then at room temperature
Brine mud	0.5	75.00	62.43	At room temperature
	1.0	77.08	66.60	At room temperature
	1.0	73.55	64.30	Thermal ageing $180^\circ\text{C} \times 16\text{ h}$ and then at room temperature

TABLE 6: Comparison of three kinds of oil based properties of low fluorescence lubricant.

Properties	Methods and technical indicators	Low fluorescence lubricant		
		E167	S-WD	T-YS
Lubricity	$\Delta K_f$ (%)	77.55	75.51	77.55
	$\Delta f$ (%)	76.82	77.02	68.07
	$F_{\max}$	7.08	10.50	10.98
Fluorescence performance	Corresponding of $F_{\max}$ EX (nm)	258	274	376
	Corresponding of $F_{\max}$ EM (nm)	332	325	444
	Mud + 1% X-E167, at room temperature	5.0	8.3	10.0
Foaming rate (%)	Mud + 1% X-E167, after thermal ageing $120^\circ\text{C} \times 16\text{ h}$	6.7	13.0	31.7
	Mud + 1% X-E167, after thermal ageing $150^\circ\text{C} \times 16\text{ h}$	43.3	48.0	45.0

#### 4. Conclusion

In summary, the low fluorescence lubricant used for drilling fluid was prepared, taking animal and vegetable oil as raw material. The properties were studied by many methods. It is revealed from the experimental results that, with the addition of concentrated nitric acid, the modified lubricant was qualified in low fluorescence and comprehensive good lubricating performance. In view of the influence of temperature, the E167 exhibited good lubricity after thermal ageing at  $180^\circ\text{C}$  for 16 hours showing properties of high-temperature resistance. The foaming rate of E167 was lower when compared with similar products although which exhibited serious foaming phenomenon.

#### Conflict of Interests

The authors declare that there is no conflict of interests regarding the publication of this paper.

#### References

- [1] D.-J. Li, "Status and advances of drilling fluid lubricants," *Petroleum Drilling Techniques*, vol. 26, no. 2, pp. 35–38, 1998.
- [2] R. Caenn, H. C. H. Darley, and G. R. Gray, *Composition and Properties of Drilling and Completion Fluids*, Gulf Professional Publishing, 6th edition, 2011.
- [3] G.-J. Lv, "Low-fluorescence anti-blocking lubricant for drilling fluid and production method thereof," CN, 101717621 A, 2010-6-2.
- [4] G.-S. Feng, C.-S. Li, H. Tang, and W.-J. Wang, "Compound type vegetable oil lubricating agent for drilling fluid and preparation method thereof," CN, 101760186 A, 2010-6-30.
- [5] A. D. Patel, E. Stamatakis, S. Young et al., "High performance water based drilling fluid," US: 2008/0009422 A1, 2008-1-10.
- [6] D. Knox and P. Jiang, "Drilling further with water-based fluids—selecting the right lubricant," in *Proceedings of the SPE International Symposium on Oilfield Chemistry*, pp. 9–15, The Woodlands, Tex, USA, February 2005.
- [7] H. Wagner, R. Luther, and T. Mang, "Lubricant base fluids based on renewable raw materials: their catalytic manufacture and modification," *Applied Catalysis A*, vol. 221, no. 1-2, pp. 429–442, 2001.
- [8] N. J. Fox and G. W. Stachowiak, "Vegetable oil-based lubricants—A review of oxidation," *Tribology International*, vol. 40, no. 7, pp. 1035–1046, 2007.
- [9] P. Mousavi, D. Wang, C. S. Grant, W. Oxenham, and P. J. Hauser, "Measuring thermal degradation of a polyol ester lubricant in liquid phase," *Industrial and Engineering Chemistry Research*, vol. 44, no. 15, pp. 5455–5465, 2005.
- [10] S. Z. Erhan, B. K. Sharma, Z. Liu, and A. Adhvaryu, "Lubricant base stock potential of chemically modified vegetable oils," *Journal of Agricultural and Food Chemistry*, vol. 56, no. 19, pp. 8919–8925, 2008.
- [11] B.-R. Höhn, K. Michaelis, and R. Döbereiner, "Load carrying capacity properties of fast biodegradable gear lubricants@," *Lubrication Engineering*, vol. 55, no. 11, pp. 15–38, 1999.
- [12] B. Krzan and J. Vizintin, "Tribological properties of an environmentally adopted universal tractor transmission oil based on vegetable oil," *Tribology International*, no. 36, pp. 826–832, 2003.
- [13] J.-H. Liu and A.-Y. Qiu, "New progress in hydrogenation technology of vegetable oil(I)," *China Oils and Fats*, vol. 28, no. 8, pp. 13–17, 2003.
- [14] S.-Y. Song, "Drilling fluid lubricating additive and its preparing method," CN, 1743404A, 2006-3-8.
- [15] H. Chun, W.-L. Xie, and W. Guo, "Study on synthesis and characterization of triethanolamine dilaurate," *Cereals & Oils*, no. 7, pp. 11–13, 2008.

- [16] X. Wu, X. Zhang, S. Yang, H. Chen, and D. Wang, "Study of epoxidized rapeseed oil used as a potential biodegradable lubricant," *Journal of the American Oil Chemists' Society*, vol. 77, no. 5, pp. 561–563, 2000.
- [17] A.-J. Liu, "Understanding and pondering over fluorescence problem of drilling fluid additives," *Drilling Fluid and Completion Fluid*, vol. 20, no. 2, pp. 9–12, 2003.
- [18] A. D. Patel, "Non-fluorescing oil-based drilling fluid," US, 5869433, 1999-2-9.
- [19] Q/SY, 1088-2007, "Specifications of liquid lubricants used in drilling fluids," China National Petroleum Corporation. 12, 2006.
- [20] GB-T, 16783. 1-2006, "Petroleum and natural gas industries-Field testing of drilling fluids-Part 1: water-based fluids," China National Standard. 12, 2006.
- [21] Q/SY TZ, 0022-2000, "Specifications and analytical methods for drilling fluid lubricants," Tarim Oilfield of China National Petroleum Corporation. 12, 2000.
- [22] D. Hace, V. Kovacevic, and D. Pajc-Liplin, "Thermally stimulated oxidative degradation of high impact polystyrene with nitric acid," *Polymer Engineering and Science*, vol. 36, no. 8, pp. 1140–1151, 1996.
- [23] Y.-Q. Liu, *Modern Instrumental Analysis*, Higher Education Press, Beijing, China, 2006.